

Development of a Surface-Enhanced Raman Sensor for Detection in  
Complex Mixtures

A DISSERTATION  
SUBMITTED TO THE FACULTY OF THE GRADUATE SCHOOL  
OF THE UNIVERSITY OF MINNESOTA  
BY

Kyle Christine Bantz

IN PARTIAL FULFILLMENT OF THE REQUIREMENTS  
FOR THE DEGREE OF  
DOCTOR OF PHILOSOPHY

Christy L. Haynes, Advisor

December, 2011



## **Acknowledgements**

I would like to thank my advisor, Christy Haynes, for her guidance and support. Her passion for science and education has been a source of inspiration. Her sense of adventure and fun has also caused the years here to fly by. I count myself fortunate to be one of her students. I am honored and humbled to be one of the first few graduates from this research group.

I would also like to thank the members of the Haynes research group. You are an amazing group of scientific minds and wonderful friends. I have learned so much from each and every one of you. I would like to thank Audrey Meyer for her assistance with the SERS biosensing project and Dr. Nate Wittenberg for his initial work on the potential packing in Chapter Three.

Science is a collaborative field and I was fortunate to have found wonderful collaborators in Prof. Sang-Hyun Oh's research group. I have thoroughly enjoyed working with Prof. Oh, Hyungsoon Im and Si Hoon Lee. They are amazing engineers I worked with to develop the nanogap and nanohole SERS substrates listed in Chapter Two.

I have been very lucky to have worked with a number of talented and hard working undergraduate students. I would like to acknowledge Courtney Jones for her work on PAH and PBDE detection listed in Chapter 4. Heidi Nelson worked hard to gather all of the localized surface plasmon resonance data in Chapter 3. It has been a delight to have mentored so many students and I know that they will do amazing things in the future.

I would like to thank my husband Ian for his support (both technical and emotional) during graduate school. I do not know if I can put into words just how amazing it is to have someone like him in my life. I am also grateful for the love and support I receive both my parents and Ian's parents. I was also lucky to have a great friend in Prof. Andy Wildenberg, whose many insights on graduate school/academia, stories and encouragements have been a great help during this time in my life.

For my husband, Ian Dees, an intelligent, loving and ever supportive partner.

Also, for my friend, Bert Kleerup, may your love of science and curious nature  
never be forgotten.

## **Abstract**

Surface-enhanced Raman scattering (SERS) is a powerful analytical signal transduction mechanism for the detection of analytes in aqueous environments, largely free from interfering water signals and capable of obtaining unique molecular signatures from structurally similar analytes. These characteristics make SERS ideal for the detection of analytes of interest from biological and environmental settings. To achieve the low limits of detection needed for biological and environmental analyte detection, new SERS platforms with the highest possible enhancement factors (EF) need to be developed. Traditionally, SERS has had limited analytical use because the analyte of interest must dwell on or near the Ag, Au or Cu surfaces, regardless of substrate EF. To overcome this limitation this work employs alkanethiol partition layers in combination with novel SERS platforms for the detection of environmental pollutants (eg. polychlorinated biphenyls and polycyclic aromatic hydrocarbons) and bioactive lipids. As the use of partition layers continues to increase and more SERS platforms with higher EF are developed, the use of SERS for analytical applications will increase. Overall, this work demonstrates the power of using novel SERS platforms combined with partition layers and reveals great promise for the future of environmental and biological sensing with SERS.

Chapter One reviews the use of surface-enhanced Raman scattering detection in complex mixtures that have emerged in the last 10 years. SERS been employed for small molecule detection all the way to more complex systems, such as detection in living cells, and this chapter reviews the recent advancements and looks toward the future of SERS detection in biological systems. Chapter Two details the fabrication and characterization of new novel substrates for SERS sensing. In this chapter, three substrates are discussed, each with their own fabrication method and SERS sensing

application. The majority of our SERS sensing schemes for non-traditional SERS analytes employ a partition layer-covered SERS substrate. In Chapter Three, I investigated what fundamental properties of an alkanethiol partition layer make it an ideal partition layer for particular analytes. I discovered both the thickness of the monolayer and the amount of disorder in the partition layer that allows for analyte partitioning and are critical for facilitating the analyte to dwell within the zone of enhancement for SERS.

The last two chapters detail the implementation of partition layer-modified SERS substrates for detection in complex mixtures. Chapter Four demonstrates the use of partition layer-modified SERS substrates for the detection of environmental pollutants: polycyclic aromatic hydrocarbons, polychlorinated biphenyls and polybrominated diphenyl ethers. I was able to show that our substrate made it possible to detect and discriminate between structurally similar analytes in the presence of interfering species at environmentally relevant concentrations. The final chapter of this dissertation describes the steps I have taken towards SERS sensing in complex biological mixtures for the detection of bioactive lipids. The results of this investigation indicate that partition layer-modified AgFON substrates can facilitate the detection of phospholipids and secreted lipids at higher concentrations, but the SERS bands from the partition layer make detection of lipids at physiologically relevant concentrations challenging at this time.

## **Table of Contents**

Acknowledgements	i
Abstract	iii
List of Tables	ix
List of Figures	x
List of Abbreviations and Symbols	xiii

### **Chapter One**

#### **Introduction to Surface-Enhanced Raman Scattering in Complex Mixtures**

1.1 General Overview	2
1.2 What is SERS and how is it used?	2
1.2.1 Why is SERS a good candidate for complex mixtures?	5
1.2.2 What are potential limitations to using SERS for sensing?	6
1.3 What substrates have been used for SERS?	8
1.4 Small Molecule SERS Sensing	12
1.5 DNA/Aptamer SERS Biosensing	22
1.6 Protein/Enzyme/Peptide/Antibody SERS Sensing	30
1.7 Cellular and In vivo Sensing	38
1.8 Perspective	42
1.9 Conclusion	44

### **Chapter Two**

#### **Development of Novel Substrates for Surface-Enhanced Raman Scattering**

2.1 Introduction	46
2.2 Polymer-Templated Nanostructure SERS Substrate	47
2.2.1 Experimental Methods	49
2.2.1.1 Materials	49
2.2.1.2 Nanostructure Fabrication	49
2.2.1.3 Physical Nanostructure Characterization	51

2.2.1.4 Optical Nanostructure Characterization	51
2.2.1.5 Surface-Enhanced Raman Scattering	52
2.2.1.6 Robustness Assessment	53
2.2.1.7 Statistical Analysis	53
2.2.2 Results and Discussion	54
2.2.2.1 Polymer-Templated Nanostructures Fabricated with Varied Seed Nanoparticles	54
2.2.2.2 Polymer-Templated Nanostructures Fabricated with Varied Ionic Strength	55
2.2.2.3 Polymer-Templated Nanostructure Robustness	57
2.2.3 Conclusions	61
2.3 Self-Assembled Plasmonic Nanohole Arrays	62
2.3.1 Experimental Methods	67
2.3.1.1 Materials	67
2.3.1.2 Preparation of Substrates	68
2.3.1.3 Colloidal Self-Assembly of Hexagonal Close-Packed Nanohole Arrays	68
2.3.1.4 Electroless Plating	69
2.3.1.5 SEM Characterization	70
2.3.1.6 Optical Characterization	70
2.3.1.7 EF Calculation	71
2.3.2 Results and Discussion	71
2.3.2.1 NSL Process for Self-Assembly of Periodic Nanohole Arrays	71
2.3.2.2 Transmission Spectra and FDTD Simulation	74
2.3.2.3 SERS Measurements	77
2.3.3 Conclusions	81
2.4 Nanogap Substrates for SERS Sensing	82
2.4.1 Results and Discussion	84
2.4.2 Conclusions	88

### **Chapter Three**

#### **A Fundamental Study of Self-Assembled Monolayers on AgFON Substrates**

3.1 Introduction	92
3.2 Experimental Methods	95
3.2.1 Materials	95
3.2.1 Substrate Fabrication	95

3.2.3 LSPR Measurements	96
3.2.4 Surface Modification	96
3.2.5 SERS Measurements	97
3.2.6 LSPR Thickness Calculation	98
3.2.7 Statistical Methods	98
3.3 Results and Discussion	98
3.3.1 Assessing Monolayer Formation	99
3.3.2 Assessing Monolayer Thickness	102
3.3.3 Assessing Monolayer Crystallinity	104
3.3.4 Assessing Analyte Partitioning	109
3.4 Conclusions	109

## **Chapter Four**

### **Partition Layer-Modified Substrates for Surface-Enhanced Raman Scattering Detection of Complex Environmental Mixtures**

4.1 Introduction	112
4.1.1 Polychlorinated Biphenyls	114
4.1.2 Polycyclic Aromatic Hydrocarbons	115
4.2 Experimental Methods	116
4.2.1 Materials	116
4.2.2 SERS Substrate Fabrication and Characterization	117
4.2.3 Optical Characterization	119
4.2.4 SERS Instrumentation	120
4.2.5 Statistical Analysis	120
4.3 Results and Discussion	121
4.3.1 Effect of Partition Layer SAM	121
4.3.2 Identification of PAH Bands for Analysis	123
4.3.3 Sensitivity of the Decanethiol-coated AgFON to Environmental Pollutants	125
4.3.4 Distinguishing between PCB and PAH Compounds using SERS	129
4.3.5 Dissolved Organic Matter does not Inhibit SERS Detection of PCB-47 or PAHs	131
4.3.6 Reversibility of Pollutant Partitioning and Reusability of the SERS Sensor	131
4.3.7 Insight into the Partitioning Mechanism	134
4.3.8 Comparison of the PAH and PCB Detection with DT-coated AgFON	136
4.3.9 Detection of Polybrominated Diphenyl Ethers	138
4.4 Conclusions	138

## **Chapter Five**

## **Partition Layer-Modified Substrates for Surface-Enhanced Raman Scattering Detection in Biological Mixtures**

5.1 Introduction	141
5.2 Experimental Methods	143
5.2.1 Materials	143
5.2.2 SERS Substrate Fabrication and Characterization	144
5.2.3 SERS Instrumentation	144
5.2.4 Statistical Analysis	145
5.3 Results and Discussion	145
5.3.1 Utilizing Partition Layers for Lipid Detection	145
5.3.2 Identification of Lipid Bands for SERS Analysis	147
5.3.3 Sensitivity of Partition Layers to Phospholipids and Secreted Lipids	150
5.3.4 Distinguishing between Phosphatidylserine and Phosphatidylcholine	151
5.3.5 Insight into Lipid Partitioning Mechanism	151
5.3.6 Comparison of Partition layers for Secreted Lipids and Phospholipid Detection	152
5.4 Conclusions	154
<b><u>Chapter 6</u></b>	
<b>Conclusion and Future Work</b>	156
<b><u>Bibliography</u></b>	159
<b><u>Appendix</u></b>	
<b>Curriculum Vitae</b>	173

## List of Tables

### Chapter One

1.1 Metallic Nanostructures for SERS	11
--------------------------------------	----

### Chapter Two

2.1 Analysis of Polymer-Templated Nanostructures with Varied Ionic Strength	56
2.2 SEM-Determined Substrate Surface Areas	72
2.3 Average EF Values over Three Different Wavelengths	78
2.4 Average EF Values for Two Different Plating Conditions and Wavelengths	80
2.5 Surface Areas Used to Calculate Spatially Averaged and Local EFs	87

### Chapter Three

3.1 $\lambda_{\max}$ LSPR Shifts for Potential Packed Substrates	101
--	-----

### Chapter Four

4.1 SERS Band Ratios for Anthracene, Pyrene and DT	137
--	-----

## List of Figures

### Chapter One

1.1 SEM image of AgFON	9
1.2 SERS spectra of DMPC vesicles	18
1.3 A flatbed scanner image of Raman probes	28
1.4 Detection scheme for label-free protein sensing with SERS	33
1.5 Schematic of SERS immunoassay	35
1.6 <i>In vivo</i> cancer marker detection using SERS	41

### Chapter Two

2.1 Schematic of the polymer-templated nanostructure substrate preparation	50
2.2 AFM images of five polymer-templated nanostructure substrates	55
2.3 SERS spectra on a BZT-doped polymer-templated nanostructure	57
2.4 Extinction spectra measured from BZT-doped polymer-templated	58
2.5 Robustness of PTN substrate vs AgFON	59
2.6 Nanohole fabrication scheme	69
2.7 SEM of nanohole arrays	73
2.8 Schematic of angle deposition	74
2.9 FDTD transmission spectra	75
2.10 FDTD intensity map of the plasmonic field	76
2.11 SERS spectra of BZT on nanohole array	77
2.12 SEM of electroless plated nanohole arrays	79
2.13 SERS spectra of electroless plated nanohole arrays	81
2.14 Nanogap fabrication scheme	83
2.15 SEM images of different types of nanogap arrays	85

2.16 Confocal imaging of SERS substrates	86
2.17 Local enhancement factors	88
<b>Chapter Three</b>	
3.1 LSPR spectra of alkanethiols on AgFONs	100
3.2 LSPR shifts for alkanethiols on AgFONs	102
3.3 Alkanethiol monolayer thickness	103
3.4 SERS of decanethiol	104
3.5 Plots of the C-C <sub>T</sub> /C-C <sub>G</sub> crystallinity ratio	105
3.6 Change in C-S gauche band	106
3.7 Plots of SERS crystallinity ratios	107
<b>Chapter Four</b>	
4.1 AgFON fabrication scheme	117
4.2 LSPR of decanethiol and perfluorodecanethiol	121
4.3 SERS spectra of PCB-47 in decanethiol and perfluorodecanethiol	122
4.4 SERS spectra of anthracene and pyrene	124
4.5 SERS spectra of PCB-47 and limit of detection curve	126
4.6 Limit of detection curve for anthracene and pyrene	128
4.7 Structure and SERS spectra of PCB-47 and PCB-77	129
4.8 Reversibility of PCB-47 SERS sensor	132
4.9 Reversibility of pyrene SERS sensor	133
4.10 Reusability of pyrene SERS sensor	134
4.11 Aromatic band intensity is monitored for PCB-47 and C-S stretch band shift as a function of PCB-47 concentration	136
<b>Chapter Five</b>	

5.1 Structures of phospholipids	146
5.2 SERS spectra of PC	147
5.3 SERS spectra of PAF	148
5.4 SERS spectra of PS	149
5.5 PAF, PC and PS in a decanethiol-modified AgFON	152
5.6 PAF, PC, and PS in a mixed monolayer-modified AgFON	153

## List of Abbreviations and Symbols

Å	angstrom
AAO	anodic aluminum oxidation
AFM	atomic force microscopy
Ag	silver
AgFON	silver film over nanosphere
Al	aluminium
ALD	atomic layer deposition
Au	gold
BiPy	4,4'-bipyridine
BRAC1	breast cancer gene
BSA	bovine serum albumin
BZT	benzenethiol
C8	octanethiol
C10	decanethiol
C16	hexadecanethiol
C18	octadecanethiol
CaDPA	calcium dipicolinate
CD	circular dichroism
CE	capillary electrophoresis
Cm	centimeter
Cr	chromium
$\rho$	density
DMPC	dimyristoylphosphatidylcholine
DNA	deoxyribonucleic acid
DPPC	palmitoylphosphatidylcholine
DPPE-MPA	dipalmitoylphosphatidylethanolamine-
mercaptopropionamine	
DSMB	5, 5'-dithiobis(succinimidyl-2-nitrobenzoate)
DT	decanethiol
EBL	electron beam lithography
EF	enhancement factor
EG3	1-mercaptoundeca-11-yl)tri(ethylene glycol)
EM	electromagnetic field
EOT	extraordinary optical transmission
EPA	Environmental Protection Agency
FDTD	finite difference time domain
FITC	fluorescein isothiocyanate
FIB	focused ion beam
FWHM	full width half max
g	grams
GC	gas chromatography
GLAD	glancing angle deposition
GSH	glutathione
GSSH	glutathione disulfide
h	hour
HDT	hexadecanethiol
HBL	hybrid bilayer
HMD	hexamethylenediamine
HRP	horseradish peroxidase

LC	liquid chromatography
$\lambda_{\text{ex}}$	excitation wavelength
$\lambda_{\text{max}}$	peak wavelength
LOD	limit of detection
LSPR	localized surface plasmon resonance
m	milli
$\mu$	micro
MBA	4-mercaptobenzoic acid
2-MeOBT	2-methoxybenzenethiol
3-MeOBT	3-methoxybenzenethiol
MGITC	malachite green isothiocyanate
MH	mercaptohexanol
MS	mass spectrometry
mV	millivolt
MW	molecular weight
NAADP	nicotinic acid adenine dinucleotide phosphate
NaCl	sodium chloride
4-NBT	4-nitrobenzenethiol
nm	nanometer
NPs	nanoparticles
NSL	nanosphere lithography
NT	2-naphthalenethiol
ODT	octadecanethiol
OT	octanethiol
p	p-value
PA	protective antigen
PAF	platelet activating factor
PAH	polyaromatic hydrocarbon
PATP	p-aminothiophenol
PC	phosphatidylcholine
PCB	polychlorinated biphenyls
PCR	polymerase chain reaction
PDADMAC	poly(diallyldimethylammonium chloride)
PDGF	platelet-derived growth factor
PE	phosphatidylethanolamine
PEG	polyethylene glycol
PEEL	a combination of phase-shift lithography, etching, electron-beam deposition, and lift-off
PFDT	perfluorodecanethiol
PI	phosphatidylinositol
PLS-LOO	partial least squares leave one out
PNA	peptide nucleic acid
PS	phosphatidylcholine
PVP	polyvinylpyrrolidone
R6G	rhodamine 6G
RIE	reactive ion etching
SAM	self-assembled monolayer
SHINERS	shell-isolated nanoparticle-enhanced Raman spectroscopy
SEM	scanning electron microscopy
SEHRS	surface-enhanced hyper Raman scattering

SERS	surface-enhanced Raman scattering
SERRS	surface-enhanced resonance raman scattering
SP	surface plasmon
SPM	scanning probe microscopy
SWNT	single-walled carbon nanotubes
TEM	transmission electron microscopy
TERS	tip-enhanced Raman scattering
THF	tetrahydrofuran
TMV	tobacco mosaic virus
TP	thiophenol
UV	ultraviolet
v/v	volume/volume ratio

# Chapter One

## Surface-Enhanced Raman Scattering Detection in Complex Mixtures

This chapter was adapted from

Bantz, KC; Meyer, AF; Wittenberg, N.J.; Im, H.; Kurtulus, O.; Lee, S.H., Lindquist, N.C.; Oh, S-H., Haynes, C.L., *Recent progress in SERS for Biosensing*, Physical Chemistry Chemical Physics, 2011, 13, p. 11551-11567

## 1.1 General Overview

Rapid and reliable detection of a diverse set of biomolecules, such as metabolites, pharmaceuticals, nucleic acids, amino acids, proteins and peptides require analytical techniques capable of label-free chemical identification. Though Raman scattering seems an unlikely signal transduction mechanism for this task based on its inherently small scattering cross-section, a series of fundamental and technological advancements in the past three decades have made Raman a viable option for biosensing.<sup>1-6</sup> Specifically, the advent of surface-enhanced Raman scattering (SERS) has facilitated Raman spectroscopic detection of numerous biomolecules using relatively simple laboratory equipment and even field-portable devices.<sup>7-11</sup>

## 1.2 What is SERS and how is it used?

Raman scattering is an inelastic process wherein incident photons either gain energy from or lose energy to the vibrational and rotational motion of the analyte molecule. The resulting Raman spectra consist of bands corresponding to vibrational or rotational transitions specific to the molecular structure, and therefore provide chemical "fingerprints" to identify the analyte. However, this is a feeble phenomenon, as only approximately 1 in  $10^6$ - $10^{10}$  photons are scattered inelastically.<sup>12-14</sup> Typical Raman scattering cross-sections are between  $10^{-31}$  and  $10^{-29}$   $\text{cm}^2/\text{molecule}$ . In contrast, typical fluorescence dyes have cross-sections of  $\sim 10^{-15}$   $\text{cm}^2/\text{molecule}$ . It should be noted that resonant Raman scattering can dramatically increase the cross-section. For example, the resonant Raman cross-section of rhodamine 6G (R6G) at 532 nm can be as high as  $10^{-23}$   $\text{cm}^2/\text{molecule}$ .<sup>15</sup>

Between the time of discovery (1928) and the 1960s, Raman measurements were largely limited to neat solvents. The range of accessible analytes and analyte

concentrations was improved upon invention of the laser in the 1960s, but weak signals still limited the utility of this phenomenon for chemical analysis. This changed in the 1970s when Jeanmaire and Van Duyne reported, following Fleischmann's initial observation<sup>16</sup>, that molecular adsorption onto or near a roughened noble metal surface led to drastically increased Raman signal intensity due to electromagnetic and chemical enhancement mechanisms.<sup>17,18</sup>

Fleischmann and coworkers originally reported intense vibrational spectra of pyridine, sodium carbonate, formic acid, and potassium formate adsorbed to redox-cycled silver electrodes as well as pyridine adsorbed to copper electrodes.<sup>16,19,20</sup> Jeanmaire and Van Duyne further examined factors such as surface features and potential of the electrode, solution analyte concentration, and electrolyte composition of the solution, that affect the intensity of the Raman bands of adsorbed molecules.<sup>17</sup> A series of subsequent experiments confirmed that noble metal films with roughened surfaces or nanoscale patterns can dramatically increase Raman scattering signals of analytes and produce enhancement factors (EFs) of  $10^4$ - $10^8$  over normal Raman scattering.<sup>21,22</sup>

The enhancement factors for SERS, as compared to normal Raman scattering, are attributed to two mechanisms: an electromagnetic mechanism and a chemical mechanism.<sup>23,24</sup> The chemical mechanism contributes to enhancement through chemisorption of the molecule to the noble metal surface, allowing the electrons from the molecule to interact with the electrons from the metal surface. These interactions lead to an enhancement of signal up to  $10^2$ , but the chemical mechanism can vary between substrates, substrate adsorption sites, and adsorbed molecules.<sup>13,25</sup> The electromagnetic enhancement is a wavelength-dependent effect arising from the excitation of the localized surface plasmon resonance (LSPR). This

collective oscillation of conduction electrons can occur in noble metal nanoparticles (NPs), sharp metal tips, or roughened metal surfaces, and enhances the incident electric field intensity  $|E|^2$  by  $10^2$ - $10^4$  times in the vicinity of the metal surface (viz. 0-50 nm of the surface).<sup>13,26</sup> SERS enhancement factors ranging from  $10^6$  to  $10^8$  have been observed from a variety of substrates.<sup>13,17,27</sup> Unfortunately, EF calculations are not always consistent from research group to research group; accordingly, care must be taken when comparing EF values from different sources. For single molecule SERS of R6G, enhancement factors of up to  $10^{14}$  have been reported, but it was recently determined that these enhancements are partially attributable to the unusually large Raman cross-section of R6G. In this case, the surface or electromagnetic enhancement is actually  $\sim 10^8$ , with the remainder of the enhancement due to the Raman scattering cross-section of R6G and its resonance Raman contribution of  $\sim 10^6$ .<sup>5</sup>

Although SERS detection does not require the adsorbate to be in direct contact with the metal surface, the EM enhancement sharply decreases as the distance between the adsorbate and the surface increases. For example, Van Duyne and coworkers observed from their silver film over nanospheres (AgFON) substrates that a 2.8 nm separation between the adsorbate and the Ag surface decreased the SERS intensity tenfold.<sup>28</sup> Clearly, to measure intense SERS signals, analytes must dwell within a few nanometers of the substrate surface. For this reason, many SERS studies have been performed on molecules containing a thiol or amine group which can chemically adsorb to the metal surface.<sup>13</sup> To take advantage of the sensitivity and selectivity of SERS for the detection of molecules unlikely to dwell within 2-4 nm of the nanoscale roughness features, an alkanethiol self-assembled monolayer (SAM) has been employed on the surface of the substrate to facilitate the approach

and concentration of the analyte within the zone of enhancement.<sup>29,30</sup> This method is the focus of chapters 3, 4, and 5 herein. Though this approach has not been broadly applied to biomolecule analytes, there are a few examples where a partition layer has been employed to model lipid bilayers and as a tether in aptamer-based sensors.<sup>31,32</sup>

SERS detection of biomolecules has been accomplished in both intrinsic and extrinsic formats. In intrinsic SERS biosensing, the molecular signature for the analyte of interest, such as small molecule, DNA strand, or protein, is acquired directly. In extrinsic SERS, the analyte or interaction of interest is associated with a molecule with an intense and distinguishable Raman signature, traditionally a commercially available fluorescent dye, and it is the SERS spectrum of the tag that is used for sensing or quantification. In either format, SERS has unique advantages for biosensing.

### **1.2.1 Why is SERS a good candidate for complex mixtures?**

Rapid label-free identification of small target analytes is of importance for broad applications ranging from biomarker detection to homeland security. SERS is particularly well-suited to these tasks because of the high sensitivity, the "fingerprinting" ability to produce distinct spectra from molecules similar in structure and function, and the elimination of expensive reagents or time-consuming sample preparation steps associated with other techniques such as polymerase chain reaction (PCR) or immunoassays. In addition, water has a very small Raman scattering cross-section, which leads to minimal background signal from aqueous samples.

In addition, extrinsic SERS detection can provide further advantages over conventional fluorescence-based assays: (1) Raman peaks typically have 10-100

times narrower spectral widths than fluorescence labels, minimizing the overlap between different labels and increasing multiplex capability; (2) when the laser excitation wavelength is matched with the substrate LSPR wavelength, strong SERS signal is achieved from any SERS-active molecule within the zone of electromagnetic enhancement, thus a single source can be used for multiple labels; and (3) SERS labels are not susceptible to photobleaching.<sup>33,34</sup>

### **1.2.2 What are the potential limitations to using SERS for sensing?**

While SERS has the capacity for sensor signal transduction, there have been several real or perceived limitations to widespread use. Though the SERS community has largely come to agreement about the mechanisms responsible for enhanced inelastic scattering, as detailed above, the impression remains that fundamental information is missing. This supposed knowledge gap may have delayed large-scale investment in SERS sensing platforms by major instrument manufacturers and funding agencies. In the instance of single molecule SERS, it is true that there is a lack of fundamental mechanistic understanding; while the SERS community is exploring this phenomenon, only limited application of this very high EF detection scheme is possible. Another perception perpetuated in the literature is that SERS substrates do not have reproducible enhancement factors. In fact, there are many examples where a given substrate has been fabricated and used in multiple laboratories with little discrepancy.<sup>35-38</sup> It is true that very slight changes to a nanostructured noble metal surface can lead to significant LSPR shifts and that the performance of substrates with narrow plasmons will be influenced by this shift. These shifts, and the resulting changes in enhancement factors, are well-understood based on electrodynamic theory. There are also many SERS substrates with broad localized surface plasmon resonances that are not nearly as sensitive to

substrate changes.<sup>39-41</sup> Finally, there is a perceived (but incorrect) limitation of SERS that Ag substrates, which generally have larger enhancement factors than substrates made from any other element, are handicapped due to the formation of an oxide layer. While it is true that an Ag<sub>2</sub>O layer forms on Ag, this layer is thin (viz. 2 nm) and known to be self-limiting. In addition, this oxide layer is displaced upon covalent attachment of molecules to the surface.<sup>42</sup>

There are some real limitations to the widespread adoption of SERS sensors. First, based on the fundamental cross-sections of fluorescence and Raman scattering, even a small amount of fluorescence has the potential to mask SERS signals. Clearly, this problem can be ameliorated by using infrared excitation or metallic NPs/surfaces to quench fluorophores or by performing confocal SERS, where a smaller sample thickness is probed. However, if the fluorophore is not in direct contact with the SERS substrate, background fluorescence will result. A similar issue exists with elastic scatter, a process that is also much more efficient than Raman scattering. Elastic scatter becomes an issue when capturing very small wavenumber shift Raman bands or when trying to capture inelastically scattered photons through a complex sample (e.g. a biological cell). The ability to distinguish low wavenumber shift Raman bands is completely dependent on the filtering technology used to eliminate transmitted excitation light. When expanding SERS to detection in complex biological fluids or environmental samples, elastic scatter may occur in all directions from the various intracellular features (i.e. organelles, cytoskeleton, etc) or dissolved organic matter (i.e. humic or fulvic acid, etc), creating significant background signal. In addition, interfering species and non-specific binding can mask SERS signal from the analyte of interest. This can be addressed by using antibody-based detection and/or partition layers, as pioneered by Van

Duynes.<sup>29,30,43,44</sup> Finally, the practical issue of instrumentation cost limits use of SERS; while there is precedent for inexpensive Raman spectrometers,<sup>9</sup> for the most part, the cost of a laser, optics, spectrograph, and detector is high and thus, prohibitive to many researchers.

### **1.3 What substrates have been used for SERS?**

Inexpensive high-throughput fabrication of SERS substrates with reproducible and large Raman enhancement is a prerequisite for biosensor applications. To date, a large portion of SERS research has utilized colloidal Au/Ag NPs or roughened metal surfaces. Although high EFs have been observed from these substrates, practical applications require engineered SERS substrates that provide tunability as well as reproducibility because maximum SERS intensity is observed when the laser excitation wavelength is tuned near the plasmon resonance maximum of the substrates.<sup>45</sup> Therefore, many groups have been developing new techniques for making nanospheres, nanoshells, nanogaps, nanoholes, and sharp tips with tailored optical properties. Table 1.1 summarizes a variety of engineered metallic structures that have been used for SERS detection. Of particular importance for the future of substrate engineering is the development of novel nanofabrication methods for precise, repeatable, and high-throughput reproduction of various metallic nanostructures.

For the most part, Au or Ag have been used for making SERS substrates, although other metals such as Al, In, Cu, and Ga can also support plasmon resonances in the UV-vis-NIR range. Among these, Al and Cu are of potential interest for SERS and plasmonic biosensing because of their abundance and low cost. Furthermore, aluminum has plasmon resonances in the UV regime and thus can extend the spectral range of Au- or Ag-based devices. Rapid formation of

aluminum oxide or copper oxide, however, presents significant challenges to using Al or Cu for practical applications, since the unwanted oxide layers sharply degrade

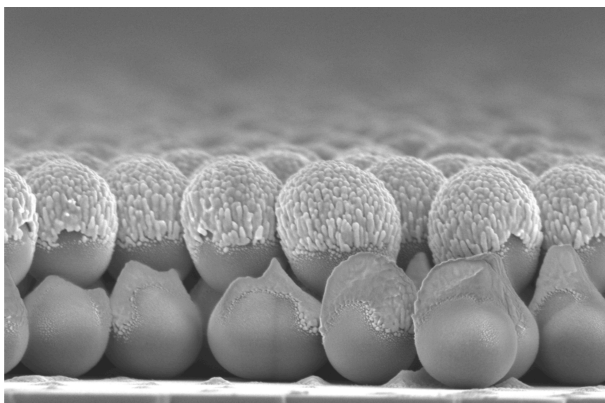


**Figure 1.1** Scanning electron micrograph of a AgFON, a widely used substrate for SERS. Figure adapted from with permission from the American Chemical Society: *Acc. Chem. Res.*, 2010, 43, 782-791.

the detection sensitivity or dampen the LSPR.<sup>46,47</sup> Although the poor chemical stability is often cited as a major concern for Ag-based substrates, Van Duyne and coworkers demonstrated AgFON substrates (Figure 1.1) with temporal stability exceeding 9 months by coating the Ag surfaces with a sub-1-

nm alumina overlayer.<sup>48</sup>

Tip-enhanced Raman spectroscopy (TERS) is an emerging new branch of SERS, wherein the substrate is fabricated on or mounted to the probe of a scanning probe microscope (SPM).<sup>49</sup> In this configuration, the apex of a laser-irradiated metal tip captures incident light and generates a strong LSPR for SERS.<sup>50</sup> Typically, the tip is a metal-coated SPM tip or a thin silver or gold wire. Single-crystalline silver wires have also been used.<sup>51</sup> The radius of the tip is much smaller than the diffraction-limited spot size, allowing ultra-high-resolution SERS imaging. This combination of SERS chemical fingerprinting and SPM imaging is advantageous because it can provide high sensitivity as well as contrast results with a lateral resolution down to a few tens of nanometers with a few seconds of acquisition time. Furthermore, TERS is a versatile technique that can extend the utility of SERS because the analyte does not need to be in direct contact with the SERS-active substrate. The presence of the tip is directly measurable, since when inserted, Bulgarevich and Futamata showed

that the Raman signal from an isolated diamond particle can be enhanced 1000-fold.<sup>52</sup> Theoretical modeling predicts that bringing a tip close to a metallic substrate can increase the local electric field intensity 5000-fold.<sup>53</sup> When a gold tip is brought to within one nanometer of a gold surface coated with non-resonant benzenethiol molecules, EFs of  $10^6$  to  $10^8$  have been reported.<sup>54</sup> In addition, a series of recent studies have established TERS as a promising detection technique with single molecule sensitivity.<sup>53-55</sup>

In the past decade, a variety of SERS and TERS substrates have been employed for detection of small molecules, DNA/aptamers, and proteins/peptides.<sup>56-64</sup> While small molecule detection with SERS has been predominantly accomplished with intrinsic SERS, DNA/aptamers and proteins/peptides have both been detected directly with intrinsic and extrinsic formats. This chapter covers the exciting developments of the previous decade in SERS sensing in complex mixtures and environments.

**Table 1.1 Metallic Nanostructures for SERS<sup>65</sup>**

<b>Category</b>	<b>Fabrication methods</b>	<b>Features</b>
Nanosphere	Nanosphere Lithography (NSL), Spin Coating, Nanocrescent	-Low-cost, solution based batch processing -Easily combined with LSPR biosensing -Ultrastable AgFON substrates with high EFs
Nanoparticle & Nanoshell	Nanoparticle and Nanoshell	-Geometrically tunable plasmon resonance -Solution phase SERS measurements -Near-infrared SERS probes for intracellular spectroscopy
Nanogap	E-beam Lithography, ALD, Electromigration, On-wire Lithography, Electrochemical Deposition	-Metal-insulator-metal geometry for extreme sub-wavelength energy confinement -Single molecule SERS using ultras-small nanogaps -Key challenge is reproducible fabrication
Nanotip	Electrochemical Etching, Metal deposition on a Pulled Fiber, Template Stripping, NSL Triangle	-Single molecule TERS demonstrated -Combine SERS with nano-resolution of SPM
Nanowire	Langmuir-Blodgett, Glancing Angle Deposition (GLAD), Anodic Aluminum Oxidation (AAO)	-Well-defined surfaces compared to colloidal NPs -Tunability of surface plasmon resonance -Broad plasmon for excitation wavelength flexibility
Nanohole	E-beam Lithography, NSL, FIB	-Easily combined with SPR sensors -Geometrically tunable plasmon resonance (hole shape, size, and periodicity) -Potential for high-throughput array use

## 1.4 Small Molecule SERS Sensing

### *Intrinsic*

There are a number of examples in the recent literature where SERS has been applied for detection of biologically relevant small molecules. These small molecules range from antioxidants, like glutathione, to glucose, to small molecule markers for biowarfare agents such as anthrax. Recent work from Van Duyne's group has demonstrated the use of SERS for anthrax biomarker detection.<sup>7</sup> Silver film over nanosphere (AgFON) substrates were optimized for 750 nm Ti:Saph laser excitation and combined with a battery-powered portable Raman spectrometer. Calcium dipicolinate (CaDPA) - a biomarker for bacillus spores - was detected by SERS over the spore concentration range of  $10^{-14}$  to  $10^{-12}$  M by monitoring a peak at  $1020\text{ cm}^{-1}$  shift. Overall, using an 11 minute procedure with a 1 minute data acquisition time, their platform was capable of detecting ~2,600 anthrax spores, well below the anthrax infectious dose of ~10,000 spores. Importantly, the shelf life of prefabricated AgFON substrates in air exceeded 40 days. Their next step was to chemically functionalize the silver surface to enhance the analyte binding affinity as well as the stability of substrates.<sup>48</sup> The AgFON substrates were coated with a sub-1-nm alumina layer deposited by atomic layer deposition (ALD), which simultaneously serves to stabilize the Ag surfaces of AgFON substrates and present the surface chemistry of alumina. Dipicolinic acid displays strong binding to the ALD alumina-modified AgFON, and this strong affinity for carboxylate groups makes the alumina-coated AgFON substrate an ideal candidate for bacillus spores detection. The limit of detection (LOD) was further improved to ~1,400 spores with a 10 second data collection time. More importantly, the alumina overlayer dramatically increased the shelf life of prefabricated substrates to at

least 9 months. Although the controlled deposition of sub-1-nm alumina films is not a trivial task, ALD facilitates fabrication of functionalized SERS substrates while simultaneously protecting the metal surface against unwanted oxidation or environmental contamination. Another toxin target for SERS is saxitoxin, which is found in harmful algal blooms, and if ingested by humans, can cause death. Hall and coworkers used Ag colloid solutions mixed with saxitoxin to detect the presence of the toxin in solution after a 1 min collection time.<sup>66</sup> They obtained an LOD of 3 nM for saxitoxin by monitoring the strong Raman band at 1604  $\text{cm}^{-1}$  shift caused by a combination of the ring stretch/ $\text{NH}_2^+$  deformation/ $\text{C}=\text{N}$  stretch.

In addition to detection of markers of exogenous species, like anthrax biomarkers and saxitoxin, SERS can be employed to detect endogenous molecules like the antioxidant glutathione. Multiple schemes have been demonstrated for SERS detection of glutathione – a biologically important tripeptide that exists both in the reduced form (glutathione, GSH) and oxidized dimeric form (glutathione disulfide, GSSG) in tissues. Glutathione plays a role in the respiration of mammalian and plant tissues, protects cells against hydrogen peroxide, and serves as a cofactor for various enzymes. Glutathione is readily detectable with SERS by monitoring the C-S stretching band at 660  $\text{cm}^{-1}$  shift. Ozaki and coworkers mixed glutathione with Ag colloidal solution, heated (60-100°C) until dry, and acquired SERS spectra of dry films, which improved Raman signals from glutathione compared to samples that were not heat-treated.<sup>57</sup> Increased aggregation of Ag NPs was observed with glutathione. The linear concentration range for glutathione detection was 100-800 nM, the LOD was 50 nM, and EF on these agglomerated Ag NPs was  $7.5 \times 10^6$ . In another study, Deckert and coworkers measured TERS spectra of oxidized glutathione (GSSG) immobilized on a thin gold nanoplate.<sup>58</sup> The SERS spectra were mainly dominated by carboxyl bands at 1408  $\text{cm}^{-1}$  shift and

amide bands at  $1627\text{ cm}^{-1}$  shift. TERS measurements were performed in back reflection mode through a transparent 20-nm-thick gold nanoplate, which was synthesized with a smooth top surface to facilitate homogeneous adsorption and orientation of GSSG molecules. The SERS spectra were recorded at numerous positions on the nanoplate and were consistent in all locations, leading to the conclusion that GSSG adsorbed to the gold in a consistent manner via the carboxyl terminus of the glutamyl, the sulfur of the cystinyl and the amide groups. Consistent immobilization of peptides in this manner will be important for future efforts in characterizing and sequencing peptides with SERS.

In another example of endogenous small molecule detection, Gogotsi and coworkers used a glass substrate coated with gold NPs for SERS detection of nicotinic acid adenine dinucleotide phosphate (NAADP), a calcium secondary messenger that plays a crucial role for intracellular  $\text{Ca}^{2+}$  release.<sup>67</sup> Analysis of standards was performed in a sample volume of  $1\ \mu\text{L}$ , and SERS detection of  $100\ \mu\text{M}$  NAADP was demonstrated. At these high concentrations, the adenine band at  $733\text{ cm}^{-1}$  shift dominates the spectrum. Using principal component analysis, NAADP from cell extracts was detected in response to treatment with the agonists ATP, acetylcholine and histamine (after acid extraction of NAADP from cultured breast cancer SkBr3 cells). This work suggests an interesting possibility of intracellular SERS detection of the calcium messengers, which could help elucidate the mechanisms of calcium signaling pathways in cells.

Among the many small molecule biological analytes intrinsically detectable with SERS, glucose stands out because of its intimate connection with diabetes, which according to the National Institutes of Health affects 10.7% of Americans over the age of 20 and 23.1% of those over the age of 60. Traditional electrochemical methods of glucose monitoring require blood samples to be taken. Though these samples have

very small volumes, in some cases as low as 300 nL, they still require collection of blood from the patient.<sup>68</sup> Many groups are working on minimally invasive optical techniques to detect and monitor glucose, and SERS is at the forefront of these efforts. In order to be a viable glucose monitoring method, SERS must prove to be accurate and reliable in the clinically relevant concentration range. According to the guidelines set by the National Institute of Diabetes and Digestive and Kidney Diseases (an institute of the NIH) fasting glucose levels below 50 mg/dL (2.7 mM) indicate severe hypoglycemia and potential brain function impairment, while glucose concentrations of 70 – 99 mg/dL are considered normal. Concentrations over 100 mg/dL are indicative of a pre-diabetic condition and a reading of greater than 126 mg/dL (7.0 mM) generally results in a diagnosis of diabetes. Because SERS is compatible with aqueous solutions and it can discriminate interferants by spectral characteristics, it is an attractive method for glucose monitoring in complex biological fluids.

A large challenge, however, is the minimal adsorption of glucose to bare SERS-active substrates such as roughened silver. To overcome this challenge, Van Duyne's group implemented a SAM of decanethiol on a AgFON substrate.<sup>60</sup> The SAM functions as a partition layer that concentrates glucose near the AgFON surface. Without the partition layer, glucose was undetectable, but with it was detectable at concentrations lower than 5 mM by monitoring the appearance of vibrational bands at 1123 and 1064  $\text{cm}^{-1}$  shift. By employing a partial least squares leave one out (PLS-LOO) method of analysis, they demonstrated quantitative detection of glucose over a large, clinically relevant concentration range. Building on this initial work, the Van Duyne group switched to an ethylene glycol-terminated SAM as the partition layer.<sup>69</sup> In this work, a SAM of (1-mercaptoundeca-11-yl)tri(ethylene glycol) (EG3) was formed on a AgFON and was exposed to glucose in aqueous humor-containing bovine serum albumin

(BSA), a model interferant. EG3 is known to resist protein adsorption and improve biocompatibility, and in this work was shown to form a stable monolayer on the AgFONs in saline for 3 days. They showed quantitative detection of glucose over large and physiologically relevant concentration ranges (0 – 4,500 mg/dL, 0 – 250 mM and 0 – 450 mg/dL, 0 – 25 mM, respectively), reversibility of the glucose sensor, and that exposure to BSA did not hamper glucose detection.

To further improve the performance of partition layer glucose sensors, a mixed monolayer of decanethiol and mercaptohexanol (DT/MH) was formed on an AgFON and employed for real-time sensing.<sup>70</sup> The DT/MH monolayer was shown to be stable for 10 days, and was used as a partition layer for quantitative analysis of glucose with less calibration error than observed for glucose detection using the EG3 SAM. Moreover, this sensing strategy proved useful for real-time detection of physiological concentrations of glucose (0 - 450 mg/dL) in a complex biological milieu, bovine plasma. In a flow cell setup, they demonstrated glucose sensing and departitioning with time constants of 25 and 28 seconds, respectively.

After optimizing the partition layer the next steps were to provide a more stable surface for SAM formation, improve chemometric analysis, and shift SERS resonances to near-IR wavelengths to facilitate the use of lower cost lasers.<sup>71</sup> This was accomplished by replacing the AgFON with a AuFON and using a shorter chain length version of EG3 as the partition layer. Using a AuFON not only resulted in a SAM layer that was stable for at least 11 days, but also red-shifted the SERS resonance, lowering the biological autofluorescence and allowing greater biological tissue depth penetration. Accurate glucose detection was possible over a larger concentration range (10 – 800 mg/dL, 0.5 – 44 mM), making this sensing strategy applicable to a more diverse set of diabetes patients.

To demonstrate multianalyte sensing capabilities with partition layer-modified substrates, Van Duyne and coworkers used AgFONs with DT/MH mixed SAMs to detect both glucose and lactate, which is an important indicator of potential mortality in intensive care patients.<sup>72</sup> Like earlier studies on glucose alone, they showed both partitioning and departitioning of lactate from the SAM layer. Upon partitioning into the SAM, lactate bands at 1463, 1422, 1272, 1134, 1094, 1051, 936 and 868  $\text{cm}^{-1}$  shift were readily apparent. Using PLS-LOO methods, they demonstrated quantitative analysis of lactate in the concentration range of 10 – 240 mg/dL. Sequential injection of lactate and glucose into a flow cell was used to demonstrate the capability of the sensor to discriminate between the two analytes.

Another category of biomolecules intrinsically detectable with SERS are lipids. In biology, lipids are crucial as structural elements of cell membranes, as a form of energy storage as fats in adipose tissue and as important signaling molecules. Lipids display a large structural diversity, from amphiphilic structures with glycerol backbones like phospholipids to multiple ring structures like steroids. Groups have employed Raman microscopy for investigations of lipid bilayers,<sup>61</sup> but SERS for studying lipids is a newly emerging area and the focus of chapter 5 herein. Most applications of SERS to lipid sensing have focused on investigations of phospholipid bilayers and their properties, as well as their interactions with various molecules of interest.

One study by Halas and coworkers investigated the transfer of phospholipids from vesicles (spherical phospholipid bilayers 85–100 nm in diameter) to hybrid lipid bilayers (HBLs) on gold nanoshell supports.<sup>73</sup> The vesicles were composed of deuterated 1,2-dimyristoyl-sn-glycero-3-phosphocholine (D-DMPC) whereas the HBLs were a monolayer of DMPC spread over a SAM of dodecanethiol. To determine whether D-DMPC was transferred from the vesicles to the HBLs on the nanoshells, they monitored

the intensity of C-H stretch at  $2850\text{ cm}^{-1}$  shift normalized to the intensity of the C-S stretch at  $710\text{ cm}^{-1}$  shift ( $I_{\text{CH}}/I_{\text{CS}}$ ). When D-DMPC vesicles were mixed with HBL-coated nanoshells, a significant decrease in  $I_{\text{CH}}/I_{\text{CS}}$  was observed, indicating transfer of lipids

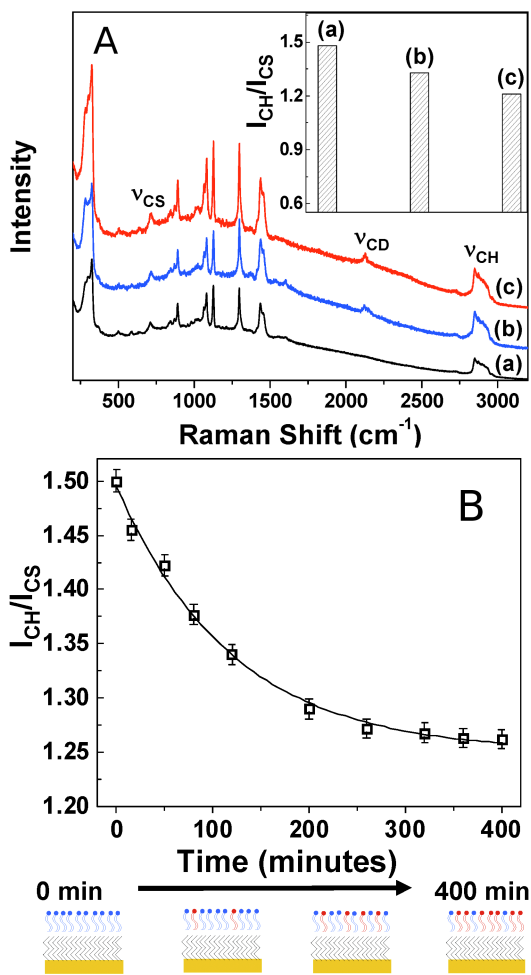


**Figure 1.2** (A) SERS spectra of (a) hybrid bilayer formed with DMPC, (b) a hybrid bilayer formed with DMPC incubated for 2 h with deuterated-DMPC. The decrease in  $I_{\text{CH}}/I_{\text{CS}}$  ( $2850$  and  $710\text{ cm}^{-1}$  shift, respectively) for the three different systems, as shown in the inset, clearly demonstrates exchange/transfer of lipids. (B) Kinetics of the transfer of deuterated lipids from vesicles to hybrid bilayers as exponential fit to the data points. Accompanied is a schematic of the plausible changes in hybrid bilayer composition. Figure adapted from ref. 73, reproduced by permission of The Royal Society of Chemistry.

from vesicles to HBLs. (Figure 1.2A) By monitoring  $I_{\text{CH}}/I_{\text{CS}}$  as a function of time, the rate constant for lipid transfer was determined. A plot of  $I_{\text{CH}}/I_{\text{CS}}$  versus time was fit to a first order exponential curve to give a rate constant of  $K = 1.3 \times 10^{-4}\text{ s}^{-1}$ . (Figure 1.2B)

In another study by Halas and coworkers, the interaction of a small molecule drug (ibuprofen) with HBL-coated nanoshells was investigated.<sup>62</sup> The interaction of ibuprofen with lipid bilayers in the gastrointestinal tract has been suggested as one of the mechanisms of observed side effects, such as gastrointestinal bleeding.

When HBL nanoshells were incubated with ibuprofen, ring modes at  $803$ ,  $1185$ ,  $1205$ , and  $1610\text{ cm}^{-1}$  shift were present due to ibuprofen partitioning into the HBL, and the intensity of the peaks increased with increased ibuprofen concentration. By monitoring the peak at  $1610\text{ cm}^{-1}$  shift, it was

determined that ibuprofen partitioned into the HBL with isotherm-like behavior. Their results also indicate that ibuprofen partitioning into a deuterated-HBL disrupted the order of the HBL. This was determined by monitoring the carbon-deuterium stretch as a function of ibuprofen concentration. As the ibuprofen concentration was increased, the carbon-deuterium stretch intensity decreased.

To interface lipid bilayers with solid substrates, many groups employ tethered lipid bilayers. In these systems, a lipid molecule with a thiolated linking group is deposited on a surface as a SAM and then a second lipid monolayer is deposited to form a bilayer. In many cases, the ordering of the lipid SAM can be determined by SERS. In one study, a dipalmitoylphosphatidylethanolamine-mercaptopropionamine (DPPE-MPA) SAM was used as the lipid tether and its organization on a roughened polycrystalline gold substrate was assessed with SERS.<sup>74</sup> In this work, they observed a significant difference in the conformation of the linking moiety of the DPPE-MPA monolayer in air compared to aqueous solution. In air, the trans conformation was determined to be the dominant for the S-C-C tether due to a large peak at  $720\text{ cm}^{-1}$  shift. Conversely, in aqueous solution the gauche form of the tether predominated as judged by a large peak at  $643.5\text{ cm}^{-1}$  shift. These results were confirmed electrochemically and gave insight into the formation of tethered lipid bilayers for biosensing applications.

SERS for the study of lipids is a developing field, and expanding the types of lipids studied could have impacts in membrane and lipid biology. For example, lipids such as sphingosine-1-phosphate and platelet activating factor are known to function as cellular signaling molecules, but can be challenging to detect. With partition layer schemes, lipid signaling molecules could be detected in complex mixtures based on their spectroscopic profiles and this scheme will be explored in chapter 5 herein.

Along with biomolecules and toxins, SERS can also be utilized for organic small

molecule detection. Malachite green is a waterborne environmental target that is used as an antiseptic, but is thought to be genotoxic and carcinogenic. Lee and coworkers used a PDMS lab-on-a-chip scheme to mix differing concentrations of malachite green with Ag colloids and a confocal Raman setup for detection. The peak at  $1615\text{ cm}^{-1}$  shift was monitored, and an LOD of 1-2 ppb was attainable, which is well within the concentration range mandated by the U.S. Food and Drug administration for detection of malachite green in residues on fish and comparable to traditional LC-MS detection. Another class of organic molecule targets for SERS are polycyclic aromatic hydrocarbons (PAHs) and substituted benzenes, where the very strong benzene breathing and ring stretches have strong Raman intensities. These molecules generally have no affinity for the Ag surface, so the surface must be modified by a partition layer to trap the molecule within the SERS zone of enhancement. PAH detection has been achieved with many different types of partition layers including: alkanethiol partition layers<sup>75,76</sup>, thiolated cyclodextrin<sup>44</sup>, humic acid<sup>77</sup>, and utilizing host-guest chemistry<sup>78</sup>. New techniques utilize SERS as a detection scheme after a simple preconcentration or separation step. Long and coworkers used screen printed Ag electrodes to preconcentrate phenol and aniline derivatives by passing a modest potential of  $-0.1$  to  $+0.1$  mV through the electrodes. Using this scheme they were able to detect methyl violet, benzoic acid, aniline, p-phenylenediamine, p-nitroaniline, phenol, 1-naphthol, and hydroquinonecarboxylic acid in picomolar concentrations. In another experiment, Li et.al separated substituted aromatic pollutants on a thin layer chromatography and then placed a drop of Ag colloid on the separated spots for SERS detection. In on-site implementation of their sensing scheme they were able to detect p-toluidine, p-nitroaniline, and lentine at 91, 193 and 274 ppm, respectively. These results were comparable to the traditional detection method of GC-MS for substituted aromatic

detection. The introduction of partition layers and new hyphenated detection schemes where SERS is combined with preconcentration or separation steps will introduce SERS as a detection method in new areas.

### *Extrinsic*

The limited use of extrinsic SERS for small molecules is due in large part to the ease of obtaining the structural vibrations and rotations directly from small molecules as opposed to more complex systems like DNA and proteins, which are discussed later in this paper. However, some extrinsic small molecule SERS detection schemes do exist. Also focused on anthrax biosensing, Chung and coworkers used Au NPs modified with a 16 amino acid peptide or antibody coupled to the Raman reporter 5, 5'-dithiobis(succinimidyl-2-nitrobenzoate) (DSMB) to detect a different anthrax biomarker, protective antigen (PA).<sup>79</sup> In this example, either the peptide or antibody which binds to PA and DSMB is detected by its characteristic band at 1336  $\text{cm}^{-1}$  shift. The peptide binding partner was shown to be as efficient as an antibody binding partner, and LODs for their biomarker were in the low fM range. As discussed in the intrinsic SERS section, SERS detection can be employed to detect endogenous species like glutathione as well as previously mentioned examples of exogenous species. Ozaki and coworkers developed an extrinsic SERS method for detection of glutathione.<sup>80</sup> In this 'reversed reporting agent' scheme, SERS signal of reporting agent-capped Ag colloids is reduced upon addition of glutathione, which induces aggregation of the Ag colloids. Various reporting agents were tested, but 5  $\mu\text{M}$  R6G was the only viable candidate for glutathione sensing. The LOD using this scheme was 1  $\mu\text{M}$ , which is much higher than for their heat-induced SERS sensing of glutathione.

SERS has been applied broadly to small molecule and lipid sensing due to the small number of vibrational bands associated with the analyte. This field of study would

benefit from substrates with higher EFs for improved LODs, tailoring of substrate surface chemistry to the desired analytes, making detection from complex mixtures easier, reducing fouling of the substrate, and minimizing sample preparation time. While intrinsic and extrinsic small molecule sensing employ relatively easy detection schemes, more complex biological molecules like DNA and aptamers present new SERS sensing challenges.

### **1.5 DNA/Aptamer SERS Biosensing**

#### *Intrinsic*

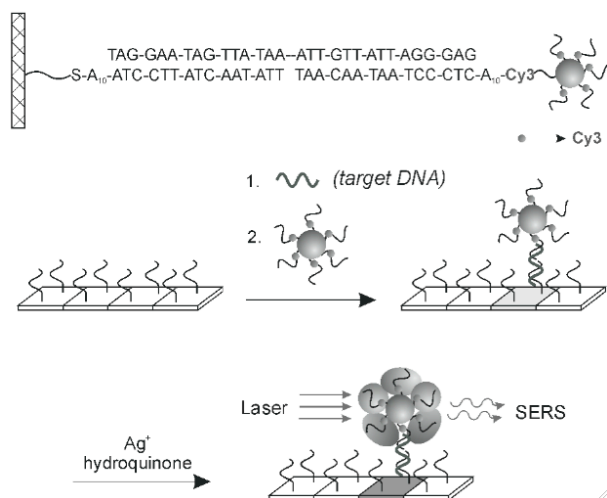
Intrinsic SERS and TERS measurements can also be employed beyond small molecule detection for DNA and aptamer biosensing. Recent advances in achieving low limits of detection and good reproducibility make SERS a useful tool for either single or double-stranded thiolated DNA oligomer detection. For example, Halas and coworkers used Au nanoshells bound to glass substrates to obtain SERS spectra of DNA, which were dominated by adenine vibrational bands at  $729\text{ cm}^{-1}$  shift.<sup>63</sup> Moreover, they observed changes in the dsDNA spectrum upon interaction with cisplatin and transplatin, cis and trans forms of common chemotherapy agent, revealing an opportunity for SERS to contribute to pharmaceutical research. Critical to the achievement of highly reproducible DNA spectra in this work was a thermal pretreatment that promoted extended linear conformation of ssDNA and dsDNA on the Au nanoshell substrate. The report of adenine as the dominant base was not particularly surprising since this is the only DNA base showing single-molecule detection to date, suggesting a large Raman scattering cross-section.<sup>81-83</sup> An alternate approach to thermal pretreatment for achieving label-free, target-specific and highly sensitive SERS of DNA employs an electrokinetic preconcentration method, electrophoresis. Lee and coworkers used negatively charged plate electrodes as SERS

substrates for detection of positively charged adenine.<sup>84</sup> They illustrated that application of a constant electric field,  $0.6 \text{ V cm}^{-1}$  for adenine measurement, resulted in a 51-fold amplification in signal over open circuit detection of adenine. Although, this measurement combination is limited owing to pH sensitivity and substrate contamination issues, it is a promising method for label-free analysis of charged biomolecules. Other intrinsic SERS studies of DNA have focused on detection of changes in conformation rather than individual base detection. Neumann and coworkers demonstrated high-specificity detection of DNA and lower-specificity detection of small molecules upon using SERS to examine conformational changes caused by interactions between an aptamer and analyte molecules. In this case, they used Au nanoshells immobilized on quartz substrates which display either an anti-platelet-derived growth factor (anti-PDGF) aptamer for PDGF detection or an anti-cocaine aptamer for cocaine detection. Comparison of the conformational changes indicated using SERS and the standard technique of circular dichroism (CD) showed high correlation in this work. In addition, comparison between substrate incubation with specific (PDGF) versus non-specific (lysozyme) target analyte confirmed the high specificity of this biosensing scheme. On the contrary, the anti-cocaine aptamer showed non-specific binding to both caffeine and benzocaine, suggesting that more work needs to be done for aptamer-based SERS sensing of specific small molecule targets. However, this limitation for aptamer-target specificity could be exploited for identification of multiple targets by a single aptamer.<sup>85</sup>

TERS has also been proposed for direct DNA and RNA sequencing, identification of biomacromolecules, and characterization of single viruses at the molecular level. Bailo and Deckert used TERS for direct, label-free detection of a single stranded RNA cytosine homopolymer.<sup>86</sup> All spectra obtained along the length of a 20-nm-long single

strand of RNA showed spectral features of cytosine with little variation in band intensities or positions. Moreover, as deduced from this experiment, it is possible to find the sequence of RNA with controlled movement of the TERS probe from base to base. Deckert and coworkers have also demonstrated that TERS is a powerful tool for direct detection of single virus particles belonging to different species.<sup>87</sup> All TERS virus spectra measured in this work showed bands that were attributed to spectral features of a single tobacco mosaic virus (TMV) due to interaction between the coat proteins and RNA with the Ag-coated AFM tip. They obtained EFs of  $10^6$ , and they claimed that higher EFs are achievable if the excitation wavelength overlaps with plasmon absorption profile of the nanoroughened Ag on the AFM tip.

Even though there are certainly challenges related to fabrication of uniform, highly sensitive and reproducible SERS substrates for biosensing, there has been clear progress on the application of SERS and TERS to DNA, aptamer, and single



**Scheme 1.1** A SERS probe consisting of a 13-nm-diameter Au nanoparticle functionalized with a Raman dye-labelled oligonucleotide. A three-component sandwich assay is used in a microarray format and the Raman probe detected, after Ag enhancing, by SERS. Figure adapted from ref. 101, reproduced with permission from the American Academy for Advancement of Science.

biomolecule detection.

### *Extrinsic*

are relatively few examples of intrinsic SERS for DNA and aptamer detection, DNA aptamer monitoring via extrinsic employed extensively. As shown in Scheme 1, a common detection scheme for DNA binding events is to functionalize a Au or Ag NP with a reporter molecule (usually a fluorescent dye) and a single stranded piece of DNA. Upon hybridization with

a complementary strand of DNA, typically bound to another Au or Ag surface, the SERS or surface-enhanced resonant Raman scattering (SERRS) signal of the reporter molecule is observed. Many groups have employed this DNA detection scheme to achieve various goals: (1) Vo-Dinh and coworkers used an immobilized DNA capture strand on a Ag surface for the detection of the breast cancer gene (BRCA1);<sup>88</sup> (2) Moskovits and coworkers used a sandwich assay between ssDNA attached to a flat Ag layer and a Ag NP labeled with the complementary DNA strand to detect hybridization;<sup>89</sup> (3) Mirkin and coworkers used on-wire lithographically produced Ag nanorods with etched gaps for the detection of DNA binding;<sup>90</sup> and (4) Moskovits and coworkers detected a protein after a Au NP functionalized with dsDNA bound and the SERRS signal was further enhanced by electroless Ag plating onto the complex.<sup>91</sup>

The intentional creation of DNA strands with single nucleotide polymorphisms allows researchers to evaluate how specific their assays are for the complementary ssDNA capture strands. Graham and coworkers found that DNA hybridization was observed only when a fully complementary DNA sequence was added to their DNA-functionalized Ag NPs,<sup>92</sup> proving that they could detect single nucleotide polymorphisms when present in the DNA mixtures. They were also able to modulate the SERRS signal by heating or cooling the analyte solutions to influence extent of DNA hybridization. The LOD of these hybridization assays can be further improved by functionalizing the Au or Ag surface. Graham and coworkers also employed commercially available Klarite gold substrates for the detection of dye-labeled oligonucleotides,<sup>93</sup> and they had the most reproducible results when they functionalized the Au surface with a bidentate SAM of a ssDNA capture ligand, resulting in a LOD of  $10^{-7}$  M. Along with tailoring the surface chemistry of the Klarite substrates for DNA hybridization and attachment, Graham and coworkers also investigated the surface chemistry that would best allow DNA to attach to Ag

NPs.<sup>94</sup> Through their investigations, they determined the number of amine modifications needed so that the overall strand has a positive charge and would attach most efficiently to a Ag NP; this strategy yielded a LOD of around  $10^{-12}$  M. With qualitative detection of DNA hybridization clearly feasible, Graham and coworkers also began pushing for quantitative detection of DNA. The researchers optimized oligonucleotide detection conditions by employing 8 commercially available fluorescent dyes attached to Ag NPs.<sup>95</sup> After optimization of Ag NP dilution and aggregating agent, calibration curves were created for each dye to facilitate quantitative SERRS detection. With this approach, they calculated LODs for optimized conditions with all 8 dyes; in the best case, a LOD of 0.5 fM was achieved.

Using multiple SERS tags for the labeling or detection of DNA associated with disease has been covered in a review by Natan and coworkers.<sup>34</sup> This review identified the great potential of a SERS multiplex sensing platform, as was demonstrated in 2006 by Mirkin and coworkers.<sup>96</sup> This work used various DNA sequences immobilized on glass beads, hybridized with a Au NP, and labeled with a complementary ssDNA and reporter molecule.<sup>96</sup> The multiple Raman labels were created by using single and quantitative mixtures of fluorescent dyes attached to the Au NP. They labeled DNA sequences for Hepatitis A, Hepatitis B, HIV, Ebola virus, Variola virus (smallpox), *Bacillus anthracis*, *Francisella tularensis*, and hog cholera segment with the Raman labels. The bead-NP complexes were then further enhanced with Ag plating to increase the SERS signal. Similarly, Graham and coworkers used 5 different DNA sequences, each labeled with a different fluorescent dye and a Ag NP.<sup>97</sup> They labeled a probe for human papillomavirus with R6G, the VT2 gene of *E.coli* 157 with ROX, and a universal primer with FAM, CY5.5, and BODIPY TR-X. They found LODs from  $10^{-11}$  and  $10^{-12}$ , and since DNA sequence choice does not affect the SERRS signal, the

detection scheme can be generalized to any target. The linear response of these probes at biologically relevant concentrations with all 5 probes simultaneously indicates a promising future for DNA detection with multiplex labels.

DNA-based SERS sensors are not limited to only DNA detection; by using aptamers generated to detect other biomarkers, these schemes can be broadly adapted. For example, Lee and coworkers fabricated an aptamer-based SERRS sensor using gold NPs bound to a glass slide coated with a thrombin-binding aptamer; a methylene blue reporter molecule facilitated detection of thrombin binding events.<sup>98</sup> This simple detection scheme had a LOD of 100 pM, which was lower than the disassociation constant of 25 nM for thrombin. A LOD lower than the disassociation constant indicates that thrombin has a higher affinity for the substrate bound thrombin-binding aptamer.

While the formation of DNA-NP complexes is generally used for the detection of specific binding events, the complex formed between DNA, or DNA-like molecules, and NPs can also be used to create SERS hotspots, or small volumes with extremely large electromagnetic fields. Graham and coworkers used fluorescent dye and locked nucleic acid-labeled Ag NPs for controlled aggregation of NPs to induce SERRS hotspots.<sup>99</sup> When the probes were combined with appropriate target DNA sequences they took one of three different conformations, head to head, tail to tail, or tail to head, all of which caused enhancement of SERRS signal. DNA hybridization can also be achieved with peptide nucleic acids (PNA), as demonstrated by Moskovits and coworkers, who exploited the electrostatic interactions between surface bound PNA and target DNA to create SERS hotspots.<sup>100</sup> The DNA-PNA hybrid in this work had a net negative charge, which then allowed a positively charged Ag NP to attach to the DNA-PNA hybrid. Upon exposure to R6G, Raman hot spots could be observed where the DNA-PNA complex had formed.

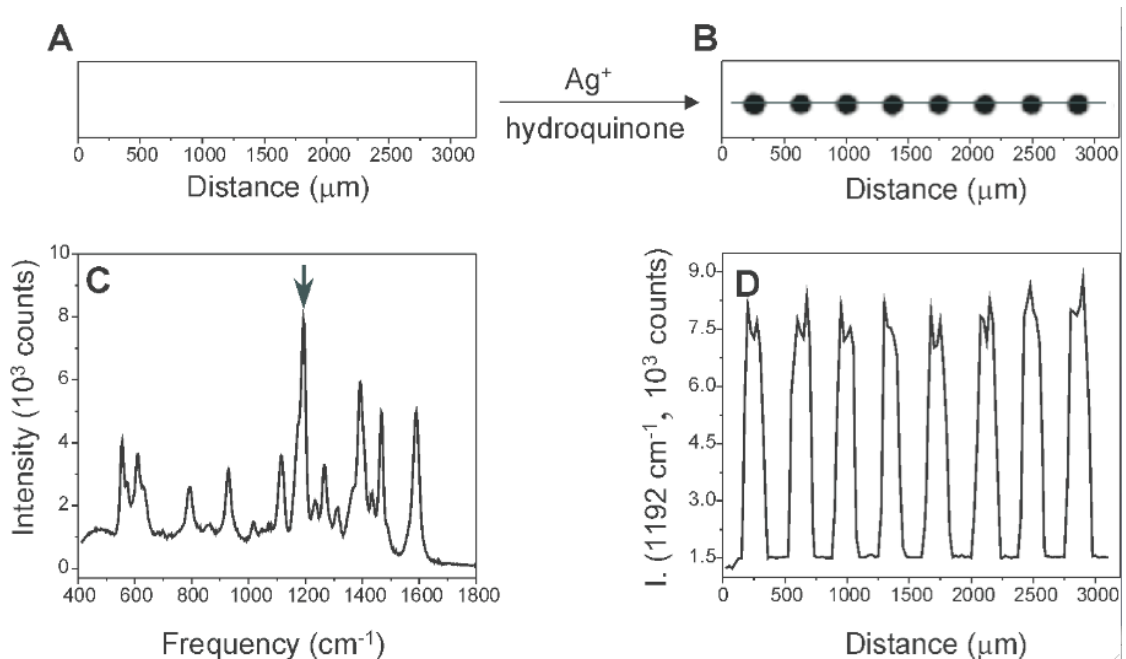


**Figure 1.3** A flatbed scanner image of Raman probes (A) before and (B) after Ag enhancement. (C) A SERS spectrum of one of the Ag spots. (D) Raman intensity of the 1192 cm<sup>-1</sup> shift as the laser is scanned across the chip from left to right. Figure adapted from ref. 101, reproduced with permission from the American Academy for the Advancement of Science.

Detailed above are multiple ways DNA hybridization is detected or exploited; a similar scheme can also be employed for RNA detection. Mirkin and coworkers accomplished this by starting with a typical sandwich assay where DNA immobilized on a slide was hybridized with a complementary DNA strand with a dye-functionalized Au NP.<sup>101</sup> (Figure 1.3) As detailed in aforementioned examples, this complex was further enhanced with a Ag plating bath to increase the SERS signal. The group then went further and immobilized two different RNA strands that can bind to the same DNA capture strand but have single nucleotide polymorphisms. After stringent washing to denature and remove the imperfect DNA/RNA complexes, they were able to detect only perfectly matched RNA strands.

Gene detection using Au or Ag NPs functionalized with ssDNA and a SERS or SERRS reporter molecule has also been demonstrated. Vo-Dinh and coworkers used a scheme similar to that described above to detect a SERS signal from the HIV-I gene

based on its hybridization to DNA labeled with a NP-reporter molecule complex.<sup>102</sup> In another paper, Vo-Dinh and coworkers utilized a Au NP functionalized with a hairpin ssDNA sequence for the detection of HIV-I gene, which, upon the addition of the complementary DNA sequence caused the SERS signal to decrease in the presence of the target, however they did see a 10% decrease in signal when non-complementary DNA was present.<sup>103</sup> Most recently, this group was able to detect the presence of two target genes indicative of breast cancer with this hairpin detection scheme.<sup>104</sup>

While the intrinsic work on SERS for DNA has been limited, the future of this field and its applications to DNA sequencing look very promising due to the opportunity for label-free and target-specific detection. Recently, Halas and coworkers demonstrated label-free SERS detection of DNA. Replacement of adenine with 2-aminopurine in the capture DNA strand allowed for the adenine band of the target DNA to be monitored and hybridization efficiency monitored.<sup>105</sup> In most cases, it is the low EFs of the substrates and the inability to create zones of enhancement small enough to see SERS signal from one nucleotide base at a time that have been the limiting factors. While multiplexing SERS tags and quantitative extrinsic SERS is interesting, we will eventually reach a limit as to how many tags we can discriminate within a mixture. The area where extrinsic SERS is the most promising is in the gene detection schemes proposed by Vo-Dinh, Graham and Mirkin. The recent emergence of some hyphenated extrinsic SERS techniques has opened doors into more forensic science and genotyping areas of interest. The SERS-melting (either electrochemical or thermal) combination demonstrated by Bartlett and coworkers allowed them to effectively detect short tandem repeats and single nucleotide polymorphisms of DNA bound to an Au sphere segment void substrate.<sup>106,107</sup> Batt and coworkers utilized the combination of ligase detection reaction with SERS to quantitatively detect single nucleotide

polymorphisms in oncogenic K-Ras with a 10 pM detection limit.<sup>108</sup> The ability to detect the presence of diseases quickly, with little sample preparation and without the need to amplify the amount of DNA present is one of the most exciting directions for further work using extrinsic SERS.

## **1.6 Protein/Enzyme/Peptide/Antibody SERS sensing**

### *Intrinsic*

While intrinsic SERS measurements are relatively straightforward for small molecules, lipids, and DNA where each target has a small number of vibrational modes, it is also feasible to perform SERS biosensing on more complicated, larger molecules such as peptides, proteins, enzymes, and antibodies.<sup>109</sup> Unlike the more tractable small molecules, band assignments for spectra from these larger species are often based on general motifs seen through the molecules rather than localized vibrational modes.

One commonly used example is the characteristic aromatic amino acid bands present at  $\sim 950\text{ cm}^{-1}$  shift, for the C-COO- stretch, and  $\sim 1400\text{ cm}^{-1}$  shift, for the COO-symmetric stretch. Another commonly used spectral feature is the broad amide (CO-NH) I and III bands, at  $1600\text{-}1700\text{ cm}^{-1}$  shift and  $1200\text{-}1350\text{ cm}^{-1}$  shift, respectively, used in intrinsic peptide and protein analysis to describe both primary and secondary structure characteristics.<sup>110</sup>

SERS sensing of the simplest amino acid structures, peptides, has been pursued both from a fundamental perspective, with the goal of assigning Raman bands to particular amino acids, and from an applied perspective, to sense particular biomarkers. Proniewicz and coworkers used a series of homodipeptides on Ag colloids to assign Raman bands for Cys, Gly, Leu, Met, Phe, and Pro.<sup>111</sup> Their results also yield insight about adsorption orientation of the amino acids, specifically resolving a previous controversy about Gly-Gly adsorption to show that it initially adsorbs through its C-

terminus but rearranges to adsorb through its N-terminus with time. Hartgerink and coworkers also used dipeptides, where different aromatic amino acids were linked to cysteine, to demonstrate that one amino acid can be distinguished from another.<sup>64</sup> In this case, Au nanoshells were the SERS substrate and the cysteine was employed to promote covalent attachment of the peptide to the nanoshell. Comparison of the measured SERS spectra directly to normal Raman spectra showed little shift in the Stokes Raman bands but significant broadening of the SERS peaks. As a proof-of-concept for measurement of more complicated peptides, this paper also includes the prediction and measured SERS spectrum of a 19 amino acid cell-penetrating peptide known as penetratin, and this spectrum is dominated by the aromatic features from 3 amino acids within the molecule. With a more applied goal, Ozaki and coworkers have employed SERS to sense bombesin, a 14 amino acid neurotransmitter that is a tumor marker.<sup>112</sup> This group's work characterizes the Ag colloid adsorption behavior of bombesin and bombesin fragments and compares the measured spectra with density functional theory predictions. While this is a significant first step toward making SERS a viable biosensor for bombesin, much work must still be done to determine sensor limits of detection as well as sensing in the presence of interfering species. In parallel with the peptide work detailed above, many groups are also pursuing SERS detection of more complicated amino acid structures such as proteins.

Moskovits and coworkers recently demonstrated protein SERS spectra after sandwiching double cysteine mutants of the small protein FynSH3, a common model protein for kinetic and thermodynamic studies, between two Ag NPs.<sup>113</sup> If this protein remains in its native state between two NPs, the distance between the linked NPs would be 2.3 nm, creating a small gap and large electromagnetic enhancement. The captured SERS spectra clearly show evidence of the cysteine linkage to the Ag NP as

well as bands for the aromatic amino acids histidine, tryptophan, and phenylalanine. The band intensities varied from second to second during collection, suggesting that the spectrum was sensitive to protein conformation/orientation. In some cases, they saw momentary spectra indicating graphitic carbon (protein degradation), quickly replaced by a new amino acid spectrum, suggesting that they were measuring spectra from single or small numbers of protein molecules within an electromagnetic hot spot. In another recent example, Ozaki and coworkers adapted traditional Western Blot analysis of proteins to include SERS and SERRS detection.<sup>114</sup> First, they separated a protein mixture using gel electrophoresis followed by electroblotting onto nitrocellulose to immobilize proteins. After applying a Ag NP stain, they recorded confocal SERRS or SERS of 2 model proteins, myoglobin and bovine serum albumin, respectively. While they could distinguish these two proteins using amide and aromatic amino acid bands, there was, unfortunately, no clear linear relationship between the amount of protein and SERS band intensities. Another concern was that the SERS spectra after Ag NP staining did not look like the bulk Raman spectra, perhaps because only a portion of the protein is within the large electromagnetic fields responsible for SERS. Deckert and coworkers also used myoglobin as a model protein to demonstrate SERS detection following free flow electrophoresis separation with isotachophoretic focusing.<sup>115</sup> Using a microfluidic platform, they were able to focus a Ag NP/myoglobin mixture to elute from only 2 channels. Though the myoglobin concentration was quite high (410  $\mu\text{M}$ ) and there were some issues with Ag NPs clogging the microfluidic channels, this work shows the promise of SERS detection within "hyphenated techniques" and on microfluidic platforms.

While previous examples focus mainly on identifying proteins or protein components, SERS has also been used to look at an important sub-class of proteins, enzymes.

Ozaki and coworkers measured the intrinsic SERS spectra of the enzymes lysozyme, ribonuclease B, avidin, catalase, hemoglobin, and cytochrome c with low  $\mu\text{g/mL}$  -  $\text{ng/mL}$  limits of detection.<sup>116</sup>

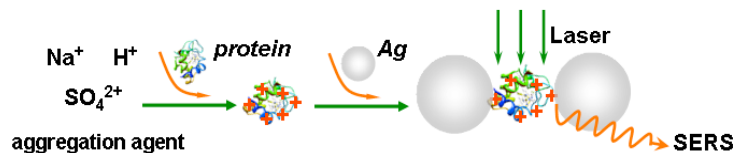


**Figure 1.4** Detection scheme for label-free protein sensing with SERS. The presence of protein induces the aggregation of Ag nanoparticles, which is then used to produce a strong SERS signal. Figure adapted from ref. 116, reproduced by permission of the American Chemical Society.

They accomplished this by mixing the enzymes first with acidified sulfate

and then colloidal silver before capturing NIR SERS spectra, as shown

in Figure 1.4. The acidified solutions and sulfate greatly enhanced the detection limits for proteins examined, and again, the spectra were mostly characterized based on amide and aromatic amino acid band locations and intensity. In a distinct effort to perform single enzyme analysis, Käll and coworkers used immobilized protein/NP aggregates (with 90-nm-diameter Ag NPs) to measure single molecule SERRS spectra of horseradish peroxidase (HRP) at various points in its enzymatic cycle.<sup>117</sup> They found that Ag NPs alone denatured the protein but that the NPs could be made biocompatible simply by adding  $\text{H}_2\text{O}_2$  before adding enzyme. In 1 second SERS collections with low concentration HRP, the SERRS spectra fluctuate, and the authors suggest that these fluctuations correspond to the various forms of HRP found within the catalytic cycle.

While the protein spectra measured here are promising and there are clear spectral differences between different mutants and different proteins, *ab initio* identification of proteins from measured SERS spectra is still not possible. This may be feasible with advanced chemometric or peak deconvolution techniques but recent focus in this area has been mainly on using extrinsic SERS for protein, and even antibody, biosensing.

### *Extrinsic*

To address the challenges of intrinsic SERS detection of proteins, Raman reporter molecules have been used when specific protein spectra are not necessary, and the goal is to quantitatively detect either individual proteins or total protein content. For extrinsic SERS detection of proteins, reporter molecules must (1) maintain stability during tagging and measurement and (2) generate a robust and consistent Raman spectrum under the conditions of the SERS measurement.<sup>34</sup> For protein detection, commonly used SERS reporter molecules include 5,5'-dithiobis(succinimidyl-2-nitrobenzoate) (DSNB) with intensity monitored at 1336  $\text{cm}^{-1}$  shift,<sup>118-121</sup> 4-mercaptobenzoic acid (MBA) with intensity monitored at 1585  $\text{cm}^{-1}$ , 4-nitrobenzenethiol (4-NBT) with intensity monitored at 1336  $\text{cm}^{-1}$  shift, 2-methoxybenzenethiol (2-MeOBT) with intensity monitored at 1037  $\text{cm}^{-1}$  shift, 3-methoxybenzenethiol (3-MeOBT) with intensity monitored at 992  $\text{cm}^{-1}$  shift, and 2-naphthalenethiol (NT) with intensity monitored at 1384  $\text{cm}^{-1}$  shift.<sup>122</sup> Also used as extrinsic Raman labels for SERS are 4,4'-bipyridine (BiPy), with strong bands present at 1609, 1227, 1291  $\text{cm}^{-1}$  shift, thiophenol (TP), with strong bands at 994 and 1570  $\text{cm}^{-1}$  shift, and p-aminothiophenol (PATP), with strong bands at 390, 1077, and 1578  $\text{cm}^{-1}$  shift.<sup>123</sup> Fluorescein isothiocyanate (FITC) and malachite green isothiocyanate (MGITC), which are widely used fluorescence tags, have also been used as common Raman reporter molecules for SERRS and SERS detection of proteins. FITC intensity is monitored at 1630  $\text{cm}^{-1}$  shift following excitation at 514.5 nm, and MGITC intensity is monitored at 1615  $\text{cm}^{-1}$  shift when excitation at 647.4 nm is used.<sup>124,125</sup>

Many of the aforementioned extrinsic Raman labels have been used for immunoassays, which rely on the specificity of the interaction between antibodies and their corresponding antigens.<sup>43</sup> Multiple formats have been employed for SERS-based immunoassays, including the use of silver island films, colloids in solution, immobilized

colloids, and modified colloids as probe molecules.<sup>43</sup>

An immunoassay using SERS was first reported in 1989 by Tarcha and colleagues.<sup>126</sup> In this early SERS-based immunoassay, SERS was employed for the detection of thyroid stimulating hormone. The sandwich format used a silver island film as the substrate to which a capture antibody was attached, followed by incubation with antigen, then addition of another antibody conjugated to p-dimethylaminoazobenzene. Since then, SERS-based immunoassays have largely utilized colloids as SERS

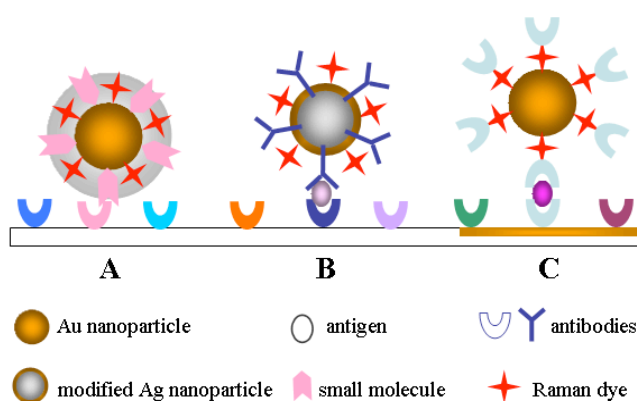


**Figure 1.5** Schematic of SERS immunoassay. Multiple formats are available for detection: (A) shows a Au NP core coated with a shell into which extrinsic Raman labels and antibodies are immobilized, (B) shows an Au-coated Ag NP probe conjugated to both extrinsic Raman labels and capture antibodies, and (C) shows antibodies conjugated to a Au NP using extrinsic Raman labels. Figure adapted from ref. 109, reproduced by permission of The Royal Society of Chemistry.

substrates to address the challenge of reproducibly manufacturing island films with nanoscale roughness.<sup>127</sup> The use of colloids as SERS substrates also offers versatility in immunoassays, including the possibility for multiplexing and extension into in vitro and in vivo SERS.<sup>43</sup> A common format involves a sandwich assay

similar to those used in the aforementioned SERS DNA detection schemes: antibodies are immobilized, then exposed to antigen, followed by exposure to gold NPs conjugated to antibodies as well as probe molecules. Variations of this format for SERS-based immunoassays are shown in Figure 1.5. Using the sandwich structure, Hepatitis B virus surface antigen has been detected using murine monoclonal and polyclonal antibodies.<sup>128</sup> To improve the LOD of the virus surface antigen to 0.5  $\mu\text{g/mL}$ , a silver

staining step was incorporated into the immunoassay as well.<sup>128</sup> Feline calcivirus and *Mycobacterium avium* subsp. *paratuberculosis* have been detected using a sandwich format as well.<sup>120,121</sup> Porter and coworkers optimized the conditions for feline calcivirus detection and detected virus concentrations as low as  $1 \times 10^6$  viruses/mL, or 70 captured viruses.<sup>120</sup> Porter and coworkers were also able to detect 200 ng/mL (1000 bacteria/mL) of *Mycobacterium avium* subsp. *paratuberculosis* in a milk matrix.<sup>121</sup>

To evaluate the potential of SERS-based immunoassays to replace or augment current immunoassay technology, it is necessary to compare the LODs of the aforementioned SERS immunoassays to the LODs of widespread immunoassays. Fluorescence and microcantilever detection of viruses have been achieved at concentrations on the order of  $10^5$  viruses/mL while microbial detection with ELISA can be achieved with  $10^4$  cells/mL.<sup>120,129-131</sup> Electrochemical methods were employed for detecting *E. Coli* O517:H7 or *Salmonella* at concentrations as low as  $6 \times 10^2$  or  $5 \times 10^3$  colony forming units (living bacterial cells/mL), respectively.<sup>132,133</sup>

Multiplexing is also possible with SERS immunoassays. Tian and colleagues used two approaches to multiplex a sandwich-format SERS immunoassay: immobilized antibodies were exposed to the target analytes (mouse or human IgG), then to (1) gold NPs with antibodies and 2 reporter molecules attached or (2) gold and gold/silver bimetallic NPs with antibodies and 1 reporter molecule attached.<sup>123</sup> With the first detection scheme, 50  $\mu$ g/mL mouse and human IgG were detected simultaneously. With their second detection scheme, the multianalyte assay was not successful due to overlapping peaks of the Raman reporter label on gold and gold/silver bimetallic NPs, but mouse and human IgG were detected individually at 100  $\mu$ g/mL.<sup>123</sup> Porter and colleagues developed a tetraplexed assay to detect IgG from four species using four Raman reporters by employing mixed monolayers of extrinsic Raman labels on gold

NPs.<sup>122</sup>

Direct detection of enzymes using SERS has been mentioned previously, but direct detection is difficult due to enzyme denaturation and loss of activity.<sup>6</sup> Indirect detection of enzyme activity, in which an enzyme produces a SERRS-active dye as a product, have been used for enzyme-based immunoassays. Extrinsic SERS detection of proteins has also been accomplished by modifying colloids to produce NP probes.<sup>134,135</sup> Using gold NPs and electroless silver plating, Mirkin and colleagues coated NPs with a hydrophilic oligonucleotide, Raman dye label and a small molecule to detect protein-small molecule interactions.<sup>134</sup> In another probe design to detect protein-protein interactions, they coated NPs with antibodies and labeled them with oligonucleotide and a Raman dye.<sup>134</sup> A similar probe design using Coomassie Blue was developed by Ozaki and coworkers.<sup>135</sup>

Though many SERS-based immunoassays have used colloids as substrates, single-walled carbon nanotubes (SWNT) have been used by Dai and coworkers to achieve lower LODs. They used functionalized SWNTs as multicolor Raman tags for highly sensitive detection of protein interactions on microarrays.<sup>136</sup> They used a sandwich-assay scheme wherein an analyte (antibody) from a serum sample was captured by immobilized proteins in a microarray, followed by incubation of SWNTs conjugated to goat anti-mouse antibody that specifically bind to the capture analyte. The strong SERS signal produced by the SWNT tag enabled protein detection sensitivity down to 1 fM, demonstrating great potential for extrinsic SERS detection toward applications in proteomics and autoimmune disease research.

The use of Raman labels for protein detection is not limited to immunoassays. A protein concentration assay developed by Han et al., uses the SERS signal of Coomassie Brilliant Blue dye adsorbed non-specifically to silver colloids to monitor the

total protein concentration.<sup>135</sup> The SERS signal of Coomassie Brilliant Blue displayed a linear and inverse relationship to protein concentration over a bovine serum albumin concentration range of  $10^{-5}$  to  $10^{-9}$  g/mL.<sup>135</sup> Clearly, extrinsic SERS has enabled protein sensing *ex vitro*; in fact, a similar approach can be adopted to perform SERS detection inside cells as well.

Direct SERS detection of proteins is limited by the spectral similarities of many proteins. Indirect SERS detection of protein concentration through immunoassays is promising, but the use of antibodies and detection limits on the order of ELISA assays with fluorescence detection prevent SERS-based immunoassays from replacing the more widespread enzyme-based immunoassays for clinical and diagnostic use.

## **1.7 Cellular and in vivo Sensing**

### *Intrinsic*

In a relatively small number of cases, SERS biosensing of proteins, DNA, and small molecules has been extended from the aforementioned examples toward cellular and *in vivo* systems. However, there are only a few where direct, intrinsic, SERS detection is performed in cells: this is due to the complex biological environment which can mask signals from analytes of interest or cause fluorescence. The Van Duyne group first demonstrated *in vivo* application of intrinsic SERS by measuring the glucose concentration from the interstitial fluid of a rat.<sup>137</sup> A SAM-functionalized AgFON substrate was surgically implanted under the skin of a rat such that it was in contact with the interstitial fluid and optically addressable through a glass window placed along the midline of the rat's back. The SERS spectra from glucose were acquired through the window using a 785 nm Ti:sapphire laser with a power of 50 mW for 2 minutes. The glucose concentrations obtained from the implanted AgFON sensor matched the data from a commercial glucometer. With further refinements and miniaturization in the

system, SERS biosensors could help the treatment and care of diabetics or other conditions that would benefit from time lapse monitoring. SERS spectra have also been successfully measured from endosomes in live cells (rat renal proximal tubule cells and mouse macrophages) using gold NPs.<sup>138</sup> Both cell lines were exposed for 30 minutes to gold NPs, which were then localized in the endosomes of the cells. In this case, cells were raster-scanned with a low-power (2 mW) NIR excitation laser for 1 sec to prevent interference from normal Raman scattering and possible change in the live cells due to laser illumination. The strongest SERS signal was acquired 120 minutes after exposure to NPs, when gold aggregates formed in the lysosomes. Gold aggregates in both cell lines produced tentatively assigned bands in the spectra that indicate the presence of proteins, lipids, carbohydrates, and nucleotides chemical nano-environments of lysosomes. In addition, the spectral signature of adenosine phosphate was detected in macrophage endosomes, which indicates differences in the endosomes of the two cell lines. To date, intrinsic SERS of the cellular milieu provides general information about the types of biomolecules present, but provides limited information about specific biomarkers of interest. The use of extrinsic Raman labels in the examples that follow are one approach to overcome this weakness, showing increased specificity for biomolecules of interest.

#### Extrinsic

The use of extrinsic SERS in cellular and in vivo sensing is extensive due to the ability of extrinsic Raman labels to overcome background signals from a complex biological matrix and associate with specific biomolecules. Many groups have used extrinsic SERS for mapping the local pH in cells based on the important role pH plays in regulating cellular function.<sup>139-141</sup> Kneipp and coworkers measured pH-dependent SERS spectra of p-mercaptobenzoic acid (pMBA), a pH-sensitive Raman tag, on aggregated

gold NPs.<sup>139</sup> The accessible pH range of SERS and surface-enhanced hyper-Raman scattering (SEHRS) were  $5.5^{-8}$  and  $2^{-8}$ , respectively, but the high laser power ( $\sim 10$  mW) and long collection time (10 sec) required for SERS were not suitable for scanning live cells. Moskovits and coworkers also showed pH dependence of SERS spectra using pMBA-functionalized NP clusters and mapped local pH in live HeLa cells.<sup>141</sup> In this work, Ag clusters were linked using bifunctional hexamethylenediamine (HMD) molecules and encapsulated by polyvinylpyrrolidone (PVP) to prevent aggregation during MBA tag infusion. The SERS-active clusters were also coated by dye-labeled streptavidin with BSA to track the distribution of Ag NP clusters in cells and correlate the fluorescence and SERS pH maps. The MBA molecules infused through the polymer coat into junctions between NPs and facilitated measurement of pH values inside live HeLa cells using a relatively low laser power (1.1 mW) and short integration time (250 ms). These pH mapping probes could be used to understand intracellular interactions, including endocytotic pathways. Vo-Dinh and co-workers used a Ag-coated sub-micron sized fiber-optic probe functionalized by pMBA for similar purposes.<sup>142</sup> The probe was physically inserted into a live cell using a micromanipulator. The intracellular pH value was determined by comparing SERS intensity of pMBA bands to a calibration curve obtained from standard pH solutions ranging from pH 6.0 to 7.5.

Clearly, it is feasible to perform extrinsic SERS detection in cells using a single extrinsic Raman labels but there is also significant interest in multiplex biomarker detection. In fact, Gambhir and coworkers have demonstrated multiplexed extrinsic SERS.<sup>143</sup> They used 10 SERS-NP complexes for multiplex imaging, and each particle consisted of a unique Raman reporter molecule layer adsorbed onto a 60-nm-diameter Au core coated with silica, making the total diameter about 120 nm. Each molecular layer shows distinguishable SERS spectra, and five of them were used for in vivo SERS

imaging in a nude mouse. A mixture of four kinds of unique NPs of varying concentrations was injected either intravenously or subcutaneously into the mouse where a linear correlation of SERS signal with the concentrations was measured.

SERS has also been utilized for extrinsic detection of cancer markers in a live cell. Oh and coworkers used Au/Ag core-shell NPs where R6G Raman tags were adsorbed

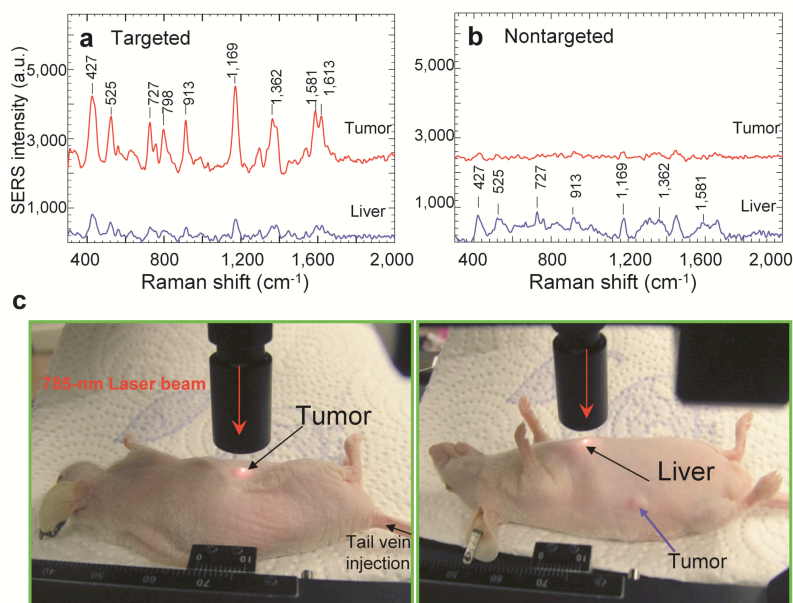


**Figure 1.6** In vivo cancer marker detection using surface-enhanced Raman with scFv-antibody conjugated gold nanoparticles that recognize the tumor marker. (A) SERS spectra obtained from the tumor (red) and liver (blue) by using targeted nanoparticles and (b) non-targeted nanoparticles. (c) Photographs showing a laser beam focusing on tumor or liver sites. In vivo SERS spectra were obtained with a 785 nm laser at 20 mW and 2 s integration. Figure adapted from ref. 4, reproduced by permission of The Nature Publishing Group.

cell showed significant Raman signal, based on the 1650 cm<sup>-1</sup> shift R6G peak, that correlated well with quantum dot-labeled fluorescence images. Moving from imaging of cancer markers in live cells to tumor targeting, Nie and coworkers used PEGylated gold NPs as extrinsic SERS labels with tumor-targeting ligand to identify tumors both in vitro and in vivo.<sup>4</sup> A core size of 60-80 nm diameter was chosen to position the LSPR peaks

on the gold surface with a BSA layer.<sup>144</sup> Subsequently, the NPs were conjugated with IgG antibodies that selectively bind to phospholipase C $\gamma$ 1 biomarker proteins (PC $\gamma$ 1) on HEK293 (human embryonic kidney) cells. While no normal Raman signal from R6G was measured from a control cell, the cancer

within the 'water window' (630-785 nm) where the optical absorption of water is minimal. SERS tags were over 200 times brighter than NIR-emitting quantum dots. They could measure SERS spectra at targeted tumor sites up to 2 cm below the skin. After injecting NPs into the tail vein, SERS spectra could be obtained from a targeted tumor site with some non-specific biodistribution into liver and spleen, but not into brain, muscle or other major organs. (Figure 1.6) Moreover, Stone and coworkers proposed deep Raman spectroscopy with citrate-reduced Ag conjugated nanoparticles for detecting low concentration of molecules through tissues of up to 25 mm thick. It demonstrated a potential use of SERS nanoparticles for detecting target molecules deeply buried within tissues.<sup>145</sup>

Because of the high sensitivity, label-free detection and multiplex capability, applications of SERS targeting in live cells, tissues and *in vivo* detection will continue to expand. At the same time, many hurdles need to be overcome, which include the stability as well as toxicity of SERS tags, and the background noise resulting from the structural similarity of many proteins and molecules.

### **1.8 Perspective**

This review article summarized recent advances in harnessing SERS toward rapid *in vitro* and *in vivo* detection of a wide range of biological analytes. Theoretical and experimental work in the last decade have vastly expanded our understanding of SERS mechanisms and the ability to control plasmon resonances in nanostructured metals. Researchers have employed noble metal particles, shells, tips, gaps, wires and holes to demonstrate SERS substrates with tuned plasmon resonances and high EFs. Going forward, widespread applications of SERS biosensing will hinge on the ability to mass-produce reliable substrates with well-defined nanoscale patterns, precisely tailored LSPR bands, large and reproducible EFs, and highly specific surface chemistry. One

likely scheme for practical use of these substrates will begin with SPR/LSPR based screening, where a plasmon shift indicates a "hit", followed by SERS interrogation to characterize the chemical nature of the newly associated species. Toward this aim, SERS substrates fabricated with the NSL method have already demonstrated inexpensive wafer-scale processing, EFs of  $\sim 10^8$ , and an excellent temporal stability.<sup>48</sup> Various techniques to fabricate ultrathin metallic nanogaps will further enhance our understanding of deep subwavelength optical confinement toward single-molecule SERS, nonlinear spectroscopy and plasmonics.<sup>146</sup> In addition, TERS will open up an exciting new avenue, since it empowers SERS to probe a small number of molecules with a nanoscale imaging resolution. Furthermore, TERS will be particularly useful in the cases where target analytes cannot be brought into contact with the substrates, e.g. probing of cell membrane molecules. Several fabrication challenges should be addressed before TERS can be used as a reliable and widely available technique. Nanoscale roughness in the substrate supporting the sample can also significantly affect the TERS signals, leading to large imaging artifacts.<sup>54</sup> In this regard, making ultrasmooth substrates with roughness less than 1 nm may be required.<sup>147</sup> Furthermore, recently developed methods of template stripping patterned metals can create ultrasmooth patterned surfaces with tunable optical properties if synergistic interaction of the substrate and TERS probe is required.<sup>148</sup> The fabrication of smooth features as well as ultrasharp (<10 nm radius) pyramidal tips will likely advance both SPM and TERS.<sup>149</sup>

While substrates like the ones described above will be of great use to intrinsic and extrinsic small molecule detection, immunoassays, and development of DNA arrays for clinical settings, many cellular and *in vivo* applications of SERS require further development of nanoparticle substrates in suspension. Recently, Kotov and coworkers

developed gold lace nanoshells with SERS hotspots on the nanoparticle surface producing EFs of  $10^2$  larger than traditional Au spheres of the same diameter.<sup>150</sup> Such improvements over widely used Au nanoparticles will allow for more sensitive SERS detection within cells and *in vivo*. Au nanoparticles are an especially important substrate for intracellular or *in vivo* SERS based on significantly better biocompatibility than their Ag counterparts.

Another technique that allows SERS to probe for molecules without being in contact with the substrate, like TERS, is the shell-isolated nanoparticle-enhanced Raman spectroscopy (SHINERS) pioneered by Tian and coworkers.<sup>151</sup> In this method, a spherical gold core is coated with a thin oxide layer (~2 nm of SiO<sub>2</sub> or Al<sub>2</sub>O<sub>3</sub>) to yield a particle that can be dusted onto an area of interest for SERS detection. The group demonstrated SHINERS use in the monitoring of biological targets and food safety, and their results show promise for surface-based and portable applications of SERS biosensing. Rapid progress in nanofabrication on both wafer and nanoparticle scale, in conjunction with advances in surface chemistry, microfluidics, modeling as well as fundamental understanding of SERS mechanisms, show great promise for the future of SERS biosensing.

## **1.9 Conclusions**

SERS research is a truly multi-disciplinary field that has benefited from dynamic interactions among chemists, physicists and engineers. New and exciting developments presented herein show a bright future for the widespread adoption of SERS and will facilitate the transition of SERS from research laboratories to real-world diagnostics, biomedical sensing, and field applications.

# Chapter Two

## Development of Novel Substrates for Surface-Enhanced Raman Scattering

This chapter was adapted from

Bantz, K.C. and Haynes, C.L. *Surface-Enhanced Raman Scattering Substrates Fabricated using Electroless Plating on Polymer-Templated Nanostructures*, Langmuir, 2008, 24, p. 5862-5867

Bantz, K.C., Lee, S.H., Lindquist, N.C., Oh, S.-H., and Haynes, C.L., *Self-Assembled Plasmonic Nanohole Arrays*, Langmuir, 2009, 23, p. 13685-13693

All substrate fabrication and SEM imaging was performed by Si Hoon Lee, with FDTD simulations performed by Nate Lindquist, while SERS measurements, EF calculations, and electroless plating was performed by Kyle C. Bantz.

Im, H., Bantz, K.C., Lindquist, N.C., Haynes, C.L., and Oh, S.-H., *Vertically Oriented Sub-10 nm Plasmonic Nanogap Arrays*, Nano Letters, 2010, 10, p. 2231-2236. All fabrication, imaging, and SERS measurements were performed by Hyungsoon Im, with FDTD simulations performed by Nate Lindquist and EF and surface area calculations were performed by Kyle C. Bantz.

## 2.1 Introduction

Surface-enhanced Raman scattering (SERS) is a powerful spectroscopic technique that relies on the generation of surface plasmons (SPs) - density fluctuations of the conduction electron plasma<sup>1</sup> - in metallic nanostructures to detect and identify proximate molecules.<sup>2-4</sup> While the surface-enhanced Raman scattering (SERS) phenomenon has been recognized for 30 years now,<sup>3</sup> it is not often used as an analytical signal transduction mechanism based on its reputation for an incomplete understanding of the enhancement mechanism and irreproducibility. This underutilization is unfortunate because SERS holds great analytical potential based on the fact that the measured spectra contain unique molecular signatures for each chemical species, and the method can easily be employed in aqueous environments based on the small Raman scattering cross-section of water.<sup>5</sup>

In actuality, the SERS community is in agreement regarding the enhancement mechanisms responsible for ensemble-averaged SERS, with contributions from both the electromagnetic<sup>6</sup> and chemical<sup>7</sup> enhancement mechanisms and electrodynamic calculations that largely predict measured enhancement factors (EFs). Several research groups have also demonstrated substrates that yield reproducible enhancement factors, especially when special care is paid to the relationship between the optical properties of the adsorbate-covered substrate and the excitation laser source.<sup>8</sup> Recent SERS experimental efforts have been focused on exploring the fundamental "hot spot" phenomenon that yields single molecule detection levels (EFs~ $10^{14}$ - $10^{15}$ )<sup>9,10</sup> and making homogeneous noble metal substrates with narrow localized surface plasmon resonances.<sup>11-13</sup> Because of the collective motion of the conduction electrons, SPs can substantially enhance the local electromagnetic (EM) field, while the evanescent nature of the SPs allows their energy to be localized to subwavelength dimensions.<sup>14,15</sup> Illuminating metallic nanoparticles,<sup>9,10,16-18</sup> gaps,<sup>19-22</sup> or

sharp tips<sup>23-25</sup> can create these subwavelength SERS "hotspots", producing dramatically enhanced Raman signals from adsorbates. The enhanced light-matter interactions in these metallic nanostructures are responsible for SERS as well as many other sensing and imaging applications in the emerging field of plasmonics.<sup>26-28</sup> However, the lack of reproducible high-throughput fabrication methods has limited the widespread adoption of SERS as a general sensing technique.

This chapter will focus on the development of novel fabrication techniques for SERS substrates. When fresh SERS substrates need to be fabricated in a field setting utilizing traditional fabrication techniques that are employed for our plasmonic nanohole arrays and nanogap arrays is not possible. For our field fabricated SERS sensor we aim to achieve stable high EFs ( $>10^5$ ), present a broad localized surface plasmon resonance (LSPR) so that it can be used with a variety of excitation wavelengths, inexpensive fabrication using simple techniques, and tolerance of various solvent environments. To that end, we present just such a substrate, the polymer-templated Ag nanostructure. Later in this chapter, we explore the use of two different types of SERS substrates with tunable, narrow plasmons and high EFs ( $>10^5$ ) that require multiple fabrication steps in a lab. To this end two substrates have been developed: the self-assembled plasmonic nanohole array and nanogap array. We will begin by discussing the substrate with the most simple fabrication scheme, the polymer-templated Ag nanostructure.

## **2.2 Polymer-Templated Nanostructure SERS Substrate**

The traditional fabrication of noble metal SERS substrates involves either solution-phase metal salt reduction to form colloidal nanoparticles<sup>29</sup> or vapor deposition to form nanostructured films.<sup>2</sup> Solution-phase colloidal SERS substrates generally yield small

and unstable SERS signal intensities while also requiring molecular exchange between the stabilizing ligand and the analyte molecule. Deposition of the noble metal colloids onto a substrate yields formation of uncontrollable nanoparticle aggregates with EF variation of over 10 orders of magnitude on a single substrate.<sup>30</sup> Vapor deposition produces substrates with tunable optical properties and reproducible EFs but the required apparatus is expensive and makes it impossible to fabricate substrates outside of the laboratory. The ability to easily generate fresh SERS substrates becomes especially important when exploiting the high EFs of Ag SERS substrates due to the nanostructured metal's propensity to oxidize.<sup>31</sup> In previous work done by Natan and coworkers, where a polymer-coated substrate was used to immobilize Au or Ag colloids with controlled interparticle spacing, SERS enhancement factors were shown to be large and strongly dependent on nanoparticle coupling.<sup>32,33</sup> Herein, a similar initial fabrication step is used to immobilize colloidal nanoparticles but, in this case, the colloidal nanoparticles act as autocatalytic growth sites to create a fully coated Ag SERS substrate. While the structures presented herein are less topographically homogeneous, the broad LSPR and high surface area for target adsorption present significant practical advantages. Throughout the results presented herein, the novel polymer-templated substrate will be compared with the Ag film over nanospheres (AgFON) substrate, one of the most commonly used thermal vapor deposition SERS substrates because of its large uniform surface area and reproducible EFs of  $10^5$  or greater.<sup>34-39</sup> This direct comparison reveals that the robust polymer-templated Ag nanostructure has comparable EFs and broad optical properties without requiring the time, expense, or equipment of vapor deposition. Accordingly, this simple substrate will be a good candidate for future analytical applications of SERS in biological or environmental sensing.

## **2.2.1 Experimental Methods**

### **2.2.1.1 Materials**

All the chemicals were of reagent grade or better and used as purchased. AgNO<sub>3</sub>, HAuCl<sub>4</sub>, sodium citrate, 35% (v/v) poly(diallyldimethylammonium chloride), silver enhancement kit, ethanol, sodium chloride, tetrahydrofuran and benzenethiol were all purchased from Sigma-Aldrich. 18-mm-diameter round coverslips from VWR and punched copper discs from McMaster-Carr (Chicago, IL) were used as substrates. 500-nm ( $\pm$  20 nm)-diameter silica nanospheres were purchased as a 10% solids solution from Duke Scientific (Palo Alto, CA). All water samples were ultrapure (18.2 M $\Omega$  cm) from a Millipore water purification system (Long Beach, CA). Silver wire for electron beam deposition was purchased from Kamis Inc. (Mahopac Falls, NY).

### **2.2.1.2 Nanostructure Fabrication**

Ag and Au seed colloids were synthesized via citrate-reduction of either AgNO<sub>3</sub> or HAuCl<sub>4</sub>. All glassware was cleaned with aqua regia (3:1 HCl:HNO<sub>3</sub>) and rinsed before use in nanoparticle synthesis. Citrate-reduced Ag colloids were synthesized by the addition of 90 mg of AgNO<sub>3</sub> to 500 mL of H<sub>2</sub>O, the solution was brought to a boil, and 10 mL of a 1% sodium citrate solution was added. The solution was then kept at boiling for one hour. This preparation yields a turbid green-brown solution with an extinction maximum at 433.9 nm. Citrate-reduced Au colloids were synthesized by the addition of 60.2  $\mu$ l of 30% HAuCl<sub>4</sub> to 10 ml of a 4.0 mM sodium citrate solution, followed by sonication for 30 minutes in a nitrogen environment. This preparation yields a dark purple solution with an extinction maximum at 542.6 nm. Based on TEM analysis, the Ag nanoparticles were  $81 \pm 55$  nm in their longest dimension and the Au nanoparticles were  $28 \pm 7$  nm in diameter. After synthesis, the colloid solutions were stored at room

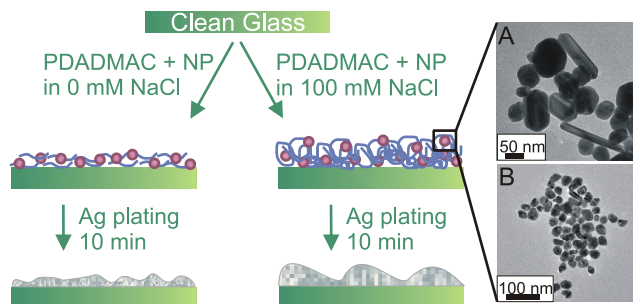


**Figure 2.1** Schematic of the polymer-templated nanostructure substrate preparation using (A) Ag and (B) Au seed colloids.

temperature in brown glass bottles and were stable against aggregation for > 6 months.

For polymer-templated nanostructure fabrication (Figure 2.1),

a 35% (v/v) solution of poly(diallyldimethylammonium chloride) (PDADMAC, MW 100,000) was first diluted to a 1% (v/v) solution in water and then further diluted to a 100:1 (v/v) solution with Ag or Au seed colloids as synthesized. Glass coverslips were cleaned by sonicating in a solution of 10:1:1 H<sub>2</sub>O/30%H<sub>2</sub>O<sub>2</sub>/NH<sub>4</sub>OH for an hour, rinsed, dried, and then ~200 μL of the colloid/PDADMAC solution was deposited onto the coverslips and allowed to dry in ambient conditions. The dry polymer-templated substrates were then placed in a 1:1 (v/v) mixture of the Solution A and Solution B from the silver enhancement kit. After a 10 minute incubation, the substrates were removed and allowed to dry. The average thickness of the polymer-templated substrate (polymer + metal) was 200 nm as determined by atomic force microscopy (AFM).

AgFON substrates were fabricated on copper disks that had been polished and cleaned by sonicating in a solution of 10:1:1 H<sub>2</sub>O/30%H<sub>2</sub>O<sub>2</sub>/NH<sub>4</sub>OH for an hour; copper discs were necessary due to the poor adhesion of the AgFON substrate to glass. After rinsing the copper discs, 10 μL of silica nanosphere solution was deposited onto the surface, and the disc was manually agitated to promote a homogeneous nanosphere layer and then allowed to dry in ambient conditions. Silica nanospheres were used in place of the traditional polystyrene latex nanospheres in order to promote adhesion and avoid polystyrene signal interference during the Raman experiments. Ag was vapor

deposited to a thickness of 200 nm onto the nanosphere mask using electron beam vapor deposition (Airco Temescal, Berkeley, CA) at a pressure of  $7 \times 10^{-6}$  Torr. The rate of deposition, 2 Å/second, and thickness were measured using a quartz crystal microbalance.

### **2.2.1.3 Physical Nanostructure Characterization**

The noble metal seed colloids were characterized using a JEOL JEM-1200 transmission electron microscopy (TEM) with a 120 kV accelerating voltage. Samples were prepared for TEM by drop-coating colloidal solution onto Formvar-coated copper grids (Ted Pella, Inc., Redding, CA). The polymer-templated Ag nanostructures and AgFONs were characterized using a Digital Instruments Dimension 3000 AFM (Veeco, Woodbury, NY) in a temperature- and humidity-controlled environment. The scan size was  $5 \mu\text{m} \times 5 \mu\text{m}$ , and all data was collected in tapping mode using an aluminum-coated silicon nitride tip with a 10 nm radius of curvature and a resonance frequency of  $\sim 400$  kHz. Feature analysis was performed using Digital Instruments software as well as the Gwyddion software package to evaluate average Ag island size, overall surface area, and RMS roughness. Island size describes the area of raised roughness features and was determined by measuring the length and width of the silver islands using AFM line scans. Overall surface area within a given  $25 \mu\text{m}^2$  area was evaluated using the triangulation scheme in Gwyddion. RMS roughness was measured by calculating the average of the height deviation from the mean height.

### **2.2.1.4 Optical Nanostructure Characterization**

LSPR measurements for the polymer-templated nanostructures were recorded using a DH-2000 Deuterium Tungsten Halogen light source, 200- $\mu\text{m}$ -core-diameter fiber optics, and a USB2000 spectrometer (Ocean Optics, Dunedin, FL) while a 200- $\mu\text{m}$ -core diameter reflectance probe was used for AgFON optical characterization. A 200-nm-

thick thermal vapor deposition Ag film was deposited onto a copper substrate for use as a blank in the reflectance probe measurements.

### 2.2.1.5 Surface-Enhanced Raman Scattering

Both polymer-templated Ag nanostructures and AgFONs were dosed from 1 mM solutions of benzenethiol (BZT) in ethanol unless otherwise specified. Each substrate was placed in 2 mL of the BZT solution for 16 hours at ambient conditions to facilitate monolayer assembly. The substrates were removed from the solution and rinsed with ethanol before being mounted in the macroscale Raman sample holder.

In all data presented herein, a Millennia Vs 532 nm excitation laser (Spectra-Physics, Mountain View, CA) was used with added neutral density filters to achieve desired incident powers. The laser beam first passed through an interference filter (Melles-Griot, Rochester, NY) and was then guided to the sample using an Al-coated prism to achieve a spot size of 1.26 mm<sup>2</sup>. Scattered light was collected using a 50-mm-diameter achromatic lens (Nikon, Melville, NY), and the Rayleigh scattered light was removed using a notch filter (Semrock, Rochester, NY). Detection was accomplished using a 0.5 m SpectraPro 2500i single monochromator and a Spec 400B liquid-nitrogen cooled CCD chip (both from Princeton Instruments/Acton, Trenton, NJ).

EFs were all calculated using the intense ring breathing stretch at 1000 cm<sup>-1</sup> shift from both liquid and surface-adsorbed BZT and the equation:

$$EF = \frac{N_{vol} \times I_{surf}}{N_{surf} \times I_{vol}}$$

, where  $N_{vol}$  is the number of BZT molecules contributing to the normal Raman scattering signal,  $N_{surf}$  is the number of BZT molecules contributing to the SERS signal, and  $I_{surf}$  and  $I_{vol}$  are the intensities of the scattering band of interest in the SERS and normal Raman scattering spectra, respectively. The packing density for BZT on Ag surfaces, as reported in the literature, is  $6.8 \times 10^{14}$  molecules/cm<sup>2</sup>.<sup>40,41</sup> Using this value,

the surface area information obtained from AFM images, and the laser spot size, it is possible to calculate  $N_{\text{surf}}$ . The probe volume for the neat liquid BZT in the liquid Raman cell was  $4.13 \times 10^{-3}$  mL, as determined from the probe size and known thickness of the sample cell. Using the density of benzenethiol ( $\rho=1.073 \text{ g cm}^{-3}$ ) and the probe volume, it is possible to calculate  $N_{\text{vol}}$  to be  $2.43 \times 10^{19}$ . When calculating the SERS enhancement factor, it is necessary to assume that the Raman scattering cross-section for free BZT and substrate-bound BZT are not significantly different.<sup>42</sup> Intrasubstrate EF variation was assessed by measuring SERS spectra from five randomly chosen spots on each substrate and aggregating the data from multiple substrates fabricated using the same experimental conditions.

#### **2.2.1.6 Robustness Assessment**

To monitor substrate longevity, each sample was dosed with BZT as described above, and the LSPR and SER spectra were measured every 24 hours for 5 days, each time placing the substrate into a vial of water between measurements. Initial AgFON comparison experiments were completed using traditional polystyrene nanospheres on glass substrates; however, these films degraded very quickly in water and yielded large fluorescence backgrounds due to revealed nanospheres. The AgFON substrates are much more stable when fabricated using silica nanospheres on copper substrates, and thus, that is the data presented herein.

#### **2.2.1.7 Statistical Analysis**

Linear regression analysis and t-tests were performed in Excel using the data analysis package, with values of  $p < 0.05$  used to determine statistical significance. Unless otherwise noted, all values are reported as the average  $\pm$  the standard error of the mean (SEM).

## 2.2.2 Results and Discussion

### 2.2.2.1 Polymer-Templated Nanostructures Fabricated with Varied Seed Nanoparticles

Both citrate-stabilized Ag and Au colloids were added to separate PDADMAC solutions to be used as the autocatalytic sites for electroless deposition. Nanoparticle aggregation was not apparent in either of the solutions based on transmission LSPR monitoring. Upon casting the PDADMAC/nanoparticle solutions onto glass substrates, the Ag-seeded film had a slight yellow/green color and the Au-seeded film had a slight red color, indicating that the nanoparticles were well-dispersed within the dried film. After electroless plating, incubation in BZT, and SERS measurement, the substrates fabricated using Ag seed nanoparticles yielded an average EF of  $2.3 \times 10^6$  and those fabricated using Au seed nanoparticles yielded an average EF of  $1.2 \times 10^6$ ; t-test results reveal that the Ag seed nanoparticle EF is significantly larger than the Au seed nanoparticle EF ( $p < 0.00004$ ). The LSPR spectra after electroless plating for substrates fabricated using Ag and Au seed nanoparticles are indistinguishable, with the bulk Ag plasmon visible at  $\lambda_{\max} = 370$  nm and a broad extinction band across the visible that can be attributed to heterogeneous roughness features. AFM analysis of both substrates revealed that the substrate fabricated with Ag seed nanoparticles had an average RMS roughness of  $228 \pm 23$  nm while the substrate fabricated with Au seed nanoparticles had an average RMS roughness of  $120 \pm 20$  nm ( $p < 0.01$ ). The significantly smaller roughness on the Au-seeded substrates is partially due to the fact that the Au seed nanoparticles have nearly a 10-fold smaller surface area than the Ag seed nanoparticles. Additionally, topographic images reveal that the majority of the plated silver localized around the Au seed nanoparticles, leaving much of the substrate covered in a smoother and thinner Ag film. This topographic heterogeneity explains the

EF standard deviation of 37% measured from the Au-seeded substrates in contrast to the 9% EF standard deviation measured from the Ag-seeded substrates. The more uniform Ag electroless plating on the substrates fabricated using Ag seed nanoparticles is likely due to both the increased surface area where catalytic reduction can occur and  $\text{Ag}^+$  remaining in the nanoparticle solution that infiltrates the PDADMAC layer during mixing and promotes efficient Ag deposition during reduction. Based on the more uniform surface features and EFs, all further work was completed using Ag seed nanoparticles. The EF and the standard deviation in EF on the Ag-seeded substrate compare favorably both with those previously achieved by Park et. al. using an electroless Ag deposition SERS substrate,<sup>43</sup> Natan and coworkers using immobilized colloid substrates,<sup>32,33</sup> and with those measured from a traditional AgFON substrate -  $2.5 \times 10^6$  with 16% standard deviation.

### 2.2.2.2 Polymer-Templated Nanostructures Fabricated with Varied Ionic Strength

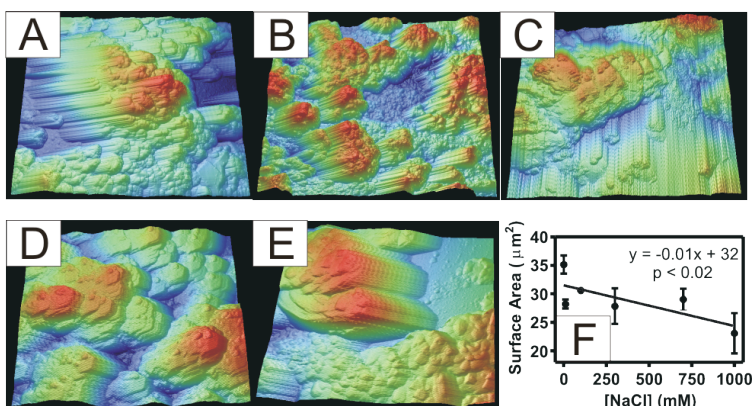


**Figure 2.2** AFM images of five polymer-templated nanostructure substrates with increasing ionic strength: (A) 0 mM NaCl, (B) 1mM NaCl, (C) 10 mM NaCl, (D) 100 mM NaCl, and (E) 1 M NaCl. (F) Plot showing the change in total surface area in a  $5 \mu\text{m} \times 5 \mu\text{m}$  scan area with varied deposition solution ionic strength.

The effects of varied ionic strength on the polymer-templated nanostructure were probed using solutions of Ag nanoparticle-seeded solutions of 1% PDADMAC prepared in 1 mM, 10 mM, 100 mM and 1000 mM aqueous NaCl. Any

changes in the polymer conformation, from extended to globular or vice versa, should create a varied template for the growth of the electroless plated silver and, perhaps, a shift in the LSPR that influences the SERS EF. When the polymer chains are extended

(i.e. rod-like), smaller surface features would be expected than when the polymer chains are in a globular conformation. This effect may be muted in this work because the polymer structure may collapse during drying on the glass substrate. Based on AFM analysis (Figure 2.2A-E, Table 2.1), the silver island size increases and the total surface

**Table 2.1** Analysis of Polymer-Templated Nanostructures with Varied Ionic Strength

[NaCl] (mM)	Ag island size ( $\mu\text{m}^2$ )	overall surface area ( $\mu\text{m}^2$ ) in a $5 \mu\text{m} \times \mu\text{m}$ scan	rms roughness (nm)
0	$0.86 \pm 0.13$	$35.15 \pm 1.60$	$228 \pm 23$
10	$1.18 \pm 0.24$	$28.22 \pm 0.78$	$187 \pm 90$
100	$0.81 \pm 0.14$	$30.60 \pm 0.18$	$143 \pm 7$
300	$2.30 \pm 0.44$	$31.46 \pm 2.76$	$174 \pm 41$
700	$0.94 \pm 0.12$	$33.94 \pm 0.81$	$227 \pm 40$
1000	$2.25 \pm 0.02$	$23.09 \pm 3.53$	$191 \pm 44$
AgFON	$0.25 \pm 0.02$	$34.75 \pm 2.91$	$79 \pm 6$

area decreases as the ionic strength of the solution increases, signifying that the polymer takes on a more globular conformation. Linear regression analysis reveals that the total surface area decreases by  $0.01 \mu\text{m}^2$  for each 1 mM increase in deposition solution NaCl concentration ( $p < 0.02$ ) in a  $5 \mu\text{m} \times 5 \mu\text{m}$  area (Figure 2.2F). Work done by Liu and coworkers is in agreement with this AFM data; they demonstrated that addition of NaCl to PDADMAC in solution causes the positive charge on the polymer backbone to be shielded by the extra chloride ions and that the conformation shifts from a rod structure to a random coil structure because the positive charges are no longer repelling each other.<sup>44</sup> While there are significant changes in the topographical structure of the substrate with varied NaCl concentration, extinction spectra demonstrate that substrate optical properties do not vary significantly, with the bulk plasmon evident at  $\lambda_{\text{max}} = 370 \text{ nm}$  and a broad ( $\sim 80 \text{ nm}$  FWHM) LSPR centered at  $\sim 525 \text{ nm}$ . The broad and stable LSPR is likely due to the highly heterogeneous nature of the polymer-templated roughness features. While this broad LSPR would be a

disadvantage for fundamental plasmonic or SERS studies, it is quite useful for analytical applications of SERS because it endows flexibility in Raman excitation wavelength choice.

SER spectra captured from each of these substrates demonstrate that any added NaCl up to 100 mM yields the same EF as substrates made using PDADMAC in pure water,  $2.3 \times 10^6$ ; however, addition of 1 M NaCl yields a significantly higher EF of  $3.2 \times 10^6$  ( $p < 0.05$ ). The increased EF without an obvious change in LSPR indicates that the high ionic strength deposition solution may promote the formation of a small number of SERS hot spots. However, the standard deviation in EF also increased with increasing NaCl concentration up to 26% standard deviation for the 1 M NaCl; based on the large variation in EF, the high ionic strength PDADMAC solutions were not pursued any further. In general, the large and stable EFs achieved on the polymer-templated

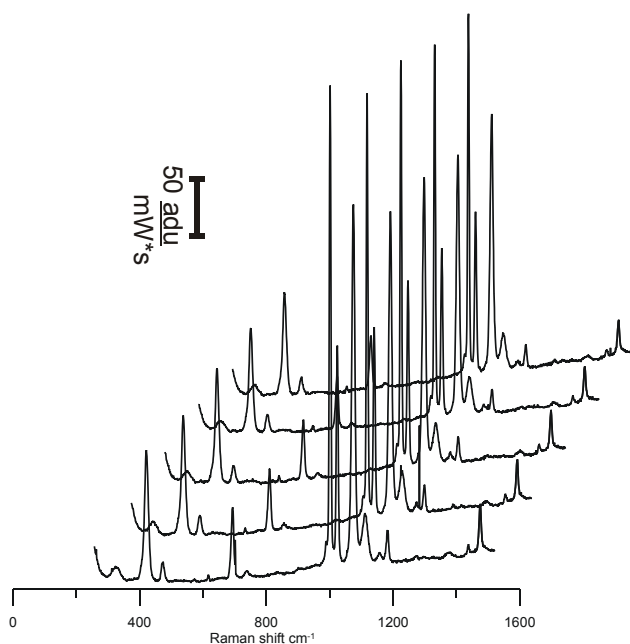


**Figure 2.3** SERS spectra measured from five randomly chosen areas on a BZT-dosed polymer-templated nanostructure made using Ag seed particles and PDADMAC in 10 mM NaCl solution.

nanostructures (Figure 2.3) suggest that wherever the analyte adsorbs or is within the  $\sim 5$  nm of the surface nanostructure, the EM fields are similar and, thus, these substrate can be used for routine SERS analyses.

### 2.2.2.3 Polymer-Templated Nanostructure Robustness

A critical feature for practical SERS substrates is structural and optical stability in varying solvent conditions and with various sample

exposure times. When both the polymer-templated nanostructures and the AgFON

substrates were incubated in solutions made using tetrahydrofuran (THF), the polymer-templated substrate showed remarkable structural and optical stability while the AgFON began to degrade when placed in the THF solution. It was impossible to measure SERS spectra from the AgFON substrate because the evaporated silver had peeled off in multiple places, leaving the silica spheres and the original copper surface exposed.

More important for potential field applications of SERS is the substrate's stability when exposed to aqueous samples. Both the polymer-templated nanostructure and the AgFON appear stable when incubated in water. To quantitatively assess the robustness of each sample, they were first exposed in duplicate to 1 mM BZT and the initial SER spectra were measured. Then, the samples were stored in water for an additional 5 days, collecting LSPR and SER spectra every 24 hours. In both cases, the

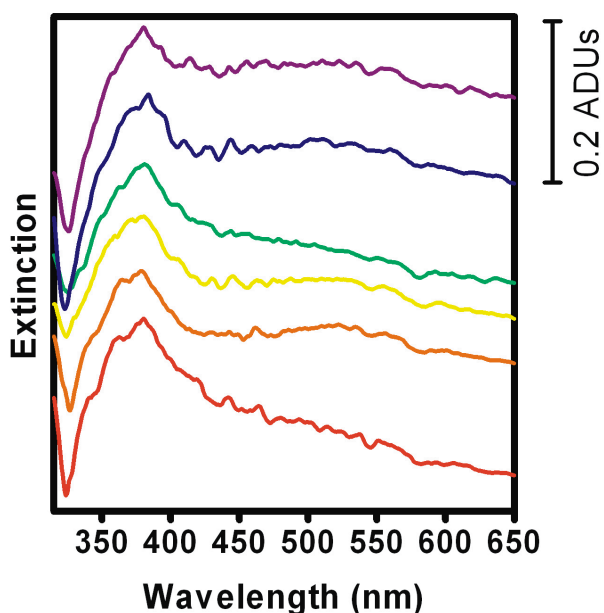


**Figure 2.4** Extinction spectra measured from BZT-doped polymer-templated nanostructures made using Ag seed particles and PDADMAC in 10 mM NaCl solution after varied exposure times to aqueous environment (bottom to top): 0, 24, 48, 72, 96, and 120 h. The spectra are artificially offset from one another for clarity.

LSPR spectra were stable (Figure 2.4) and good S/N SER spectra were still measurable at the end of the experiment. The EF measured after each 24 hour incubation in water is displayed in Figures 2.5A and 2.5B for two polymer-templated nanostructures and two AgFONs, respectively. In these robustness experiments, the intrasubstrate enhancement factor variation on the polymer-templated

nanostructures (and thus, the error bars) is larger than the aforementioned 9%; one

possible explanation for the increased variation is that pinholes in the deposited Ag layer allow water to interact with the PDADMAC layer. In this situation, the heterogeneous PDADMAC thickness would contribute to changes in surface structure, and thus, EF variation. In future work, significant effort will be devoted to decreasing the EF variation through a substrate drying step, efforts to more evenly distribute the initial PDADMAC layer, and/or electroless plating bath formulation.

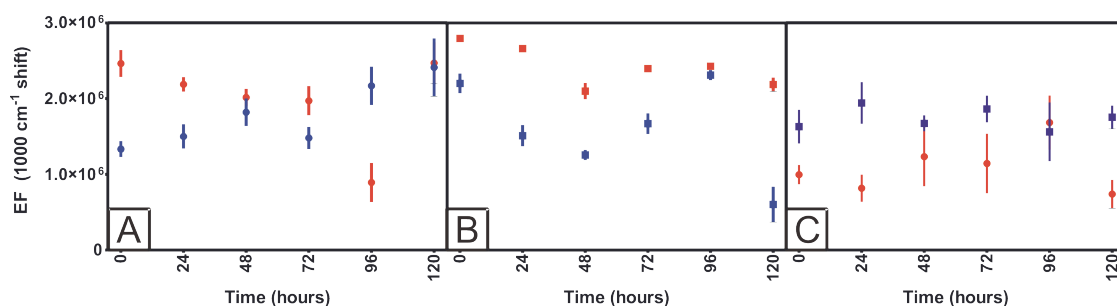


**Figure 2.5** Plots displaying the change in EF for the 1000 cm<sup>-1</sup> shift BZT aromatic stretch from (A) two replicate 1mM BZT-dosed polymer-templated nanostructures, (B) two replicate 1 mM BZT-dosed AgFONs, and (C) 100 mM BZT-dosed polymer template nanostructure (red circles) and AgFON (blue squares) after varied exposure times to aqueous environment (0-120 h). Plots show the average EF measured from five randomly chosen spots on each substrate with error bars representing the standard error of the mean.

The AgFON EFs measured during the water exposure experiment were similar in magnitude to those measured using the polymer-templated nanostructures. In both cases, the EFs vary by significantly less than an order of magnitude and would be useful for analytical SERS applications. There are four possible contributing factors to the measured variation in EFs during the five day aqueous incubation on either of these substrates: (1) LSPR shifting that leads to better or worse matching of the excitation laser, LSPR, and Stokes-shifted vibrational frequency, (2) a change in the number of BZT molecules in the probe volume, (3) variation in the charge-transfer band that contributes to the chemical enhancement mechanism, and (4) modification of the BZT molecular orientation on the substrate that influences the effective induced dipole. Measurement of the LSPR for all of these substrates at each time point demonstrates a negligible change in the LSPR (Figure 2.4). There is no source for increased BZT

molecules during the water incubations, and the solubility of BZT in water is quite small,<sup>45</sup> making it unlikely that the number of BZT molecules in the probe area is changing significantly. The chemical enhancement mechanism is dependent on the Ag-S bond formed during monolayer assembly; the character of this strong interaction is unlikely to vary significantly during water incubation. The most likely explanation is rearrangement of the BZT molecular orientation over the course of this experiment. The largest aromatic ring stretch Raman signal will be achieved when the ring is perpendicular to the SERS substrate. There is ample evidence that perfect monolayers do not form in less than 48 hours,<sup>46,47</sup> and thus, the effects seen here are likely due to monolayer reordering. The exact aromatic stretch band location was examined for direct evidence of this phenomenon but the small variation between 1000 - 1004  $\text{cm}^{-1}$  shift is likely minimized based on the ensemble-averaged nature of these macroscale Raman measurements. However, when analogous 120 hour experiments were performed using polymer-templated nanostructures and AgFON substrates dosed in 100 mM BZT instead of 1 mM BZT, the time point-to-time point EF variation was eliminated (Figure 2.5C). Pairwise t-testing of the EF measured at each time point versus the consecutive time point and the original EF versus the final EF yielded no significant differences for either substrate. Additionally, the S-H stretch of unbound BZT molecules was apparent after 100 mM BZT incubation, based on the appearance of a small band at 2450  $\text{cm}^{-1}$  shift that is not apparent after 1 mM BZT incubation. These facts taken together indicate that dosing from a higher concentration BZT solution provides an excess of BZT molecules (more than a monolayer), presenting less opportunity for molecular rearrangement, and thus, less EF variation over time. In future studies, the potentiometric methods of Lennox and coworkers<sup>46</sup> will be employed to promote faster ordering of the adsorbate to achieve even less EF fluctuation.

### 2.2.3 Conclusions

Herein we present a simple SERS substrate that exploits electroless deposition onto a nanoparticle-seeded polymer scaffold that can be fabricated quickly and without specialized equipment. While there are still many fabrication parameters to be explored, this work demonstrates (1) that large (viz., 80 nm diameter) Ag nanoparticle seeds are more effective plating catalysts than small (viz., 28 nm diameter) Au nanoparticle seeds, yielding a more uniform substrate with larger RMS roughness and SERS EFs; (2) that the highly heterogeneous surface features of the polymer-templated nanostructure generate a broad LSPR, making excitation laser wavelength choice flexible; (3) that changes in polymer deposition solution ionic strength induce topographic variations in the final SERS substrate, though these topographic variations do not induce significant shifts in the substrate optical properties; and (4) that the polymer-templated nanostructure yields comparable SERS EFs and resistance to degradation in 5-day aqueous exposures when compared to the traditional AgFON SERS substrate. This data, in addition to the substrate behavior in alternate solvents such as THF, and the major advantage of the polymer-templated substrate over the AgFON regarding ease of fabrication, leads to the conclusion that these novel substrates will be particularly well-suited to analytical spectroscopy applications. Specifically, it will be possible to generate fresh substrates in a field setting since vapor deposition is not required, and thus, will facilitate the application of the SERS technique to a new class of analyses.

The polymer-templated Ag nanostructure substrates are ideal for on-site SERS substrate fabrication, but, for some applications, substrates with higher enhancement factors or narrow, tunable plasmons are desired. To this end, we present the self-

assembled plasmonic nanohole array substrate.

### **2.3 Self-Assembled Plasmonic Nanohole Arrays**

Since Ebbesen and coworkers discovered extraordinary optical transmission (EOT) through subwavelength noble metal nanohole arrays in 1998,<sup>14,48</sup> there has been significant effort to fabricate nanohole arrays with well-controlled electromagnetic properties.<sup>49,50</sup> For the most part, nanohole arrays have been fabricated using expensive and time-intensive high-resolution serial techniques such as electron beam lithography (EBL)<sup>51</sup> and focused ion beam (FIB) milling.<sup>48,52</sup> In some cases, advanced soft lithography methods such as PEEL (a combination of phase-shift lithography, etching, electron-beam deposition, and lift-off) or soft nanoimprint techniques have been successfully employed to fabricate nanohole arrays.<sup>53,54</sup> In a recent example, Chen et al. fabricated square lattice gold nanohole arrays with sub 250-nm-diameter using UV nanoimprint lithography combined with reactive ion etching and a Cr/Au lift-off process.<sup>55</sup> With this method, the authors varied the nanohole diameter and periodicity with well-ordered nanohole arrays over total areas of 1 cm<sup>2</sup> and examined systemic shifts in the transmission spectra with structural variations, baths with varied refractive index, and thiol chemisorption. While these methods have facilitated important fundamental studies, the field would greatly benefit from a simpler, massively parallel fabrication method that can pattern nanohole arrays with a deep ultraviolet (DUV) patterning resolution, i.e. around 200 nm, without using an exposure tool, photomask, or imprint mold. The work presented herein capitalizes on the nanosphere lithography (NSL) technique conceived of (as "natural lithography") by Deckman et al.<sup>56</sup> and popularized by Van Duyne and coworkers.<sup>57</sup> Instead of employing an as-assembled 2D colloidal array as a shadow mask for nanostructure deposition, this work employs a reactive ion etching (RIE) step to shrink the nanospheres before metal deposition,

facilitating the formation of nanohole arrays after removal of the nanospheres. By controlling the original nanosphere size, etching time, metal deposition thickness, and metal deposition angle, it is possible to tune the nanohole spacing, size and aspect ratio, and accordingly, the plasmonic properties.

While EBL and FIB have been employed in the vast majority of nanohole array studies, there have been a few advances in addition to the aforementioned PEEL and nanoimprint techniques toward implementing high throughput methods. As early as 1995, Masuda et al. used an anodic alumina template and multiple polymer/metal deposition steps to achieve a nanohole array structure; however, this work did not focus on topographic tunability, optical characterization, or use the substrate as a surface-enhanced spectroscopy platform.<sup>58</sup> A decade later, Jiang and McFarland employed a specialized spin-coating technique to create 2D non-close-packed nanospheres for use as a deposition mask, again focusing only on structural fabrication and characterization.<sup>59</sup> More recently, Peng and Kamiya formed randomly ordered nanohole arrays by spin coating a solution of polystyrene beads onto the surface of a silicon wafer, controlling relative bead density by adjusting the ionic strength of the nanoparticle solution, followed by Au film deposition.<sup>60</sup> Nanoholes were then formed by scanning probe microscopy tip machining where the tip is used to expose the gold-coated polystyrene bead and then wet chemistry is used to remove the remaining polystyrene. These nanoholes were then characterized using atomic force microscopy and used to create nanoscale transistors. With a similar focus on only fabrication methodology, close-packed NSL-assembled nanospheres were recently used by Wu et al. as nanolenses for forming a nanohole array.<sup>61</sup> Lee and coworkers reported the combination of NSL and vertical angle ion milling to create nanocrescent holes; however, the holes are disordered, with variable spacing throughout the sample.

Localized surface plasmon resonance (LSPR) characterization of the nanocrescent holes was completed, but the nanostructures were not assessed as surface-enhanced spectroscopy substrates.<sup>62</sup>

While NSL is most often employed as a direct templating method, where metal is deposited into the void space between as-assembled nanospheres, there is precedent for creating more complex nanostructures by combining NSL with plasma or reactive ion etching (RIE) as is done in this work. Van Duyne and coworkers combined NSL and RIE to fabricate embedded triangular nanoparticles that are less prone to solvent remodeling than their non-embedded counterpart.<sup>63</sup> After assembling the nanosphere mask, they use  $\text{CF}_4$  to etch the glass between nanospheres and then deposit Ag through the nanospheres and into the wells. Variation of  $\text{CF}_4$  etch time facilitated plasmon tuning, and SERS enhancement factors as high as  $10^8$  were estimated for chemisorbed benzenethiol. Huang et al used colloidal templating to create a double-layer colloidal crystal mask with two different nanosphere diameters, performed an oxygen etch, a Au deposition, and removal of the top colloidal crystal layer to create gold nanohole substrates.<sup>64</sup> While plasmonic characterization was not performed, the specular reflection was shown to be attenuated compared to glass substrates. Live and Masson prepared microhole arrays by drop coating a polymer microsphere suspension onto glass slides followed by plasma treatment to reduce the size of the spheres and then metal evaporation.<sup>65</sup> Controlled evaporation of the microsphere solution yielded large defect-free areas. Both the localized and propagating plasmons were characterized for these substrates with varied hole diameters and refractive index environments, suggesting utility for microhole arrays in plasmonic biosensing; however, nanoscale features were not attempted in this work. Ctistis et al. recently reported the use of the same method to fabricate nanohole arrays but was focused on the size-

dependent magnetic properties of nanoholes in a cobalt thin film.<sup>66</sup> Lou et al published a short report where NSL and RIE were combined to create nanoholes in Au.<sup>67</sup> This work characterized plasmonic transmission with a fixed hole diameter and varied spacing and used the nanohole array as a substrate for cell growth. Unfortunately, the typical defect-free domain sizes were small, only a few microns, impeding many potential sensor applications. Clearly, there is a great interest and need for massively parallel nanohole fabrication with well-characterized plasmonic and surface-enhanced spectroscopic properties — this is the goal of the work presented herein.

Significant progress has been made in understanding and modeling the plasmonic properties of nanohole arrays fabricated by traditional EBL or FIB methods. A recent systematic study by Lee et al. compared the LSPR spectra and refractive index sensitivity of EBL-fabricated nanohole and nanoslit arrays.<sup>68</sup> Käll and coworkers demonstrated the influence of the dielectric substrate's refractive index on the LSPR shift per refractive index unit (i.e. the sensitivity) that can be achieved using FIB-fabricated nanohole arrays.<sup>52</sup> Parsons et al. examined the effect of nanohole periodicity on the resultant LSPR both experimentally using FIB fabrication, and in finite difference time domain (FDTD) modeling.<sup>69</sup> Schatz and coworkers performed FDTD modeling of both isolated and square arrays of nanoholes in Au to predict the electromagnetic fields due to the interaction of the propagating and localized surface plasmons as well as the optical transmission spectra.<sup>70</sup> Their modeling predicted concentrated fields at both the top and bottom surface of the nanoholes and transmission spectra with multiple features from nanohole arrays. Optical properties have also been characterized in more exotic versions of the nanohole array. For example, Kim et al. characterized optical transmission through arrays of equilateral triangle nanoholes made by ion milling<sup>71</sup> and Brolo and coworkers demonstrated enhancements in spontaneous

emission by coupling quantum dots to plasmonic FIB-fabricated nanohole arrays.<sup>72</sup> These fundamental studies of nanohole optical properties, and correlations with FDTD modeling, are critical for the application of these substrates.

Several groups have also used nanohole arrays for SPR biosensing and imaging.<sup>54,73-77</sup> Oh and coworkers achieved multiplex SPR biosensing and measurement of binding kinetics using FIB-fabricated nanohole arrays in a microarray format.<sup>78-80</sup> Brolo and coworkers also integrated a FIB-manufactured nanohole array into a fluidic device where chemical species could flow through the etched nanoholes, rather than just over the top, in an effort to maximize molecular binding events at the hole edges where the electromagnetic fields should be most intense.<sup>81</sup> In an alternate approach to achieve maximal refractive index sensitivity, Brolo and coworkers also demonstrated SPR sensing of binding events after coating the nanohole array with a dielectric layer such that the only revealed Au surface was within the interior area of the nanoholes.<sup>82</sup> While each of these examples demonstrates the capability of nanohole arrays to act as sensor signal transduction elements, efforts to date have largely been limited to model analyte systems (e.g. biotin/streptavidin) partly due to the low throughput and expensive nature of nanohole array fabrication strategies.

Because nanohole arrays show great promise for SPR and LSPR sensing, they are also inherently promising as surface-enhanced spectroscopy substrates. To date, there are only a few examples of SERS measurements using nanohole arrays as the enhancing substrate. Brolo and coworkers measured SERS spectra from both copper and gold nanohole arrays fabricated using FIB but did not quantify the enhancement factor based on complications in their experimental system.<sup>73,83</sup> Wallace and coworkers also measured SERS spectra from EBL-fabricated Au nanohole arrays, achieving enhancement factors as high as  $4.2 \times 10^5$ .<sup>84</sup> Rowlen and coworkers used EBL-

fabricated nanohole arrays to demonstrate that SERS enhancement decreased as hole lattice spacing increased.<sup>85</sup> While these results are promising, further demonstration of SERS on nanohole arrays is warranted, especially if this can be accomplished using arrays produced using a massively parallel fabrication strategy.

Herein we report a simple method to produce nanohole arrays in a massively parallel fashion where the shape of the nanohole profile can be varied based on the tilt angle during metal deposition. The surface plasmon-enhanced transmission is characterized and correlates well with FDTD simulations. The simulations reveal that the electromagnetic fields are focused at the hole edges, as expected, and that the two measured transmission peaks can be attributed to separate plasmons at the Ag/air and Ag/glass interfaces. Support of two separate plasmons will facilitate optimized SERS enhancement at two different laser excitation wavelengths. High S/N SERS spectra are measured from these nanohole array substrates and the resulting enhancement factors are an order of magnitude better than a silver film without the nanoholes. Further, we demonstrate that the achieved enhancements can be improved by another order of magnitude by using electroless plating to superimpose a textured Ag film over the nanohole array.

### **2.3.1 Experimental Section**

#### **2.3.1.1 Materials**

All the chemicals were of reagent grade or better and used as purchased. All water samples were ultrapure ( $18.2 \text{ M}\Omega \text{ cm}^{-1}$ ) from a Millipore water purification system (Long Beach, CA). Commercially available 400 nm and 600 nm diameter carboxylated polystyrene (PS) nanospheres (Invitrogen, Carlsband, CA, 4 wt%) were used to form a 2D self-assembled single layer. For nanosphere dilution and surface tension control,

1:1 (v/v) MilliQ water:ethanol (Sigma-Aldrich, Milwaukee, WI) were used. Benzenethiol (99%) was purchased from Sigma-Aldrich. 99.999% purity Ag pellets for vapor deposition was purchased from Kamis Inc (Mahopac Falls, NY).

### **2.3.1.2 Preparation of Substrates**

To obtain the hydrophilic substrate necessary for nanosphere self-assembly, standard glass microscope slides were rinsed with acetone, methanol, isopropyl alcohol (IPA) and deionized water, and then sonicated in a cleaning solution of  $\text{NH}_4\text{OH}/30\%\text{H}_2\text{O}_2/\text{H}_2\text{O}$  (volume ratio 1:1:10) for 1 hour. Finally, they were cleaned in a piranha solution ( $70\%\text{H}_2\text{SO}_4/30\%\text{H}_2\text{O}_2$ ) for 30 min. After rinsing thoroughly, they were stored in deionized water and dried with high purity  $\text{N}_2$  immediately before nanosphere deposition. To facilitate large areas of perfect nanosphere packing, the nanosphere solution spreading area was controlled by the presence of lithographically defined polydimethylsiloxane (PDMS, Sylgard) wells. Standard soft lithography methods were employed to create the PDMS wells.<sup>86</sup> A negative photoresist, SU-8 50, was spin-coated onto a silicon wafer and patterned to create the master mold. A 10:1 ratio of PDMS and curing agent was degassed in vacuum, cast onto the master mold, and wiped with a plastic film to remove excess uncured PDMS, creating a 50-200  $\mu\text{m}$  thick layer, and creating holes several millimeters in diameter. After curing the PDMS at 70  $^\circ\text{C}$  overnight, the PDMS sheet was carefully peeled off and aligned onto the glass slide substrate, defining the PDMS wells for nanosphere assembly. The PDMS wells were reused many times.

### **2.3.1.3 Colloidal Self-Assembly of Hexagonal Close-Packed Nanohole Arrays**

Figure 2.6(a) shows a schematic of the colloidal self-assembly using PDMS-defined assembly areas. After dropping the nanosphere suspension onto the glass slides, a single layer of nanospheres is formed from the center and grows toward the outside as

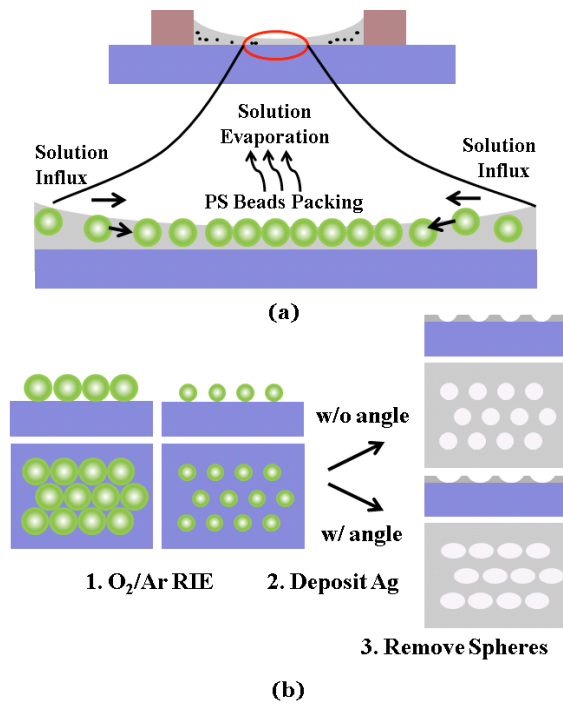


**Figure 2.6** (a) Schematic representation of the colloidal assembly using PDMS-defined areas and (b) process steps for fabricating nanohole arrays using NSL.

location. A mixture of oxygen and argon gas was used in the etch process with the experimental parameters of  $O_2(35\text{sccm})/Ar(10\text{sccm})$ , 60mTorr, 60W. After etching the PS nanospheres, an e-beam evaporator (Temescal) was used to deposit a 50-nm-thick silver film onto the templated substrate. The substrate holder was rotating during normal incidence deposition, whereas it was not in the case of angled deposition. The evaporation chamber pressure and deposition rate were  $5 \times 10^{-6}$  Torr and  $1 \text{ \AA/s}$ , respectively, and the deposition thickness was monitored by a quartz crystal microbalance. Finally, the PS nanospheres were removed with 3M Scotch tape, leaving behind the nanohole array. Residue and any remaining nanospheres were dissolved using dichloromethane and ultrasound sonication at 70 W for 20 min. The processing steps for nanohole array fabrication using NSL are illustrated in Figure 2.6(b).

the solution evaporates. To pattern large areas, the nanospheres were diluted in 1:1 (v/v) milliQ water:ethanol to control the concentration and the surface tension at the liquid-vapor interface. A  $0.5 \mu\text{L}$  droplet of the colloidal suspension was placed onto the glass slides within the 3-mm-diameter PDMS-defined wells and dried at room temperature. The closely packed polystyrene nanospheres were then etched with RIE (Reactive Ion Etch, STS320), causing them to shrink while retaining their original crystalline lattice

### 2.3.1.4 Electroless Plating

Electroless plating of silver onto the nanohole array was accomplished using a protocol described by Halas and coworkers.<sup>87</sup> A nanohole array substrate was submerged in a solution of 1.2 mL of acacia (500 mg/L) with 0.2 mL of buffer solution (1.5 M citric acid/0.5 M sodium citrate, pH = 3) and 0.3 mL of silver lactate (37 mM in water). Then, 0.3 mL of hydroquinone (0.52 M in water) was added while stirring the mixture vigorously. The acacia stabilizes the silver ions and allows for slower reduction of the silver, which causes the formation of "spiky" silver deposition. The substrates were removed from the solution after 4, 6 or 8 min.

#### **2.3.1.5 SEM Characterization**

Scanning electron microscope (SEM) images were taken with a JEOL 6500 field emission gun scanning electron microscope with an accelerating voltage of 5.0 kV. The samples were sputtered with 50 Å of Pt prior to imaging to reduce charging effects.

#### **2.3.1.6 Optical Characterization**

Transmission spectra were measured using a tungsten-halogen lamp and a microscope objective (50X, NA=0.55). The transmitted light was collected using an optical fiber (200- $\mu$ m-diameter core), and the zero-order transmission spectrum was analyzed with an Ocean Optics USB4000 Fiber Optic Spectrometer in the 400-850 nm spectral range. More detailed data collection and spectral normalization methods can be seen in previous work.<sup>76</sup>

Both Ag nanohole arrays and Ag film over nanosphere (AgFON) substrates, prepared as previously described,<sup>88</sup> were dosed with 1 mM benzenethiol (BZT) in ethanol unless otherwise specified. Each substrate was placed in 2 mL of the ethanolic BZT solution for 16 h at ambient conditions to facilitate monolayer formation. The substrates were then removed from the ethanolic solution and rinsed with ethanol before they were mounted in the microscale Raman sample holder. SERS was excited

with a Millennia Vs 532 nm excitation laser with p-polarization (Spectra-Physics, Mountain View, CA) or a 12 mW HeNe 632.8 nm excitation laser with random polarization (Newport Corporation, Irvine, CA). Neutral density filters were added to the optical path to achieve desired incident powers. In both cases, the laser beam was first passed through the appropriate interference filter (Melles-Griot, Rochester, NY) and was then guided into a 20x microscope objective (Nikon, Melville, NY) and onto the sample. The scattered light was collected back through same 20x objective and Rayleigh scattered light was removed using the appropriate notch filter (Semrock, Rochester, NY) before collection. Detection was accomplished using a 0.5 m Spectra-Pro 2500i single monochromator and a Spec 400B liquid nitrogen-cooled CCD chip (both from Princeton Instruments/Acton, Trenton, NJ). In all cases, SERS spectra were measured from three randomly chosen areas on a given substrate. Spectra recorded with near-infrared excitation (752 nm) were excited using an Innova90 Krypton laser (Coherent Inc., Santa Clara, CA) and collected with a WITec alpha300 R scanning confocal Raman microscope with a UHTS300 spectrometer and DV401 CCD detector (all from WITec, Savoy, IL) with a 100x objective (Olympus, Center Valley, PA). In this case, spectra were measured from a 10  $\mu\text{m}$  x 10  $\mu\text{m}$  area.

#### **2.3.1.7 EF Calculation**

EFs were all calculated with the intense benzene breathing stretch at approximately 1000  $\text{cm}^{-1}$  shift for both the liquid and surface-adsorbed. The packing density for BZT on Ag, as reported in the literature, is  $6.8 \times 10^{14}$  molecules/ $\text{cm}^2$ .<sup>40,41</sup> Using the surface area obtained from AFM or SEM measurements (Table 2.2) and the laser spot size, it is then possible to calculate the enhancement factor.

### **2.3.2 Results and Discussion**

#### **2.3.2.1 NSL Process for Self-Assembly of Periodic Nanohole Arrays**

**Table 2.2** SEM-Determined Substrate Surface Areas for Enhancement Factor Calculation

sample tilt angle (deg)	surface area (cm <sup>2</sup> )		
	$\lambda_{\text{ex}} = 532$	$\lambda_{\text{ex}} = 633$	$\lambda_{\text{ex}} = 752$
0	$9.15 \times 10^{-9}$	$1.30 \times 10^{-8}$	$5.66 \times 10^{-9}$
30	$8.34 \times 10^{-9}$	$1.18 \times 10^{-8}$	$5.16 \times 10^{-9}$
45	$8.34 \times 10^{-9}$	$1.18 \times 10^{-8}$	$5.16 \times 10^{-9}$
50	$8.34 \times 10^{-9}$	$1.18 \times 10^{-8}$	$5.16 \times 10^{-9}$
55	$7.93 \times 10^{-9}$	$1.12 \times 10^{-8}$	$4.91 \times 10^{-9}$
60	$7.53 \times 10^{-9}$	$1.07 \times 10^{-8}$	$4.65 \times 10^{-9}$

While the simple "drop and dry" method commonly used for nanosphere lithography can produce a relatively large area 2D packed structure ( $\sim 1 \text{ mm}^2$ ), it is difficult to obtain a single crystalline domain over a large area. When a droplet of colloidal suspension is placed onto the substrate, it spreads out and forms concentric circles before drying. The convex, dome-shaped structure of the droplet hinders the collision and redistribution of the nanospheres at the drying edge, degrading the quality of 2D packing. In addition, since it is difficult to control the exact area over which the droplet spreads out, the local concentration of the nanospheres is not precisely controlled.

Since Nagayama and coworkers observed capillary force-induced 2D self assembly using a Teflon ring,<sup>89</sup> many researchers have been working to improve the quality of the 2D self-assembled structures by using a concave (instead of convex) meniscus relative to the surface of a substrate.<sup>90-92</sup> Using the concave meniscus facilitates the convective flow and enhances the rearrangement of nanospheres just before leading edge solvent evaporation. In this work, a PDMS well encourages formation of a concave meniscus on the substrate and controls the local concentration of nanospheres, facilitating the formation of a packed monolayer over  $\sim 1 \text{ mm}$ -diameter region with a typical single crystalline, defect-free domain size of  $\sim 30 \times 30 \mu\text{m}^2$ . A larger PDMS well can increase the size of a single layer although it becomes more difficult to control the drying pattern and uniformity. We used a 3 mm-diameter well (hole through the PDMS sheet) and

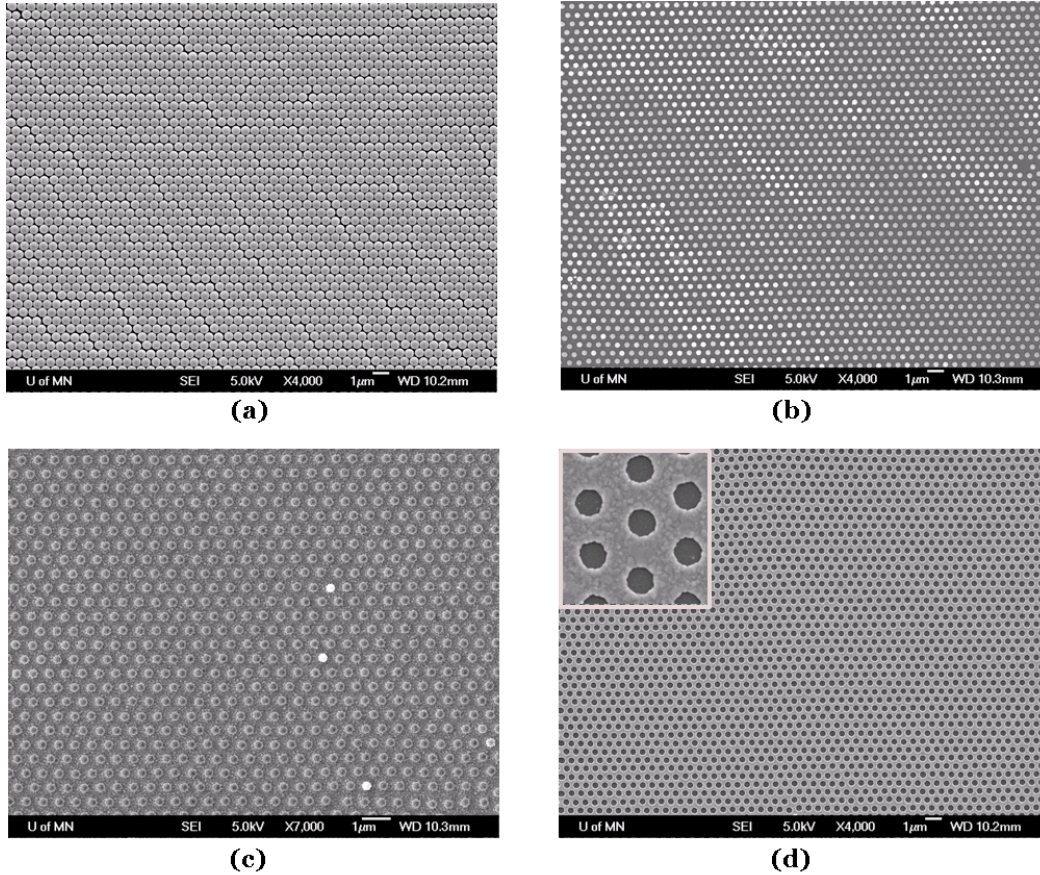


**Figure 2.7** Scanning electron micrographs of (a) single layer formation with PS nanospheres (600 nm diameter), (b) nanosphere template after size reduction using reactive ion etching, (c) nanosphere template after 50 nm thick Ag deposition, and (d) the resulting large area ( $\sim 30 \times 30 \mu\text{m}^2$ ) single crystalline hexagonal nanohole array.

could easily produce poly-crystalline single nanosphere layers  $\sim 1$  mm across. The PDMS wells also allow parallel fabrication of multiple arrays in a reproducible way.

The self-assembly of nanospheres was followed by an RIE process in oxygen plasma to reduce the nanosphere size in a controlled manner. Importantly, the RIE process left the lattice position of each nanosphere intact (Figure 2.7b). Subsequently, a 50 nm-thick Ag film was evaporated onto the nanosphere template (Figure 2c), using each size-reduced PS nanosphere as a shadow mask. Then the nanospheres were removed with tape and solvent cleaning. Figure 2.7d shows the nearly defect-free, crystalline nanohole arrays produced by these steps. The average diameter of the hole

after bead removal was  $196\pm 11$  nm and  $298\pm 7$  nm when using 400 nm-diameter and 600 nm-diameter nanospheres, respectively.

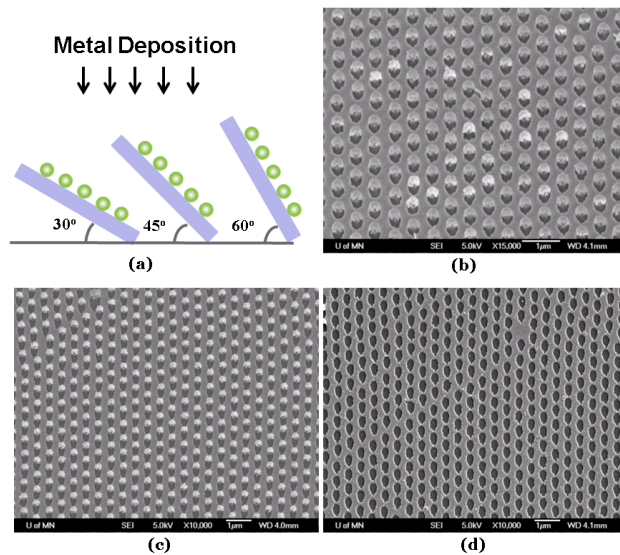


**Figure 2.8** (a) Schematic illustration of the angle-resolved metal deposition process. SEM of (b) an elliptical nanohole array ( $45^\circ$  tilt angle) before nanosphere removal, (c) an elliptical nanohole array ( $60^\circ$  tilt angle) before nanosphere removal, and (d) after nanosphere removal.

angle-resolved deposition process using NSL,<sup>57</sup> many researchers have utilized tilted metal deposition techniques for making nanostructures.<sup>93-95</sup> The ellipticity of the holes depends on the size of nanospheres and the tilt angle of the substrate — smaller nanospheres with a steeper substrate tilt angle produce ellipses with higher aspect ratios. Figures 2.8b and 2.8c show SEM images of  $45^\circ$  and  $60^\circ$ , respectively, tilted metal deposition onto etched nanosphere templates before removing the nanospheres. In Figure 2.8d, the aspect ratio measured after removing the nanospheres was 1.6 when the substrate was tilted to  $60^\circ$ .

### 2.3.2.2 Transmission Spectra and FDTD Simulation

Based on the critical optical properties for SPR, EOT, or SERS biosensing, transmission extinction measurements were completed on circular nanohole arrays. Figure 2.9a presents the experimental results obtained from substrates with circular

Using the NSL process, the size of each nanohole can be easily tuned by changing the RIE processing time. Furthermore, elliptical hole shapes can be created by simply tilting the substrate during the metal deposition, adding another degree of freedom to tailor the plasmon resonance characteristics of the nanohole arrays, shown in Figure 2.8a. Since Haynes and coworkers demonstrated an

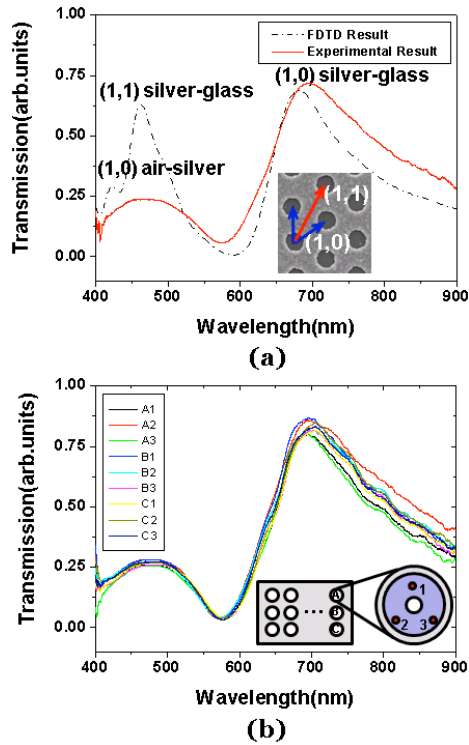


**Figure 2.9** (a) Experimental and computational (FDTD) transmission spectra for a hexagonal nanohole array with a periodicity of 400 nm and a circular hole shape.(inset) The direction of (1,0) and (1,1) resonances. (b) Experimental spectra measured at nine different locations on a nanohole array substrate.

holes made using 400-nm-diameter nanospheres. Finite-difference time-domain (FDTD) calculations (Fullwave, Rsoft Design Group) were performed on the analogous structure and are represented as a dashed line. The spectral position of the maximum transmission peaks can be approximated with the following equation:<sup>96</sup>

$$\lambda_{\max} = \alpha_0 \left[ \frac{4}{3} (i^2 + ij + j^2) \right]^{-1/2} \sqrt{\frac{\epsilon_d \epsilon_m}{\epsilon_d + \epsilon_m}}$$

Where  $\alpha_0$  is the periodicity of the array, the integers (i, j) represent the Bragg resonance orders, and  $\epsilon_m$  and  $\epsilon_d$  are the dielectric functions of the metal and the dielectric, respectively. The calculations and the experimental measurements are in good

agreement. The (1,0) transmission peaks at the silver/glass interface calculated by FDTD and measured by the spectrometer appear at 672 nm and 695 nm, respectively. The (1,1) transmission peak at the silver/glass interface and the (1,0) transmission peak at the silver/air interface overlap at ~500nm, resulting in a broader resonance. Maintenance of two separate surface plasmon resonances on one sample will be convenient because it will facilitate a broader range of possible excitation wavelengths that yield good SERS enhancement factors. Although the probe area in the optical measurements was larger than the size of the perfectly crystalline areas, both the transmitted intensity and the peak wavelengths measured at 9 different locations on the

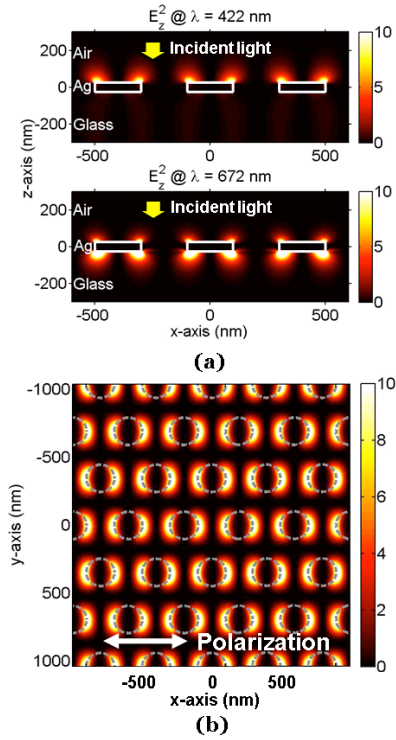


**Figure 2.10** (a) Time-averaged intensity map of the plasmonic field (z-component of the electric field) at  $\lambda=422 \text{ nm}$  and  $\lambda=672 \text{ nm}$ . The FDTD result confirms the wavelength of the transmission peak at each interface. (b) A top-down view of the electric field intensity at the air/silver interface at  $\lambda=422 \text{ nm}$ .

nanohole array sample, as shown in Figure 2.9b, are very similar, centered at  $\lambda=695 \pm 5 \text{ nm}$ .

FDTD modeling facilitates visualization of the electromagnetic field distribution in plasmonic structures. Figure 2.10a shows a time-averaged intensity map of the z-component of the electric field. Periodic boundary conditions are used to simulate an infinite hexagonal array with a periodicity of 400 nm. Since the domain size of the fabricated nanohole arrays are larger than the propagation length of the surface plasmon at visible frequencies,  $\sim 10 \mu\text{m}$  on a smooth Ag film, using such periodic boundary conditions are justified. Furthermore, the propagation length of a surface plasmon within an array is reduced due to scattering introduced by the nanoholes. A non-

uniform mesh was used for computational efficiency, with a nominal grid size of 5 nm and an edge/interface grid size of 2 nm. The dispersion of the silver film was modeled with a Drude/Lorentzian model fit to experimental optical constants. Both electric field maps were extracted from the FDTD calculation at the (1,0) resonance direction (x-axis) at different wavelengths. Light is incident from the top (+z) and excites surface plasmons on the nanohole array at each interface. The optical energy is confined strongly at the air/silver interface with  $\lambda_{\text{max}} = 422 \text{ nm}$ , and to the glass/silver interface with  $\lambda_{\text{max}} = 672 \text{ nm}$ . These results confirm the wavelength of the transmission peak at each interface in Figure 2.9a. Furthermore, the air/silver interface shows high electric

field intensity at both wavelengths, which contributes to the SERS enhancement. Figure 2.10b shows a top-down view of the electric field intensity at the air/silver interface with

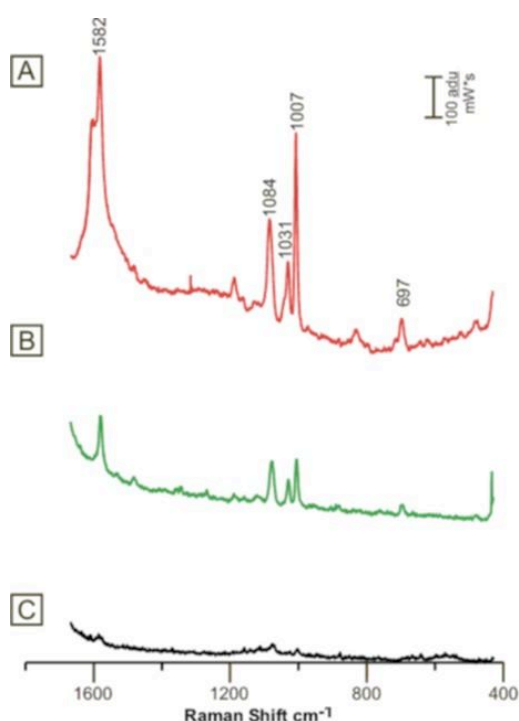


**Figure 2.11** SERS spectra of (A) 1 mM BZT on a AgFON, (B) 1 mM BZT on a circular hole nanoarray, and (C) 1 mM BZT on 50 nm flat silver.  $P=0.32$  mW,  $t=180$  s and  $\lambda_{ex}=532$  nm.

$\lambda_{max} = 422$  nm. As has been seen in previous nanohole modeling, the electromagnetic fields are largely concentrated to the edges of the nanohole features. The surface plasmon resonance was measured and modeled for the elliptical nanoholes as well, but continued work with these and higher aspect ratio nanoholes will be the subject of future work.

### 2.3.2.3 SERS Measurements

Based on the predicted and measured optical properties, these large area nanohole arrays are good candidate SERS substrates. For initial SERS characterization, all substrates were dosed with benzenethiol, an efficient Raman scatterer with well-characterized surface coverage. SERS measurements were performed on the circular nanohole arrays as well as the elliptical nanohole arrays and compared to both flat Ag substrates and the commonly used AgFON substrate. As can be seen in Figure 2.11, the circular nanohole arrays yield high signal-to-noise SERS spectra, with no spectral evidence for polystyrene residue on the substrate. At 532 nm excitation wavelength, the calculated enhancement factor,  $1.70 \times 10^4$ , is comparable to that measured from a AgFON,  $2.62 \times 10^4$ , and significantly higher than that measured from a flat 50-nm-thick Ag film,  $1.07 \times 10^3$ . Based on the understanding that SERS enhances both exciting and scattered photons, the ideal

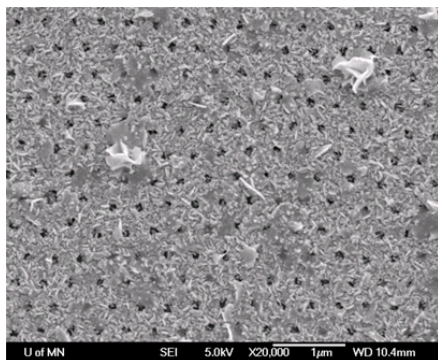
**Table 2.3** Average EF Values over Three Different Wavelengths

sample tilt angle (deg)	average EF		
	$\lambda_{\text{ex}} = 532$	$\lambda_{\text{ex}} = 633$	$\lambda_{\text{ex}} = 752$
0	$1.70 \times 10^4$	$8.13 \times 10^5$	$1.24 \times 10^5$
30	$1.85 \times 10^4$	$1.88 \times 10^6$	$4.18 \times 10^4$
45	$1.63 \times 10^4$	$7.51 \times 10^5$	$2.05 \times 10^4$
50	$1.35 \times 10^4$	$7.15 \times 10^5$	$8.89 \times 10^4$
55	$2.23 \times 10^4$	$5.42 \times 10^5$	$7.03 \times 10^4$
60	$2.97 \times 10^4$	$1.11 \times 10^6$	$4.48 \times 10^4$
flat Ag	$1.07 \times 10^3$	$5.55 \times 10^4$	N/A
AgFON	$2.62 \times 10^4$	$9.04 \times 10^4$	N/A

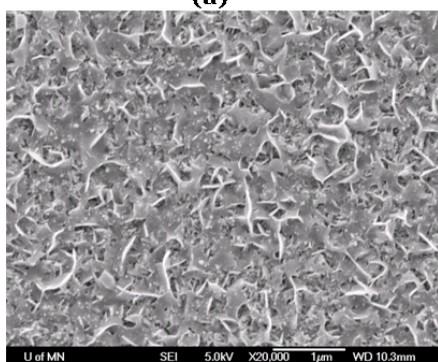
nanohole substrate would have a SPR centered between the excitation wavelength and the Stokes scattering wavelength of interest. When considering the  $1000 \text{ cm}^{-1}$  shift band of benzenethiol, the ideal SPR wavelengths for 532 nm, 632.8 nm, and 752 nm excitations are 547 nm, 654 nm, and 782 nm, respectively. As can be seen in the measured transmission spectra in Figure 2.9a, the 532 nm excitation is off-resonance compared to the other two wavelengths and is expected to yield lower enhancement factors even though Raman scattering is inherently more efficient at shorter excitation wavelengths.

Table 2.3 summarizes the enhancement factors measured at all three excitation wavelengths for the circular nanohole arrays, with values up to  $8 \times 10^5$ . These enhancement factors are comparable to or higher than those reported in the literature for nanohole arrays fabricated using traditional methods,<sup>84,85</sup> and as expected, are significantly larger with the on-resonance 632.8 and 752 nm excitation wavelengths than with the off-resonance 532 nm excitation. Comparison to a flat Ag film of the same thickness demonstrates that the nanohole array gives an order of magnitude better average enhancement. In addition, SERS spectra were also measured from the elliptical nanohole array substrates (Table 2.3). In general, the elliptical profile did not

yield a significantly different enhancement factor than the circular profile. Based on the



(a)



(b)

**Figure 2.12** SEM of (a) 4 min Ag electroless plating onto the nanohole array and (b) 6 min Ag electroless plating onto the nanohole array.

producing high surface area "spiky" features.<sup>87</sup> One literature precedent applying electrolessly plated Ag for SERS was performed by Green et al., where noble metal nanoscale pillars were fabricated using island lithography.<sup>97</sup> In this case, fabrication began with deposition of CsCl islands onto a silica film followed by Cr deposition on top of the CsCl islands. When the islands are removed, the SiO<sub>2</sub> layer was etched, leaving pillars with Cr caps. The Cr is then removed and Ag is electrolessly plated into the gaps between the SiO<sub>2</sub> pillars, and then the SiO<sub>2</sub> is etched away to reveal the final nanostructure. The conditions of the electroless plating bath were altered to give different Ag structures, and high signal-to-noise SERS spectra were measured from adsorbed pyridine though characterization of the LSPR is not done. Herein, for control

predicted concentration of electromagnetic fields in higher aspect ratio nanostructures, future work will focus on polarized SERS measurements from the elliptical nanohole arrays.

While the periodic structure of the nanohole array clearly yields improved SERS performance, further improvement of the enhancement factor would facilitate lower detection limits in future sensor applications. The FDTD simulations reported herein suggest that the majority of the electromagnetic enhancement originates at the edges of the nanoholes. In an effort to exploit the

remainder of the substrate, the nanohole arrays were immersed in a Ag plating bath known for producing high surface area "spiky" features.<sup>87</sup> One literature precedent applying electrolessly plated Ag for SERS was performed by Green et al., where noble metal nanoscale pillars were fabricated using island lithography.<sup>97</sup> In this case, fabrication began with deposition of CsCl islands onto a silica film followed by Cr deposition on top of the CsCl islands. When the islands are removed, the SiO<sub>2</sub> layer was etched, leaving pillars with Cr caps. The Cr is then removed and Ag is electrolessly plated into the gaps between the SiO<sub>2</sub> pillars, and then the SiO<sub>2</sub> is etched away to reveal the final nanostructure. The conditions of the electroless plating bath were altered to give different Ag structures, and high signal-to-noise SERS spectra were measured from adsorbed pyridine though characterization of the LSPR is not done. Herein, for control

**Table 2.4** Average EF Values for Two Different Plating Conditions and Wavelengths

sample	average EF	
	$\lambda_{\text{ex}} = 532$	$\lambda_{\text{ex}} = 633$
nanohole array	$1.70 \times 10^4$	$8.13 \times 10^5$
nanohole array + 4 min plating	$1.58 \times 10^5$	$3.26 \times 10^6$
nanohole array + 6 min plating	$7.51 \times 10^4$	$2.08 \times 10^5$
flat Ag film	$1.07 \times 10^3$	$5.55 \times 10^4$
flat Ag film + 4 min plating	$2.39 \times 10^4$	$1.18 \times 10^6$
flat Ag film + 6 min plating	$2.09 \times 10^4$	$6.11 \times 10^4$

purposes, the previously described nanohole substrate and a flat Ag film were immersed in the plating bath simultaneously. Figure 2.12a shows the resulting structures after 4 minutes in the plating solution; 6 minute plating bath exposure was also performed on identical substrates (Figure 2.12b). Figure 2.13 includes representative benzenethiol SERS spectra recorded from both the normal and enhanced substrates with 532 nm excitation while Table 2.4 delineates the measured enhancement factors using both 532 nm and 632.8 nm excitation for both flat and nanohole array substrates before plating and after either 4 or 6 minutes in the plating bath. These data demonstrate that a 4 minute immersion in the plating bath gives an additional order of magnitude SERS enhancement on either a flat or a nanohole array substrate at either excitation wavelength, yielding enhancement factors as large as  $3 \times 10^6$ . Due to the roughness of the electrolessly plated silver it was not possible to obtain AFM data for the enhanced substrates. EF estimates are based on the original surface areas found for the nanohole substrate. Transmission measurements of the SPR were attempted on these substrates but the recorded spectra were very broad, indicating extremely heterogeneous topographical features. While the substrates that were immersed in the plating bath for 6 minutes do give a slightly improved enhancement factor over the unplated substrates, these substrates were not as efficient as the substrates immersed for only 4 minutes. Electron microscopy analysis of the substrates

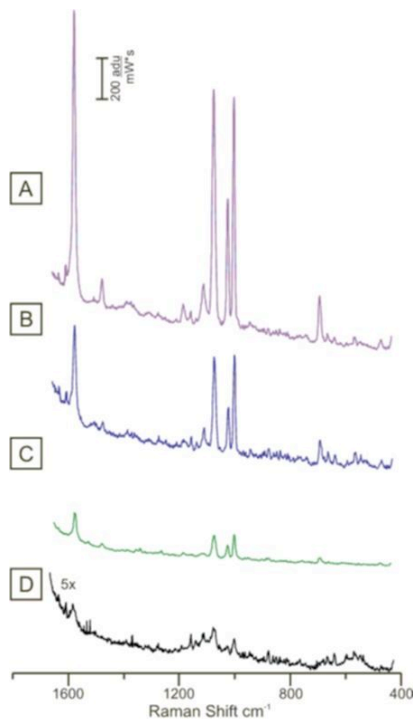


**Figure 2.13** SERS spectra of (A) 4 min Ag plated nanohole array, (B) 4 min Ag plated flat Ag film, (C) a standard nanohole array, and (D) 5x a flat Ag film. All substrates were exposed to 1 mM BZT prior to SERS measurements.  $P=0.32$  mW,  $t=180$  s and  $\lambda_{ex}=532$  nm.

immersed for 6 minutes (Figure 2.12b) revealed that the nanohole structure was nearly entirely obscured, largely negating the enhancement introduced by the nanohole grating structure. Effort was made to avoid obscuring the nanohole substrate by performing the plating directly on the RIE-etched template before sphere removal (without a vapor deposited metal layer). Plating bath immersion times of 4, 6, and 8 minutes all produced a substrate where the nanosphere mask could not be removed by normal means; thus, it was not possible to achieve the desired nanohole array structure.

### 2.3.3 Conclusions

This work has demonstrated a simple and massively parallel nanofabrication technique to produce large defect-free areas ( $>30 \times 30 \mu\text{m}^2$ ) of noble metal nanohole arrays, with demonstrated hole sizes of 300-nm-diameter, across a mm-sized patterning area. The nanohole profiles can be varied simply by controlling the deposition angle onto the etched nanosphere template. The optical transmission properties of the nanohole arrays are extremely homogeneous across a sample, and FDTD simulations predict the optical characteristics accurately, revealing two resonance peaks due to surface plasmons at the two different dielectric interfaces. The nanohole arrays give good signal-to-noise ratio SERS spectra at three demonstrated excitation wavelengths with the largest enhancement factors,  $8 \times 10^5$ , occurring when the plasmon resonance is nearly

centered between the excitation wavelength and the Raman scattering wavelength. The nanohole structure contributes an order of magnitude to this enhancement factor regardless of the excitation wavelength employed. To exploit the substrate region between the nanoholes, Ag electroless plating was implemented on the nanohole arrays to introduce additional surface roughness, yielding enhancement factors as large as  $3 \times 10^6$ . These substrates hold great promise for further application as SERS substrates as well as platforms for extraordinary optical transmission and surface plasmon resonance biosensing.

It was discussed earlier, that the largest EM enhancements from SERS occur at edges of nanoparticles, gaps or sharp tips and this was observed in the FDTD simulation from the nanoholes, where the strongest EM fields were at the edges of the nanohole. In the next section we take advantage of this phenomena and fabricate a substrate with small nanogaps that have large SERS EFs ( $>10^5$ ).

## **2.4 Nanogap Substrates for SERS Sensing**

While the mechanism responsible for single-molecule sensitivity in SERS is not firmly established, it is widely believed that this large enhancement occurs when a SERS-active molecule is positioned within the substantial plasmonic EM fields generated in the gap between two closely spaced metallic nanostructures.<sup>98</sup> Therefore, a large portion of current SERS research is focused toward fabricating nanogap structures via electron-beam lithography,<sup>19</sup> electromigration,<sup>21</sup> nanosphere lithography,<sup>20,57,94</sup> or electrochemical metal growth.<sup>99</sup> In addition, extreme subwavelength confinement of EM energy in nanogaps has critical applications in biosensing, nonlinear optics<sup>100</sup> and plasmonics. However, a reproducible fabrication method, especially one using conventional optical lithography techniques, for the

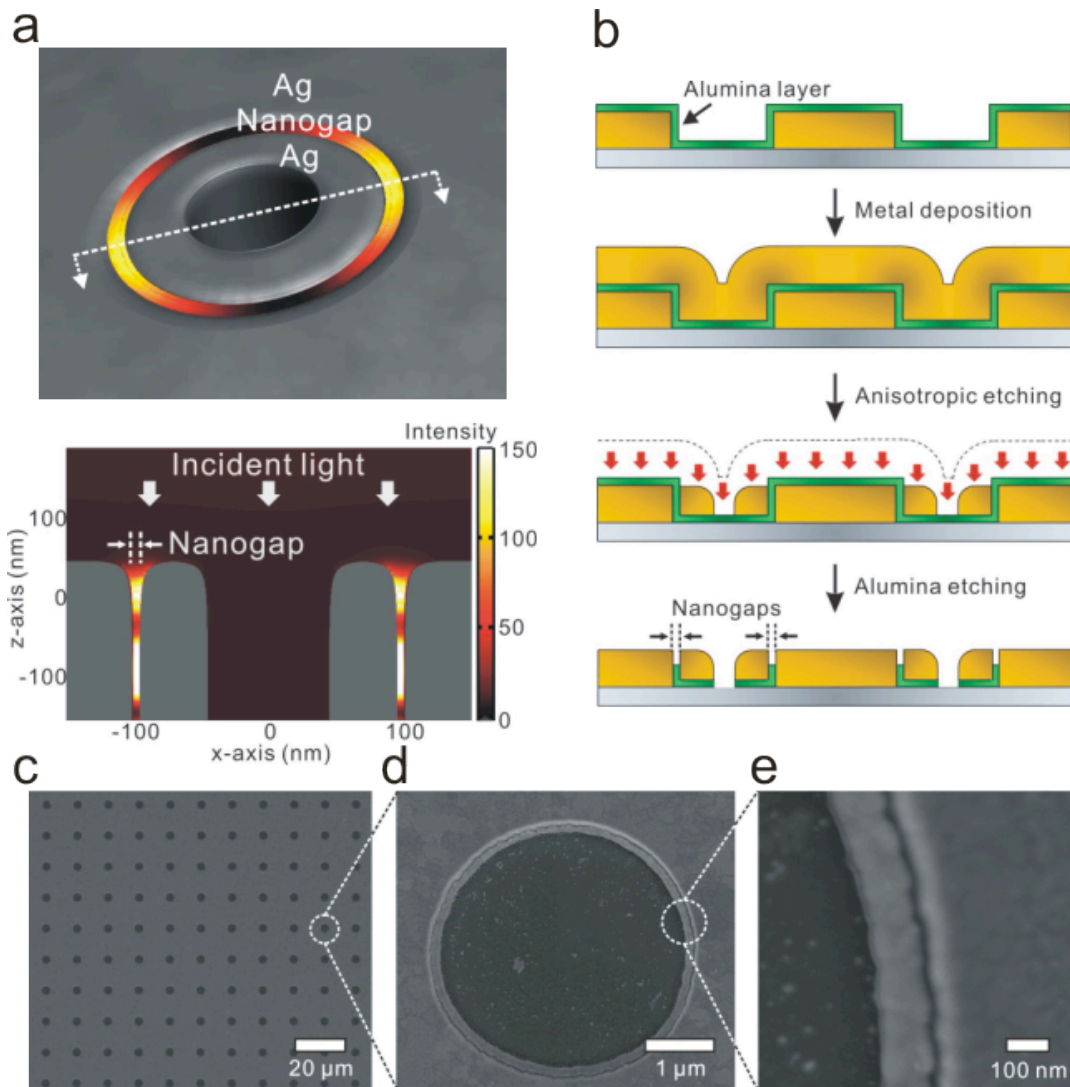


**Figure 2.14** (a) 3-D FDTD simulation results showing significant field intensity enhancement within a 5 nm nanogap. (b) Fabrication process schematic of the nanogap array. Starting from patterned substrates, the secondary metal layer is separated by a thin alumina spacer deposited using ALD. Using sidewall spacer processing, the nanogap size is determined by the thickness of the alumina layer. (c) SEM image of a nanogap array with a circular pattern. (d) The magnified image of a single ring-shaped element shown in panel c. (e) The magnified image of a 10 nm nanogap formed along the ring-shaped element.

production of sub-10-nm gaps with precise control of the gap's size, position, shape, and orientation remains a significant challenge.

It is well-known that thin film deposition techniques such as physical/chemical vapor deposition and atomic layer deposition (ALD) can provide a level of nanometric precision not achievable by even the most advanced electron-beam lithography. Thin

film deposition has been employed to fabricate nanoscale gap or cavity structures with lithography independent control of the critical dimensions.<sup>101-103</sup> In particular, Miyazaki et al. demonstrated nanometric confinement of visible light in a plasmonic nanocavity where two metal layers were separated by a 3-nm-thick SiO<sub>2</sub> layer.<sup>101</sup> However, a major limitation in utilizing such planar structures is the difficulty in coupling normally incident light into and out of the in-plane nanogap. It is problematic to perform Raman spectroscopy over a large array of in-plane nanogaps, since the illumination and collection of the light are shadowed by the metallic overlayers.

#### **2.4.1 Results and Discussion**

Here, this key fabrication challenge is addressed by using ALD - a technique that can readily achieve film thicknesses with subnanometer precision - to form vertically oriented metal-dielectric-metal nanogap structures. Such structures can generate significant field enhancements and tight localization in the gap with normally incident light as shown in Figure 2.14a. The nanogap fabrication process is illustrated in Figure 2.14b. A standard lithography technique, such as optical lithography, defines the initial metal pattern. This is followed by the deposition of an ultrathin sacrificial alumina layer using ALD, which conformally covers the top and vertical sidewall surfaces.<sup>104</sup> After the deposition of a second metallic layer, anisotropic ion milling is performed to create metallic sidewalls spaced by the now exposed alumina. The nanogaps are formed by partially removing the alumina layer with a buffered oxide etchant. In this process, the critical dimension of the nanogap structure is precisely determined by the thickness of the conformal alumina layer, which, in our structures, ranges from 5 to 20 nm. A continuous nanometric gap is created along the perimeter of the patterned metal areas, providing a wide variety of design freedom for making SERS substrates and plasmonic

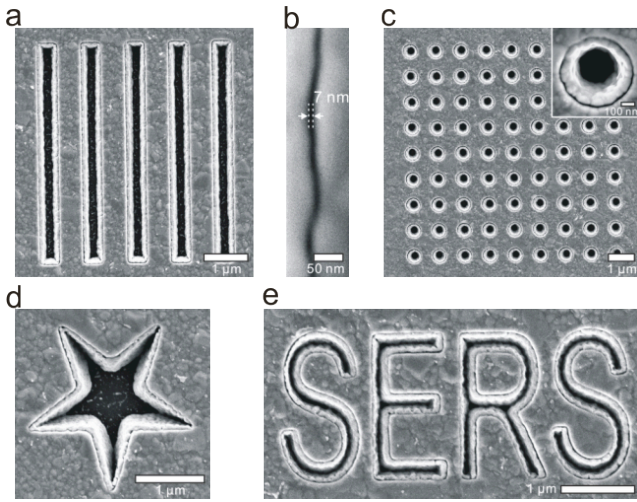


**Figure 2.15** SEM images of different types of nanogap arrays: (a) slit array with 500 nm width and 1.5  $\mu\text{m}$  periodicity; (b) the magnified image of 7 nm nanogap from a slit pattern shown in panel a; (c) 9 x 9 nanohole array with 500 nm diameter, the inset to panel c shows the magnified image of one hole; (d) nanogap on a single star-shaped substrate; (e) nanogap structures, where the initial nanogap formed along a “SERS” character pattern.

patterns were defined using focused ion beam milling, are shown in Figure 2.15. The key advantage of this fabrication scheme is the ability to confine and manipulate LSPRs and their associated high field intensities along the entire vertically oriented metal-air-metal nanocavities.<sup>105</sup>

To characterize the SERS performance of the silver-air-silver nanogap arrays, substrates were incubated in 1 mM benzenethiol (BZT), a well-characterized and efficient Raman scatterer. Ag film over nanosphere (AgFON) substrates,<sup>34</sup> which have been widely used for SERS applications, were used as reference samples. On the AgFON substrates, the field distribution varies with position, where only a few dominant Raman “hotspots” contribute to the overall signal.<sup>106</sup> In contrast, with our structures, it is possible to generate well-defined, high-density hotspots along the entire length of the nanogap.

For a quantitative comparison, confocal Raman microscopy was used to map the

devices such as waveguides and resonators.<sup>105</sup> Figure 2.14c-e shows a circular gold-air-silver nanogap array, where the circles were defined using optical lithography over a 4-in. Si wafer. Each circle in the gold film contains a 10 nm nanogap structure along its inner wall. By use of photoresist with opposite polarity, inverse structures were also made. Various other silver-air-silver nanogap structures, where the initial

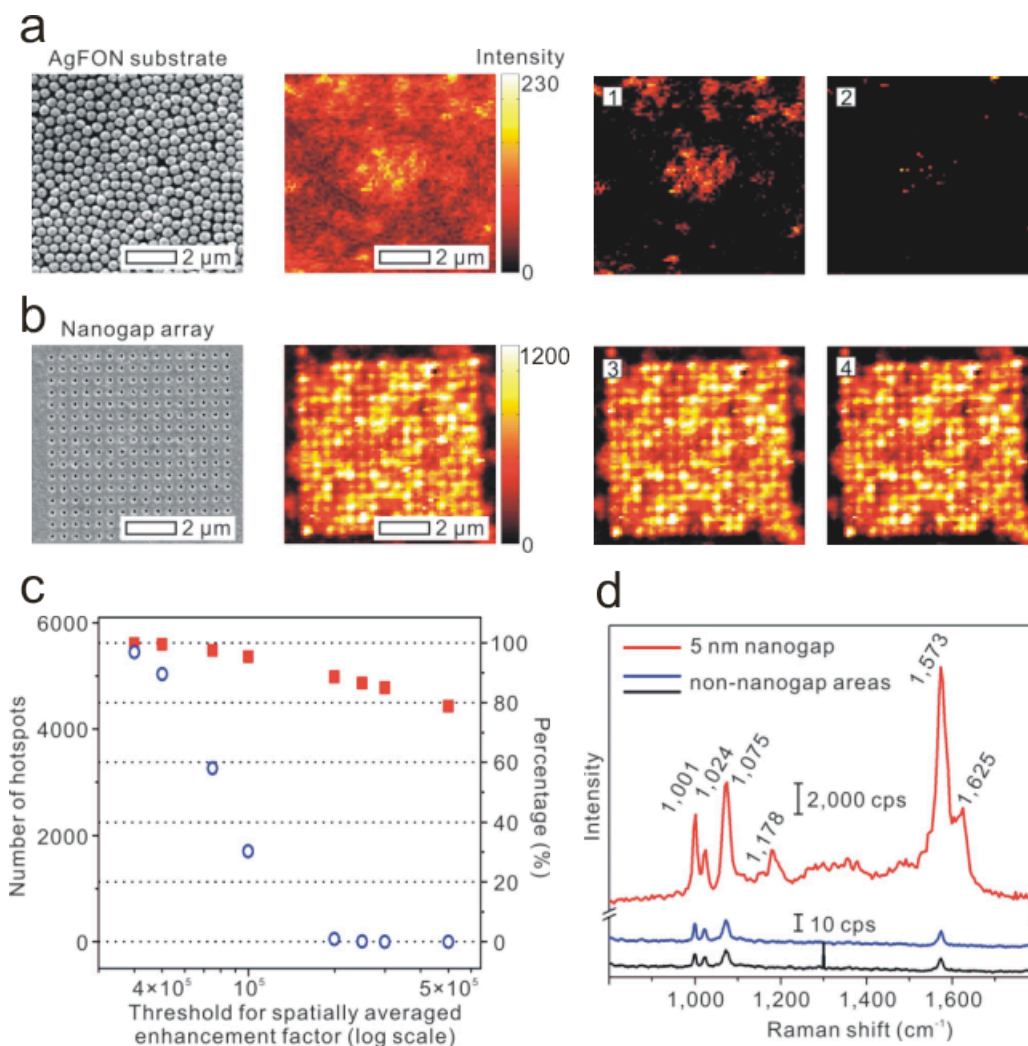


**Figure 2.16** (a) Confocal Raman imaging of a AgFON substrate, and (b) nanogap array of hole patterns with different spatially averaged thresholds ( $1 \times 10^5$  and  $2 \times 10^5$  in panels 1 and 3 and 2 and 4, respectively). (c) The number and percentage surface coverage of SERS hotspots above various EF thresholds. Open circles are measurements from AgFON substrates, while closed squares are measurements from nanogap arrays. The numbers (1, 2, 3, and 4) refer to representative images in panels a and b. (d) comparison of Raman spectra of benzenethiol from nanogap (red line) and non-nanogap (blue and black lines) areas.

spatial distribution of hotspots and to calculate SERS enhancement factors from several substrates. A diffraction-limited 514.5 nm laser spot was scanned over the substrates, and Raman spectra were collected as a function of position. Each pixel in the Raman intensity images was generated by calculating the height of the band at  $1,075 \text{ cm}^{-1}$  shift, an aromatic breathing mode in BZT. While an  $8 \times 8 \mu\text{m}^2$  area of an AgFON substrate shows randomly distributed hotspots (Figure. 2.16a), a nanogap device made on a

periodic nanohole pattern with an ALD- defined gap size of 5 nm shows a more homogeneous distribution of hotspots with stronger Raman signals for the same incident laser power covering the same area (Figure 2.16b). We chose the nanohole periodicity (500 nm) to give high nanogap density, but spaced far enough apart to resolve individual nanogap hotspots with our excitation laser wavelength (514.5 nm). While not presented here, the array periodicity may be further optimized for resonant operation. The Raman intensity images were then filtered according to a specific spatially averaged enhancement factor (EF) threshold (Figure 2.16a,b, panels 1-4). Clearly, the nanogap device has a significantly higher density of hotspots with a spatially averaged EF above  $1 \times 10^5$  and  $2 \times 10^5$  (panels 3 and 4, respectively) than does the AgFON substrate (panels 1 and 2, respectively). Indeed, less than 30% of the AgFON substrate has spatially averaged EFs above  $1 \times 10^5$ , while the nanogap sample shows more than 90% coverage. This drops only slightly when the threshold is raised to  $5 \times 10^5$ , whereas less than 1% of the AgFON area exceeds this EF(Figure 2.16c). Additionally, the ALD-defined nanogaps exhibit a signal-to-background contrast of more than 500 between nanogap and non-nanogap areas (Figure 2.16d). It should be noted that the nanogap EFs calculated here are spatially averaged over the spot size of the incident laser, and the local EF along the nanometer gap itself is much higher, as explained below.

**Table 2.5** Surface Areas Used to Calculate Spatially Averaged and Local EFs of 5 nm Nanogap Structures

	surface area (cm <sup>2</sup> )	
	spatially averaged EF	local EF
200 nm slit	$1.27 \times 10^{-10}$	$2.94 \times 10^{-12}$
500 nm slit	$2.25 \times 10^{-10}$	$1.83 \times 10^{-12}$
1000 nm slit	$2.25 \times 10^{-10}$	$1.83 \times 10^{-12}$
200 nm hole	$3.02 \times 10^{-10}$	$2.18 \times 10^{-12}$
500 nm hole	$3.41 \times 10^{-10}$	$1.90 \times 10^{-12}$
1000 nm hole	$5.10 \times 10^{-10}$	$1.83 \times 10^{-12}$

With the 5 nm gap structures studied here, the gap size, rather than the specific shapes of the initial lithographically defined patterns, determines the local EF. Figure

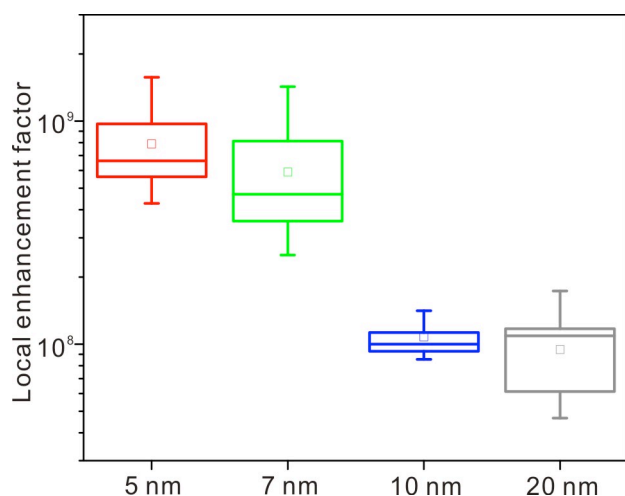


**Figure 2.17** The local enhancement factors of nanogap arrays with different nanogap sizes ranging from 5 to 20 nm. Lines in error bars represent values of minimum, 25%, median, 75%, and maximum, and a square represents the mean value.

2.17 shows the calculated local EFs for various fabricated nanogap structures with different gap sizes ranging from 5 to 20 nm. In this case, local nanogap EFs are calculated based on the assumption that the hotspots are positioned at the edge of the nanogaps, in an area much smaller than the diffraction-limited laser spot size. A very small portion of the adsorbed molecules contribute a

disproportionate share of the entire spatially averaged EFs given in Figure 2.16 (Table 2.5). It was experimentally shown that the Raman signal from a non-nanogap area (background) is less than 1% of that from a nanogap area (Figure 2.16d), supporting the assumption that the SERS signal is coming predominantly from the nanogap regions. A patterned substrate without an ALD step (no nanogap) has spatially averaged EFs less than  $\sim 10^5$  (not shown) whereas a 20 nm gap structure has spatially averaged EFs of  $\sim 10^6$  and a local EF of  $\sim 10^8$ . The EF increases as the nanogap size decreases, and a 5 nm gap structure has spatially average EFs above  $10^7$  with the maximum local EF value exceeding  $\sim 10^9$ . This behavior of increasing EFs with decreasing gap size is consistent with theoretical calculations.<sup>107</sup>

#### 2.4.2 Conclusions

Together, these results demonstrate high-throughput fabrication of sub-10-nm

plasmonic nanogap arrays via the conformal deposition of ultrathin sacrificial layers using ALD on the vertical sidewalls of patterned metal films. The gap size is precisely controlled by the ALD film thickness, and the nanogap is aligned vertically, enabling simple optical excitation and collection over a large area. The position, shape, and packing density of the vertically aligned nanogap structures are determined by an initial metal patterning step. An array of densely packed 5 nm gaps exhibits high density SERS hotspots with local EFs exceeding  $10^9$ . By combining high-throughput nanofabrication techniques such as nanosphere lithography,<sup>57</sup> nanoimprint lithography,<sup>101</sup> or template stripping,<sup>108</sup> these nanogap structures can be easily and inexpensively fabricated over large areas, opening up many avenues for reproducible and efficient SERS detection. Furthermore, although significant processing challenges remain ahead, if the residual roughness of the patterned metals is eliminated<sup>108</sup> and state-of-the-art ALD techniques are employed to push the limits of our nanogap scheme, it may be possible to make well-defined nanogaps with 1-2 nm gap sizes. Access to plasmonic substrates with large area vertically oriented nanogaps in arbitrary patterns will facilitate control of plasmons and will likely contribute to applications in nonlinear optics,<sup>100</sup> biosensing,<sup>109</sup> and molecular electronics.<sup>110</sup>

In this chapter three novel substrates for SERS sensing were discussed. The first has a simple fabrication scheme that has broad plasmons, EFs of  $10^5$  can be fabricated in a field setting. The second substrate, nanohole arrays, can be used for SERS, surface plasmon sensing or EOT sensing, and the plasmons can be tuned by altering the nanohole size or shape. The third substrate is the nanogap substrate, which, due to its flexible fabrication scheme, allows a gap to be formed along the edge of any metal architecture for SERS sensing. With the expansion of SERS into the areas of biosensing<sup>111</sup>, environmental sensing<sup>112</sup> and homeland security<sup>113</sup>, new and novel

substrates like those discussed herein will provide platforms for advancement in SERS sensing.

# Chapter Three

## A Fundamental Study of Self-Assembled Monolayers on AgFON Substrates

This chapter was adapted from

Bantz, K.C., Nelson, H.D. and Haynes, C.L. *Plasmon-enabled Study of Self-Assembled Alkanethiol Ordering on Roughened Ag Substrates*, Journal of Physical Chemistry C, *Submitted*. All LSPR measurements and SAM thickness calculations were performed by Heidi Nelson and all SERS measurements and data analysis was performed by Kyle Bantz.

### 3.1 Introduction

Since its discovery in the 1970's, surface-enhanced Raman spectroscopy (SERS) has become a powerful tool to investigate and characterize the structural and chemical properties of molecules on plasmonic metal surfaces.<sup>1,2</sup> Upon excitation of the substrate's localized surface plasmon resonance (LSPR), large electromagnetic fields are generated at the surface of the substrate, causing the induced dipole of the analyte to be amplified and enhancing Raman scattering. SERS has great potential as an analytical signal transduction mechanism but has faced limitations because large spectroscopic signals are only achieved when the Raman-active analyte dwells near (viz., within 5 nm) the roughened plasmonic metal substrate. Self-assembled monolayers (SAMs) have been used for years as coatings on metals to reduce corrosion, for mimicking extracellular matrix in cell studies, and for passivating surfaces for electrochemistry.<sup>3-5</sup> Recently, SAMs have been employed as partition layers on plasmonic metal substrates to facilitate SERS detection of non-traditional analytes.<sup>6-8</sup> The use of SAMs allows non-traditional SERS molecules, those that have no attraction to the metal surface, to be concentrated within the zone of electromagnetic enhancement at the surface of the SERS substrate based on hydrophobic interactions. In chapter four, our group has utilized alkanethiol monolayers assembled on a silver film over nanosphere (AgFON) substrate for the detection of polycyclic aromatic hydrocarbons (PAHs) and polychlorinated biphenyls (PCBs).<sup>9,10</sup> During this work, it was determined that, among the variety of SAMs employed, a decanethiol monolayer best facilitated partitioning of the hydrophobic environmental pollutants. This was surprising because shorter alkanthiol partition layers (that would lead the analyte to dwell closer to the enhancing substrate) were considered but gave comparatively small analyte SERS intensities. This result suggests that a fundamental understanding of what makes an

ideal partition layer is needed. Toward that end, the work presented herein uses LSPR and SERS to assess alkanethiol monolayer formation on the AgFONs as well as the influence of the partitioned species on the SAM structure.

Many studies have examined the formation and interfacial properties of SAMs on monocrystalline Au (111), flat Ag films, or on assembled colloidal films.<sup>11-14</sup> Carron and coworkers examined some properties of alkanethiols on chemically roughened Ag foil and found lower monolayer wettability for SAMs on roughened Ag compare to smooth Ag,<sup>15</sup> and Pemberton and coworkers saw increases in gauche band intensity in the SERS spectra of short chain alkanethiols on roughened Ag electrodes compared to monolayers formed on smooth Au or Ag.<sup>16</sup> While the substrates examined in these literature precedents presented some roughness, most commonly used SERS substrates have significantly larger roughness, likely influencing the SAM properties. One common SERS substrate, and the one employed herein, is the AgFON<sup>17-21</sup> which contains roughness from a nanosphere layer and additional roughness from metal deposition over this nanosphere mask; for example, a AgFON made with 400-nm-diameter nanospheres and 200-nm-thick deposited Ag has a RMS roughness of  $79 \pm 6$  nm.<sup>22</sup> To date, no experiments have been conducted to explore monolayer formation or crystallinity on these roughened AgFON surfaces. It has been assumed that the formation of the monolayers on flat Ag would be similar to those formed on the roughened surface, but in our experience with the monolayers formed on AgFONs, this is likely not the case.

Self-assembled monolayers are traditionally studied during there three different formation stages: 1) low coverage alkanethiol where molecules lay across the surface, 2) intermediate coverage where alkanethiols display many different organizational states and 3) high coverage where a well-packed monolayer has formed.<sup>23</sup> When

monolayers are packed at open circuit potential, it can take 72h or longer for monolayers to reach the final stage of a well-packed monolayer. This long time period is needed because, while the initial adsorption of the SAM to the metal surface occurs quickly, the second stage in monolayer formation is slow.<sup>11</sup> During this slow step, the alkanethiol chains reorganize, and the stability of the monolayer is improved as any trapped solvent is eliminated. This long packing time for SAMs is not ideal; to combat this shortcoming, Lennox and coworkers demonstrated formation of well-packed monolayers in just 15 min by passing a modest potential of +300mV vs. Ag/AgCl through Au electrodes.<sup>24</sup> They used cyclic voltammetry and electroimpedance spectroscopy to characterize their well-packed layers and found, in all cases, that the layers formed faster and blocked electroactive species better than the open circuit packed monolayers.<sup>24,25</sup> Herein, potential packed monolayers on AgFONs are compared to the traditional open circuit packed monolayers, aiming to control the formation and crystallinity of the partition layer as a way to better understand what fundamental SAM characteristics influence analyte partitioning.

There are many analysis methods to probe SAMs on metal surfaces, but some, such as scanning tunneling microscopy<sup>12,26</sup> and ellipsometry<sup>27,28</sup>, fail when the substrate is exceedingly rough. Since the surface area of the AgFON is variable from substrate to substrate, electrochemistry techniques such as cyclic voltammetry and electrochemical impedance spectroscopy do not give reproducible results.<sup>24,25</sup> The work presented herein utilizes SERS band analysis and LSPR monitoring to look at formation of alkanethiol self-assembled monolayers on AgFONs. Herein, two short chain monolayers, octanethiol and decanethiol, and two long chain monolayers, hexadecanethiol and octadecanethiol, were employed to look for SAM thickness and ordering effects over a 72h time period and under potential control. LSPR spectral shifts

upon SAM assembly yields insight about the formation and thickness of the monolayer on the AgFON while SERS band analysis gives information about the monolayer structure as it forms. Overall, the results demonstrate that both the distance a molecule is held from the AgFON surface and the monolayer crystallinity influence which SAM will be an effective partition layer.

## **3.2 Experimental Methods**

### **3.2.1 Materials**

All chemicals used were of reagent grade or better and used as purchased. 1-Octanethiol, 1-decanethiol, and 1-hexadecanethiol were all purchased from Alfa Aesar (Ward Hill, MA). For brevity, the thiols will be referred to as C8, C10, C16, respectively, and octadecanethiol as C18. 1-Octadecanethiol, ethanol, ammonium hydroxide, hydrogen peroxide, tetrahydrofuran, lithium perchlorate and 18-mm-diameter glass coverslips were all purchased from Sigma-Aldrich (Milwaukee, WI). 2,2',4,4'-Tetrachlorobiphenyl (PCB-47) was purchased from Accustandard (New Haven, CT). Polystyrene nanospheres (400 nm diameter) were purchased as a 4% solids solution from Invitrogen (Carlsbad, CA). Silver wire for electron beam deposition was purchased from Kamis Inc. (Mahopac Falls, NY).

### **3.2.2 Substrate Fabrication**

Traditional silver film over nanospheres (AgFON) substrates were fabricated on glass coverslips. The substrates were first cleaned in a solution of 3:1  $\text{H}_2\text{SO}_4/30\%\text{H}_2\text{O}_2$  for 1 h. Afterwards, the substrates were rinsed thoroughly with water before being cleaned by sonication in a solution of 10:1:1  $\text{H}_2\text{O}/30\%\text{H}_2\text{O}_2/\text{NH}_4\text{OH}$  for 1 h. Three microliters of undiluted polystyrene nanosphere solution was deposited on the surface and manually agitated to create a homogeneous layer. The nanosphere masks are

stable on the glass substrates following solvent evaporation based on the formation of a two-dimensional colloidal crystal array. Ag was vapor deposited to a thickness of 200 nm onto the nanosphere mask using electron beam deposition (Airco Temescal, Berkeley, CA) at a pressure of  $4 \times 10^{-6}$  Torr. The rate of deposition, 2 Å/s, and thickness were monitored using a quartz crystal microbalance.

### 3.2.3 LSPR Measurements

LSPR measurements were collected using a BPS101 tungsten halogen light source (BWTek, Newark, DE) and a USB2000 spectrometer with R200-7-UV/VIS reflectance probe (Ocean Optics, Dunedin, FL). All measurements were collected with the dry sample under  $N_2$  in a flow cell, and spectra were recorded from five spots on each substrate. A glass coverslip with 200 nm deposited Ag (and no nanospheres) was used as the blank. For each LSPR spectrum, the peak wavelength  $\lambda_{\max}$  was determined by fitting a Gaussian function to the data in a region of  $\pm 40$  nm around the peak position using GraphPad Prism software.

### 3.2.4 Substrate Modification

A home-built 402  $\mu$ L flow cell was used to control the external environment of the AgFON. Prior to modification, the AgFONs were solvent annealed with hexanes and methanol to stabilize the LSPR.<sup>29</sup> Each AgFON was then incubated in a 1 mM solution of a given alkanethiol in ethanol for up to 72 hours. Samples were rinsed with ethanol to remove unbound alkanethiol and dried with  $N_2$  in the flow cell before LSPR measurements were collected. For each sample, LSPR measurements were collected after 1, 10, and 30 min and 1, 4, 16, 24, 48, and 72 h of incubation.

For potential packed experiments, the AgFON was placed in a 100 mM lithium perchlorate ethanol solution with constant stirring. A 600C potentiostat (CH Instruments, Austin, TX) three electrode system was used with the AgFON as the

working electrode, a Ag/AgCl reference electrode, and a platinum counter wire. Upon initiating the amperometry program, the thiol was added so that the final concentration of thiol in the beaker was 1 mM and the substrates were held at 100 or 200 mV vs Ag/AgCl for 10 min. The substrates were removed from the beaker after potential packing experiments, placed in the flow cell, rinsed with ethanol to remove any unbound thiol, and then dried with N<sub>2</sub> before LSPR measurements were taken. The same three electrode system was used to monitor the potential of the AgFON under open circuit potential SAM formation for 10 min. It was found that the potential of the substrate decreases below 0 mV vs Ag/AgCl upon addition of a SAM.

### **3.2.5 SERS measurements**

After fabrication, the partition-layer modified AgFON substrates were dried and then mounted for SERS measurements. SERS was excited with a Millennia Vs 532 nm excitation laser (Spectra-Physics, Mountain View, CA) with added neutral density filters to achieve the desired incident powers. In all cases, the laser power was chosen to avoid local heating of the sample, even with long exposure times, that would result in the appearance of amorphous carbon Raman bands. The laser beam first passed through an interference filter (Melles-Griot, Rochester, NY) and was then guided to the sample using an Al-coated prism to achieve a spot size of 1.26 mm<sup>2</sup>. Scattered light was collected using a 50-mm-diameter achromatic lens (Nikon, Melville, NY), and the Rayleigh scattered light was removed using a notch filter (Semrock, Rochester, NY). Detection was accomplished using a 0.5 m SpectraPro 2500i single monochromator and a Spec 400B liquid nitrogen-cooled CCD chip (both from Princeton Instruments/Acton, Trenton, NJ). In all cases, SERS spectra were measured from a minimum of five randomly chosen sample areas on a given substrate.

For PCB exposure experiments, the partition-layer modified substrate was immersed

in a 5 mM solution of PCB-47 in THF for 1 min. The substrate was then removed, immersed in methanol to remove any unassociated PCB and allowed to air dry before SERS measurements were recorded.

### 3.2.6 LSPR Thickness Calculation

The thickness of the alkanethiol layer ( $d$ ) was calculated from the LSPR response using the equation

$$(1) \quad d = -(l_d / 2) \ln(1 - R / R_{\max})$$

where  $l_d$  is the decay length of the substrate (25 nm)<sup>30</sup>,  $R$  is the LSPR shift and  $R_{\max}$  is the theoretical LSPR shift for an infinitely thick, perfectly packed alkanethiol layer, calculated from the equation;

$$(2) \quad R_{\max} = m(n_a - n_s)$$

where  $m$  is the slope of the refractive index sensitivity calibration curve,  $n_a$  and  $n_s$  are the refractive indices of the adsorbate and bulk solution, respectively. For each thiol, the calculated layer thickness after 72 hours was compared to the theoretical layer thickness based on the length of the alkanethiol molecules.

### 3.2.7 Statistical Analysis

Linear regression analysis was performed in Graphpad Prism using the data analysis package with values of  $p < 0.05$  used to determine statistical significance. T-tests were also performed in Graphpad Prism assuming equal variance, and a two-tailed value of  $p < 0.05$  was used to determine statistical significance.

## 3.3 Results and Discussion

Previous experiments demonstrated that the signal generated from an analyte exposed to partition layers of various thickness did not scale directly with likely proximity to the SERS substrate.<sup>9,15</sup> For example, C10 was the best partition layer in

PCB detection experiments, even though other monolayers likely facilitated PCB exposure to higher electromagnetic field enhancement.<sup>9</sup> To explore the roles of partition layer thickness and ordering, this work exploits LSPR to monitor monolayers as they formed on the AgFON and utilizes SERS band analysis to assess the crystallinity of the monolayer. Potential packing was also used to influence both time scale and extent of monolayer ordering.

### 3.3.1 Assessing Monolayer Formation

The localized surface plasmon resonance (LSPR) was used to monitor the formation of the alkanethiol monolayers based on the well-characterized refractive index sensitivity of noble metal nanostructures. This method was chosen because the AgFON is quite sensitive, yielding a shift of 481 nm/RIU (refractive index unit), facilitating detection of small changes to the local environment. Other groups have demonstrated that changes in self-assembled monolayer length can be monitored by LSPR.<sup>31</sup> The changes in C8, C10, C16 and C18-coated AgFON LSPR shifts were monitored over a 72 h time period and also after applying a modest potential of +100-300 mV vs Ag/AgCl to the AgFON. The spectra in Figure 3.1 show that the initial formation of a SAM on the AgFON causes a red shift in the LSPR spectrum for all alkanethiol chain lengths and that the longer chains (C16, C18) cause larger shifts in the spectra over time. These LSPR shifts over time are graphed in Figure 3.2. For short chain monolayers, C8 and C10, there is no significant trend in monolayer thickness or formation over the 72h time frame. The overall LSPR  $\lambda_{\max}$  shifts for C8 and C10 are 2.4 and 3.3 nm, respectively. The LSPR shifts for the longer chains, C16 and C18, do have significant trends over the 72h time frame. For C16, an increase in the LSPR  $\lambda_{\max}$  shift over time, with a slope of 0.00136 nm/min, is observed, and there is a significant difference between the substrate LSPR after 1h compared to the longer

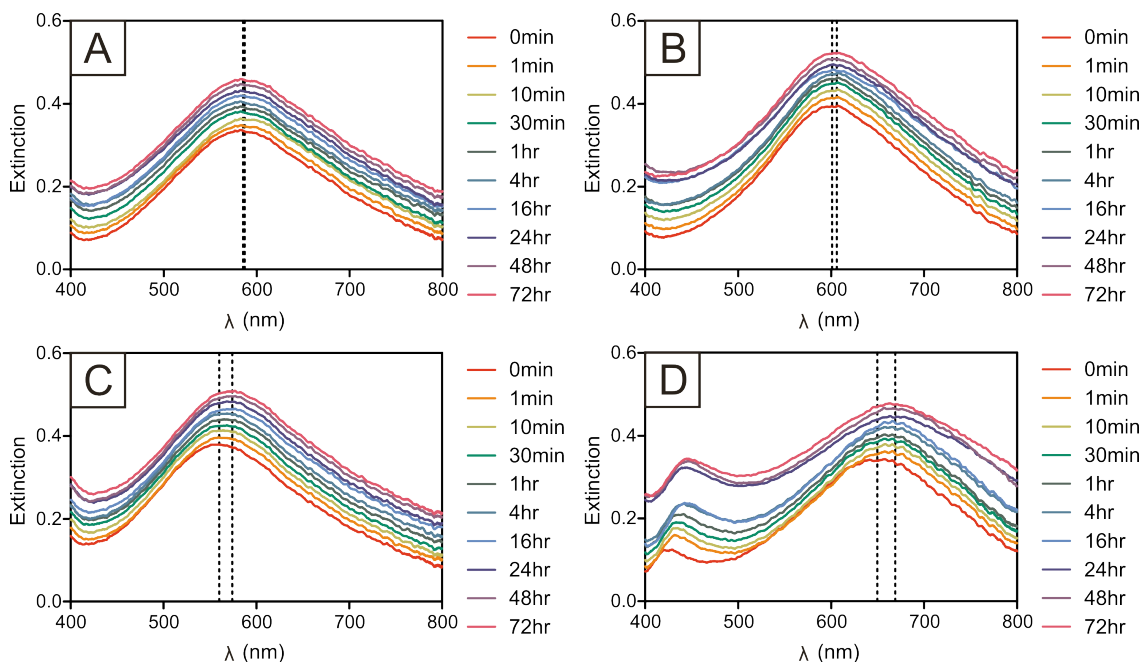


**Figure 3.1** Spectra showing the LSPR shift over 72h for (A) octanethiol, (B) decanethiol, (C) hexadecanethiol, and (D) octadecanethiol. The dashed lines indicate the  $\lambda_{\max}$  shift from T=0 h to T=72 h. Each spectrum is an average from five randomly chosen spots on a substrate. packing times of 24-72 h, with the overall LSPR  $\lambda_{\max}$  shift at 72 h being 12.2 nm.

Like C16, C18 displays a significant increase in LSPR shift over time, with a slope of 0.00156 nm/min, and a significant difference between the substrate LSPR after 1h and the longer packed times of 16-72h, with the final average LSPR  $\lambda_{\max}$  shift at 72 h being 18.6 nm.

For monolayers packed at open circuit potentials, short chain monolayers form quickly, and there is no observable change in LSPR shift over time, but long chain monolayers take longer to form and can take as long as 72h or longer, to reach a full, optimally packed monolayer. In this case, the LSPR data is able to capture the initial fast adsorption step of all thiols on the AgFON, but the slow step reorganization and transitions from SAMs laying on the surface of the AgFON to their standing transitions cannot be detected by the LSPR data for the short chain monolayers. This could be due to the overall roughness of the AgFON, overshadowing any of the small organizational steps the short chain thiols undergo during the second step. On the

other hand, the short chain thiol reorganization may occur on a short enough time scale that LSPR measurements at these time points are not able to capture the transition.

**Table 3.1**  $\lambda_{\max}$  LSPR shifts for potential packed substrates

Potential (vs. Ag/AgCl)	Alkanethiol $\lambda_{\max}$ LSPR Shift			
	C8	C10	C16	C18
0 mV	0.7 ± 2.1	1.3 ± 3.4	3.1 ± 1.8	N/A
100 mV	0.3 ± 2.2	1.2 ± 2.9	6.0 ± 1.9	10.65 ± 2.6
200 mV	6.2 ± 1.9	7.2 ± 2.3	15.2 ± 3.0	17.25 ± 1.5
300 mV	12.1 ± 1.8	82.4 ± 14.5	N/A	N/A

In addition, LSPR shifts were recorded after applying a modest potential to promote monolayer assembly. Potentials of 0, 100, 200 and 300 mV vs Ag/AgCl were used, and the LSPR shift data is listed in Table 3.1. The table shows that the LSPR  $\lambda_{\max}$  shifts for the substrates experiencing 0 or 100 mV vs Ag/AgCl were very small when compared to the open circuit packed monolayers. On the other hand, increasing packing potential to 300 mV vs Ag/AgCl caused discoloration of the substrates and unrealistic  $\lambda_{\max}$  shifts given the known lengths and refractive indices of the alkanethiols. The voltage of 200 mV vs Ag/AgCl was chosen for continued work because the resulting LSPR shifts from the monolayers at this potential were reasonable, and there was no apparent damage to the AgFON itself. Based on the LSPR shift, the 200 mV vs Ag/AgCl packing for 10 minutes created a monolayer that was equivalent to, if not better than, the open circuit potential packed monolayer made in 24 hours for all chain lengths (Figure 3.2). The short chains had average LSPR shifts of 6.2 and 7.2 nm for C8 and C10 at 200 mV vs Ag/AgCl, respectively. These LSPR shifts were larger than the 72 h averages for C8 and C10, which indicates that the monolayer is likely packing more densely on the surface of the AgFON. The longer chain thiols had shifts of 15.2 and 17.3 nm for C16 and C18, respectively. These shifts are comparable to the open circuit packed 72 h LSPR shifts for the longer chain alkanethiols, indicating that potential packing for C16-

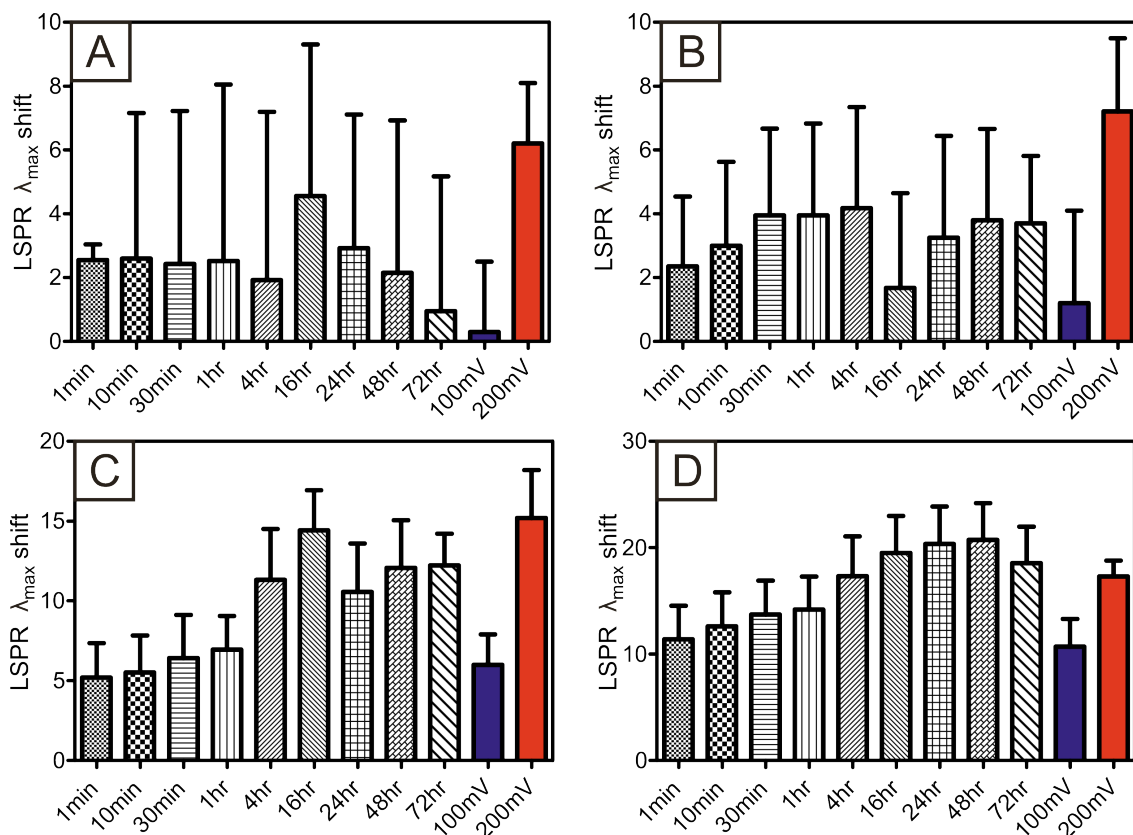


**Figure 3.2** Plots of the LSPR  $\lambda_{\max}$  shift at different time points as well as 100 and 200mV vs Ag/AgCl applied potential for (A) octanethiol, (B) decanethiol, (C) hexadecanethiol and (D) octadecanethiol. Each time point is an average of at least 5 different spots on at least two substrates, and the error bars are the standard deviation.

18 does not lead to large differences in monolayer packing as it does for the shorter chains (though the SAMs are formed much more quickly).

### 3.3.2 Assessing Monolayer Thickness

From the LSPR  $\lambda_{\max}$  shift data, we can use equation (1) to convert  $\lambda_{\max}$  shifts to monolayer thickness.<sup>32</sup> When using this equation, some inherent assumptions are made: (1) early in the derivation, it is assumed that the response to the changes in the bulk index of refraction can be approximated as linear and (2) for the  $R_{\max}$  calculation, it is assumed that the bulk refractive index of the alkanethiol is the same as the refractive index of the thiol when bound to the AgFON surface.<sup>32</sup> When the values calculated based on the LSPR  $\lambda_{\max}$  shifts measured here are compared with the values for calculated alkanethiol monolayer thicknesses on flat Ag, it is clear that in all cases, the

thickness of the AgFON-supported monolayers is much lower than that of the theoretical value (Figure 3.3).<sup>27</sup> The slope of the 72 h packed monolayers is 0.096 nm/-

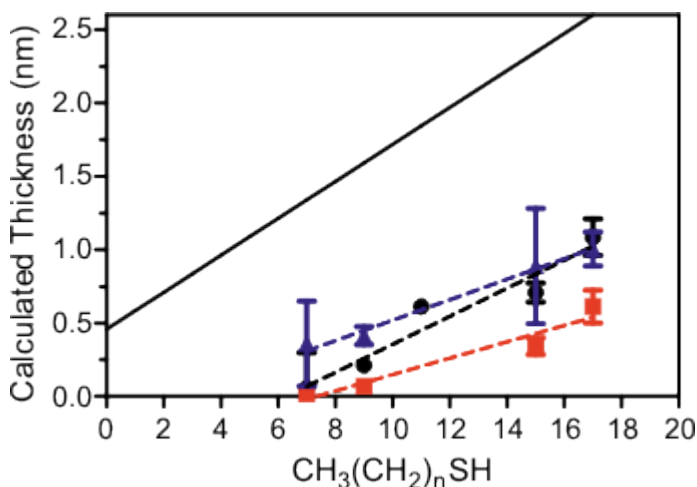


**Figure 3.3** A plot of the calculated thickness of alkanethiol monolayers. The solid line represents the theoretical monolayer thickness on flat Ag as calculated by Porter and coworkers.<sup>27</sup> The 72h open circuit potential packed thickness is represented by the *black circles*, the 100 mV vs Ag/AgCl data is represented by the *red squares*, and the 200 mV vs Ag/AgCl data is represented by the *blue triangles*.

thickness between the literature values and the experimental values has two possible explanations. Unlike the cited literature data, the AgFON surface is not smooth, and the roughness caused by the polystyrene and deposited Ag surface may cause the alkanethiols to pack differently, influencing the tilt angle and thickness compared to those packed on flat crystalline Ag. Another possibility is that the high degree of AgFON curvature leads to less dense alkanethiol packing, yielding a smaller change in effective refractive index and thus, smaller LSPR shifts and lower apparent monolayer thickness values. These data tell us that C10 was a good partition layer because its thickness was small enough for the partitioned PCB to strongly experience the EM enhancement from the Ag surface. If this was the only reason C10 was a good partition layer, we would have expected to see PCB signal scale directly with proximity to the surface, but that was not the case. There is clearly another factor influencing analyte

CH<sub>2</sub> unit, which is similar to but lower than that of the theoretical and experimental ellipsometry values; this is also true for potential packed layers which have slopes of 0.056 and 0.070 nm/-CH<sub>2</sub> for 100 and 200 mV vs

Ag/AgCl, respectively. There is no significant difference between the slopes of the potential packed layers. The difference in

partitioning beyond the thickness of the monolayer.

### 3.3.3 Assessing Monolayer Crystallinity

While partition layer thickness likely plays a role in analyte detection, the ordering of the partition layer is also likely important. The crystallinity of an alkanethiol monolayer can be investigated by looking at the intensity ratio of the trans C-S ( $\nu(\text{C-S}_T)$ ) to gauche ( $\nu(\text{C-S}_G)$ ) bands as an indicator of the quality and crystallinity of the monolayer at the substrate interface.<sup>16,33</sup> Also, by monitoring the  $\nu(\text{C-C}_T)/\nu(\text{C-C}_G)$  ratio, information is gained about the ordering of the upper portion of the monolayer during assembly. An increase in the ratio indicates a more crystalline layer while a decrease indicates

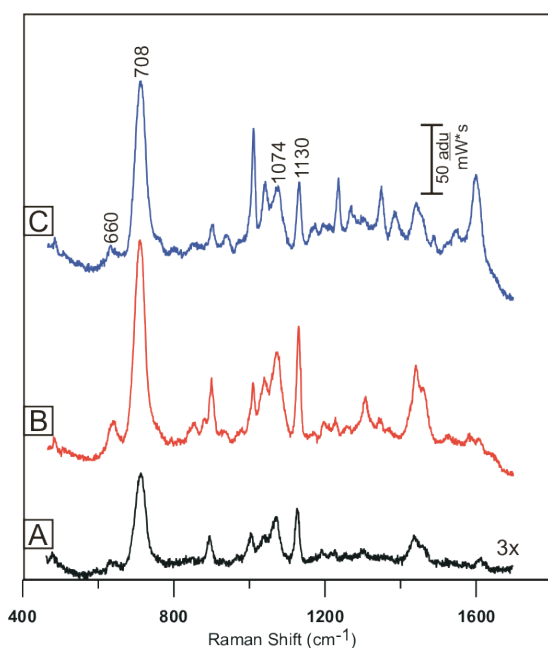


**Figure 3.4** Surface-enhanced Raman scattering (SERS) spectra of decanethiol after (A) 24h in a 1 mM ethanolic decanethiol solution, (B) 10 min in a 1mM decanethiol solution held at 100 mV vs Ag/AgCl and (C) 10 min in a 1mM decanethiol solution held at 200 mV vs Ag/AgCl. In all cases, 2.44 mW of 532 nm excitation laser light was used to record a 10-s spectrum, and calibration was done using a neon lamp.

disorder in the layer. As indicated in the representative C10 spectra shown in Figure 3.4, the  $\nu(\text{C-S}_G)$  band occurs at 660  $\text{cm}^{-1}$  shift, the  $\nu(\text{C-S}_T)$  band at 708  $\text{cm}^{-1}$  shift,  $\nu(\text{C-C}_G)$  band at 1074  $\text{cm}^{-1}$  shift, and the  $\nu(\text{C-C}_T)$  band at 1130  $\text{cm}^{-1}$  shift. Band analysis during monolayer assembly and before/after analyte presentation will reveal how crystallinity correlates with monolayer thickness and impacts analyte partitioning.

First under consideration will be the crystallinity of the upper C-C portion of the monolayer, since this is the first molecular region an analyte will encounter. The short chain alkanethiol C8 displays an increase in

crystallinity with time, with a slope of  $0.0047 \text{ min}^{-1}$ , and a significant difference in the

upper layer crystallinity when comparing 1 min and 72 h alkanethiol assembly times (Figure 3.5). While one might expect that the other short chain alkanethiol would exhibit similar behavior of increasing crystallinity in the upper monolayer with time, instead the opposite trend is apparent. Time evolution of order for the C10 chain is more similar to the longer chain C16 and C18 monolayers. In all cases, the monolayers C10-18 show a decrease in C-C region crystallinity as time progresses, with the largest negative slope occurring in the longest alkanethiol. The slopes for the chains are  $-7.2 \times 10^{-6}$ ,  $-6.7 \times 10^{-5}$  and  $-2.0 \times 10^{-3} \text{ min}^{-1}$  for C10, C16 and C18, respectively. From the LSPR data,

it is known that it takes the long

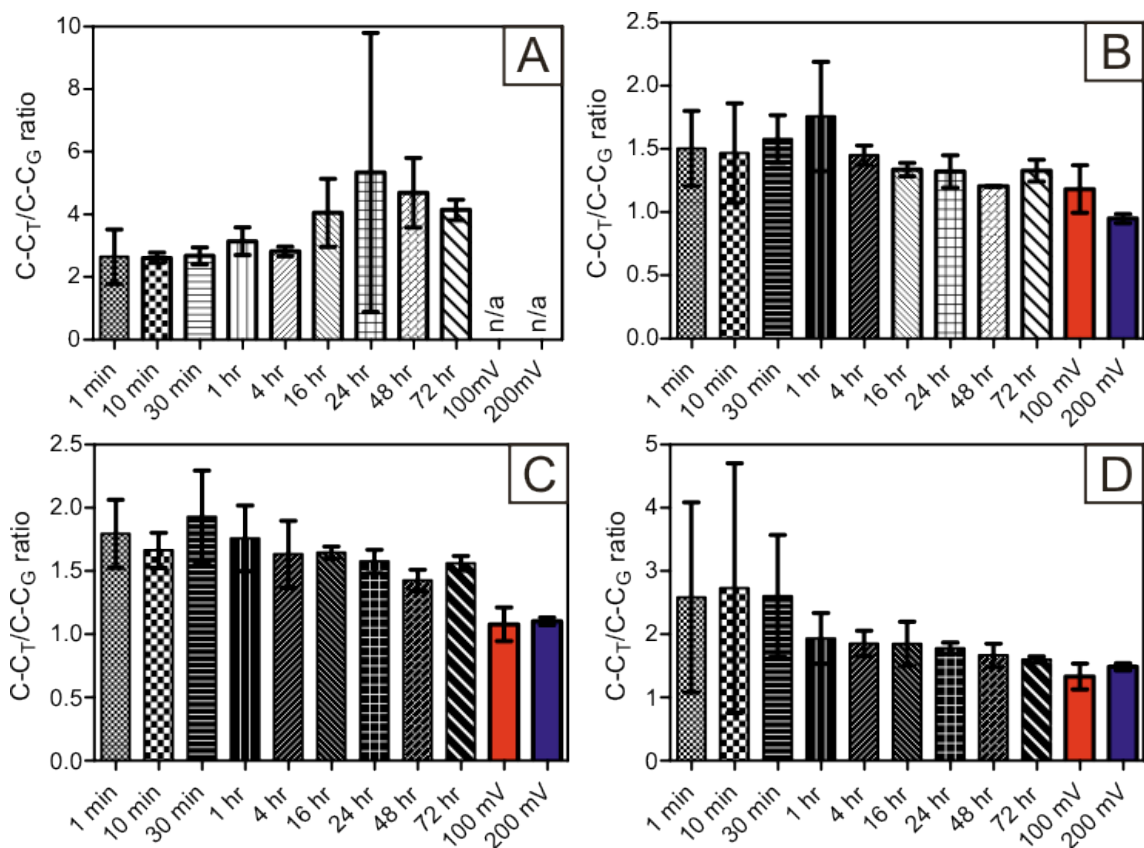


**Figure 3.5** Plots of the C-C<sub>T</sub>/C-C<sub>G</sub> crystallinity ratio for (A) octanethiol, (B) decanethiol, (C) hexadecanethiol, and (D) octadecanethiol. The data points on the plot represent the average  $\pm$  the standard deviation after measurements from three separate AgFON substrates.

alkanethiol monolayers more time to assemble, and the crystallinity data in the upper layer indicates that as time progresses the layers become more disordered. If the

upper layer crystallinity ratio is plotted against monolayer thickness, an inverse correlation is apparent for the long chain monolayers - as the monolayer becomes thicker there is more disorder in the upper layer. There is no correlation between crystallinity in the upper layer and monolayer thickness for the short alkanethiol layers.

The inner layer crystallinity band ratio, which assesses the layer near the substrate surface, is evaluated by comparing the C-S<sub>T</sub> band intensity to the C-S<sub>G</sub> band intensity.

The ratios reveal that the C-S<sub>T</sub>/C-S<sub>G</sub> ratio does not change significantly over time for any of the monolayers (data not shown). However, upon examination of the SERS spectra measured after long assembly times (viz., greater than 24 hrs), many of the SERS spectra were missing the C-S gauche band altogether. The disappearance of the gauche band decreased the number of ratio values averaged for a monolayer at a given time point and increased the standard deviation in the data, making it impossible

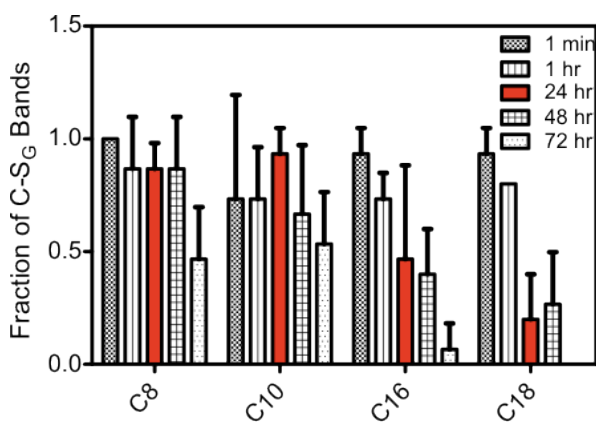


**Figure 3.6** A plot demonstrating the change in C-S gauche band appearance in SERS spectra for the four different alkanethiols as time increases. The data points on the plot represent the average  $\pm$  the standard deviation after 5 replicate measurements from three separate AgFON substrates.

to discern a time-based trend. Because the gauche band indicates disorder in a monolayer, a monolayer that is perfectly packed will have no measurable gauche band in the SERS spectra. Figure 3.6 shows that the number of measurable C-S<sub>G</sub> bands decrease as assembly time

increases. This indicates that as assembly time increases, the monolayer at the substrate surface does become more crystalline. If, for example, we

consider the 24-hour time point, which is the traditional time period that alkanethiol monolayers are allowed to assemble for sensing experiments, it is clear that the SERS

spectra for the short chain monolayers have a larger fraction of gauche bands than the

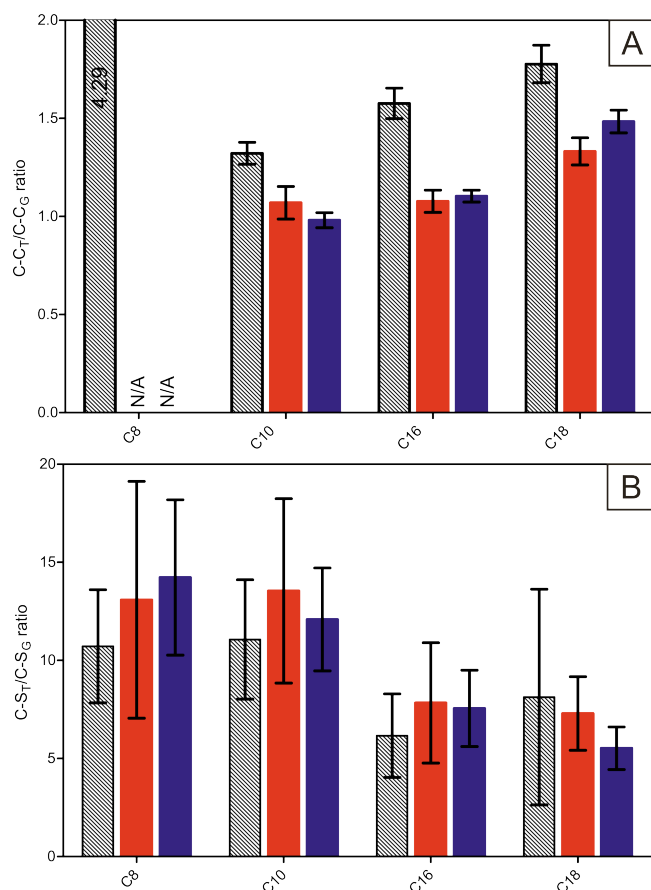


**Figure 3.7** Plots of (A) the ratio of the C-C<sub>T</sub>/C-C<sub>G</sub> bands for C8, C10, C16 and C18 and (B) the ratio of the C-S<sub>T</sub>/C-S<sub>G</sub> bands for C8, C10, C16 and C18. The 24h data is represented by the *shaded bars*, the 100 mV vs Ag/AgCl data is represented by the *red bars*, and the 200 mV vs Ag/AgCl data is represented by the *blue bars*.

SERS spectra for the long chain monolayers. This result indicates more disorder in the inner monolayer for short chain alkanethiols than the long chain alkanethiols at 24 hours. This is consistent with other studies that have monitored alkanethiol formation on flat Ag surfaces and roughened Ag electrodes.<sup>16,34</sup>

SERS band analysis was also used to examine the crystallinity of the potential packed monolayers. As a point of illustration, the analysis here will focus on comparing the 100 and 200 mV vs Ag/AgCl packed layers to the 24 h open circuit assembled monolayer.

The potential packed C8 layer displayed no gauche character in the upper monolayer; accordingly, no ratio values are displayed on the bar graphs (Figure 3.5 & 3.7). In all cases, the potential packed layers displayed similar ratios as the 24h open circuit packed layer. The C10-C18 layers after 24 h assembly display a trend of increasing crystallinity as the monolayer thickness increases with a slope of 0.053 -CH<sub>2</sub><sup>-1</sup>. The same trend is observed with the 200 mV vs Ag/AgCl potential packed layer with a slope

of  $0.056 \text{ -CH}_2^{-1}$ . The 100 mV vs Ag/AgCl upper layers were not as well packed as the 24h open circuit and 200 mV vs Ag/AgCl monolayers and have a smaller slope of  $0.025 \text{ -CH}_2^{-1}$ .

The inner monolayer at the Ag surface has the opposite trend from that observed for the upper layer. In all cases, the potential packed monolayer exhibits the same amount of crystallinity as the 24h packed monolayers. There is no trend for the 24h data across monolayer length, but there is a trend of decreasing crystallinity as the monolayer length increases for the potential packed monolayers (as was measured for the open circuit assembled SAMs). The C-S band ratios were calculated for the potential packed layers, and slopes of  $-0.928$  and  $-0.673 \text{ -CH}_2^{-1}$  were calculated for 100 and 200 mV vs Ag/AgCl, respectively. This indicates that, while potential packing drives the alkanethiol chains to bond to the surface of the AgFON faster, it does not increase packing crystallinity in the inner monolayer for a given alkanethiol chain. This is somewhat confusing when looking at the SERS spectra for C10 (Figure 3.4) where the 100 and 200 mV vs Ag/AgCl spectra are more intense than the 24h spectrum. The difference in intensities would indicate that there are either more alkanethiol molecules on the surface of the AgFON for the potential packed substrates or that their conformation is more favorable compared to the 24h packed substrate, and a change in the packing of the monolayer would be expected with either of these cases; however, the SERS band ratios demonstrate that this is not the case. While more molecules adhere to the surface, the SERS C-S band ratio remaining constant argues that the crystallinity of the inner monolayer is impacted by the overall roughness of the underlying AgFON architecture. Meanwhile, the SERS C-C band ratio remaining constant argues that the influx of alkanethiol molecules packed together more tightly than is observed with under open circuit conditions does not cause a more favorable conformation, instead the extra

molecules actually cause a decrease in crystallinity in the C-C backbone.

### 3.3.4 Assessing Analyte Partitioning

One of the goals of this study was to determine what partition layer characteristics influence hydrophobic analyte partitioning for SERS detection, with specific interest in why PCB and PAH partitioning seemed most efficient in a C10 monolayer. Previous studies showed that the highest intensity aromatic breathing stretch from PCB-47 was achieved when using a 16 h open circuit packed C10 monolayer, compared to C8, C16 and C18 layers packed for the same amount of time. Upon addition of the PCB-47 analyte, all of the monolayers had changes in  $C-C_T/C-C_G$  band ratio, indicating that packing of the layer is perturbed by the partitioning of the PCB. This perturbation was further supported by shifts in the C-S stretch bands. After exposure to PCB-47, the 100 mV vs Ag/AgCl C8 layer went from having no gauche character to having spectra that did contain gauche bands. The same phenomenon of the PCB causing a disruption in the SAM ordering is observed in the  $C-S_T/C-S_G$ , but there is no trend to the interruption. The  $1008\text{ cm}^{-1}$  shift PCB-47 stretch that was used to evaluate partitioning before was also used to evaluate PCB partitioning into the potential packed monolayers here. The largest PCB-47 signal is observed in the 200 mV vs Ag/AgCl C10 monolayer. This layer is less disordered in the upper layer and displays the same amount of ordering in the inner layer when compared with the 24h open circuit packed layer, so it is not surprising that the PCB partitioned favorably into this layer.

### 3.4 Conclusion

To understand the fundamentals of what makes an ideal partition layer, the formation of various monolayers was analyzed with LSPR and SERS band analysis. In general, the packing of alkanethiols on AgFONs is different from that observed on smooth Ag

surfaces. When looking at the monolayer thickness data, it becomes obvious that the extreme roughness of the FON affects alkanethiol packing. LSPR data revealed that short chain alkanethiols form monolayers quickly and the monolayer reorganization step is not observable, while long chain thiols form more slowly and the reorganization can be observed with LSPR measurements. The SERS band analysis revealed that in the case of C8, the order of the upper monolayer increases with time while conversely the C-C backbone ordering decreases with increasing packing time for the long chain alkanethiols. In this study, the data show that the fundamental properties that make a good partition layer are a combination of (1) monolayer thickness and (2) the crystallinity of the upper and lower monolayer. It would seem that the C10 monolayer is a good partition layer for PCBs due to its small monolayer thickness and its balance between monolayer order and disorder.

The ability to recreate the same balance of order and disorder with an applied potential of 200 mV vs Ag/AgCl confirms that the balance in ordering is what makes C10 an ideal partition layer. This balance can be created in part by applying a modest potential of 200 mV vs Ag/AgCl to pack the alkanethiol on the surface of the SERS substrate. This generates crystallinity that is comparable to the 24h open circuit packed substrate, but the thickness of the monolayer is greater than that observed at 24-72h. The ability to create SAMs on substrates in a fast and reproducible manner will increase the use of SAMs for SERS, since a 24h time period isn't needed to form a monolayer. Specifically, this work allows the tailoring of monolayer thickness and crystallinity via potential packing for a short period of time, a large advantage over traditional monolayer formation.

# Chapter Four

## Partition Layer-Modified Substrates for Surface-Enhanced Raman Scattering Detection of Complex Environmental Mixtures

This chapter was adapted from

Bantz, K.C., Jones, C.L., and Haynes, C.L., *Partition Layer-modified Substrates for Reversible Surface-enhanced Raman Scattering Detection of Polycyclic Aromatic Hydrocarbons*, *Analytical and Bioanalytical Chemistry*, 2009, 394, p. 303-311 All data interpretation, EF calculations, SERS band analysis, and departitioning experiments were performed by Kyle Bantz and all SERS PAH spectra and PBDE spectra were taken by Courtney Jones.

Bantz, K.C. and Haynes, C.L., *Surface-enhanced Raman Scattering Detection and Discrimination of Polychlorinated Biphenyls*, *Vibrational Spectroscopy*, 2009, 50, p. 20-35

## 4.1 Introduction

Raman scattering holds great potential as a signal transduction mechanism for analytical sensors based on its basic ability to perform label-free identification of molecular species in water. However, the small inelastic scattering cross-section of molecular species requires either very high laser powers or very long collection times to detect Raman-active species in solution or mixtures.<sup>1</sup> Surface-enhanced Raman scattering (SERS) on nanostructured noble metal substrates offers significant improvements over normal Raman scattering as the excitation of the localized surface plasmon resonance generates large electromagnetic fields within a few nanometers of the substrate, greatly increasing the changes in electron cloud polarization and thus, the Raman scattering signal. SERS sensors have been successfully employed to detect a wide range of small molecule and protein analytes, including DNA,<sup>2</sup> antigens,<sup>3</sup> biowarfare agents,<sup>4,5</sup> and foodborne pathogens.<sup>6</sup> However, the detectable analytes are largely limited to species that have a natural affinity for either the noble metal surface or something that binds to the noble metal surface, where the large electromagnetic fields are localized. Recently, there has been significant effort to develop strategies that facilitate the use of SERS for non-traditional SERS analytes by employing a substrate-bound partition layer to pre-concentrate the analyte of interest within the zone of electromagnetic enhancement without having to employ a binding partner for each particular target analyte.<sup>7-9</sup> This approach will facilitate detection of a broad range of analytes, either individually or simultaneously, using a single substrate. The work presented herein employs assembly of a partition layer onto the SERS substrate to concentrate the target analytes within the enhancing EM fields.

Addition of self-assembled partition layers onto a SERS substrate transforms an analytical technique with limited molecular targets into one that can be developed to

detect nearly any species. Many different types of monolayers can be utilized to concentrate a wide variety of analytes. If a hydrophilic partition layer is needed, a polyethylene glycol (PEG) self-assembled monolayer (SAM) can be employed since the ether groups on the PEG can hydrogen bond with the analyte. This approach was used by Van Duyne and workers, who assembled a (1-mercaptoundeca-11-yl)tri(ethylene glycol) SAM onto a SERS substrate to detect physiologically relevant concentrations of glucose based on the hydrogen bonding interactions between the glucose alcohol groups and the oxygens in the SAM.<sup>10</sup> Alternatively, straight-chain alkanethiols can be employed to take advantage of van der Waal interactions with hydrophobic analytes. Carron and coworkers were the first to employ partition layers on SERS substrates to detect non-traditional environmental SERS analytes.<sup>11</sup> Their work demonstrated that octadecanethiol monolayers on roughened Ag foil could be used to distinguish different xylene isomers<sup>12</sup> and detect adsorbed chlorinated ethylenes.<sup>13</sup> Because the substrates used in this work had SERS enhancement factors of  $2 \times 10^3$ , detection limits in the parts per million range or higher could be achieved with long collection times (500 s) and high laser powers (40 mW). One goal of this work is to improve these detection limits and spectra collection conditions by using SERS substrates with higher enhancement factors and more optimal partition layers. In addition, this work aims to demonstrate that the partition-layer modified SERS substrates are reusable and immune to interference by common soil constituents.

Choice of molecular chain length will greatly influence the achieved SERS signal both based on the EM field decay and the effects of order/disorder on the partitioning mechanism. In some cases, shorter alkanethiol chains may be preferable over the longer hydrophobic chains because the longer chains pack more efficiently and leave little space for an analyte to partition. In other cases, the highly ordered long chains

may be necessary to achieve optimal partitioning as the analyte displaces solvent molecules within the assembled partition layer.

An AgFON substrate is used for these experiments and has an enhancement factor of  $2.5 \times 10^6$ , at least three orders of magnitude higher than the silver foil used in the work done by Carron and coworkers.<sup>9,14</sup> Herein, hydrophobic alkanethiol and perfluoroalkane-thiol SAMs are employed to demonstrate SERS as an analytical signal transduction mechanism for environmental pollutants, specifically polychlorinated biphenyls (PCBs) and polycyclic aromatic hydrocarbons (PAHs), that occur in complex mixtures and environments. In this work the alkanethiol partition layer chain length was varied to find the optimal partition layer, and, of those used, decanethiol yielded the lowest limits of detection. The limit of detection is significantly influenced by both the quality and the thickness of the monolayer because the analyte molecule must be able to enter the partition layer and, once embedded, must be held within the exponentially decaying localized electromagnetic fields.

#### **4.1.1 Polychlorinated Biphenyls**

PCBs are listed by the Environmental Protection Agency (EPA) as persistent organic pollutants, compounds that resist chemical, biological and photolytic degradation.<sup>15</sup> PCBs were first manufactured in 1929<sup>16</sup> and production increased until the mid 1970's as PCBs were used as industrial oil additives, coolants, and in some consumer products.<sup>16</sup> Production and use were stopped in the 1970's because PCBs were found to be toxic to humans but PCBs can still be found today in high concentrations in waste disposal sites, natural waters, and in the aquatic life of those waters.<sup>17,18</sup>

PCB contamination exists as mixtures of up to 209 congeners that have 1-10 chlorines, and the maximum EPA-allowed PCB contaminant level has been set at

0.00050 mg/L.<sup>15</sup> Bulk detection of PCB mixtures has been available since the mid 1980's, when high resolution capillary gas chromatographic columns with an electron capture detector<sup>19,20</sup> were first employed to detect Arochlor mixtures and individual PCB standards became available. Immunoassays<sup>21</sup> and ion detection<sup>15</sup> techniques have also been used for bulk detection since the 1990's though identification and quantitation of individual congeners is also necessary to assess varied toxicity and optimal remediation strategies. Individual congener detection can be accomplished using high-resolution mass spectrometry<sup>20</sup> but the high cost and time intensive nature of the measurements inhibit widespread use. Ideally, a viable sensor would be sensitive to pM concentrations of PCBs with fast time response, facilitate identification of individual congeners even in the presence of confounding species, and be reusable in a field portable measurement system. Herein, significant progress toward this goal is reported using partition layer-assisted SERS.

#### **4.1.2 Polycyclic Aromatic Hydrocarbons**

PAHs are produced during the incomplete combustion of fuels and can also be found in tar and coal deposits. Based on the extensive use of fossil fuels and coal, many industrial areas suffer from soil contaminated with PAHs. While hundreds of PAHs are present as environmental contaminants, the EPA has identified 16 priority pollutant PAHs that are monitored frequently for regulatory purposes. In the Great Lakes region, for example, 42 "areas of concern" were identified by an international committee as having PAH-contaminated sediment, and this contaminated sediment complicates environmental remediation.<sup>22</sup> The large  $K_{OW}$  values and low Henry's constants for PAHs cause the pollutants to accumulate in sediment.<sup>23</sup> Even though PAH release has decreased with improved pollution control measures, polluted sediment remains and the PAHs can be mobilized when sediment is disrupted. Contamination of drinking

water most often occurs when natural bodies of water are contaminated or when PAHs leach out of coal tar and asphalt linings of water storage tanks.<sup>24</sup> The concentration of different PAH species in drinking water is unknown but the EPA predicts up to 0.01 mg/L of PAHs at optimum leaching conditions. Based on the similarity of PAH structures and the low limits of detection required, detection and discrimination of PAHs presents a formidable analytical challenge. Traditional detection methods for PAHs include solid-phase microextraction combined with gas chromatography-mass spectrometry<sup>25-27</sup>, capillary electrophoreses with laser-induced fluorescence detection, high-pressure liquid chromatography with fluorescence detection<sup>28,29</sup> and immunoassays.<sup>30,31</sup> Each of these methods either requires a time-intensive separation step or the use of PAH-specific binding moieties; the goal of this work is to eliminate the need for either of these requirements. The likely success of this platform for SERS sensing of PAHs is evaluated using two model compounds, anthracene, a small PAH, and pyrene, a larger PAH. To be effective, the SERS sensor must facilitate distinction of PAHs with similar structure, have a limit of detection in the range relevant for environmental samples, resist fouling by interfering species, and be reusable for multiple sampling events. The work presented herein demonstrates significant progress on each of these fronts and the overall potential of partition-layer modified AgFON SERS substrates for general analytical use. In addition, band analysis of the information-rich SERS spectra facilitate mechanistic interpretation of the relative success of each molecule at partitioning into the self-assembled monolayer and comparison to other pollutant species.

## **4.2 Experimental Methods**

### **4.2.1 Materials**

All of the chemicals were reagent grade or better and used as purchased. 1-Octanethiol, decanethiol, hexadecanethiol, octadecanethiol, perfluorodecanethiol, benzenethiol, pyrene, hydrogen peroxide, ammonium hydroxide, ethanol, methanol, tetrahydrofuran, and 1-octanol were purchased from Sigma-Aldrich (Milwaukee, WI). Punched copper disks from McMaster-Carr (Chicago, IL) were used as substrates. 500-nm ( $\pm 20$  nm)-diameter silica nanospheres were purchased as a 10% solids solution from Duke Scientific (Palo Alto, CA). All aqueous solutions were prepared with ultrapure ( $18.2 \text{ M}\Omega \text{ cm}^{-1}$ ) water from a Millipore water purification system (Long Beach, CA). Silver wire for electron beam deposition was purchased from Kamis Inc. (Mahopac Falls, NY). The polychlorinated biphenyl compounds, PCB-47 (2,2',4,4'-tetrachlorobiphenyl) and PCB-77 (3,3',4,4'-tetrachlorobiphenyl), and anthracene were purchased from Accustandard, Inc. (New Haven, CT). Suwannee River fulvic acid was obtained from the International Humic Substances Society (St. Paul, MN).

#### 4.2.2 SERS Substrate Fabrication and Characterization

Ag Film over nanosphere (AgFON) substrates were fabricated on copper disks (Figure 4.1) that had been polished and cleaned by methods mentioned in previous chapters. Silica nanospheres were used in place of the traditional polystyrene latex nanospheres in order to promote adhesion and avoid polystyrene



**Figure 4.1** A diagram demonstrating the fabrication process of the partition-layer modified AgFON. First, silica spheres are packed on clean copper disks, then 200 nm of Ag is deposited onto the nanosphere mask, and then the monolayer is formed during exposure of the substrate to an ethanolic alkanethiol solution.

signal interference during the Raman experiments. Ag was vapor deposited to a thickness of 200 nm onto the nanosphere mask using electron beam vapor deposition

(Airco Temescal, Berkeley, CA) at a pressure of  $7 \times 10^{-6}$  Torr. The rate of deposition, 2 Å/second, and thickness were measured using a quartz crystal microbalance. Once the AgFON surface was fabricated, the disks containing the nanosphere-based roughness features were placed in 2 mL of 1 mM ethanolic decanethiol for 16 hours at ambient conditions to facilitate monolayer formation.

The enhancement factor (EF) for the AgFON substrates was characterized using the intense ring breathing stretch at  $1000 \text{ cm}^{-1}$  shift from both liquid and surface-adsorbed benzenethiol (BZT). When calculating the SERS enhancement factor, it is necessary to assume that the Raman scattering cross-section for free BZT and substrate-bound BZT are not significantly different. Intrasubstrate EF variation was assessed by measuring SERS spectra from five randomly chosen spots. With this method, the AgFON EF measured was  $2.5 \times 10^6$  with a 16% standard deviation; these values are in good agreement with previously published reports.<sup>14</sup>

It is critical for a SERS PCB sensor to be stable when exposed to aqueous samples for long periods of time or multiple times. To quantitatively assess the robustness of the AgFON substrate, a bare AgFON was first exposed to 1 mM BZT, and initial SERS spectra were measured from five randomly chosen locations across the substrate. The sample was then stored in water for an additional 5 days, collecting LSPR and SER spectra every 24 hours. The LSPR spectra were stable and good S/N SER spectra were still measurable at the end of the experiment (data not shown). Overall, the EF varies by significantly less than an order of magnitude between equivalent substrates, different sample areas on the same substrate, and after 5 day exposure to aqueous conditions, and thus, will be useful for analytical SERS applications.<sup>9</sup>

For PCB sensor experiments, self-assembled partition layer formation was performed in ambient conditions. Afterwards the AgFON was removed from solution,

rinsed with ethanol, and allowed to dry. Unless otherwise noted, the dry AgFONs were incubated in 1 mL of PCB solutions for four hours. High concentration PCB-47 experiments were performed with the PCB dissolved in THF because the PCB is not soluble in water at these high concentrations, 5 mM to 100  $\mu\text{M}$  ( $C^{\text{sat}} 3.09 \times 10^{-7} \text{ mol L}^{-1}$ ).<sup>34</sup> The lower concentration experiments, using 1  $\mu\text{M}$  to 500 nM PCB-47, were performed in an aqueous solution. After PCB exposure, the substrate was mounted in the Raman liquid cell and water was injected to fill the cell before SERS measurements.

For PAH experiments, PAHs were partitioned into the monolayer by placing the AgFONs in 1 mL of PAH solution for 1 min. This incubation time was chosen based on previous studies that demonstrated no increased partitioning efficiency for PCBs with longer exposures.<sup>35</sup> Anthracene is not soluble in water for concentrations greater than 100 nM, so methanol was used as the solvent for solutions of 500 nM and greater, while water was used as solvent for concentrations 100 nM and smaller.<sup>23</sup> Pyrene is not soluble in water for concentrations greater than 500 nM, so methanol was used as solvent for solutions of 1  $\mu\text{M}$  and greater, while water was used as solvent for concentrations 500 nM and smaller.<sup>23</sup> As a control, each PAH (1 mM solution) was exposed to the AgFON surface without the decanethiol monolayer to verify that the self-assembled partition layer was required for detection; in both cases, neither PAH species was detected on a bare AgFON.

#### **4.2.3 Optical Characterization**

LSPR measurements for the AgFON substrates were recorded using a DH-2000 Deuterium Tungsten Halogen light source and a USB2000 spectrometer with a 200- $\mu\text{m}$ -core diameter reflectance probe (Ocean Optics, Dunedin, FL) from dry substrates. A 200-nm-thick thermal vapor deposition Ag film was deposited onto a copper substrate for use as a blank in the reflectance probe measurements.

#### 4.2.4 SERS Instrumentation

After fabrication, the DT-modified AgFON substrates were mounted into a liquid cell, exposed to the PAH solution, and then rinsed with and maintained in water for spectroscopic evaluation. In all data presented herein, SERS was excited with a Millennia Vs 532 nm excitation laser (Spectra-Physics, Mountain View, CA) with added neutral density filters to achieve the desired incident powers. In all cases, the laser power was chosen to avoid local heating on the sample, even with long exposure times, that would result in monolayer or PAH degradation and the appearance of amorphous carbon Raman bands. The laser beam first passed through an interference filter (Melles-Griot, Rochester, NY) and was then guided to the sample using an Al-coated prism to achieve a spot size of 1.26 mm<sup>2</sup>. Scattered light was collected using a 50-mm-diameter achromatic lens (Nikon, Melville, NY), and the Rayleigh scattered light was removed using a notch filter (Semrock, Rochester, NY). Detection was accomplished using a 0.5 m SpectraPro 2500i single monochromator and a Spec 400B liquid nitrogen-cooled CCD chip (both from Princeton Instruments/Acton, Trenton, NJ). In all cases, SERS spectra were measured from a minimum of five randomly chosen sample areas on a given substrate.

#### 4.2.5 Statistical Analysis

In the PCB partitioning experiments, the SERS intensity was assessed using the 1000 cm<sup>-1</sup> shift peak from the aromatic breathing mode of the PCB. The peak intensity at 1000 cm<sup>-1</sup> shift was subtracted from the background intensity at 980 cm<sup>-1</sup> shift, and this intensity difference was then used for all signal evaluations. In the PAH partitioning experiments, the SERS limit of detection was assessed using the 597 cm<sup>-1</sup> shift for pyrene and the 1410 cm<sup>-1</sup> shift for anthracene. The peak intensity was measured by subtracting the background intensity from the intensity at the respective peak. Linear

regression analysis was performed in Excel using the data analysis package with values of  $p < 0.05$  used to determine statistical significance. T-tests were also performed in Excel assuming equal variance, and a two-tailed value of  $p < 0.05$  was used to determine statistical significance.

### 4.3 Results and Discussion

#### 4.3.1 Effect of Partition Layer SAM

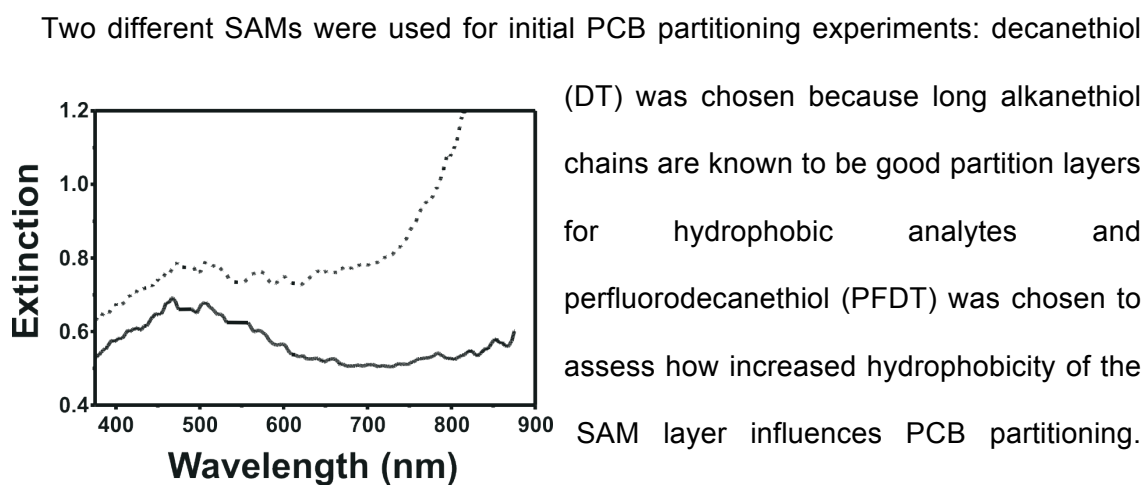


**Figure 4.2** Localized surface plasmon resonance spectra for decanethiol (solid line) and perfluorodecanethiol (dashed line) on AgFON substrates.

(DT) was chosen because long alkanethiol chains are known to be good partition layers for hydrophobic analytes and perfluorodecanethiol (PFDT) was chosen to assess how increased hydrophobicity of the SAM layer influences PCB partitioning.

While PFDT and DT do not have the same packing density due to the larger van der Waals diameter of the perfluorocarbon chain or monolayer thickness due to tilt angle differences,<sup>36</sup> the partitioning capability was still assessed by qualitative comparison. In both cases, fresh AgFON substrates were incubated in 1 mM thiol solutions before a 4 hour PCB-47 exposure, and the resulting LSPR spectra from the partition layer-covered substrates are shown in Figure 4.2. In both cases the LSPR  $\lambda_{\max}$  occurs at  $\sim 495$  nm with a full-width at half-maximum of  $\sim 150$  nm, indicating that this substrate will provide good electromagnetic enhancement when using blue or green laser excitation wavelengths;<sup>37</sup> accordingly, an excitation wavelength ( $\lambda_{\text{ex}}$ ) of 532 nm was used for the remainder of this work. SERS

spectra captured from both DT- and PFDT-dosed AgFONs are shown in Figures 4.3A and 4.3B, respectively. Ideally, a partition layer would not exhibit Raman bands in the spectral regions where the PCB molecular signatures will appear, namely in the C-Cl deformation region (220-320  $\text{cm}^{-1}$  shift), the C-Cl stretch region (510 - 760  $\text{cm}^{-1}$  shift), or the biphenyl C-C bridge stretch (1280 - 1320  $\text{cm}^{-1}$  shift);<sup>38</sup> clearly, both the DT and PFDT layer have spectral features in these regions but the PFDT layer is preferable, with only low intensity bands below 1200  $\text{cm}^{-1}$  shift. While the DT spectrum shows a broad, intense C-S stretch band at

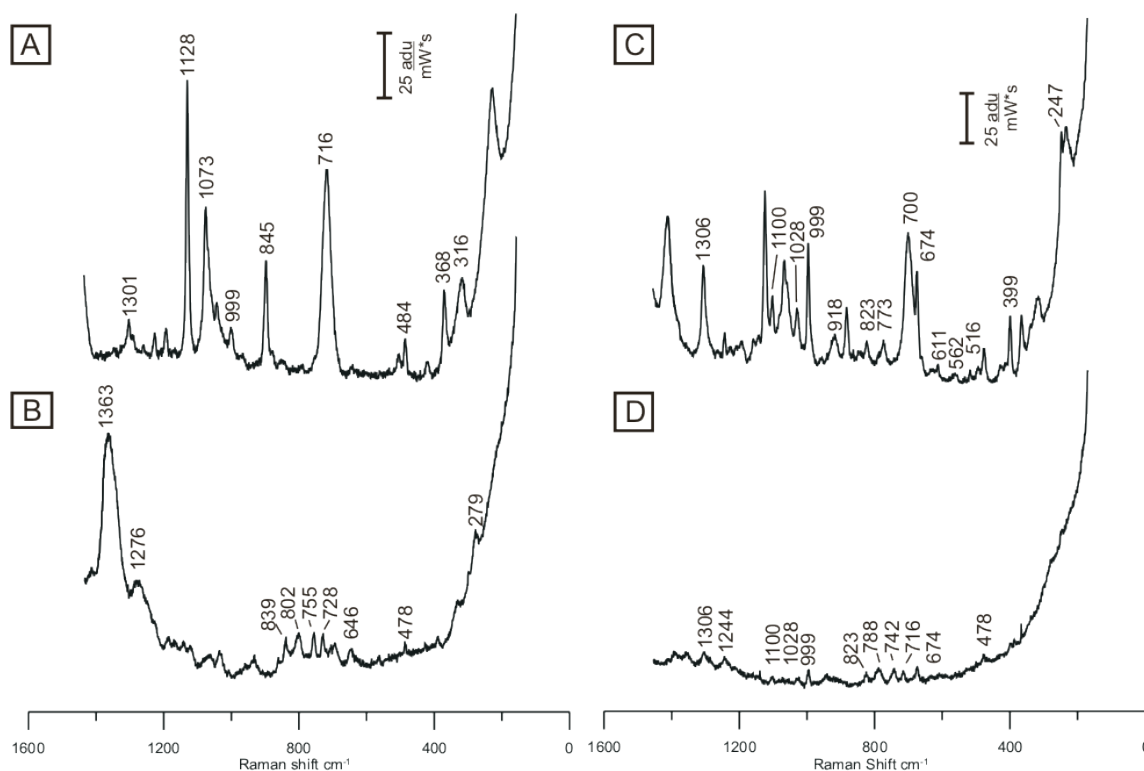


**Figure 4.3** SERS spectra of (A) decanethiol and (B) perfluorodecanethiol self-assembled onto AgFON substrates from 1 mM ethanolic solutions for 16 h. After 4 h incubation in 5 mM PCB-47, SERS spectra were again captured from the (C) decanethiol-modified AgFON and (D) the perfluorodecanethiol-modified AgFON. In both cases, 3.09 mW of 532 nm excitation laser light was used to record 30-s spectra, and calibration was done using a neon lamp.

716  $\text{cm}^{-1}$  shift, clearly indicating the presence of a somewhat ordered DT monolayer, the PFDT spectrum shows multiple, low intensity bands in the C-S stretch region,

indicating either a highly disordered PFDT monolayer or sub-monolayer coverage. The most prominent spectral feature in the PFDT SERS spectrum is the C-F stretch at 1363  $\text{cm}^{-1}$  shift.

As was expected, the PFDT SAM created a barrier against the solvent during dosing with 5 mM PCB-47, decreasing the likelihood of effective partitioning. Figures 4.3C and 4.3D show the SERS spectra captured from the DT- and PFDT-coated AgFONs after 4 hour PCB-47 exposure. New bands are clearly visible in the DT spectrum (Figure 4.3C) indicating the presence of PCB-47 within the zone of electromagnetic enhancement, including the C-Cl deformation band at 247  $\text{cm}^{-1}$  shift, a C-Cl stretch band at 674  $\text{cm}^{-1}$  shift (as well as other possible C-Cl stretch bands at 516, 562, and 611  $\text{cm}^{-1}$  shift), aromatic bands at 999, 1028, and 1100  $\text{cm}^{-1}$  shift, and the biphenyl C-C bridge stretch at 1306  $\text{cm}^{-1}$  shift. Additionally, the DT C-S stretch band has shifted from 716 to 700  $\text{cm}^{-1}$  shift, indicating rearrangement of the DT monolayer during PCB-47 exposure. These new PCB-47 bands are not as apparent in the spectrum captured using the PFDT partition layer (Figure 4.3D) but are, in fact, present. The small signal indicates either poor wetting, poor partitioning, or inappropriate orientation of partitioned PCB-47 relative to the enhancing EM fields. Based on this result, the PFDT partition layer was not pursued any further in this work but will be revisited in future work if higher enhancement factor substrates can be fabricated.

#### **4.3.2 Identification of PAH Bands for Analysis**

The aforementioned work demonstrated successful partitioning of polychlorinated biphenyl compounds into a decanethiol monolayer, so this same sensor design modified with a decanethiol monolayer will be applied to another important class of environmental pollutants, PAHs. PAHs cannot be detected without the presence of a DT monolayer on the AgFON (data not shown). Upon assembly of the DT layer,

Raman bands are measured at 1443  $\text{cm}^{-1}$  shift ( $\text{CH}_2$  or  $\text{CH}_3$  deformation), 1301  $\text{cm}^{-1}$  shift ( $\text{CH}_2$  wag), 1130  $\text{cm}^{-1}$  shift (trans C-C stretch), 1074  $\text{cm}^{-1}$  shift (gauche C-C

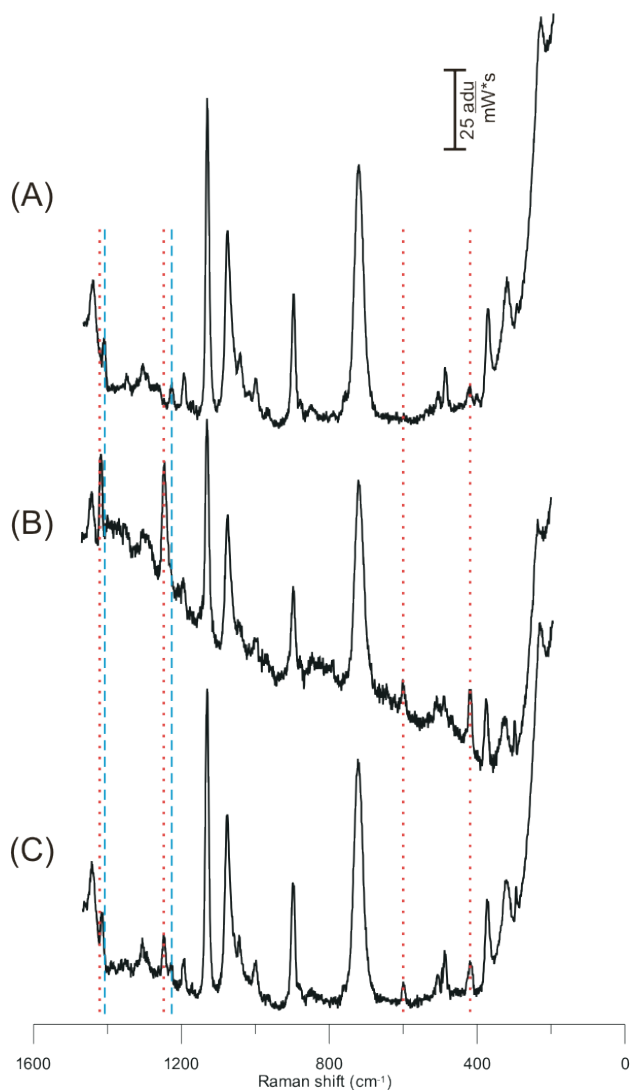


**Figure 4.4** SERS spectra of (A) 1 mM anthracene, (B) 1 mM pyrene, and (C) a mixture of 1 mM anthracene and 1 mM pyrene partitioned into DT-coated AgFON substrates after 1 min exposure. In all cases, 2.84 mW of 532 nm excitation laser light was used to record 30-s spectra, and calibration was done using a neon lamp. Anthracene peaks are indicated by *dashed lines* and pyrene peaks are indicated by *dotted lines*. All other Raman bands originate from DT.

distinctive bands which allow for identification of the molecule. The band at 418  $\text{cm}^{-1}$  shift is due to out-of-plane anthracene deformation. The characteristic anthracene

stretch), 999  $\text{cm}^{-1}$  shift ( $\text{CH}_3$  rock), 899  $\text{cm}^{-1}$  shift ( $\text{CH}_3$  rock), 715  $\text{cm}^{-1}$  shift (trans C-S stretch), and 638  $\text{cm}^{-1}$  shift (gauche C-S stretch).<sup>39</sup> To assess the capability of DT-coated AgFON substrates for PAH detection, the substrates were exposed to anthracene and pyrene as models with significantly different hydrophobicities, and  $K_{\text{OW}}$  values of 5.34 and 4.79, respectively.<sup>40,41</sup> Initial exposures to 1 mM analyte in methanol reveal that both species can be detected after 1 minute exposure and that they can be distinguished from one another. Figure 4.4A and B

shows spectra of a DT-coated AgFON after exposure to 1 mM anthracene and 1 mM pyrene, respectively. The Raman spectrum for anthracene on the DT-coated AgFON has five

bands are at 759 and 956  $\text{cm}^{-1}$  shift, stretches caused by para-disubstituted benzenes. The 1227  $\text{cm}^{-1}$  shift is attributed to *o-p*-disubstituted benzene vibrations. The 1408  $\text{cm}^{-1}$  stretch is caused by cumulative vibrations of the entire anthracene molecule.<sup>42</sup> The Raman spectrum for partitioned pyrene is easily distinguished from that of anthracene. The Raman spectrum for pyrene on the DT-coated AgFON has four distinctive bands which allow for identification of the molecule. The 416  $\text{cm}^{-1}$  shift band shows the out of plane deformation of pyrene while the band that occurs at 597  $\text{cm}^{-1}$  shift band is caused by vibration of 1,2,3 tri-substituted benzenes. Distinct bands are also visible at 1246  $\text{cm}^{-1}$  shift and 1415  $\text{cm}^{-1}$  shift. These peaks are caused by ring stretches in anthracenes and naphthalenes.<sup>43,44</sup> Exposure of a DT-coated AgFON to either pyrene or anthracene alters the order of the DT monolayer. Spectra of DT before PAH exposure have an intense C-S stretch at 715  $\text{cm}^{-1}$  shift. After anthracene exposure, the band shifts to 710  $\text{cm}^{-1}$  shift, and after pyrene exposure, the C-S stretch shifts to 721  $\text{cm}^{-1}$  shift. These shifts, easily distinguished with the 2  $\text{cm}^{-1}$  shift resolution of this instrument, indicate that the PAH molecules partition into the layer rather than adsorbing at the interface. The roughly equal magnitude shift in the C-S stretch band upon anthracene or pyrene exposure indicates that both PAHs partition similarly into the DT monolayer, as would be expected based on their planar geometry.

#### **4.3.3 Sensitivity of the Decanethiol-coated AgFON to Environmental Pollutants**

One of the difficulties in fabricating a chemosensor for PCBs and PAHs is that, in the environment, these species exist at very low (i.e. pM) concentrations. To assess the limit of detection that will be accessible with the DT-coated AgFON SERS substrate, the SERS band intensity was measured after exposure to various PCB-47, anthracene, or pyrene concentrations. To date, 500 nM PCB-47 is the lowest concentration attempted, and it was easily detected, making it possible to extrapolate to an expected limit of

detection. An example spectrum of the DT-coated AgFON, the same AgFON after exposure to 5 mM PCB-47, and the resulting difference spectrum of PCB-47 are presented in Figures 4.5A-C, respectively. Figure 4.5D shows the 1000  $\text{cm}^{-1}$  shift aromatic band intensity measured as a function of PCB-47 exposure concentration; each spectrum was measured from a separate substrate after four hours incubation in the PCB-47 solution even though this long incubation time was not required (*vide infra*). The data points on this plot represent the average  $\pm$  the standard error of the mean after measurements

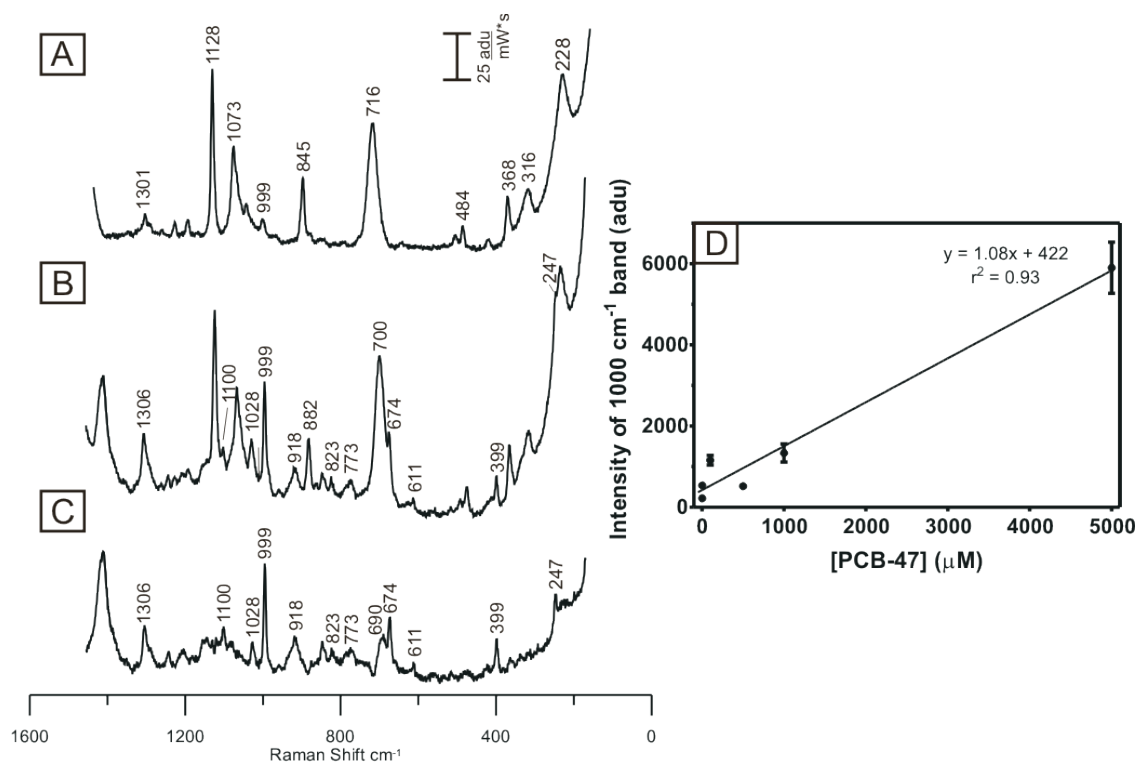


**Figure 4.5** SERS spectra of a decanethiol-modified AgFON (A) before PCB-47 exposure, (B) after 5 mM PCB-47 exposure for 4 h, and (C) the difference spectrum of (A) subtracted from (B). Systematic exposure of decaenthiol-modified AgFONs to various PCB-47 concentrations (from 500 nM to 5 mM) yields (D), a plot indicating a linear dependence of the aromatic stretch band intensity of PCB-47 exposure concentration. The data points on this plot represent the average  $\pm$  the standard error of the mean after measurements from three separate AgFON substrates. In all cases, 3.09 mW of 532 excitation laser light was used to record 30-s spectra, and calibration was done using a neon lamp.

from 3 separate AgFON substrates. A linear regression was performed on the data and

demonstrated an  $r^2$  value of 0.93, indicating that the partitioning efficiency is linear within this concentration regime. With the assumption that this linear trend continues as the PCB-47 concentration is further decreased, and considering the S/N characteristics of the Raman instrument being used, we predict a PCB-47 limit of detection of 50 pM. In fact, this projected detection limit can be significantly reduced in future work by exploiting SERS substrates with higher average enhancement factors.<sup>45-48</sup> Further, the majority of the data points on this intensity versus concentration plot were generated with PCB-47 dissolved in THF, and there is significantly less driving force for a PCB to partition from THF into the DT layer than from an aqueous solution into the DT layer. Accordingly, as the limit of detection is further explored with aqueous PCB-47 samples, we fully expect more efficient partitioning to occur. Carron and coworkers performed a similar study with polycyclic aromatic hydrocarbons and were able to achieve an LOD of 2.3 ppm;<sup>12</sup> they predicted a lower LOD for PCBs based on their higher  $K_{ow}$  value. Based on the EPA's maximum contamination level for all PCBs of 0.00050 mg/L or 1.7 nM for PCB-47, this DT-coated AgFON will likely have the sensitivity to detect PCBs at environmentally relevant concentrations after further optimization.

The 4 hour PCB incubation used in all aforementioned measurements was arbitrarily chosen. Accordingly, a systematic study was conducted to examine the time required for PCB-47 to concentrate within the zone of EM enhancement. A series of DT-modified AgFON substrates were exposed to a 1 mM PCB solution for 10 s, 1 min, 20 min, 60 min and 4 hours. Based on the  $1000\text{ cm}^{-1}$  shift band intensity, the PCB adsorption/partitioning was complete within 1 min, as no significant signal change was observed with longer exposure times (data not shown). These results are encouraging since short exposure times would be preferred for field work, and all future work will exploit one minute incubation periods.

To measure the limit of detection of the DT-coated AgFON surface for each of the

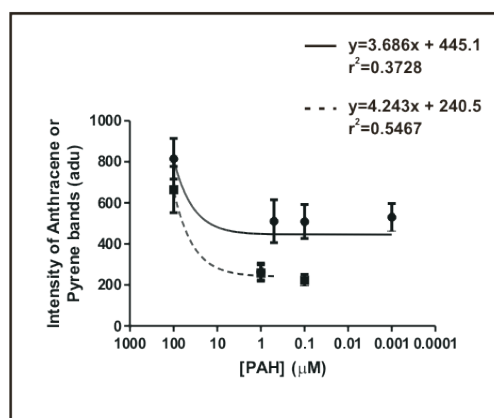


**Figure 4.6** A plot demonstrating the dependence of aromatic stretch intensities for anthracene and pyrene on PAH concentration after 1 min exposure. The data points on this plot represent the average  $\pm$  the standard error of the mean for spectra recorded from five randomly chosen areas on the substrate. Anthracene is represented by the *solid line*, and pyrene is represented by the *dashed line*. PAH concentrations above 100  $\mu\text{M}$  are not included on this plot.

two model PAH compounds, the SERS band intensity was measured after exposure to various concentrations of both anthracene and pyrene. To date, the lowest concentration of anthracene measured is 1 nM, and the lowest concentration of pyrene measured is 100 nM. By analyzing the intensity of distinguishing bands detected in

each spectrum, and extrapolating to a signal-to-noise ratio of 3, it is possible to predict the limit of detection for each species. For limit of detection calculation, concentrations of the PAHs above 100  $\mu\text{M}$  were excluded during linear fit and

extrapolation due to apparent differences in partitioning behavior at high concentrations.

Figure 4.6 shows the 1408 and 597  $\text{cm}^{-1}$  shift band intensities as a function of anthracene and pyrene exposure concentration, respectively; each spectrum was measured from a different substrate after a 1 min incubation time in the PAH solution.

The data points represent the average  $\pm$  the standard error of the mean after measurements from five randomly chosen areas on one substrate. Based on this analysis, the limits of detection (using the laser power and collection times chosen for this study) for anthracene is 300 pM and for pyrene is 700 pM. While the EPA has not published allowed contamination levels for anthracene or pyrene, it has established maximum contamination levels for related compounds; for example, the known

carcinogen benzo(a)pyrene has a maximum allowed contamination level of 0.2 ppb, or approximately 790 pM, which is well within the limits of detection estimated herein. The limit of detection for anthracene and pyrene, at 0.05 and 0.14 ng/mL respectively, are comparable to other analytical techniques like immunoassays and GC/MS analysis which have LODs of 0.1-2 ng/mL and require much more sample clean-up time.

#### 4.3.4 Distinguishing between PCB and PAH Compounds using SERS

Having demonstrated that the partition layer SERS substrate is likely to reach the necessary detection limits for analytical sensor applications, the next milestone was to

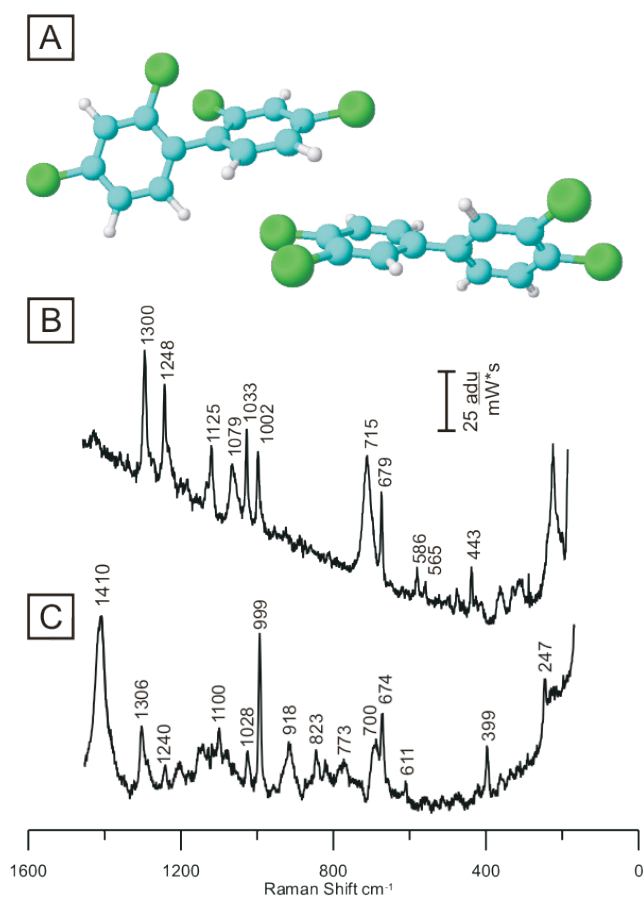


**Figure 4.7** (A) Structures of PCB-47 and PCB-77 drawn and optimized in ACD/ChemSketch, version 8.17. Difference SERS spectra after 4 h exposure of a DT-coated AgFON to (B) PCB-77 and (C) PCB-47. In both cases, 3.09 mW of 532 nm excitation laser light was used to record 30-s spectra, and calibration was done using a neon lamp.

compare the SERS signatures from similar PCB compounds and similar PAH compounds and verify that similar individual PCBs and PAHs could be distinguished from another. While the aromatic bands and biphenyl bridge stretch band locations are likely to be very similar from PCB to PCB, differences in the C-Cl band locations may be sufficient for identification. In this work, the spectral features for partitioned PCB-47 were compared to those from PCB-77, a compound with the same number of chlorine substituents but significantly more planar character (Figure 4.7A). After

a 4 hour exposure of a DT-modified AgFON to 5 mM solutions of the individual PCBs, SERS spectra were recorded and difference spectra were compared (Figures 4.7B and 4.7C) to demonstrate that these two compounds are, in fact, readily distinguished from one another. The C-Cl stretch deformation is not apparent upon partitioning of the PCB-77; however the main C-Cl stretch band occurs at  $679\text{ cm}^{-1}$  shift, a  $5\text{ cm}^{-1}$  shift difference that is easily distinguished from the PCB-47 band with the  $< 2\text{ cm}^{-1}$  shift resolution of this instrument. Immediate future work will focus on further optimizing the partition layer by increasing monolayer homogeneity. Ideally, the width of the C-S stretch band would be reduced so that the proximate C-Cl stretch band is more easily detected. A more ordered DT monolayer can be achieved using longer AgFON immersions in the SAM solution (i.e. 72 hrs) or, as Lennox and coworkers and we have shown in chapter 3, by applying a potential to the substrate for 10-15 min.<sup>49</sup> When comparing the PCB-47 and PCB-77 spectra, there are also shifts in the aromatic, para and ortho-para disubstituted ring vibration and biphenyl bridge band locations that may be useful when identifying PCBs in mixtures. Interestingly, unlike in the case of PCB-47 partitioning, there is no shift in the decanethiol C-S stretch band upon exposure to PCB-77, indicating that the PCB-77 may adsorb at the top of the DT partition layer rather than partitioning into the layer. Future work will focus on the relative partitioning efficiency and partitioning mechanisms of various PCB compounds, including experiments where PCB mixtures are presented to the DT-modified AgFON to examine preferential interactions.

A DT-coated AgFON substrate was exposed to a mixture of 1 mM anthracene and 1 mM pyrene in methanol for 1 min, and the SERS spectrum was recorded (Figure 4.4C). When this spectrum is compared to the individual spectra for pyrene and anthracene, it is clear that the two compounds are both present in the new spectrum, and that they

can be distinguished from one another. Bands at 416, 597, and 1246  $\text{cm}^{-1}$  shift indicate that pyrene is present in the mixture while bands at 966 and 1280  $\text{cm}^{-1}$  shift indicate the presence of anthracene. The anthracene stretch band present in both individual spectra at 1408 and 1415  $\text{cm}^{-1}$  shift overlaps in the mixture spectrum, making it difficult to use for species characterization without further band deconvolution analysis.<sup>50</sup> The mixture of pyrene and anthracene also influences the order of the DT monolayer, shifting the C-S stretch band to 706  $\text{cm}^{-1}$  shift, indicating cumulative partitioning of both species.

#### **4.3.5 Dissolved Organic Matter does not Inhibit SERS Detection of PCB-47 or PAHs**

PCB and PAH contaminated water or soil samples collected from test sites will contain many different environmental and man-made species that may interfere with SERS detection of these environmental pollutants. Oils, dissolved organic matter, or other corrosives may cause fouling or degradation of the substrate. In initial efforts to explore the influence of interfering species, substrates with PCB-47, anthracene or pyrene partitioned into the DT-coated AgFON were challenged with exposure to 0.5 mg/L Suwannee River fulvic acid for 2-5min. Fulvic acids are highly soluble, low molecular weight components found in dissolved organic matter.<sup>51</sup> Captured spectra reveal that none of the analytes were affected by the fulvic acid, as SERS bands did not significantly vary in intensity or spectral location even though there was an increase in background fluorescence (data not shown). In future studies, the DT-coated AgFONs will be exposed to humic acids in addition to fulvic acids before, during, and after PCB or PAH exposure. If necessary, the composition of the partition layer will be modified to minimize adsorption or partitioning of non-PCB or PAH species, and a sample clean-up step may be added before SERS substrate exposure.

#### 4.3.6 Reversibility of Pollutant Partitioning and Reusability of the SERS Sensor

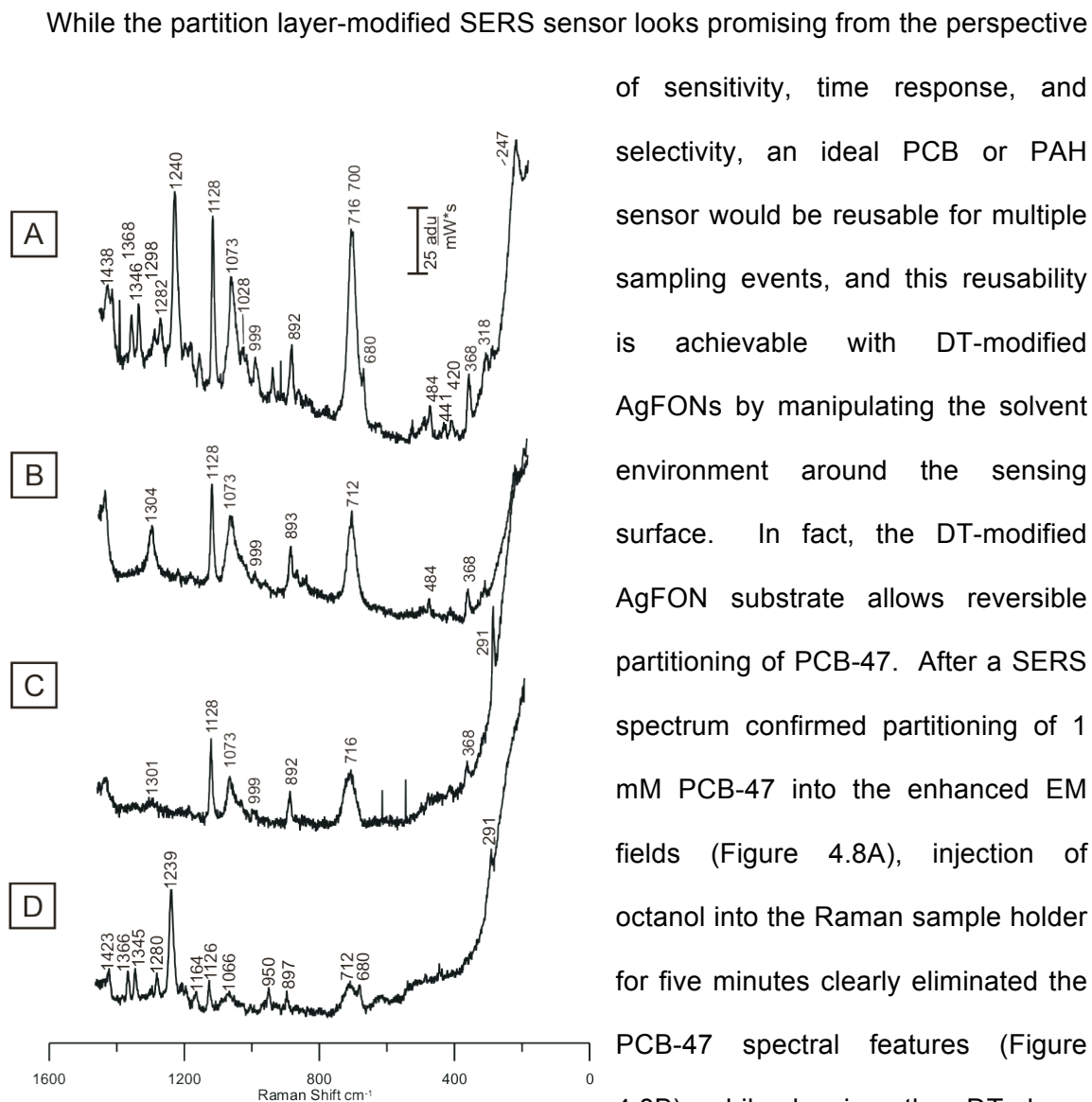


**Figure 4.8** SERS spectra demonstrating the reversibility and reusability of partition-layer SERS substrates. SERS spectra of (A) a DT-modified AgFON after a 4 h exposure to 1 mM PCB-47, (B) the same AgFON after a 5 min exposure to 1-octanol, (C) the same AgFON after an additional 16 h incubation in the 1 mM ethanolic DT partition layer solution, and (D) the same AgFON after 4 h re-exposure to a 1 mM PCB-47 solution. In all cases, 3.09 of 532 nm excitation laser light was used to record a 30-s spectra, and calibration was done using a neon lamp.

of sensitivity, time response, and selectivity, an ideal PCB or PAH sensor would be reusable for multiple sampling events, and this reusability is achievable with DT-modified AgFONs by manipulating the solvent environment around the sensing surface. In fact, the DT-modified AgFON substrate allows reversible partitioning of PCB-47. After a SERS spectrum confirmed partitioning of 1 mM PCB-47 into the enhanced EM fields (Figure 4.8A), injection of octanol into the Raman sample holder for five minutes clearly eliminated the PCB-47 spectral features (Figure 4.8B) while leaving the DT layer intact. No new octanol bands were apparent, and the C-S stretch band that shifted upon partitioning the PCB-47 had nearly returned to its original location. While it may have been unnecessary based on the promising

appearance of the post-octanol DT spectrum, this substrate was incubated in a 1 mM ethanolic DT solution for an additional 16 hours before repartitioning of PCB-47 was attempted. The spectrum captured after SAM reassembly (Figure 4.8C) is not

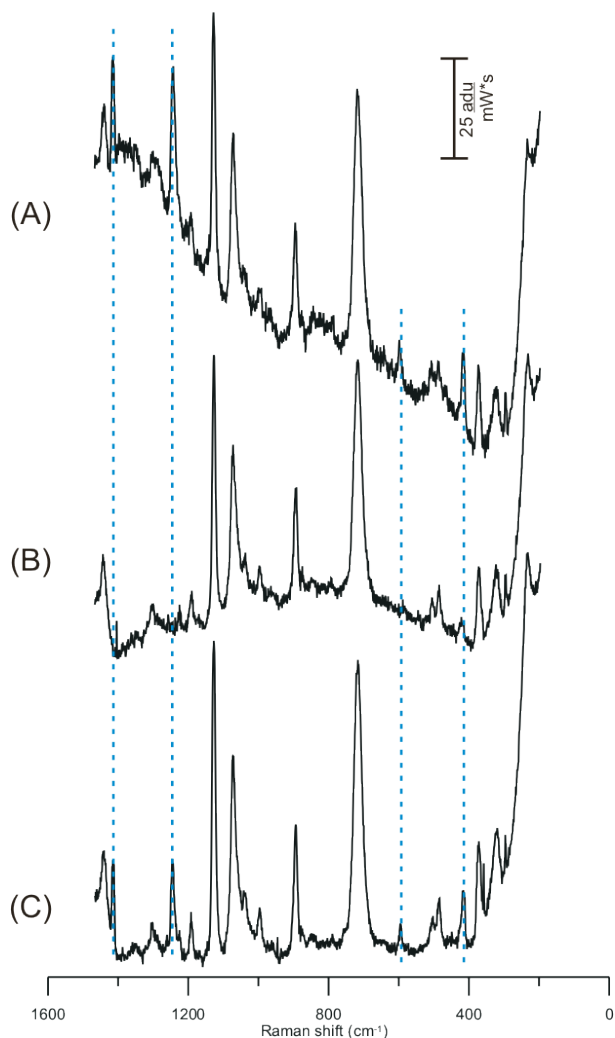


**Figure 4.9** SERS spectra demonstrating the reversibility and reusability of the DT-coated AgFON substrates. SERS spectra of one DT-coated AgFON substrate after (A) a 1-min exposure to 1 mM pyrene, (B) a sequential 5-min exposure to 1-octanol, and (C) another sequential 1-min exposure to 1 mM pyrene. Pyrene Raman bands are indicated by the dashed lines; all other bands originate from DT. In all cases, 2.84 mW of 532 nm excitation laser light was used to record 30-s spectra, and calibration was done using a neon lamp.

significantly different from the original DT spectrum or the spectrum shown in Figure 4.8B. After exposure to another four hour dose of 1 mM PCB-47, there is some evidence for repartitioning into the DT layer (e.g. the 674  $\text{cm}^{-1}$  shift C-Cl stretch in Figure 4.8D) but the signal intensity is not nearly as large as the original exposure. Perhaps the decreased signal intensity is due to octanol partitioning into the DT layer; because octanol spectral band locations overlap with the DT bands, it is not possible to verify this spectroscopically. In future work, more vigorous rinsing of the octanol-exposed SAMs will be applied in hopes of overcoming the van der Waals attractions among the alkyl chains while maintaining the covalent surface modification.

The same repartitioning experiment

was performed with a PAH solution and spectra were taken before octanol exposure and after reexposure to the PAH solution (Figure 4.9A) The PAH can be removed from

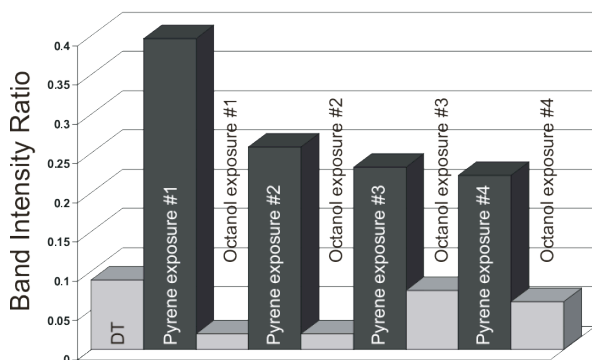


**Figure 4.10** The band ratio of the 1,415  $\text{cm}^{-1}$  shift pyrene band to the 721  $\text{cm}^{-1}$  shift DT band during four consecutive cycles of 1 min exposure to 1 mM pyrene followed by 5 min exposure to 1-octanol. In all cases, 2.84 mW of 532 nm excitation laser light was used to record 30-s spectra, and calibration was done with a neon lamp.

PAH solution (Figure 4.9C). Figure 4.10 shows the Raman band intensity ratio detected with four sequential exposures of pyrene and then octanol on the same substrate. While there is some variation in both the DT and PAH bands measured, the pyrene is still successfully repartitioned back into the DT layer and detected each time. The intensity of PAH signal after repartitioning does not significantly vary from the intensity of the original exposure to the PAH, but there is a variation in background noise with each subsequent repetition of the experiment. This is expected due to the nature of the monolayer, which rearranges as molecules are added to or removed from the monolayer. The background noise with the repeated octanol exposure does not influence the reusability of the PAH sensor. While only four sequential exposures are shown in figure 4.10, this is the largest number attempted and further octanol/PAH exposures are possible.

#### 4.3.7 Insight into the Partitioning Mechanism

the DT layer on the substrate by exposing the substrate to 6.4 M octanol for 5 min (Figure 4.9B), just like observations made with with for PCB-47, and this treatment removes the PAH to at least below the sensor limit of detection, as is shown for pyrene in Figure 4.9, leaving the DT layer intact.

After octanol treatment, the substrate can be reused for exposure to another

In Chapter Three, we found that decanethiol is an ideal monolayer because the layer is disordered and is thin enough that the analyte dwells within the zone of enhancement. If the PCB is partitioning into the DT SAM, the C-S stretch band should shift as the PCB influences the ordering of the pure monolayer. In Figure 4.11B, the C-S shift using the DT partition layer is shown as a function of PCB-47 concentration, demonstrating that more PCB-47 molecules (and more Raman signal intensity) correlates with a larger C-S band shift up to a maximum shift of  $16\text{ cm}^{-1}$ .

Examination of the position of the DT C-S stretch can be analyzed for the PAHs as well and indicates that both anthracene and pyrene partition into the DT layer, disturbing the order of the monolayer. However, it is possible to gain further insight into the PAH partitioning mechanism by monitoring changes in the ratios of certain characteristic partition layer Raman bands before and after PAH exposure.<sup>53</sup> A perfectly crystalline self-assembled monolayer would have no gauche character; accordingly, changes in the trans and gauche SERS band intensities reveal changes in the crystalline character of the monolayer. By comparing the trans C-S ( $\nu(\text{C-S}_T)$ ) and gauche C-S ( $\nu(\text{C-S}_G)$ ) bands, the overall quality of the DT monolayer at the interface with the substrate is indicated. Also, by monitoring the  $\nu(\text{C-C})_G/\nu(\text{C-C})_T$  ratio, information is gained about the ordering of the upper portion of the monolayer during partitioning. For this analysis, the band ratios of  $\nu(\text{C-S})_T/\nu(\text{C-S})_G$  at  $715/638\text{ cm}^{-1}$  shift and  $\nu(\text{C-C})_G/\nu(\text{C-C})_T$  at  $1074/1130\text{ cm}^{-1}$  shift were calculated for a DT-coated AgFON before and after exposure to either anthracene or pyrene (Table 4.1).

Statistical comparison of the C-S band ratio for unexposed DT and substrates exposed to the highest anthracene concentrations show no significant difference in the order of the monolayer at the molecule-substrate interface. However, the C-S ratio increases as the concentration of anthracene decreases, indicating that, at low

concentrations, the anthracene is not partitioning deeply into the monolayer but still facilitates enhanced crystallinity at the partition layer-AgFON interface. This, in concert with the C-S band shift data, indicates that anthracene likely partitions into the upper portion of the DT monolayer. Analysis of the gauche and trans contributions to the C-C stretch bands indicate that, for most cases, addition of anthracene leads to an increased population of the trans C-C stretch intensity. This is likely due to effective

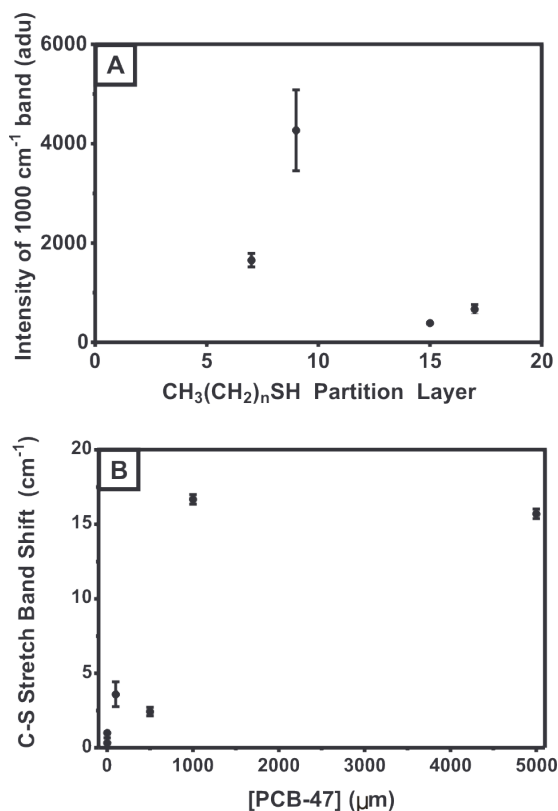


**Figure 4.11** In plot (A) the aromatic band intensity is monitored with varied alkanethiol partition layer chain length, and in plot (B) the C-S stretch band shift is monitored as a function of PCB-47 concentration. The data points on these plots represent the average  $\pm$  the standard error of the mean after measurements from 2 to 4 separate AgFON substrates. In both cases, 3.09 mW of 532 nm excitation laser light was used to record 30-s spectra, and calibration was done using a neon lamp.

hydrophobic interactions as the anthracene partitions into the upper portion of the DT monolayer. Exclusion of the highest anthracene concentrations (1 mM and 500  $\mu\text{M}$ ) from the LOD calculation is further supported by the apparent deviation in partition behavior based on this band analysis.

Upon partitioning into the monolayer, pyrene causes a much greater change in the DT monolayer than anthracene based on both the C-S stretch and C-C stretch

band ratios, which is expected based on molecular size. The C-S band ratio increases for all pyrene concentrations, indicating that the presences of pyrene leads to a monolayer-AgFON interface with more crystalline character. Similarly, the

decreased C-C stretch band ratio in the presences of all pyrene concentrations

indicates increased trans character in the carbon backbone of the DT partition layer.

#### 4.3.8 Comparison of the PAH and PCB Detection with DT-coated AgFON

The work presented herein demonstrates that the DT-coated AgFONs are appropriate for both PCB and PAH detection. Based on the possibility of co-contamination of environmental sites with both PCBs and PAHs, it is useful to compare the sensor characteristics for these two classes of organic pollutants. The signal

**Table 4.1** SERS band ratios for anthracene, pyrene and DT

Anthracene	Band		1 mM	500 $\mu$ M	100 $\mu$ M	1 $\mu$ M	500 nM	100 nM	1 nM	DT
	Location									
$\nu(\text{C-S})_{\text{T}}/\nu(\text{C-S})_{\text{G}}$	$I_{710}/I_{638}$		$4.95 \pm 0.55$	$4.6 \pm 0.59$	$5.52 \pm 1.47$	$7.51 \pm 0.86$	$7.42 \pm 0.47$	$7.19 \pm 0.64$	$7.73 \pm 2.52$	$4.40 \pm 0.82$
$\nu(\text{C-C})_{\text{G}}/\nu(\text{C-C})_{\text{T}}$	$I_{1130}/I_{1074}$		$0.554 \pm 0.019$	$0.584 \pm 0.045$	$0.727 \pm 0.062$	$0.768 \pm 0.032$	$0.670 \pm 0.034$	$0.581 \pm 0.034$	$0.574 \pm 0.041$	$0.766 \pm 0.016$
$\nu(\text{C-S})_{\text{T}}$			710	711	717	716	715	718	718	715
<b>Pyrene</b>										
$\nu(\text{C-S})_{\text{T}}/\nu(\text{C-S})_{\text{G}}$	$I_{720}/I_{638}$		$10.51 \pm 0.55$	$9.42 \pm 1.52$	$5.56 \pm 0.38$	$6.80 \pm 0.39$		$9.47 \pm 1.40$		$4.40 \pm 0.82$
$\nu(\text{C-C})_{\text{G}}/\nu(\text{C-C})_{\text{T}}$	$I_{1130}/I_{1074}$		$0.613 \pm 0.013$	$0.547 \pm 0.009$	$0.594 \pm 0.007$	$0.654 \pm 0.015$		$0.574 \pm 0.004$		$0.766 \pm 0.016$
$\nu(\text{C-S})_{\text{T}}$			721	721	719	713		718		715

intensity for anthracene at high concentrations is on average 2-5 times greater than the PCB-47 signal, when comparing the intensity of the PCB-47 1000  $\text{cm}^{-1}$  shift to the anthracene 1408  $\text{cm}^{-1}$  shift. However, at lower concentrations, no general trend can be discerned likely due to differences in the partitioning mechanism. However, there is a discernible trend at low mM concentrations when comparing the 597  $\text{cm}^{-1}$  shift pyrene band intensity to that of PCB-47, where PCB-47 intensity increases to 4-10 times the intensity of pyrene as target concentration decreases. This indicates that the DT-coated AgFON is a good sensor for PAHs, but based on signal intensities it can be inferred that PCBs partition more easily into the DT monolayer than PAHs. The  $\nu(\text{C-S})$  shifts can also be compared for the two different pollutant classes. As stated earlier, the anthracene and pyrene C-S stretch band moves 5 and 6  $\text{cm}^{-1}$  shift, respectively, after 1 mM exposure. The  $\nu(\text{C-S})$  shift after PCB-47 exposure at the same concentration showed a three-fold greater shift than that observed for the PAHs. This indicates that the non-planar PCBs are more disruptive and partition more easily into the inner monolayer and that PAHs behave more like PCB-77 (a planar PCB) which caused no

shift in the C-S band stretch. All of the band shift and intensity data is reflected in the predicted LODs for PAHs which are an order of magnitude higher than for PCBs (~50 pM). This enhanced partitioning of PCBs compared to PAHs is not surprising considering that the PCBs have much larger  $K_{OW}$  values than PAHs.<sup>23</sup> Both the PCB and PAHs can depart out of the DT monolayer with octanol exposure but removal of the PCBs causes a greater disturbance to the DT monolayer, making reuse more difficult. In both cases, a second exposure to pollutant solutions leads to a decreased SERS signal intensity. This indicates that the disorder of the monolayer after octanol washing or 1-octanol residue in the sample cell affects the repartitioning of either pollutant. Neither the PCBs nor the PAHs partitioned into a DT-coated AgFON were affected by exposing the substrate to Suwanee River fulvic acid.

#### **4.3.9 Detection of Polybrominated Diphenyl Ethers**

The DT-coated AgFON substrate is a promising substrate for partitioning PAHs, and it is also a good substrate for partitioning PCBs.<sup>35</sup> While performing the PAH studies presented herein, these substrates were also evaluated as potential sensing platforms for polybrominated diphenyl ethers (PBDEs), another important class of organic pollutants.<sup>54</sup> Unfortunately, the DT coating does not appear to be an appropriate partition layer for PBDEs. At 100  $\mu$ M concentration in isooctane, neither PBDE-47 nor PBDE-77 were able to partition into the DT layer of the substrate sufficiently to allow SERS detection. Because isooctane is not an ideal delivery solvent, the PBDEs were diluted only to 50  $\mu$ M in THF but still, neither PBDE-47 nor PBDE-77 were detected using these conditions. Modification of the AgFON substrate with a 1-hexadecanethiol monolayer instead of DT facilitated detection of 50  $\mu$ M PBDE-77 in isooctane; however, PBDE-47 was still not detected. Further research is necessary to determine the best monolayer to partition PBDEs for quantitative detection.

#### 4.4 Conclusions

Herein we have introduced a reusable SERS sensor that is able to detect and distinguish PCB congeners or similar PAHs on the minute timescale without interference from a common environmental contaminant. Specifically, this work demonstrates (1) that a DT-coated AgFON can be used to concentrate PCBs and PAHs at the surface of a AgFON for SERS detection with an expected pM limit of detection, (2) that different PCB congeners can be distinguished from one another on the basis of C-Cl and aromatic peak locations and structurally similar PAHs can be distinguished from one another based on structural stretches and deformations, (3) exposure to Suwanee River fulvic acid does not interfere with PCB or PAH detection, and (4) departitioning of the PCB or PAH can be achieved by rinsing the DT-modified AgFON with octanol so that the sensor can be reused. Further, systematic examination of the SERS spectra yields insight into the molecular interactions between the covalently bound partition layer and the hydrophobic analyte, demonstrating that some monolayer ordering is necessary to promote efficient PCB partitioning but that monolayers with highly crystalline character reduce partitioning efficiency and that larger PAH molecules create greater change in the DT monolayer. Comparison between the PCB data and PAH demonstrates that, while a lower limit of detection can be achieved for PCBs, the sensor is easier to reuse for PAHs. The development of a generalized environmental sensor that exploits the SERS signal transduction mechanism presents a new class of analytical assays for the detection of PCBs, PAHs, and, potentially, other environmental pollutants.

# Chapter Five

**Partition Layer-Modified Substrates for Surface-Enhanced Raman Scattering Detection in Biological Mixtures**

## 5.1 Introduction

In nature, cells employ a variety of molecular signals to communicate with one another, regulate cell cycle, and initiate their own death via apoptosis. For intracellular communication, signaling species are cations, such as  $\text{Ca}^{2+}$ , peptides, small molecules and lipids.<sup>1</sup> Lipids are an under-investigated signaling species, and have varying roles in the normal function of cells.<sup>2,3</sup> Mast cells are known for their production and use of lipid mediators for signaling purposes, are found in most tissues and play a primary role in allergic response.<sup>4,5</sup> While the release of electroactive species such as serotonin and histamine from mast cells has been studied extensively<sup>6,7</sup>, mast cells also use lipid mediators produced via enzymatic reactions of the cell membrane phospholipids to communicate intracellularly. Platelet activating factor (PAF) is a phospholipid that is both released by and an activator of mast cells.<sup>7,8</sup> When secreted by mast cells, PAF functions both as an autocrine and paracrine mediator, i.e. it stimulates mast cell mediator release and amplifies the release of mediators from surrounding mast cells. In inflammatory response, PAF causes platelet aggregation and activation of other immune cells. While the number of important lipid mediators in normal and disease state cell signaling is extensive, this chapter will focus on a sensing/discriminating four representative phospholipids and PAF.

Traditional analysis of lipids is done using colorimetric assays and separation techniques like gas chromatography, liquid chromatography and capillary electrophoresis. Colorimetric assays, while quick and widely used, can tell the relative amount of a phospholipid present in a sample but cannot discriminate between phospholipid headgroups.<sup>9</sup> In the case of GC analysis, many lipids are not thermally stable enough or have a volatility too low for GC analysis, and problems arise during derivitization when there is incomplete formation of derivatives and formation of

structural isomers.<sup>10,11</sup> Also, GC destroys the sample, preventing follow up analysis. The limited solubility of some lipids in aqueous buffers is a downside of CE analysis.<sup>12</sup> In recent years, mass spectrometry (MS) has been utilized for the profiling of all of the lipids present in a cell and for determination of the complex interactions between lipids and other molecules present in the cell.<sup>10,13,14</sup> The power of MS lies in its ability to detect many lipids in a sample, however, this comes at the cost of temporal resolution. MS suffers from the same issue of sample destruction that GC does, and additionally, MS instruments are prohibitively expensive for many research groups. Raman spectroscopy and surface-enhanced Raman scattering have been used to study cell membranes, lipid bilayers and membrane components due to the low Raman scattering cross-section of water. For example, Pemberton and coworkers characterized Raman stretches for dipalmitoylphosphatidic acid (DPPA) Langmuir layers on colloidal Ag films.<sup>15</sup> They found that the DPPA Langmuir layer was less crystalline than the solid DPPA and defined it as a liquid crystalline state. SERS has also been used to probe the formation of hybrid monolayers on alkanethiol alkanethiol-modified Ag substrates. Meuse et al. studied the formation of dimyristoylphosphatidylcholine (DMPC) or palmitoylphosphatidylcholine (DPPC) lipid layers on alkanethiol monolayers.<sup>16</sup> Since it is known that the electromagnetic enhancement factor decreases by a factor of  $\sim 1.3$  for every  $\sim 1$  nm distance from the metal substrate, they were able to compare the intensities of the known alkanethiol Raman stretches with the deuterated DMPC Raman stretches and found that the DMPC stretches were 5% of the intensity of the alkanethiol stretches. This confirmed the formation of hybrid bilayers and not integrated lipid-alkanethiol monolayers on the substrate surface. This group also looked at the relative intensities of the trans:gauche C-S stretches of the hexanethiol layer after the bilayer formed and saw that the addition of the lipid layer caused long range ordering of the

short monolayer. They also analyzed the formation of the hybrid layer on octadecanethiol, a longer chain thiol, and found that the lipid layer did not cause many changes due to the longer chain being more ordered initially, mitigating lipid penetration, and thus decreasing the SERS signal. In another example, Halas and coworkers used hybrid lipid bilayers on Au-coated silica nanoparticles to determine the intercalation of ibuprofen at varying pH levels.<sup>17</sup> Clearly, SERS is capable of detecting the structure of lipid bilayers, partitioning of analytes into hybrid monolayers, and crystallinity of lipid layers. In this work, SERS detection is employed for direct, label-free detection of phospholipids partitioned into self-assembled monolayers on an AgFON substrate. Detection of PAF and discrimination between two similar phospholipids was achieved.

## **5.2 Experimental Methods**

### **5.2.1 Materials**

All of the chemicals were reagent grade or better and used as purchased. Octanethiol, decanethiol, and hexadecanethiol were all purchased from Alfa Aesar (Ward Hill, MA). Dodecanethiol, 1-mercaptohexanol, octadecanethiol, hydrogen peroxide, ammonium hydroxide, ethanol, isopropanol, and methanol were purchased from Sigma-Aldrich (Milwaukee, WI). Punched copper disks from McMaster-Carr (Chicago, IL) were used as substrates. 500-nm ( $\pm 20$  nm)-diameter silica nanospheres were purchased as a 10% solids solution from Duke Scientific (Palo Alto, CA). All aqueous solutions were prepared with ultrapure ( $18.2 \text{ M}\Omega \text{ cm}^{-1}$ ) water from a Millipore water purification system (Long Beach, CA). Silver wire for electron beam deposition was purchased from Kamis Inc. (Mahopac Falls, NY). The lipids phosphatidylcholine (PC), phosphatidylethanolamine (PE), phosphatidylserine (PS) and phosphatidylinositol

(PI) were purchased from Avanti Polar Lipids (Alabaster, AL) and platelet activating factor (PAF) was purchased from Cayman Chemical (Ann Arbor, MI).

### **5.2.2 SERS Substrate Fabrication and Characterization**

Ag film over nanosphere (AgFON) substrates were fabricated on copper disks in the method described in previous chapters. Silica nanospheres were used in place of the traditional polystyrene latex nanospheres in order to promote adhesion and avoid polystyrene signal interference during the Raman experiments. Ag was vapor deposited to a thickness of 200 nm onto the nanosphere mask using electron beam vapor deposition (Airco Temescal, Berkeley, CA) at a pressure of  $7 \times 10^{-6}$  Torr. The rate of deposition, 2 Å/second, and thickness were measured using a quartz crystal microbalance. Once the AgFON surface was fabricated, the disks containing the nanosphere-based roughness features were placed in 2 mL of 1 mM ethanolic alkanethiol solutions for 16 hours at ambient conditions to facilitate monolayer formation. For mixed monolayer fabrication, the AgFON was placed in a 1 mM solution of decanethiol for 45 min and then placed in a 1 mM mercaptohexanol for 16 h.

For lipid sensing experiments, self-assembled partition layer formation was performed in ambient conditions. Afterwards, the AgFON was removed, rinsed with ethanol, and allowed to dry.

### **5.2.3 SERS Instrumentation**

After fabrication, the thiol-modified AgFON substrates were placed in a solution of 1mM lipid at 37°C for 1 h, mounted into a liquid cell, and then spectroscopic evaluation was performed both before and after water was added to the cell. In all data presented herein, SERS excitation was accomplished with a HeNe 632.83 nm excitation laser (Newport Corporation, Irvine, CA) with added neutral density filters to achieve the desired incident powers. In all cases, the laser power was chosen to avoid local heating

on the sample that would result in monolayer or lipid degradation and the appearance of amorphous carbon Raman bands with long exposure times. The laser beam first passed through an interference filter (Melles-Griot, Rochester, NY) and was then guided to the sample using an Al-coated prism to achieve a spot size of 1.26 mm<sup>2</sup>. Scattered light was collected using a 50-mm-diameter achromatic lens (Nikon, Melville, NY), and the Rayleigh scattered light was removed using a notch filter (Semrock, Rochester, NY). Detection was accomplished using a 0.5 m SpectraPro 2500i single monochromator and a Spec 400B liquid nitrogen-cooled CCD chip (both from Princeton Instruments/Acton, Trenton, NJ). In all cases, SERS spectra were measured from a minimum of five randomly chosen sample areas on a given substrate.

#### **5.2.4 Statistical Analysis**

Linear regression analysis was performed in Excel using the data analysis package with values of  $p < 0.05$  used to determine statistical significance. T-tests were also performed in Excel assuming equal variance, and a two-tailed value of  $p < 0.05$  was used to determine statistical significance.

### **5.3 Results and Discussion**

#### **5.3.1 Utilizing Partition Layers for Lipid Detection**

To demonstrate the potential of partition layer-assisted SERS detection of lipids, SERS results have been collected for four phospholipids: phosphatidylcholine (PC), phosphatidylethanolamine (PE), phosphatidylserine (PS) and phosphatidylinositol (PI) and platelet activating factor (PAF)(Figure 5.1). To determine if the monolayer was needed for lipid detection in contrast to direct adsorption of the lipids to the noble metal substrate, unmodified AgFON substrates were exposed to a 1 mM PC or PS solution in isopropanol or of PAF in water. SERS spectra after lipid exposure were recorded both with an empty flow cell (dry) and with water in the flow cell. All lipids yielded good

SERS signals on the unmodified substrate while dry but only PC and PAF bands were observed after filling the cell with water (Figure 5.2). This suggests that the dry

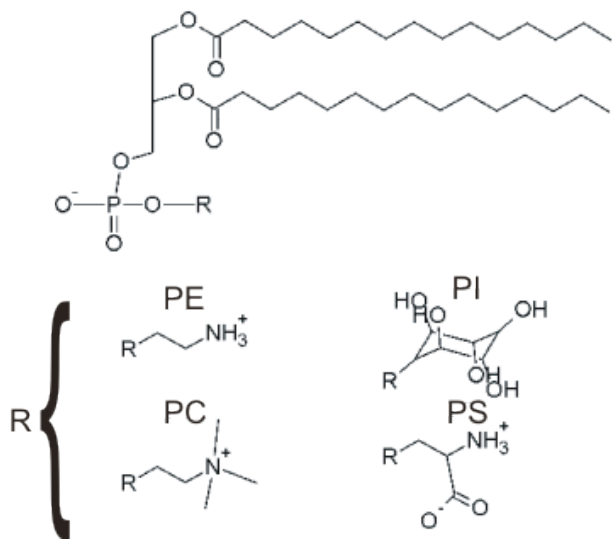


**Figure 5.1** Structures of phospholipids: phosphatidylethanolamine (PE), phosphatidylcholine (PC), phosphatidylinositol (PI) and phosphatidylserine. (PS).

spectrum may be a result of crystallized lipid on the metal surface, not an effective adsorption method for efforts to quantify lipids. Figure 5.2a shows that when PC is incubated with the bare AgFON substrate, the SERS peaks are very broad; however, when a hexadecanethiol-modified AgFON

was used, the SERS peaks for PC are very narrow, indicating a more homogeneous molecular orientation

(Figure 5.2b). The same trend is observed for PAF with only one peak at  $715\text{ cm}^{-1}$  shift observed on the bare AgFON substrate (Figure 5.3a); however, when a mixed monolayer-modified AgFON was used, there are many more SERS peaks for PAF and the peaks are very narrow (Figure 5.3b).

The inability of some lipids to adhere to the AgFON and breadth of the SERS bands indicates that partition layers are indeed necessary for the detection and discrimination of phospholipids. In further experiments, partition layer-modified AgFON substrates were exposed to an individual phospholipid (1 mM in isopropanol); each of the four chosen phospholipids was exposed to a separate substrate and the high concentration was chosen only for initial evaluation. The incubating substrates were kept at  $37\text{ }^{\circ}\text{C}$  for 1 h prior to placement in the SERS flow cell, and then water was passed through the cell before SERS analysis to remove loosely adsorbing phospholipid. Figure 5.4

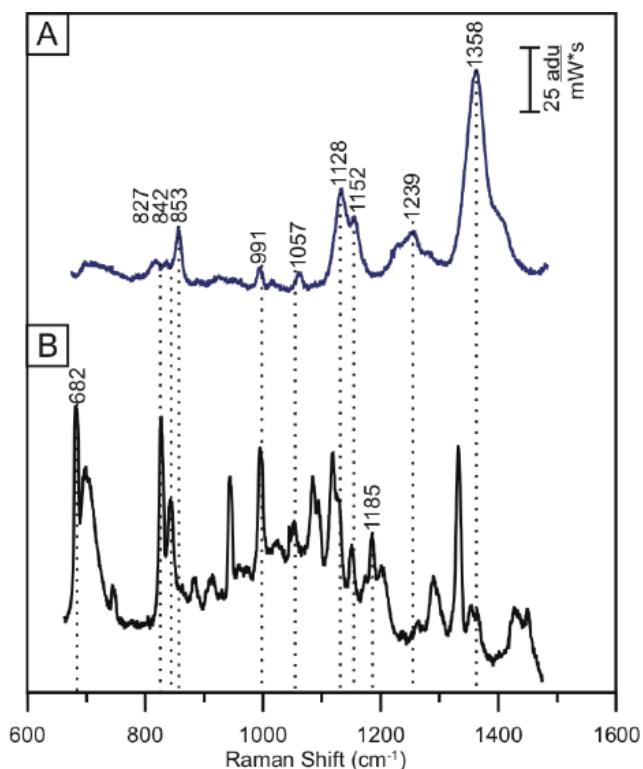


**Figure 5.2** SERS spectra of 1 mM PC on (A) a bare AgFON and (B) hexadecanethiol-modified AgFON, both were taken with water in the flow cell. Dashed lines represented the appearance of PC Raman bands.  $P = 3.18$  mW,  $t = 30$  s,  $\lambda_{\text{ex}} = 633$  nm.

shows a representative SERS spectrum from PS in a dodecanethiol-modified AgFON. It was observed during these early experiments that even slight change to the monolayer, switching from hexadecanethiol to dodecanethiol, caused PS to partition more efficiently but caused PC to partition less efficiently even though both lipids have the same tail length. A SERS spectrum of PE partitioned into a hexadecanethiol-modified AgFON has also been achieved, but is not shown here. Successful

partitioning of PI has not yet been achieved but work is ongoing to find an appropriate layer.

### 5.3.2 Identification of Lipid Bands for SERS Analysis

As shown above, detection of lipids without the addition of a partition layer is either not possible or leads to broad SERS bands due to multiple orientations of the analyte. Since a monolayer must be used to detect lipids, the monolayer Raman bands must be identified before identifying the SERS bands of the analyte in order to discriminate between the monolayer and analyte Raman bands. Upon assembly of an alkanethiol monolayer layer, Raman bands are measured at  $1443\text{ cm}^{-1}$  shift ( $\text{CH}_2$  or  $\text{CH}_3$  deformation),  $1301\text{ cm}^{-1}$  shift ( $\text{CH}_2$  wag),  $1130\text{ cm}^{-1}$  shift (trans C-C stretch),  $1078\text{ cm}^{-1}$

$1$  shift (gauche C-C stretch),  $999\text{ cm}^{-1}$  shift ( $\text{CH}_3$  rock),  $883\text{ cm}^{-1}$  shift ( $\text{CH}_3$  rock),  $698\text{ cm}^{-1}$  shift (trans C-S stretch), and  $638\text{ cm}^{-1}$  shift (gauche C-S stretch).<sup>18</sup> Many groups have done work to identify the carbon backbone of lipids and also to identify signals

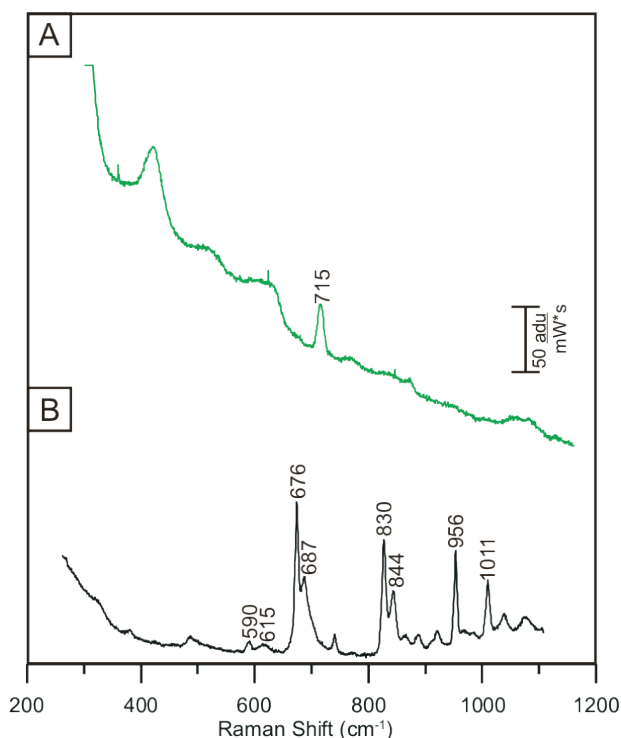


**Figure 5.3** 1 mM PAF on (A) a bare AgFON and (B) a mercaptohexanol/decanethiol-modified AgFON, both taken with water in the flow cell.  $P = 3.18\text{ mW}$ ,  $t = 30\text{ s}$ ,  $\lambda_{\text{ex}} = 633\text{ nm}$ .

from the head groups of the lipid with Raman spectroscopy.<sup>17,19</sup> To access the capability of partition layer-modified AgFONs to detect phospholipids, the substrates were exposed to a 1mM solutions of lipid in isopropanol for 1h at  $37\text{ }^\circ\text{C}$ . Various exposure times were investigated but the largest lipid signals were observed at the 1h time point. Raman bands for

PC are measured at  $1239\text{ cm}^{-1}$  shift (asymmetric  $\text{PO}_2^-$  stretch),  $1152\text{ cm}^{-1}$  shift (asymmetric CO-O-C stretch),  $1057$  and  $1128\text{ cm}^{-1}$  shift (C-C gauche and trans stretch),  $827$ ,  $842$  and  $853\text{ cm}^{-1}$  shift (symmetric C-O-C ether stretches), and  $682\text{ cm}^{-1}$  shift (choline C-N stretch).<sup>17,19</sup> The same exposure conditions were used for PS and similar results were expected since the only structural difference between PC and PS is the choline and serine group respectively. The differing Raman bands for PS are observed at  $1104\text{ cm}^{-1}$  shift is attributed to the symmetric  $\text{PO}_2^-$  stretch,  $735\text{ cm}^{-1}$  shift is the O-P-O stretch, and  $663\text{ cm}^{-1}$  shift is due to the C-N stretch of the serine headgroup.<sup>17,20</sup> The differing headgroup stretches will likely be the only way to discriminate between PC and PS in a

mixture of lipids.

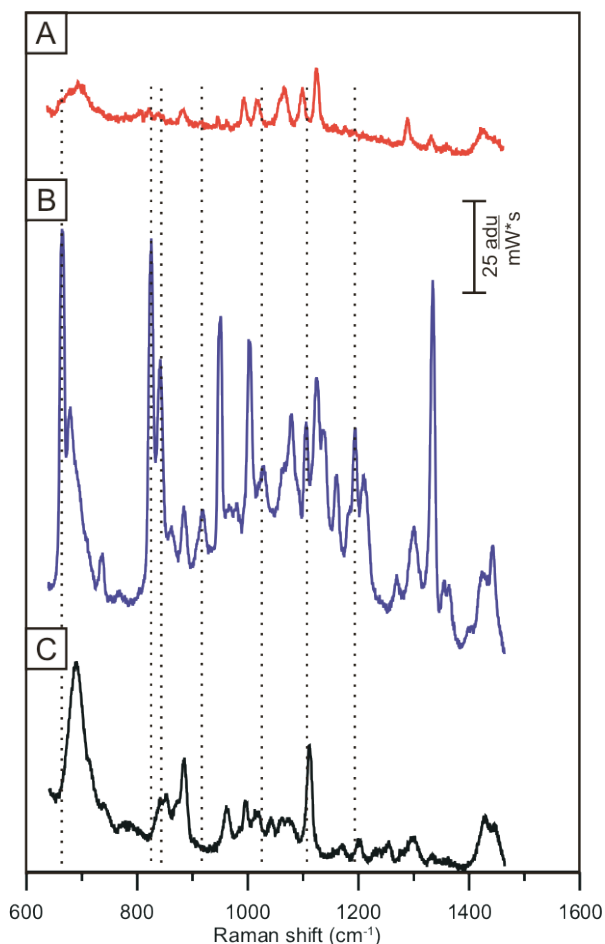


**Figure 5.4** 1 mM PS on (A) octadecanethiol-modified AgFON, (B) dodecanethiol-modified AgFON and (C) a hexanethiol-modified AgFON, all spectra were taken with water in the flow cell. Dashed lines represent the appearance of PS Raman bands.  $P = 3.18$  mW,  $t = 30$  s,  $\lambda_{\text{ex}} = 633$  nm.

This shift indicates that the lipid is integrating itself into the partition layer instead of forming a hybrid bilayer on top of the underlying partition layer. The magnitude of the shifts for the phospholipids are  $2\text{--}3$   $\text{cm}^{-1}$ , which is within the  $2$   $\text{cm}^{-1}$  resolution of our detector, demonstrating that both lipids are partitioning in a similar fashion. This would be expected since they both have carbon tails of the same length. PAF partitioning causes a greater shift,  $6$   $\text{cm}^{-1}$ , in the C-S region of the partition layer when compared to PC and PS. PC and PS are larger molecules, so it was thought that their partitioning

PAF is structurally similar to PC, both have choline headgroups, but PAF has an acyl group instead of the second carbon tail. As discussed above, without the presence of a partition layer, PAF cannot be detected, and a mixed monolayer of 6-mercaptohexanol and decanethiol was used to facilitate PAF detection. The  $676$   $\text{cm}^{-1}$  shift is the choline headgroup C-N stretch,  $830$  and  $844$   $\text{cm}^{-1}$  shift are from the ether groups, and  $956$  and  $1011$   $\text{cm}^{-1}$  shifts are backbone stretches.

The thiolated partition layers have a strong C-S stretch located at  $698$   $\text{cm}^{-1}$  shift, which shifts  $3\text{--}6$   $\text{cm}^{-1}$  upon partitioning of a phospholipid or PAF.

would cause a greater disturbance to the partition layer, however, it seems the smaller size of PAF allows it to intercalate into the monolayer more deeply than the other phospholipids and therefore causes a greater shift in the partition layer C-S stretch.

### **5.3.3 Sensitivity of Partition Layers to Phospholipids and Secreted Lipids**

There are many difficulties when designing a sensor for biological molecules: interfering species in complex mixtures, biofouling, and low concentrations of the lipids. Phospholipids are a major portion of cellular membranes but exist at low concentrations when secreted. PAF exists at nM to pM concentrations within the body, so any SERS sensor will need to be sensitive in this concentration range. To date, 100  $\mu\text{M}$  of PC and PS is are the lowest concentrations of phospholipid detectable with our partition layer-modified SERS substrates. One of the main difficulties in detecting phospholipids is that the stretches associated with the choline and serine head groups overlap with the C-S stretch from the monolayer. At low concentrations, the signature headgroup Raman shift is obscured by the C-S band and the ether backbone bands disappear, leaving only the C-C backbone Raman bands, which are not discernible from the partition layer C-C backbone at low concentrations.

This same difficulty is observed when trying to detect PAF at low concentrations. To date, 50  $\mu\text{M}$  is the lowest concentration of PAF detectable by our SERS sensor. The Raman bands with the largest intensity for PAF are the 676, 830 and 956  $\text{cm}^{-1}$  shift, which are the C-N stretch and ether backbone stretches, respectively. The choline headgroup stretch at 676  $\text{cm}^{-1}$  is obscured by the C-S Raman stretch at concentrations lower than 50  $\mu\text{M}$ , the ether stretches are not apparent, and the C-C backbone stretches are too similar to the partition layer at lower concentrations.

The limit of detection for our SERS sensor is 100  $\mu\text{M}$  for phospholipids and 50  $\mu\text{M}$  for PAF. These current limits of detection are not ideal and nowhere near the LOD that is

needed for physiological detection of lipids. To detect lipids at lower concentrations, we need to find a partition layer that has Raman bands that do not overlap with the bands of the analyte, so a shift away from alkanethiol layers might be necessary.

#### **5.3.4 Distinguishing Between Phosphatidylserine and Phosphatidylcholine**

One of the main goals is to be able to distinguish between differing phospholipids using the same partition layer modified SERS substrate. To this end, an AgFON was exposed to 1 mM isopropanol solutions of PC and PS for 1 h at 37 °C, rinsed and then mounted in a SERS flow cell for analysis. PC and PS have different Raman bands due to the choline and serine head groups at 682 and 663  $\text{cm}^{-1}$  shift, respectively, and therefore should be detected simultaneously. However, it was observed that during the dual exposure experiment, the signature Raman bands from PC dominated the SERS spectrum (data not shown). As discussed earlier, PC and PS partition preferentially into different monolayers. For the dual partitioning experiment a decanethiol partition layer was chosen since it was the only partition layer that worked for PAF, PC and PS. This layer is not ideal for PC or PS, which partitioned preferentially into hexadecanethiol and dodecanethiol, respectively. Despite efforts to find a layer that would work for all lipids, different partition layers or alternate analyte trapping mechanisms will need to be employed for general phospholipids detection.

#### **5.3.5 Insight Into Lipid Partitioning Mechanism**

In previous work we were able to gain insight into the partitioning mechanism of PCBs and PAHs by performing SERS band analysis. In this work, those these methods were also used to determine if the phospholipids partitioned into the monolayer, as the PAHs and PCBs did, or formed hybrid lipid bilayers. Using an experiment where the phospholipid signal intensity was measured with varied partition layer chain length. If bilayers are formed, the SERS signal for the phospholipid should scale as the

electromagnetic field decay length.<sup>21</sup> Alkanethiols with six, twelve and eighteen carbon chain lengths were used for these experiments, and PS was used as the model phospholipid. The measured spectra do not support the formation of bilayers; in fact, there were very few characteristic PS stretches in the six or eighteen carbon chain

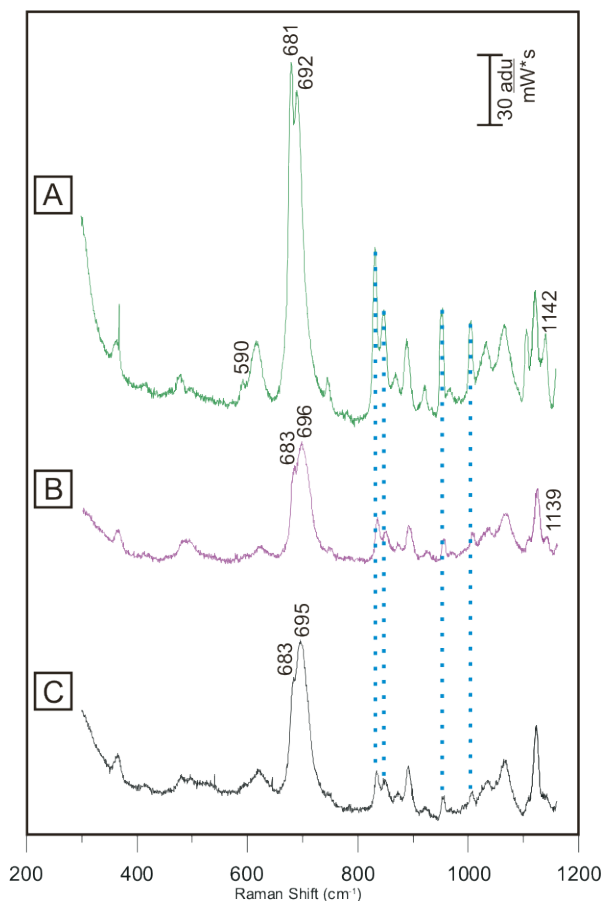


**Figure 5.5** 100  $\mu$ M (A) PAF, (B) PC and (C) PS on a decanethiol-modified AgFON. Dashed lines indicate appearance of lipid backbone stretches.  $P = 3.18$  mW,  $t = 30$  s,  $\lambda_{\text{ex}} = 633$  nm.

length while and there were clear PS SERS bands in the twelve carbon chain monolayer, Figure 5.4. This indicates that the lipids are partitioning into the monolayer rather than forming hybrid bilayers. SERS band analysis is limited in this case since the  $C-C_T/C-C_G$  ratio cannot be used due to the Raman bands of the partition layer being too similar to those of the C-C backbone Raman bands for the lipid. As was discussed earlier in this chapter, the  $C-S_T$  band shifts  $2-6$   $\text{cm}^{-1}$  upon lipid partitioning, which also indicates that the lipid is partitioning into the partition layer, instead of forming a hybrid bilayer.

### 5.3.6 Comparison of Partition Layers for Secreted Lipids and Phospholipid Detection

Initial experiments for lipid detection were performed with only alkanethiols, and while progress was made, more efficient partition layers would clearly be desirable.

The lipids were exposed at higher concentrations, 1mM in isopropanol, to various partition layer-coated AgFONs. Further consideration of partition layers in this work

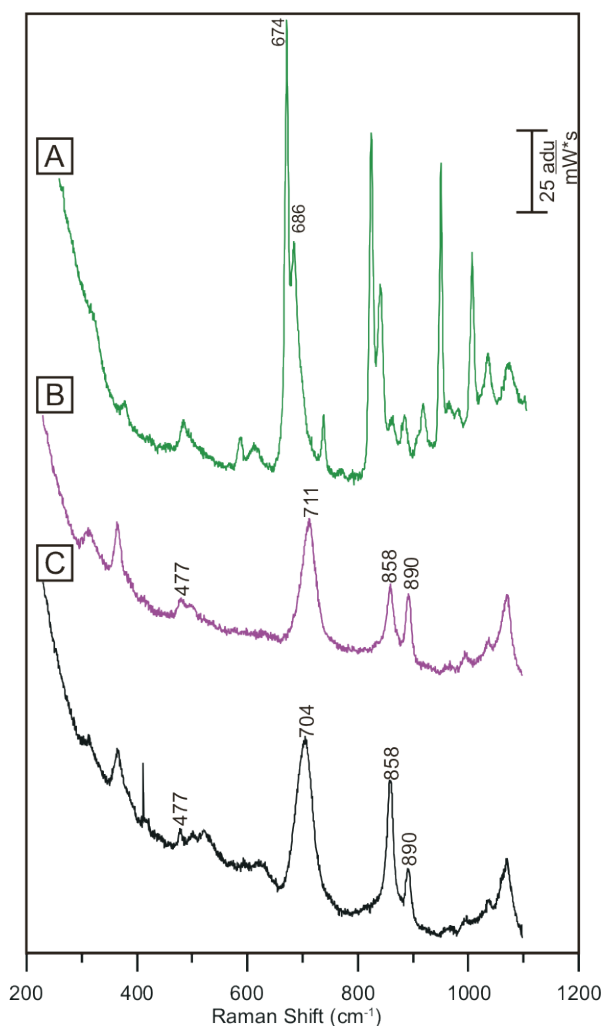


**Figure 5.6** 100  $\mu$ M (A) PAF, (B) PC and (C) PS on a mercaptohexanol/decanethiol-modified AgFON.  $P = 3.18$  mW,  $t = 30$  s,  $\lambda_{ex} = 633$  nm.

include variation of When choosing a partition layer for analytes there are many factors to consider, but the three that were investigated were: chemical functionality, hydrophobicity, and disorder. PC and PS were exposed to an AgFON modified with a carboxylic acid acid-terminated monolayer or an amine amine-terminated monolayer. In both cases, no partitioning of the lipid into these monolayers was observed. The hydrophobicity and disorder of the partition layer can be assessed in one experiment. As mentioned in Chapter 3, fundamental study of self-assembled

monolayers on AgFON clearly reveals that longer monolayers are more tightly ordered and packed, while shorter monolayers are more disordered and therefore less hydrophobic than longer monolayers. As we saw in Figure 5.4, PS partitions favorably into a dodecanethiol monolayer. This layer allows PS to dwell within the zone of enhancement and has enough disorder to allow partitioning of the lipid into the monolayer. The same experiment was performed with PC with differing results. PC partitioned into a more crystalline hexadecanethiol monolayer. However, in both cases

the lipids partitioned preferentially into longer alkanethiol partition layers. When the same experiments were performed with PAF, little to no signal was seen with the alkanethiol partition layers. The spectrum in Figure 5.5 shows that PAF can be observed at 100  $\mu\text{M}$ ; however, if a mixed monolayer of 6-mercaptohexanol and decanethiol is employed, much more intense SERS bands for PAF are observed (Figure 5.6). PAF is water soluble and has a much lower partition coefficient compared to the other phospholipids, so it is not surprising that a hydrophobic alkanethiol partition layer would not be ideal for PAF partitioning.<sup>22</sup> The addition of the 6-mercaptohexanol to the alkanethiol layer creates pockets within the decanethiol where PAF partitioning is more favorable. This difference in partitioning coefficients and, hence, in partition layers for the secreted lipids indicates that a single sensor for the detection of phospholipids and secreted lipids such as PAF is not possible and two different partition layers or sensing schemes will need to be employed for optimal detection.

#### **5.4 Conclusions**

The partition layer is one of the keys to analyte detection, and thorough characterization of the assembled layer on the AgFON is needed to understand monolayer ordering before and after analyte exposure. In previous work, assembly of single component alkanethiol monolayers was investigated, however, for detection of an analyte like PAF, further investigation of mixed monolayer formation of AgFONs is needed. Lennox and coworkers were able to assemble dual component monolayers reproducibly by passing a modest potential through a substrate and a modified version of this will be used to form mixed monolayers on AgFON for PAF detection.<sup>23</sup> Through potential control, they were able to make a true mixed monolayer instead of a decanethiol monolayer with islands of the second partition layer component.

A mixed monolayer will facilitate lower, more sensitive PAF detection, but still suffers

from overlapping bands between the partition layer and analyte. To avoid this, partition layer components without bands in the 600-800  $\text{cm}^{-1}$  shift region need to be employed, however this will be difficult since most partition layers employ the use of thiols for attachment to the AgFON surface. Better detection limits of lipids could also be achieved if substrates with greater SERS enhancement factors were used, such as the gap substrates mentioned earlier.<sup>24</sup> Overall, partition layer-modified AgFON substrates can facilitate the detection of phospholipids and secreted lipids at higher concentrations, but the SERS bands from the partition layer make detection of lipids at physiologically relevant concentrations challenging at this time.

# Chapter Six

## Conclusion and Future Work

Over the past thirty years, the multidisciplinary field of SERS has moved from a much debated phenomenon to a dynamic analytical tool that can be used for biological and environmental sensing. The work herein addressed SERS substrate fabrication, modification, and application for a variety of sensing schemes. Chapter One reviewed the use of SERS for biological and environmental sensing which occurred in the past ten years.<sup>1</sup> The continuing advancement in SERS substrate fabrication and development has led to substrates that are easily fabricated, inexpensive and have enhancement factors  $>10^5$ . In Chapter Two, three SERS substrates were presented, each of which uses unique architecture to achieve EFs that are greater than or comparable to traditional AgFON substrates. The polymer-templated SERS substrate can be fabricated in a field setting, stable in water, and has EFs comparable to a AgFON. The nanohole arrays, can be used for SERS, surface plasmon sensing or EOT sensing, and the plasmons can be tuned by altering the nanohole size or shape. The third substrate is the nanogap substrate, which, due to its flexible fabrication scheme, allows a gap to be formed along the edge of any metal architecture for SERS sensing. The continuing development of SERS substrates is needed as SERS expands into areas of homeland security<sup>2</sup>, environmental sensing<sup>3</sup> and biosensing<sup>1</sup>. Future for SERS applications in these areas require substrates to be easily fabricated, inexpensive, have consistent EFs that are  $>10^5$ .

Chapter Three explored the fundamentals of monolayer formation on a AgFON. The goal of the chapter was to understand what makes an ideal partition layer using LSPR and SERS band analysis. In this study, the data revealed that the fundamental properties that make a good partition layer are a combination of (1) monolayer thickness and (2) the crystallinity of the upper and lower monolayer. For PCB-47 partitioning the C10 layer was ideal because its balance between order and disorder

enabled concentration of the analyte within the SERS zone of enhancement. The study also showed that a modest potential of +200 mV vs Ag/AgCl can be used to quickly form monolayers that are comparable to partition layers formed over 72h incubation in alkanethiol solutions. Future work in this area will utilize the application of modest potentials to create mixed monolayers, which Lennox and coworkers<sup>4</sup> were able to form on Au.

Chapters Four and Five showed the versatility of SERS as an analytical technique for the detection of environmental pollutants and bioactive lipids. Chapter Four utilized alkanethiol partition layers for the detection of PCBs, PAHs and PBDEs. Further work in this area will expand the number of PCB congeners or PAHs detectable using this system. The partition layer approach can also be combined with the high enhancement factor SERS substrates described in Chapter Two in order to improve the limit of detection for these environmental pollutants; the same could be done with the bioactive lipids in Chapter Five. For bioactive lipids an alternate partition layer is needed, as the C-S stretch interferes with detection of the phospholipid head group stretches. An immobilized cyclodextrin could concentrate the phospholipid closer to the AgFON surface, which would increase the signal from the head group leading to higher signal from the analyte. Overall this work has shown that SERS can be employed for non-traditional analytes and will push the use of SERS further into interdisciplinary fields of study, allowing SERS to reach beyond the bounds of chemistry.

## Bibliography

### References

#### Chapter One

- (1) Kneipp, K.; Kneipp, H.; Itzkan, I.; Dasari, R.; Feld, M. *J. Phys.-Condens. Mat.* **2002**, *14*, R597–R624.
- (2) Jackson, J. B.; Halas, N. J. *Proc. Natl. Acad. Sci. U.S.A.* **2004**, *101*, 17930–17935.
- (3) Haynes, C. L.; McFarland, A. D.; Duyne, R. P. V. *Anal. Chem.* **2005**, *77*, 338 A–346 A.
- (4) Qian, X. M.; Peng, X. H.; Ansari, D. O.; Yin-Goen, Q.; Chen, G. Z.; Shin, D. M.; Yang, L.; Young, A. N.; Wang, M. D.; Nie, S. M. *Nat. Biotechnol.* **2008**, *26*, 83–90.
- (5) Wustholz, K. L.; Brosseau, C. L.; Casadio, F.; Van Duyne, R. P. *Phys. Chem. Chem. Phys.* **2009**, *11*, 7350–7359.
- (6) Larmour, I. A.; Faulds, K.; Graham, D. *Chem. Sci.* **2010**, *1*, 151–160.
- (7) Zhang, X.; Young, M. A.; Lyandres, O.; Van Duyne, R. P. *J. Am. Chem. Soc.* **2005**, *127*, 4484–4489.
- (8) Mohs, A. M.; Mancini, M. C.; Singhal, S.; Provenzale, J. M.; Leyland-Jones, B.; Wang, M. D.; Nie, S. M. *Anal. Chem.* **2010**, *82*, 9058–9065.
- (9) Young, M. A.; Stuart, D. A.; Lyandres, O.; Glucksberg, M. R.; Van Duyne, R. P. *Can. J. Chem.* **2004**, *82*, 1435–1441.
- (10) Quang, L. X.; Lim, C.; Seong, G. H.; Choo, J.; Do, K. J.; Yoo, S. K. *Lab Chip* **2008**, *8*, 2214–2219.
- (11) Yan, F.; Vo-Dinh, T. *Sens. Actuator B-Chem.* **2007**, *121*, 61–66.
- (12) Raman, C. V.; Krishnan, K. S. *Nature* **1928**, *121*, 501–504.
- (13) McCreery, R. L. *Raman Spectroscopy for Chemical Analysis*; 1st ed. Wiley-Interscience, 2000; p. 448.
- (14) Singh, R. *Physics in Perspective (PIP)* **2002**, *4*, 399–420.
- (15) Shim, S.; Stuart, C. M.; Mathies, R. A. *ChemPhysChem* **2008**, *9*, 697–699.
- (16) Fleischmann, M.; Hendra, P. J.; McQuillan, A. J. *Chem. Phys. Lett.* **1974**, *26*, 163–166.
- (17) Jeanmaire, D. L.; Van Duyne, R. P. *J. Electroanal. Chem.* **1977**, *84*, 1–20.
- (18) Albrecht, M. G.; Creighton, J. A. *J. Am. Chem. Soc.* **1977**, *99*, 5215–5217.
- (19) Paul, R.; McQuillan, A.; Hendra, P.; Fleischmann, M. *J. Electroanal. Chem.* **1975**, 248–249.
- (20) McQuillan, A.; Hendra, P.; Fleischmann, M. *J. Electroanal. Chem.* **1975**, 933–944.
- (21) Liao, P. F.; Bergman, J. G.; Chemla, D. S.; Wokaun, A.; Melngailis, J.; Hawryluk, A. M.; Economou, N. P. *Chem. Phys. Lett.* **1981**, *82*, 355–359.
- (22) Howard, R. E.; Liao, P. F.; Skocpol, W. J.; Jackel, L. D.; Craighead, H. G. *Science* **1983**, *221*, 117–121.
- (23) Kambhampati, P.; Foster, M.; Campion, A. *J. Chem. Phys.* **1999**, 551–558.
- (24) Schatz, G.; Young, M.; Van Duyne, R. *Electromagnetic mechanism of SERS; Electromagnetic mechanism of SERS; Surface-Enhanced Raman Scattering: Physics and Applications*, 2006; pp. 19–45.

- (25) Zhao, L.; Jensen, L.; Schatz, G. *Nano Lett.* **2006**, *6*, 1229–1234.
- (26) Haes, A. J.; Haynes, C. L.; McFarland, A. D.; Schatz, G. C.; Van Duyne, R. P.; Zou, S. *MRS Bull.* **2005**, *30*, 368–375.
- (27) Aroca, R. *Surface-Enhanced Vibrational Spectroscopy*; John Wiley & Sons, Ltd: Chichester, UK, 2007.
- (28) Camden, J. P.; Dieringer, J. A.; Zhao, J.; Van Duyne, R. P. *Acc. Chem. Res.* **2008**, *41*, 1653–1661.
- (29) Kennedy, B. J.; Spaeth, S.; Dickey, M.; Carron, K. T. *J. Phys. Chem. B* **1999**, *103*, 3640–3646.
- (30) Bantz, K. C.; Haynes, C. L. *Vib. Spectrosc.* **2009**, *50*, 29–35.
- (31) Chen, L. X.; Choo, J. B. *Electrophoresis* **2008**, *29*, 1815–1828.
- (32) Levin, C. S.; Kundu, J.; Barhoumi, A.; Halas, N. J. *Analyst* **2009**, *134*, 1745–1750.
- (33) Grubisha, D. S.; Lipert, R. J.; Park, H. Y.; Driskell, J.; Porter, M. D. *Anal. Chem.* **2003**, *75*, 5936–5943.
- (34) Doering, W.; Piotti, M.; Natan, M.; Freeman, R. *Adv. Mater.* **2007**, 3100–3108.
- (35) Dick, L. A.; McFarland, A. D.; Haynes, C. L.; Van Duyne, R. P. *J. Phys. Chem. B* **2002**, *106*, 853–860.
- (36) Stropp, J.; Trachta, G.; Brehm, G.; Schneider, S. *J. Raman Spectrosc.* **2003**, *34*, 26–32.
- (37) Liu, X. F.; Sun, C. H.; Linn, N. C.; Jiang, B.; Jiang, P. *J. Phys. Chem. C* **2009**, *113*, 14804–14811.
- (38) Lee, S. H.; Bantz, K. C.; Lindquist, N. C.; Oh, S.-H.; Haynes, C. L. *Langmuir* **2009**, *25*, 13685–13693.
- (39) Leverette, C. L.; Jacobs, S. A.; Shanmukh, S.; Chaney, S. B.; Dluhy, R. A.; Zhao, Y. P. *Appl. Spectrosc.* **2006**, *60*, 906–913.
- (40) Sockalingum, G. D.; Beljebbar, A.; Morjani, H.; Angiboust, J. F.; Manfait, M. *Biospectroscopy* **1998**, *4*, S71–S78.
- (41) Bantz, K. C.; Haynes, C. L. *Langmuir* **2008**, *24*, 5862–5867.
- (42) Erol, M.; Han, Y.; Stanley, S.; Stafford, C.; Du, H.; Sukhishvili, S. *J. Am. Chem. Soc.* **2009**, *131*, 7480–7481.
- (43) Shuping, X.; Xiaohui, J.; Weiqing, X.; Bing, Z.; Xiaoming, D.; Yubai, B.; Yukihiro, O. *J. Biomed. Opt.* **2005**, *10*, 031112.
- (44) Xie, Y.; Wang, X.; Han, X.; Xue, X.; Ji, W.; Qi, Z.; Liu, J.; Zhao, B.; Ozaki, Y. *Analyst* **2010**, *135*, 1389–1394.
- (45) Tripp, R. A.; Dluhy, R. A.; Zhao, Y. P. *Nano Today* **2008**, *3*, 31–37.
- (46) Chan, G. H.; Zhao, J.; Hicks, E. M.; Schatz, G. C.; Van Duyne, R. P. *Nano Lett.* **2007**, *7*, 1947–1952.
- (47) Chan, G. H.; Zhao, J.; Schatz, G. C.; Van Duyne, R. P. *J. Phys. Chem. C* **2008**, *112*, 13958–13963.
- (48) Zhang, X. Y.; Zhao, J.; Whitney, A. V.; Elam, J. W.; Van Duyne, R. P. *J. Am. Chem. Soc.* **2006**, *128*, 10304–10309.
- (49) Pettinger, B. *Tip-enhanced Raman spectroscopy (TERS)*; Surface-Enhanced Raman Scattering: Physics and Applications, 2006; *103*, 217–240.
- (50) Lal, S.; Link, S.; Halas, N. J. *Nat. Photonics* **2007**, *1*, 641–648.
- (51) You, Y.; Purnawirman, N. A.; Hu, H.; Kasim, J.; Yang, H.; Du, C.; Yu, T.; Shen, Z. *J. Raman Spectrosc.* **2010**, *41*, 1156–1162.
- (52) Bulgarevich, D. S.; Futamata, M. *Appl. Spectrosc.* **2004**, *58*, 757–761.
- (53) Roth, R. M.; Panoiu, N. C.; Adams, M. M.; Osgood, R. M.; Neacsu, C. C.; Raschke, M. B. *Opt. Express* **2006**, *14*, 2921–2931.

- (54) Zhang, W. H.; Cui, X. D.; Yeo, B. S.; Schmid, T.; Hafner, C.; Zenobi, R. *Nano Lett.* **2007**, *7*, 1401–1405.
- (55) Steidtner, J.; Pettinger, B. *Phys. Rev. Lett.* **2008**, *100*, 236101.
- (56) Bishnoi, S. W.; Rozell, C. J.; Levin, C. S.; Gheith, M. K.; Johnson, B. R.; Johnson, D. H.; Halas, N. J. *Nano Lett.* **2006**, *6*, 1687–1692.
- (57) Huang, G. G.; Han, X. X.; Hossain, M. K.; Ozaki, Y. *Anal. Chem.* **2009**, *81*, 5881–5888.
- (58) Deckert-Gaudig, T.; Bailo, E.; Deckert, V. *Phys. Chem. Chem. Phys.* **2009**, *11*, 7360–7362.
- (59) Singhal, R.; Bhattacharyya, S.; Orynbayeva, Z.; Vitol, E.; Friedman, G.; Gogotsi, Y. *Nanotechnology* **2010**, *21*, 015304.
- (60) Shafer-Peltier, K.; Haynes, C.; Glucksberg, M.; Van Duyne, R. *J. Am. Chem. Soc.* **2003**, 588–593.
- (61) Fox, C.; Uibel, R.; Harris, J. *J. Phys. Chem. B* **2007**, 11428–11436.
- (62) Levin, C. S.; Kundu, J.; Janesko, B. G.; Scuseria, G. E.; Raphael, R. M.; Halas, N. J. *J. Phys. Chem. B* **2008**, *112*, 14168–14175.
- (63) Barhoumi, A.; Zhang, D.; Tam, F.; Halas, N. J. *J. Am. Chem. Soc.* **2008**, *130*, 5523–5529.
- (64) Wei, F.; Zhang, D. M.; Halas, N. J.; Hartgerink, J. D. *J. Phys. Chem. B* **2008**, *112*, 9158–9164.
- (65) Bantz, K. C.; Meyer, A. F.; Wittenberg, N. J.; Im, H.; Kurtulus, O.; Lee, S. H.; Lindquist, N. C.; Oh, S.-H.; Haynes, C. L. *Phys. Chem. Chem. Phys.* **2011**, *13*, 11551–11567.
- (66) Pearman, W. F.; Angel, S. M.; Ferry, J. L.; Hall, S. *Applied Spectroscopy* **2008**, *62*, 727–732.
- (67) Vitol, E. A.; Brailoiu, E.; Orynbayeva, Z.; Dun, N. J.; Friedman, G.; Gogotsi, Y. *Anal. Chem.* **2010**, *82*, 6770–6774.
- (68) Heller, A.; Feldman, B. *Chem. Rev.* **2008**, *108*, 2482–2505.
- (69) Yonzon, C. R.; Haynes, C. L.; Zhang, X. Y.; Walsh, J. T.; Van Duyne, R. P. *Anal. Chem.* **2004**, *76*, 78–85.
- (70) Lyandres, O.; Shah, N. C.; Yonzon, C. R.; Walsh, J. T.; Glucksberg, M. R.; Van Duyne, R. P. *Anal. Chem.* **2005**, *77*, 6134–6139.
- (71) Stuart, D. A.; Yonzon, C. R.; Zhang, X. Y.; Lyandres, O.; Shah, N. C.; Glucksberg, M. R.; Walsh, J. T.; Van Duyne, R. P. *Anal. Chem.* **2005**, *77*, 4013–4019.
- (72) Shah, N. C.; Lyandres, O.; Walsh, J. T.; Glucksberg, M. R.; Van Duyne, R. P. *Anal. Chem.* **2007**, *79*, 6927–6932.
- (73) Kundu, J.; Levin, C. S.; Halas, N. J. *Nanoscale* **2009**, *1*, 114–117.
- (74) Krysinski, P.; Zebrowska, A.; Michota, A.; Bukowska, J.; Becucci, L.; Moncelli, M. *Langmuir* **2001**, 3852–3857.
- (75) Jones, C. L.; Bantz, K. C.; Haynes, C. L. *Anal. Bioanal. Chem.* **2009**, *394*, 303–311.
- (76) Carron, K.; Peitersen, L.; Lewis, M. *Environ. Sci. Technol.* **1992**, *26*, 1950–1954.
- (77) Alvarez-Puebla, R. A.; Santos, dos, D. S. J.; Aroca, R. F. *Analyst* **2007**, *132*, 1210–1214.
- (78) Lopez-Tocon, I.; Otero, J. C.; Arenas, J. F.; Garcia-Ramos, J. V.; Sanchez-Cortes, S. *Anal. Chem.* **2011**, *83*, 2518–2525.
- (79) Ryu, K.; Haes, A. J.; Park, H. Y.; Nah, S.; Kim, J.; Chung, H.; Yoon, M. Y.; Han, S. H. *J. Raman Spectrosc.* **2010**, *41*, 121–124.

- (80) Huang, G. G.; Hossain, M. K.; Han, X. X.; Ozaki, Y. *Analyst* **2009**, *134*, 2468–2474.
- (81) Domke, K.; Zhang, D.; Pettinger, B. *J. Am. Chem. Soc.* **2007**, 6708–.
- (82) Green, M.; Liu, F. M.; Cohen, L.; Kollensperger, P.; Cass, T. *Faraday Discuss.* **2006**, *132*, 269–280.
- (83) Bell, S. E. J.; Sirimuthu, N. M. S. *J. Am. Chem. Soc.* **2006**, *128*, 15580–15581.
- (84) Cho, H. S.; Lee, B.; Liu, G. L.; Agarwal, A.; Lee, L. P. *Lab Chip* **2009**, *9*, 3360–3363.
- (85) Neumann, O.; Zhang, D. M.; Tam, F.; Lal, S.; Wittung-Stafshede, P.; Halas, N. J. *Anal. Chem.* **2009**, *81*, 10002–10006.
- (86) Bailo, E.; Deckert, V. *Angew. Chem. Int. Ed.* **2008**, *47*, 1658–1661.
- (87) Cialla, D.; Deckert-Gaudig, T.; Budich, C.; Laue, M.; Moller, R.; Naumann, D.; Deckert, V.; Popp, J. *J. Raman Spectrosc.* **2009**, 240–243.
- (88) Pal, A.; Isola, N.; Alarie, J.; Stokes, D.; Vo-Dinh, T. *Faraday Discuss.* **2006**, 293–301.
- (89) Braun, G.; Lee, S.; Dante, M.; Nguyen, T.; Moskovits, M.; Reich, N. *J. Am. Chem. Soc.* **2007**, 6378–6379.
- (90) Banholzer, M.; Qin, L.; Millstone, J.; Osberg, K.; Mirkin, C. *Nat. Protoc.* **2009**, 838–848.
- (91) Bonham, A.; Braun, G.; Pavel, I.; Moskovits, M.; Reich, N. *J. Am. Chem. Soc.* **2007**, 14572–14573.
- (92) Graham, D.; Thompson, D. G.; Smith, W. E.; Faulds, K. *Nat. Nanotechnol.* **2008**, *3*, 548–551.
- (93) Stokes, R.; MacAskill, A.; Dougan, J.; Hargreaves, P.; Stanford, H.; Smith, W.; Faulds, K.; Graham, D. *Chem. Commun.* **2007**, 2811–2813.
- (94) Faulds, K.; McKenzie, F.; Graham, D. *Analyst* **2007**, *132*, 1100–1102.
- (95) Faulds, K.; Smith, W. E.; Graham, D. *Anal. Chem.* **2004**, *76*, 412–417.
- (96) Jin, R.; Cao, Y.; Thaxton, C.; Mirkin, C. *Small* **2006**, 375–380.
- (97) Faulds, K.; McKenzie, F.; Smith, W. E.; Graham, D. *Angew. Chem. Int. Ed.* **2007**, *46*, 1829–1831.
- (98) Cho, H.; Baker, B. R.; Wachsmann-Hogiu, S.; Pagba, C. V.; Laurence, T. A.; Lane, S. M.; Lee, L. P.; Tok, J. B. H. *Nano Lett.* **2008**, *8*, 4386–4390.
- (99) McKenzie, F.; Graham, D. *Chem. Commun.* **2009**, 5757–5759.
- (100) Fabris, L.; Dante, M.; Braun, G.; Lee, S.; Reich, N.; Moskovits, M.; Nguyen, T.; Bazan, G. *J. Am. Chem. Soc.* **2007**, *129*, 6086–6087.
- (101) Cao, Y.; Jin, R.; Mirkin, C. *Science* **2002**, *297*, 1536–1540.
- (102) Vo-Dinh, T.; Yan, F.; Wabuyele, M. *J. Raman Spectrosc.* **2005**, *36*, 640–647.
- (103) Wabuyele, M.; Vo-Dinh, T. *Anal. Chem.* **2005**, *77*, 7810–7815.
- (104) Wang, H.; Vo-Dinh, T. *Nanotechnology* **2009**, *20*, 065101.
- (105) Barhoumi, A.; Halas, N. J. *J. Am. Chem. Soc.* **2010**, *132*, 12792–12793.
- (106) Corrigan, D. K.; Gale, N.; Brown, T.; Bartlett, P. N. *Angew. Chem. Int. Ed.* **2010**, *49*, 5917–5920.
- (107) Mahajan, S.; Richardson, J.; Brown, T.; Bartlett, P. N. *J. Am. Chem. Soc.* **2008**, *130*, 15589–15601.
- (108) Lowe, A. J.; Huh, Y. S.; Strickland, A. D.; Erickson, D.; Batt, C. A. *Anal. Chem.* **2010**, *82*, 5810–5814.
- (109) Han, X.; Zhao, B.; Ozaki, Y. *Anal. Bioanal. Chem.* **2009**, 1719–1727.
- (110) Socrates, G. *Infrared and Raman Characteristic Group Frequencies: Tables and Charts*; 3rd ed. Wiley: New York, 2001.

- (111) Podstawka, E.; Ozaki, Y.; Proniewicz, L. M. *Appl. Spectrosc.* **2004**, *58*, 570–580.
- (112) Podstawka, E.; Ozaki, Y. *Biopolymers* **2008**, *89*, 807–819.
- (113) Pavel, I.; McCarney, E.; Elkhaled, A.; Morrill, A.; Plaxco, K.; Moskovits, M. J. *Phys. Chem. C* **2008**, 4880–4883.
- (114) Han, X.; Jia, H.; Wang, Y.; Lu, Z.; Wang, C.; Xu, W.; Zhao, B.; Ozaki, Y. *Anal. Chem.* **2008**, 2799–2804.
- (115) Becker, M.; Budich, C.; Deckert, V.; Janasek, D. *Analyst* **2009**, 38–40.
- (116) Han, X.; Huang, G.; Zhao, B.; Ozaki, Y. *Anal. Chem.* **2009**, 3329–3333.
- (117) Bjerneld, E.; Foldes-Papp, Z.; Kall, M.; Rigler, R. *J. Phys. Chem. B* **2002**, *6*, 1213–1218.
- (118) Driskell, J.; Uhlenkamp, J.; Lipert, R.; Porter, M. *Anal. Chem.* **2007**, *79*, 4141–4148.
- (119) Narayanan, R.; Lipert, R. J.; Porter, M. D. *Anal. Chem.* **2008**, *80*, 2265–2271.
- (120) Driskell, J. D.; Kwarta, K. M.; Lipert, R. J.; Porter, M. D.; Neill, J. D.; Ridpath, J. F. *Anal. Chem.* **2005**, *77*, 6147–6154.
- (121) Yakes, B. J.; Lipert, R. J.; Bannantine, J. P.; Porter, M. D. *Clin. Vaccine Immunol.* **2008**, *15*, 227–234.
- (122) Wang, G.; Park, H.-Y.; Lipert, R. J.; Porter, M. D. *Anal. Chem.* **2009**, *81*, 9643–9650.
- (123) Cui, Y.; Ren, B.; Yao, J.; Gu, R.; Tian, Z. *J. Raman Spectrosc.* **2007**, *38*, 896–902.
- (124) Han, X. X.; Cai, L. J.; Guo, J.; Wang, C. X.; Ruan, W. D.; Han, W. Y.; Xu, W. Q.; Zhao, B.; Ozaki, Y. *Anal. Chem.* **2008**, *80*, 3020–3024.
- (125) Hwang, H.; Chon, H.; Choo, J.; Park, J. *Anal. Chem.* **2010**, *80*, 7603–7610.
- (126) Rohr, T. E.; Cotton, T.; Fan, N.; Tarcha, P. J. *Anal. Biochem.* **1989**, *182*, 388–398.
- (127) Porter, M.; Lipert, R.; Siperko, L.; Wang, G.; Narayanan, R. *Chem. Soc. Rev.* **2008**, *37*, 1001–1011.
- (128) Xu, S.; Ji, X.; Xu, W.; Li, X.; Wang, L.; Bai, Y.; Zhao, B.; Ozaki, Y. *Analyst* **2004**, *129*, 63–68.
- (129) Donaldson, K.; Kramer, M.; Lim, D. *Biosens. Bioelectron.* **2004**, 322–327.
- (130) Ilic, B.; Yang, Y.; Craighead, H. *Appl. Phys. Lett.* **2004**, 2604–2606.
- (131) *Principles of Bacterial Detection: Biosensors, Recognition Receptors, and Microsystems*; Springer Science, 2008;
- (132) Ruan, C.; Wang, H.; Li, Y. *Trans. of ASAE* **2002**, 249–255.
- (133) Che, Y.; Li, Y.; Slavik, M.; Paul, D. *J. Food Prot.* **2000**, 1043–1048.
- (134) Cao, Y. C.; Jin, R. C.; Nam, J. M.; Thaxton, C. S.; Mirkin, C. A. *J. Am. Chem. Soc.* **2003**, *125*, 14676–14677.
- (135) Han, X.; Xie, Y.; Zhao, B.; Ozaki, Y. *Anal. Chem.* **2010**, *82*, 4325–4328.
- (136) Chen, Z.; Tabakman, S. M.; Goodwin, A. P.; Kattah, M. G.; Daranciang, D.; Wang, X. R.; Zhang, G. Y.; Li, X. L.; Liu, Z.; Utz, P. J.; Jiang, K. L.; Fan, S. S.; Dai, H. J. *Nat. Biotechnol.* **2008**, *26*, 1285–1292.
- (137) Stuart, D. A.; Yuen, J. M.; Lyandres, N. S. O.; Yonzon, C. R.; Glucksberg, M. R.; Walsh, J. T.; Van Duyne, R. P. *Anal. Chem.* **2006**, *78*, 7211–7215.
- (138) Kneipp, J.; Kneipp, H.; McLaughlin, M.; Brown, D.; Kneipp, K. *Nano Lett.* **2006**, *6*, 2225–2231.
- (139) Kneipp, J.; Kneipp, H.; Wittig, B.; Kneipp, K. *Nano Lett.* **2007**, *7*, 2819–2823.
- (140) Kneipp, J.; Kneipp, H.; Wittig, B.; Kneipp, K. *J. Phys. Chem. C* **2010**, *114*, 7421–7426.

- (141) Pallaoro, A.; Braun, G. B.; Reich, N. O.; Moskovits, M. *Small* **2010**, *6*, 618–622.
- (142) Scaffidi, J. P.; Gregas, M. K.; Seewaldt, V.; Vo-Dinh, T. *Anal. Bioanal. Chem.* **2009**, *393*, 1135–1141.
- (143) Zavaleta, C. L.; Smith, B. R.; Walton, I.; Doering, W.; Davis, G.; Shojaei, B.; Natan, M. J.; Gambhir, S. S. *Proc. Natl. Acad. Sci. U.S.A.* **2009**, *106*, 13511–13516.
- (144) Lee, S.; Kim, S.; Choo, J.; Shin, S. Y.; Lee, Y. H.; Choi, H. Y.; Ha, S. H.; Kang, K. H.; Oh, C. H. *Anal. Chem.* **2007**, *79*, 916–922.
- (145) Stone, N.; Faulds, K.; Graham, D.; Matousek, P. *Anal. Chem.* **2010**, *82*, 3969–3973.
- (146) Im, H.; Bantz, K. C.; Lindquist, N. C.; Haynes, C. L.; Oh, S.-H. *Nano Lett.* **2010**, *10*, 2231–2236.
- (147) Hegner, M.; Wagner, P.; Semenza, G. *Surf. Sci.* **1993**, *291*, 39–46.
- (148) Nagpal, P.; Lindquist, N. C.; Oh, S. H.; Norris, D. J. *Science* **2009**, *325*, 594–597.
- (149) Lindquist, N.; Nagpal, P.; Lesuffleur, A.; Norris, D.; Oh, S. *Nano Lett.* **2010**, *10*, 1369–1373.
- (150) Yang, M.; Alvarez-Puebla, R.; Kim, H.-S.; Aldeanueva-Potel, P.; Liz-Marzan, L. M.; Kotov, N. A. *Nano Lett.* **2010**, *10*, 4013–4019.
- (151) Li, J. F.; Huang, Y. F.; Ding, Y.; Yang, Z. L.; Li, S. B.; Zhou, X. S.; Fan, F. R.; Zhang, W.; Zhou, Z. Y.; Wu, D. Y.; Ren, B.; Wang, Z. L.; Tian, Z. Q. *Nature* **2010**, *464*, 392–395.

## Chapter Two

- (1) Ritchie, R. *Phys. Rev.* **1957**, *106*, 874–881.
- (2) Haynes, C. L.; McFarland, A. D.; Duyne, R. P. V. *Anal. Chem.* **2005**, *77*, 338 A–346 A.
- (3) Jeanmaire, D. L.; Van Duyne, R. P. *J. Electroanal. Chem.* **1977**, *84*, 1–20.
- (4) Moskovits, M. *Rev. Mod. Phys.* **1985**, *57*, 783–826.
- (5) McCreery, R. L. *Raman Spectroscopy for Chemical Analysis*; 1st ed. Wiley-Interscience, 2000; p. 448.
- (6) Schatz, G.; Van Duyne, R. P. *Electromagnetic Mechanism of Surface-Enhanced Spectroscopy*; Chalmers, J. M.; Griffiths, P. R., Eds. Wiley: New York City, 2002; pp. 759–774.
- (7) Champion, A.; Kambhampati, P. *Chem. Soc. Rev.* **1998**, *27*, 241–250.
- (8) Haynes, C. L.; Van Duyne, R. P. *J. Phys. Chem. B* **2003**, *107*, 7426–7433.
- (9) Kneipp, K.; Wang, Y.; Kneipp, H.; Perelman, L. T.; Itzkan, I.; Dasari, R. R.; Feld, M. S. *Phys. Rev. Lett.* **1997**, *78*, 1667.
- (10) Nie, S.; Emory, S. R. *Science* **1997**, *275*, 1102.
- (11) Jensen, T. R.; Malinsky, M. D.; Haynes, C. L.; Van Duyne, R. P. *J. Phys. Chem. B* **2000**, *104*, 10549–10556.
- (12) Lee, S. H.; Bantz, K. C.; Lindquist, N. C.; Oh, S.-H.; Haynes, C. L. *Langmuir* **2009**, *25*, 13685–13693.
- (13) Im, H.; Bantz, K. C.; Lindquist, N. C.; Haynes, C. L.; Oh, S.-H. *Nano Lett.* **2010**, *10*, 2231–2236.

- (14) Genet, C.; Ebbesen, T. *Nature* **2007**, *445*, 39–46.
- (15) Lal, S.; Link, S.; Halas, N. J. *Nat. Photonics* **2007**, *1*, 641–648.
- (16) Link, S.; El-Sayed, M. *Annu. Rev. Phys. Chem.* **2003**, *54*, 331–366.
- (17) Nikoobakht, B.; El-Sayed, M. *J. Phys. Chem. A* **2003**, *107*, 3372–3378.
- (18) Jackson, J. B.; Halas, N. J. *Proc. Natl. Acad. Sci. U.S.A.* **2004**, *101*, 17930–17935.
- (19) Gunnarsson, L.; Bjerneld, E. J.; Xu, H.; Petronis, S.; Kasemo, B.; Kall, M. *Appl. Phys. Lett.* **2001**, *78*, 802–804.
- (20) Wang, H.; Levin, C.; Halas, N. J. *J. Am. Chem. Soc.* **2005**, *127*, 14992–14993.
- (21) Ward, D. R.; Grady, N. K.; Levin, C. S.; Halas, N. J.; Wu, Y. P.; Nordlander, P.; Natelson, D. *Nano Lett.* **2007**, *7*, 1396–1400.
- (22) Qin, L.; Zou, S.; Xue, C.; Atkinson, A.; Schatz, G. C.; Mirkin, C. A. *Proc. Nat. Acad. Sci. U.S.A* **2006**, *103*, 13300–13303.
- (23) Stockle, R. M.; Suh, Y. D.; Deckert, V.; Zenobi, R. *Chem. Phys. Lett.* **2000**, *318*, 131–136.
- (24) Neacsu, C. C.; Dreyer, J.; Behr, N.; Raschke, M. B. *Phys. Rev. B* **2006**, *73*, 193406.
- (25) Lindquist, N.; Nagpal, P.; Lesuffleur, A.; Norris, D.; Oh, S. *Nano Lett.* **2010**, *10*, 1369–1373.
- (26) Barnes, W.; Dereux, A.; Ebbesen, T. *Nature* **2003**, *424*, 824–830.
- (27) Atwater, H. *Sci. Am.* **2007**, *296*, 56–63.
- (28) Anker, J. N.; Hall, W. P.; Lyandres, O.; Shah, N. C.; Zhao, J.; Van Duyne, R. P. *Nat Mater* **2008**, *7*, 442–453.
- (29) Lee, P. C.; Meisel, D. *J. Phys. Chem.* **1982**, *86*, 3391–3395.
- (30) Kim, W.-T.; Safonov, V. P.; Drachev, V. P.; Podolskiy, V. A.; Shalaev, V. M.; Armstrong, R. L. *Top. Appl. Phys.* **2002**, *82*, 149–167.
- (31) Bi, H.; Cai, W.; Zhang, L.; Martin, D.; Trager, F. *Appl. Phys. Lett.* **2002**, *81*, 5222–5224.
- (32) Freeman, R. G.; Grabar, K. C.; Allison, K. J.; Bright, R. M.; Davis, J. A.; Guthrie, A. P.; Hommer, M. B.; Jackson, M. A.; Smith, P. C.; Walter, D. G.; Natan, M. J. *Science* **1995**, *267*, 1629–1632.
- (33) Baker, B. E.; Kline, N. J.; Treado, P. J.; Natan, M. J. *J. Am. Chem. Soc.* **1996**, *118*, 8721–8722.
- (34) Dick, L. A.; McFarland, A. D.; Haynes, C. L.; Van Duyne, R. P. *J. Phys. Chem. B* **2002**, *106*, 853–860.
- (35) Stropp, J.; Trachta, G.; Brehm, G.; Schneider, S. *J. Raman Spectrosc.* **2003**, *34*, 26–32.
- (36) Stuart, D. A.; Yonzon, C. R.; Zhang, X. Y.; Lyandres, O.; Shah, N. C.; Glucksberg, M. R.; Walsh, J. T.; Van Duyne, R. P. *Anal. Chem.* **2005**, *77*, 4013–4019.
- (37) Zhang, X. Y.; Zhao, J.; Whitney, A. V.; Elam, J. W.; Van Duyne, R. P. *J. Am. Chem. Soc.* **2006**, *128*, 10304–10309.
- (38) Hulteen, J. C.; Young, M. A.; Van Duyne, R. P. *Langmuir* **2006**, *22*, 10354–10364.
- (39) Whitney, A. V.; Casadio, F.; Van Duyne, R. P. *Appl. Spectrosc.* **2007**, *61*, 994–1000.
- (40) Whelan, C. M.; Smyth, M. R.; Barnes, C. J. *Langmuir* **1999**, *15*, 116–126.
- (41) Wan, L. J.; Terashima, M.; Noda, H.; Osawa, M. *J. Phys. Chem. B* **2000**, *104*, 3563–3569.

- (42) Le Ru, E. C.; Blackie, E.; Meyer, M.; Etchegoin, P. G. *J. Phys. Chem. C* **2007**, *111*, 13794–13803.
- (43) Park, H. K.; Yoon, J. K.; Kim, K. *Langmuir* **2006**, *22*, 1626–1629.
- (44) Liu, W. H.; Yu, T. L.; Lin, H. L. *Polymer* **2007**, *48*, 4152–4165.
- (45) *CRC Handbook of Chemistry and Physics*; Lide, D. R., Ed. 77th ed. CRC Press, 2000.
- (46) Ma, F.; Lennox, R. B. *Langmuir* **2000**, *16*, 6188–6190.
- (47) Stranick, S. J.; Parikh, A. N.; Tao, Y. T.; Allara, D. L.; Weiss, P. S. *J. Phys. Chem.* **1994**, *98*, 7636–7646.
- (48) Ebbesen, T. W.; Lezec, H. J.; Ghaemi, H. F.; Thio, T.; Wolff, P. A. *Nature* **1998**, *391*, 667.
- (49) Gao, H.; Henzie, J.; Odom, T. W. *Nano Lett.* **2006**, *6*, 2104–2108.
- (50) Liu, H.; Lalanne, P. *Nature* **2008**, *452*, 728–731.
- (51) Altewischer, E.; Genet, C.; van Exter, M. P.; Woerdman, J. P.; Alkemade, P. F. A.; van Zuuk, A.; van der Drift, E. W. J. M. *Opt. Lett.* **2005**, *30*, 90–92.
- (52) Brian, B.; Sepulveda, B.; Alaverdyan, Y.; Lechuga, L. M.; Kaell, M. *Opt. Express* **2009**, *17*, 2015–2023.
- (53) Kwak, E.-S.; Henzie, J.; Chang, S.-H.; Gray, S. K.; Schatz, G. C.; Odom, T. W. *Nano Lett.* **2005**, *5*, 1963–1967.
- (54) Stewart, M. E.; Mack, N. H.; Malyarchuk, V.; Soares, J. A. N. T.; Lee, T.-W.; Gray, S. K.; Nuzzo, R. G.; Rogers, J. A. *Proc. Nat. Acad. Sci. U.S.A* **2006**, *103*, 17143–17148.
- (55) Chen, J.; Shi, J.; Decanini, D.; Cambil, E.; Chen, Y.; Haghiri-Gosnet, A. *Microelectron. Eng.* **2009**, *86*, 632–635.
- (56) Deckman, H. W.; Dunsmuir, J. H. *Appl. Phys. Lett.* **1982**, *41*, 377–379.
- (57) Haynes, C.; Van Duyne, R. *J. Phys. Chem. B* **2001**, *105*, 5599–5611.
- (58) Masuda, H.; Fukuda, K. *Science* **1995**, *268*, 1466–1468.
- (59) Jiang, P.; McFarland, M. J. *J. Am. Chem. Soc.* **2005**, *127*, 3710–3711.
- (60) Peng, X.; Kamiya, I. *Nanotechnology* **2008**, *19*, 315303.
- (61) Wu, W.; Dey, D.; Memis, O. G.; Katsnelson, A.; Mohseni, H. *Proc. SPIE Int. Soc. Opt. Eng.* **2008**, *7039*, 70390P/1–70390P/8.
- (62) Wu, L. Y.; Ross, B. M.; Lee, L. P. *Nano Lett.* **2009**, *9*, 1956–1961.
- (63) Hicks, E.; Lyandres, O.; Hall, W.; Zou, S.; Glucksberg, M.; Van Duyne, R. J. *J. Phys. Chem. C* **2007**, *111*, 4116–4124.
- (64) Huang, W.-H.; Sun, C.-H.; Min, W.-L.; Jiang, P.; Jiang, B. *J. Phys. Chem. C* **2008**, *112*, 17586–17591.
- (65) Live, L.; Masson, J. *J. Phys. Chem. C* **2009**, *113*, 10052–10060.
- (66) Ctistis, G.; Papaioannou, E.; Patoka, P.; Gutek, J.; Fumagalli, P.; Giersig, M. *Nano Lett.* **2009**, *9*, 1–6.
- (67) Lou, Y.; Westcott, N.; McGlade, J.; Muth, J.; Yousaf, M. *Mater. Res. Soc. Symp. Proc.* **2009**, 1133.
- (68) Lee, K.-L.; Wang, W.-S.; Wei, P.-K. *Plasmonics* **2008**, *3*, 119–125.
- (69) Parsons, J.; Hendry, E.; Burrows, C. P.; Auguie, B.; Sambles, J. R.; Barnes, W. L. *Phys. Rev. B: Condens. Matter* **2009**, *79*, 073412/1–073412/4.
- (70) Kim, Y.-C.; Do, Y. R. *Opt. Express* **2005**, *13*, 1598–1603.
- (71) Kim, J. H.; Moyer, P. J. *Appl. Phys. Lett.* **2006**, *89*, 121106/1–121106/3.
- (72) Brolo, A. G.; Kwok, S. C.; Cooper, M. D.; Moffitt, M. G.; Wang, C. W.; Gordon, R.; Riordon, J.; Kavanagh, K. L. *J. Phys. Chem. B* **2006**, *110*, 8307–8313.
- (73) Brolo, A. G.; Arctander, E.; Gordon, R.; Leathem, B.; Kavanagh, K. L. *Nano Lett.* **2004**, *4*, 2015–2018.

- (74) Stark, P. R. H.; Halleck, A. E.; Larson, D. N. *Methods* **2005**, *37*, 37–47.
- (75) Tetz, K. A.; Pang, L.; Fainman, Y. *Opt. Lett.* **2006**, *31*, 1528–1530.
- (76) Lesuffleur, A.; Im, H.; Lindquist, N. C.; Oh, S. H. *Appl. Phys. Lett.* **2007**, *90*, 3.
- (77) Yang, J.-C.; Ji, J.; Hogle, J. M.; Larson, D. N. *Nano Lett.* **2008**, *8*, 2718–2724.
- (78) Lesuffleur, A.; Im, H.; Lindquist, N. C.; Lim, K. S.; Oh, S.-H. *Opt. Express* **2008**, *16*, 219–224.
- (79) Im, H.; Lesuffleur, A.; Lindquist, N. C.; Oh, S.-H. *Anal. Chem.* **2009**, *81*, 2854–2859.
- (80) Lindquist, N. C.; Lesuffleur, A.; Im, H.; Oh, S.-H. *Lab Chip* **2009**, *9*, 382–387.
- (81) Eftekhari, F.; Escobedo, C.; Ferreira, J.; Duan, X.; Giroto, E. M.; Brolo, A. G.; Gordon, R.; Sinton, D. *Anal. Chem.* **2009**, *81*, 4308–4311.
- (82) Ferreira, J.; Santos, M. J. L.; Rahman, M. M.; Brolo, A. G.; Gordon, R.; Sinton, D.; Giroto, E. M. *J. Am. Chem. Soc.* **2009**, *131*, 436–437.
- (83) Anema, J. R.; Brolo, A. G.; Marthandam, P.; Gordon, R. *J. Phys. Chem. C* **2008**, *112*, 17051–17055.
- (84) Yu, Q.; Guan, P.; Qin, D.; Golden, G.; Wallace, P. M. *Nano Lett.* **2008**, *8*, 1923–1928.
- (85) Reilly, T. H.; Chang, S. H.; Corbman, J. D.; Schatz, G. C.; Rowlen, K. L. *J. Phys. Chem. C* **2007**, *111*, 1689–1694.
- (86) Xia, Y. N.; Whitesides, G. M. *Annu. Rev. Mater. Sci.* **1998**, *28*, 153–184.
- (87) Jackson, J.; Halas, N. *J. Phys. Chem. B* **2001**, *105*, 2743–2746.
- (88) Bantz, K. C.; Haynes, C. L. *Langmuir* **2008**, *24*, 5862–5867.
- (89) Denkov, N. D.; Velev, O. D.; Kralchevsky, P. A.; Ivanov, I. B.; Yoshimura, H.; Nagayama, K. *Nature* **1993**, *361*, 26–26.
- (90) Dimitrov, A. S.; Nagayama, K. *Langmuir* **1996**, *12*, 1303–1311.
- (91) Fulda, K. U.; Tieke, B. *Adv. Mater.* **1994**, *6*, 288–290.
- (92) Wang, D. Y.; Mohwald, H. *Adv. Mater.* **2004**, *16*, 244.
- (93) Kosiorek, A.; Kandulski, W.; Chudzinski, P.; Kempa, K.; Giersig, M. *Nano Lett.* **2004**, *4*, 1359–1363.
- (94) Lu, Y.; Liu, G. L.; Kim, J.; Mejia, Y. X.; Lee, L. P. *Nano Lett.* **2005**, *5*, 119–124.
- (95) Choi, D. G.; Jang, S. G.; Kim, S.; Lee, E.; Han, C. S.; Yang, S. M. *Adv. Funct. Mater.* **2006**, *16*, 33–40.
- (96) Thio, T.; Ghaemi, H. F.; Lezec, H. J.; Wolff, P. A.; Ebbesen, T. W. *J. Opt. Soc. Am. B-Opt. Phys.* **1999**, *16*, 1743–1748.
- (97) Green, M.; Liu, F. *J. Phys. Chem. B* **2003**, *107*, 13015–13021.
- (98) Jiang, J.; Bosnick, K.; Maillard, M.; Brus, L. *J. Phys. Chem. B* **2003**, *107*, 9964–9972.
- (99) Gopinath, A.; Boriskina, S. V.; Premasiri, W. R.; Ziegler, L.; Reinhard, B. M.; Dal Negro, L. *Nano Lett.* **2009**, *9*, 3922–3929.
- (100) Kim, S.; Jin, J.; Kim, Y.-J.; Park, I.-Y.; Kim, Y.; Kim, S.-W. *Nature* **2008**, *453*, 757–760.
- (101) Miyazaki, H.; Kurokawa, Y. *Phys. Rev. Lett.* **2006**, *96*, –.
- (102) Kuttge, M.; Garcia de Abajo, F. J.; Polman, A. *Nano Lett.* **2010**, *10*, 1537–1541.
- (103) Lin, J. Y.; Hasan, W.; Yang, J.-C.; Odom, T. W. *Journal of Physical Chemistry C* **2010**, *114*, 7432–7435.
- (104) Im, H.; Lindquist, N. C.; Lesuffleur, A.; Oh, S. H. *Acs Nano* **2010**, *4*, 947–954.
- (105) Bozhevolnyi, S.; Volkov, V.; Devaux, E.; Laluet, J.; Ebbesen, T. *Nature* **2006**, *440*, 508–511.

- (106) Fang, Y.; Seong, N.; Dlott, D. *Science* **2008**, *321*, 388–392.
- (107) Hao, E.; Schatz, G. *J. Chem. Phys.* **2004**, *120*, 357–366.
- (108) Nagpal, P.; Lindquist, N. C.; Oh, S. H.; Norris, D. J. *Science* **2009**, *325*, 594–597.
- (109) Im, H.; Huang, X.-J.; Gu, B.; Choi, Y.-K. *Nature Nanotechnology* **2007**, *2*, 430–434.
- (110) Song, H.; Kim, Y.; Jang, Y. H.; Jeong, H.; Reed, M. A.; Lee, T. *Nature* **2009**, *462*, 1039–1043.
- (111) Bantz, K. C.; Meyer, A. F.; Wittenberg, N. J.; Im, H.; Kurtulus, O.; Lee, S. H.; Lindquist, N. C.; Oh, S.-H.; Haynes, C. L. *Phys. Chem. Chem. Phys.* **2011**, *13*, 11551–11567.
- (112) Halvorson, R. A.; Vikesland, P. J. *Environ. Sci. Technol.* **2010**, *44*, 7749–7755.
- (113) Golightly, R. S.; Doering, W. E.; Natan, M. J. *Acs Nano* **2009**, *3*, 2859–2869.

### Chapter Three

- (1) Jeanmaire, D. L.; Van Duyne, R. P. *J. Electroanal. Chem.* **1977**, *84*, 1–20.
- (2) Albrecht, M. G.; Creighton, J. A. *J. Am. Chem. Soc.* **1977**, *99*, 5215–5217.
- (3) Jennings, G.; Laibinis, P. E. *Colloids and Surfaces A* **1998**, *116*, 105–114.
- (4) Mrksich, M. *Acta biomaterialia* **2009**, *5*, 832–842.
- (5) Gooding, J.; Mearns, F.; Yang, W. *Electroanalysis* **2003**, *12*, 81–96.
- (6) Yonzon, C. R.; Haynes, C. L.; Zhang, X. Y.; Walsh, J. T.; Van Duyne, R. P. *Anal. Chem.* **2004**, *76*, 78–85.
- (7) Shah, N. C.; Lyandres, O.; Walsh, J. T.; Glucksberg, M. R.; Van Duyne, R. P. *Anal. Chem.* **2007**, *79*, 6927–6932.
- (8) Levin, C. S.; Kundu, J.; Janesko, B. G.; Scuseria, G. E.; Raphael, R. M.; Halas, N. J. *J. Phys. Chem. B* **2008**, *112*, 14168–14175.
- (9) Bantz, K. C.; Haynes, C. L. *Vib. Spectrosc.* **2009**, *50*, 29–35.
- (10) Jones, C. L.; Bantz, K. C.; Haynes, C. L. *Anal. Bioanal. Chem.* **2009**, *394*, 303–311.
- (11) Bain, C. D.; Troughton, E. B.; Tao, Y. T.; Evall, J.; Whitesides, G. M.; Nuzzo, R. G. *J. Am. Chem. Soc.* **1989**, *111*, 321–335.
- (12) Dhirani, A.; Hines, M. A.; Fisher, A. J.; Ismail, O.; Guyot-Sionnest, P. *Langmuir* **1995**, *11*, 2609–2614.
- (13) Noh, J.; Kato, H.; Kawai, M.; Hara, M. *J. Phys. Chem. B* **2006**, *110*, 2793–2797.
- (14) Clark, B. K.; Gregory, B. W.; Avila, A.; Cotton, T. M.; Standard, J. M. *J. Phys. Chem. B* **1999**, *103*, 8201–8204.
- (15) Kennedy, B. J.; Spaeth, S.; Dickey, M.; Carron, K. T. *J. Phys. Chem. B* **1999**, *103*, 3640–3646.
- (16) Bryant, M. A.; Pemberton, J. E. *J. Am. Chem. Soc.* **1991**, *113*, 8284–8293.
- (17) Lin, W.-C.; Liao, L.-S.; Chen, Y.-H.; Chang, H.-C.; Tsai, D. P.; Chiang, H.-P. *Plasmonics* **2011**, *6*, 201–206.
- (18) Oh, Y.-J.; Park, S.-G.; Kang, M.-H.; Choi, J.-H.; Nam, Y.; Jeong, K.-H. *Small* **2011**, *7*, 184–188.
- (19) Li, Q.; Kuo, C. W.; Yang, Z.; Chen, P.; Chou, K. C. *Phys. Chem. Chem. Phys.* **2009**, *11*, 3436–3442.

- (20) Stropp, J.; Trachta, G.; Brehm, G.; Schneider, S. *J. Raman Spectrosc.* **2003**, *34*, 26–32.
- (21) Casadio, F.; Leona, M.; Lombardi, J. R.; Van Duyne, R. *Acc. Chem. Res.* **2010**, *43*, 782–791.
- (22) Bantz, K. C.; Haynes, C. L. *Langmuir* **2008**, *24*, 5862–5867.
- (23) Schreiber, F.; Eberhardt, A.; Leung, T.; Schwartz, P.; Wetterer, S.; Lavrich, D.; Berman, L.; Fenter, P.; Eisenberger, P.; Scoles, G. *Phys. Rev. B* **1998**, *57*, 12476–12481.
- (24) Ma, F.; Lennox, R. B. *Langmuir* **2000**, *16*, 6188–6190.
- (25) Boubour, E.; Lennox, R. B. *Langmuir* **2000**, *16*, 4222–4228.
- (26) Li, W.; Virtanen, J. A.; Penner, R. M. *J. Phys. Chem.* **1994**, *98*, 11751–11755.
- (27) Walczak, M. M.; Chung, C.; Stole, S. M.; Widrig, C. A.; Porter, M. D. *J. Am. Chem. Soc.* **1991**, *113*, 2370–2378.
- (28) Sai, T. P.; Raychaudhuri, A. K. *J. Phys. D Appl. Phys.* **2007**, *40*, 3182–3189.
- (29) Zhao, J.; Jensen, L.; Sung, J.; Zou, S.; Schatz, G. C.; Van Duyne, R. P. *J. Am. Chem. Soc.* **2007**, *129*, 7647–7656.
- (30) Dieringer, J. A.; McFarland, A. D.; Shah, N. C.; Stuart, D. A.; Whitney, A. V.; Yonzon, C. R.; Young, M. A.; Zhang, X.; Van Duyne, R. P. *Faraday Discuss.* **2006**, *132*, 9–26.
- (31) Malinsky, M. D.; Kelly, K. L.; Schatz, G. C.; Van Duyne, R. P. *J. Am. Chem. Soc.* **2001**, *123*, 1471–1482.
- (32) Jung, L. S.; Campbell, C. T.; Chinowsky, T. M.; Mar, M. N.; Yee, S. S. *Langmuir* **1998**, *14*, 5636–5648.
- (33) Rycenga, M.; McLellan, J. M.; Xia, Y. *Chem. Phys. Lett.* **2008**, *463*, 166–171.
- (34) Brewer, N.; Foster, T.; Leggett, G.; Alexander, M.; McAlpine, E. *J. Phys. Chem. B* **2004**, *108*, 4723–4728.

## Chapter Four

- (1) McCreery, R. L. *Raman Spectroscopy for Chemical Analysis*; 1st ed. Wiley-Interscience, 2000; p. 448.
- (2) Barhoumi, A.; Halas, N. J. *J. Am. Chem. Soc.* **2010**, *132*, 12792–12793.
- (3) Hwang, H.; Chon, H.; Choo, J.; Park, J. *Anal. Chem.* **2010**, *80*, 7603–7610.
- (4) Drachev, V. P.; Shalaev, V. M. *Top. Appl. Phys.* **2006**, *103*, 351–366.
- (5) Zhang, X.; Young, M. A.; Lyandres, O.; Van Duyne, R. P. *J. Am. Chem. Soc.* **2005**, *127*, 4484–4489.
- (6) Chu, H.; Huang, Y.; Zhao, Y. *Appl. Spectrosc.* **2008**, *62*, 922–931.
- (7) Shafer-Peltier, K.; Haynes, C.; Glucksberg, M.; Van Duyne, R. *J. Am. Chem. Soc.* **2003**, *125*, 588–593.
- (8) Shah, N. C.; Lyandres, O.; Walsh, J. T.; Glucksberg, M. R.; Van Duyne, R. P. *Anal. Chem.* **2007**, *79*, 6927–6932.
- (9) Bantz, K. C.; Haynes, C. L. *Langmuir* **2008**, *24*, 5862–5867.
- (10) Yonzon, C. R.; Haynes, C. L.; Zhang, X. Y.; Walsh, J. T.; Van Duyne, R. P. *Anal. Chem.* **2004**, *76*, 78–85.
- (11) Kennedy, B. J.; Spaeth, S.; Dickey, M.; Carron, K. T. *J. Phys. Chem. B* **1999**, *103*, 3640–3646.

- (12) Carron, K.; Peitersen, L.; Lewis, M. *Environ. Sci. Technol.* **1992**, *26*, 1950–1954.
- (13) Mullen, K.; Carron, K. *Anal. Chem.* **1994**, *66*, 478–483.
- (14) Van Duyne, R. P.; Hulteen, J. C.; Treichel, D. A. *J. Chem. Phys.* **1993**, *99*, 2101–2115.
- (15) Environmental Protection, A. Polychlorinated Biphenyls (PCBs). *epa.gov*.
- (16) Hornbuckle, K. C.; Carlson, D. L.; Swackhamer, D. L.; Baker, J. E.; Eisenreich, S. J. *Polychlorinated Biphenyls in the Great Lakes*; Hites, R. A., Ed. Springer-Verlag: Berlin, 2005; Vol. 5.
- (17) Kay, D. P.; Blankenship, A. L.; Coady, K. K.; Neigh, A. M.; Zwiernik, M. J.; Millsap, S. D.; Strause, K.; Park, C.; Bradley, P.; Newsted, J. L.; Jones, P. D.; Giesy, J. P. *Environ. Sci. Technol.* **2005**, *39*, 5964–5974.
- (18) Streets, S. S.; Henderson, S. A.; Stoner, A. D.; Carlson, D. L.; Simcik, M. F.; Swackhamer, D. L. *Environ. Sci. Technol.* **2006**, *40*, 7263–7269.
- (19) Mullin, M. D.; Pochini, C. M.; McCrindle, S.; Romkes, M.; Safe, S. H.; Safe, L. M. *Environ. Sci. Technol.* **1984**, *18*, 468–476.
- (20) USEPA Method 1668, Revision A; 2007.
- (21) USEPA Method 4020; 2003.
- (22) Aldstadt, J.; St Germain, R.; Grundl, T.; Schweitzer, R. *An In Situ laser-Induced Fluorescence System for Polycyclic Aromatic Hydrocarbong-Contaminated Sediments*; Chicago, IL, 2002.
- (23) Schwarzenbach, R. P.; Gschwend, P. M.; Imboden, D. M. *Environmental Organic Chemistry*; John Wiley & Sons, Inc.: Hoboken, NJ, USA, 2005;
- (24) USEPA Consumer Factsheet: Benzo(a)pyrene; 2006.
- (25) Hawthorne, S. B.; St Germain, R. W.; Azzolina, N. A. *Environ. Sci. Technol.* **2008**, *42*, 8021–8026.
- (26) USEPA Method 8272; 2007.
- (27) USEPA Method 610; 1997.
- (28) USEPA Method 610; 1997.
- (29) USEPA Method 550; 1990.
- (30) Waters, L. C.; Palausky, A.; Counts, R. W.; Jenkins, R. A. *Field Anal. Chem. Technol.* **1997**, *1*, 227–238.
- (31) Troisi, G. M.; Borjesson, L. *Environ. Sci. Technol.* **2005**, *39*, 3748–3755.
- (32) Whelan, C. M.; Smyth, M. R.; Barnes, C. J. *Langmuir* **1999**, *15*, 116–126.
- (33) Wan, L. J.; Terashima, M.; Noda, H.; Osawa, M. *J. Phys. Chem. B* **2000**, *104*, 3563–3569.
- (34) Opperhuizen, A.; Gobas, F.; Vandersteen, J. M. D.; Hutzinger, O. *Environ. Sci. Technol.* **1988**, *22*, 638–646.
- (35) Bantz, K. C.; Haynes, C. L. *Vib. Spectrosc.* **2009**, *50*, 29–35.
- (36) Alves, C. A.; Porter, M. D. *Langmuir* **1993**, *9*, 3507–3512.
- (37) Haynes, C. L.; Van Duyne, R. P. *J. Phys. Chem. B* **2003**, *107*, 7426–7433.
- (38) Socrates, G. *Infrared and Raman Characteristic Group Frequencies: Tables and Charts*; 13rd ed. Wiley: New York, 2001.
- (39) Bryant, M. A.; Pemberton, J. E. *J. Am. Chem. Soc.* **1991**, *113*, 8284–8293.
- (40) Donovan, S. F.; Pescatore, M. C. *J. Chromatogr. A* **2002**, *952*, 47–61.
- (41) Paschke, A.; Popp, P.; Schuurmann, G. *Fresenius J. Anal. Chem.* **1999**, *363*, 426–428.
- (42) Wang, X. H.; Valverde-Aguilar, G.; Weaver, M. N.; Nelsen, S. F.; Zink, J. I. *J. Phys. Chem. A* **2007**, *111*, 5441–5447.
- (43) Shinohara, H.; Yamakita, Y.; Ohno, K. *J. Mol. Struct.* **1998**, *442*, 221–234.

- (44) Neugebauer, J.; Baerends, E. J.; Efremov, E. V.; Ariese, F.; Gooijer, C. *J. Phys. Chem. A* **2005**, *109*, 2100–2106.
- (45) Dick, L. A.; McFarland, A. D.; Haynes, C. L.; Van Duyne, R. P. *J. Phys. Chem. B* **2002**, *106*, 853–860.
- (46) Felidj, N.; Truong, S. L.; Aubard, J.; Levi, G.; Krenn, J. R.; Hohenau, A.; Leitner, A.; Aussenegg, F. R. *J. Chem. Phys.* **2004**, *120*, 7141–7146.
- (47) Gunnarsson, L.; Bjerneld, E. J.; Xu, H.; Petronis, S.; Kasemo, B.; Kall, M. *Appl. Phys. Lett.* **2001**, *78*, 802–804.
- (48) Williamson, T. L.; Guo, X. Y.; Zukoski, A.; Sood, A.; Diaz, D. J.; Bohn, P. W. *J. Phys. Chem. B* **2005**, *109*, 20186–20191.
- (49) Ma, F.; Lennox, R. B. *Langmuir* **2000**, *16*, 6188–6190.
- (50) Osticioli, I.; Zoppi, A.; Castellucci, E. M. *Appl. Spectrosc.* **2007**, *61*, 839–844.
- (51) Chin, Y. P.; Aiken, G.; Oloughlin, E. *Environ. Sci. Technol.* **1994**, *28*, 1853–1858.
- (52) Walczak, M. M.; Chung, C.; Stole, S. M.; Widrig, C. A.; Porter, M. D. *J. Am. Chem. Soc.* **1991**, *113*, 2370–2378.
- (53) Rycenga, M.; McLellan, J. M.; Xia, Y. *Chem. Phys. Lett.* **2008**, *463*, 166–171.
- (54) Corsolini, S.; Borghesi, N.; Schiamone, A.; Focardi, S. *Environ. Sci. Pollut. Res.* **2007**, *14*, 421–429.

## Chapter Five

- (1) Raman, C. V.; Krishnan, K. S. *Nature* **1928**, *121*, 501–504.
- (2) McCreery, R. L. *Raman Spectroscopy for Chemical Analysis*; 1st ed. Wiley-Interscience, 2000; p. 448.
- (3) Jeanmaire, D. L.; Van Duyne, R. P. *J. Electroanal. Chem.* **1977**, *84*, 1–20.
- (4) Haynes, C. L.; McFarland, A. D.; Duyne, R. P. V. *Anal. Chem.* **2005**, *77*, 338 A–346 A.
- (5) Kneipp, K.; Wang, Y.; Kneipp, H.; Perelman, L. T.; Itzkan, I.; Dasari, R. R.; Feld, M. S. *Phys. Rev. Lett.* **1997**, *78*, 1667.
- (6) Nie, S.; Emory, S. R. *Science* **1997**, *275*, 1102.
- (7) Bantz, K. C.; Haynes, C. L. *Vib. Spectrosc.* **2009**, *50*, 29–35.
- (8) Jones, C. L.; Bantz, K. C.; Haynes, C. L. *Anal. Bioanal. Chem.* **2009**, *394*, 303–311.
- (9) Hannun, Y.; Obeid, L. *Nat. Rev. Mol. Cell Biol.* **2008**, *9*, 139–150.
- (10) Gough, N. *Sci STKE* **2006**, *2006*, eg2.
- (11) Im, D. *Prostaglandins Other Lipid Mediat* **2009**, *89*, 53–56.
- (12) Heib, V.; Becker, M.; Taub, C.; Stassen, M. *Br. J. Haematol.* **2008**, *142*, 683–694.
- (13) Bloemen, K.; Verstraelen, S.; Van Den Heuvel, R.; Witters, H.; Nelissen, I.; Schoeters, G. *Immunol. Lett.* **2007**, *113*, 6–18.
- (14) Okayama, Y.; Hagaman, D. D.; Metcalfe, D. D. *J. Immunol.* **2001**, *166*, 4705–4712.
- (15) Ogawa, Y.; Grant, J. A. *Immunology and Allergy Clinics of North America* **2007**, *27*, 249–260.
- (16) Nilsson, G.; Metcalfe, D. D.; Taub, D. D. *Immunology* **2000**, *99*, 314–319.
- (17) Stewart, J. *Anal. Biochem.* **1980**, *104*, 10–14.

- (18) Carrasco-Pancorbo, A.; Navas-Iglesias, N.; Cuadros-Rodriguez, L. *TrAC, Trends Anal. Chem.* **2009**, *28*, 263–278.
- (19) Christie, W. *Lipid Analysis: Isolation, Separation, Identification and Structural Analysis of Lipids*; Third. The Oily Press: Bridgewater, England, 2003.
- (20) Otieno, A.; Mwongela, S. *Analytica Chimica Acta* **2008**, *624*, 163–174.
- (21) Wenk, M. *Nat. Rev. Drug Discov.* **2005**, *4*, 594–610.
- (22) Ivanova, P.; Milne, S.; Myers, D.; Brown, H. *Curr Opin Chem Biol* **2009**.
- (23) Chamberlain, J. R.; Pemberton, J. E. *Langmuir* **1997**, *13*, 3074–3079.
- (24) Meuse, C.; Niaura, G.; Lewis, M. *Langmuir* **1998**.
- (25) Levin, C. S.; Kundu, J.; Janesko, B. G.; Scuseria, G. E.; Raphael, R. M.; Halas, N. J. *J. Phys. Chem. B* **2008**, *112*, 14168–14175.
- (26) Bryant, M. A.; Pemberton, J. E. *J. Am. Chem. Soc.* **1991**, *113*, 8284–8293.
- (27) Brown, K.; Peticolos, W.; Brown, E. *Biochem. Biophys. Res. Comm.* **1973**, *24*, 358–364.
- (28) Socrates, G. *Infrared and Raman Characteristic Group Frequencies: Tables and Charts*; Infrared and Raman Characteristic Group Frequencies: Tables and Charts; 3rd ed. Wiley: New York, 2001.
- (29) Kennedy, B. J.; Spaeth, S.; Dickey, M.; Carron, K. T. *J. Phys. Chem. B* **1999**, *103*, 3640–3646.
- (30) Snyder, F. *P Soc Exp Biol Med* **1989**, *190*, 125–135.
- (31) Ma, F.; Lennox, R. B. *Langmuir* **2000**, *16*, 6188–6190.
- (32) Im, H.; Bantz, K. C.; Lindquist, N. C.; Haynes, C. L.; Oh, S.-H. *Nano Lett.* **2010**, *10*, 2231–2236.

## Chapter Six

- (1) Bantz, K. C.; Meyer, A. F.; Wittenberg, N. J.; Im, H.; Kurtulus, O.; Lee, S. H.; Lindquist, N. C.; Oh, S.-H.; Haynes, C. L. *Phys. Chem. Chem. Phys.* **2011**, *13*, 11551–11567.
- (2) Golightly, R. S.; Doering, W. E.; Natan, M. J. *Acs Nano* **2009**, *3*, 2859–2869.
- (3) Halvorson, R. A.; Vikesland, P. J. *Environ. Sci. Technol.* **2010**, *44*, 7749–7755.
- (4) Ma, F.; Lennox, R. B. *Langmuir* **2000**, *16*, 6188–6190.

## Appendix

### Kyle Christine Bantz

---

University of Minnesota  
Department of Chemistry  
139 Smith Hall F-16  
207 Pleasant Street SE  
Minneapolis, MN 55455

Office Phone: 612-626-5282  
Home Phone: 414-916-5957  
Fax: 612-626-7541  
E-mail: bantz008@umn.edu

---

### Education

---

University of Minnesota, Twin Cities MN  
Department of Chemistry, PhD 2011  
GPA: 3.3/4.0  
Dissertation: "Development and Application of Partition Layer-Modified Surface-Enhanced Raman Scattering (SERS) Sensors for Complex Mixture Analysis"  
Committee Members: Christy Haynes (advisor), TBD

Department of Chemistry, M.S. 2008

Cornell College, Mt Vernon IA  
Chemistry and German, B.A. 2006  
GPA: 3.4/4.0

---

### Research Experience

---

University of Minnesota  
Department of Chemistry  
*Research Assistant* 2006-present  
• Advisor: Christy Haynes

Medical College of Wisconsin  
Department of Biophysics  
*Summer Research Assistant* June-August 2006  
• Under the direction of Dr. Candice Klug (PI) and Adam Buchaklian  
• Investigated the structure and transport mechanism of the protein MsbA

*Summer Program for Undergraduate Researchers Participant* 2004-2005  
• Under the direction of Dr. Candice Klug (PI) and Adam Buchaklian  
• Investigated the structure and transport mechanism of the protein MsbA

---

### Scientific Expertise

---

Surface-enhanced Raman spectroscopy	Atomic force microscopy
Nanoparticle synthesis	Nanosphere lithography
Localized surface plasmon resonance	Scanning electron microscopy

---

### Awards and Recognition

---

MN ACS Graduate Student Travel Grant	2011
ACS Division of Analytical Chemistry Summer Graduate Fellowship Sponsored by Eastman Chemical	2010
Graduate Women in Science Agnes Hansen Travel Award	2009
Society for Applied Spectroscopy Poster Session Award	2009
Coblentz Society Student Award	2009
Pfizer Graduate Travel Award in Analytical Chemistry	2008
Sons and Daughters of Brunswick Scholarship	2001 & 2003-2006
Cornell College's Academic and Community Enrichment Scholarship	2002-2006
Congress Bundestag Youth Exchange	2001-2002
<ul style="list-style-type: none"><li>• Awarded through the United States Congress and its German equivalent</li><li>• The exchange program conveys the importance of common values, mutual acceptance and lasting personal relationships to young Americans and Germans.</li><li>• One year in the city of Templin</li></ul>	

---

### Peer Reviewed Publication List (9)

---

Plasmon-enabled Study of Self-Assembled Alkanethiol Ordering on Roughened Ag Substrates, **Bantz, K.C.**, Nelson, H.D., and Haynes, C.L., *J. Phys. Chem. C*, Submitted.

SERS for Biosensing, **Bantz, K.C.**, Meyer, A.F. Im, H., Lee, S.H., Wittenberg, N.J., Lindquist, N., Haynes, C.L., Oh, S.-H., *PCCP*, 13, 11551-11567 (2011).

Vertically Oriented Sub-10 nm Plasmonic Nanogap Arrays, Im, H., **Bantz, K.C.**, Lindquist, N., Haynes, C.L., and Oh, S.-H., *Nano Lett.*, 10, 2231-2236 (2010).

Self-Assembled Plasmonic Nanohole Arrays. Lee, S.H., **Bantz, K.C.**, Lindquist, N., Oh S.-H., and Haynes, C.L., *Langmuir*, 23, 13685-13693 (2009)

---

## Peer Reviewed Publication List Cont.

---

Partition Layer-Modified Substrates for Reversible Surface-Enhanced Raman Scattering Detection of Polycyclic Aromatic Hydrocarbons. **Bantz, K.C.**, Jones, C.L., Haynes, C.L., *Anal. Bioanal. Chem.*, 1, 303-311 (2009).

Toxicity of Therapeutic Nanoparticles. Maurer-Jones, M.A., Love, S.A., **Bantz, K.C.**, Marquis, B.J., and Haynes, C.L., *Nanomedicine*, 4, 219-241 (2009).

Surface-Enhanced Raman Scattering Detection and Discrimination of Polychlorinated Biphenyls. **Bantz, K.C.** and Haynes, C.L., *Vib. Spec.*, 50, 29-35 (2009).

Surface-Enhanced Raman Spectroscopy and Confocal Imaging of Periodic Nanohole Arrays Surrounded by Plasmonic Bragg Mirrors. Lindquist, N.C., Im, H., **Bantz, K.C.**, Lesuffleur, A., Haynes, C.L., and Oh, S.-H., *MicroTAS Abstracts*, (2008).

Surface-Enhanced Raman Scattering Substrates Fabricated using Electroless Plating on Polymer-Templated Nanostructure. **Bantz, K.C.** and Haynes, C.L., *Langmuir*, 24, 5862-5867 (2008).

---

## Presentations

---

Contributed lecture, "Surface-Enhanced Raman Scattering (SERS) Monitoring of Crystallinity in Partition Layer-Modified Sensing Platforms", 241<sup>st</sup> ACS National Meeting, Anaheim, CA, March 2011. \*supported by MN ACS Travel Grant

Invited lecture, "Development of a Surface-Enhanced Raman Sensor for the Detection of Environmental Pollutants", Cornell College, Mt. Vernon, IA, January 2011.

Invited lecture, "Development and Application of Partition Layer-Modified Surface-Enhanced Raman Scattering Sensors for Complex Mixtures", Eastman Chemical Company, Kingsport, TN, October 2010.

Contributed lecture, "Vertically Oriented Nanogap Substrates for Surface-Enhanced Raman Scattering", FACSS 2010, Raleigh, NC, October 2010

Contributed poster, "Surface-Enhanced Raman Scattering Detection of a Bioactive Mediator" ICORS 2010, Boston, MA. August 2010.

Contributed lecture, "Surface-Enhanced Raman Scattering (SERS) Detection of Lipids", PittCon 2010, Orlando, FL. March 2010

---

## Presentations Cont.

---

Contributed poster, "Surface-Enhanced Raman Scattering Detection of Polycyclic Aromatic Hydrocarbons and Polychlorinated Biphenyls", FACSS 2009, Louisville, KY. October 2009 \*supported by SAS poster session award.

Contributed lecture, "Patterned Polymer-Templated Nanostructures for Surface-Enhanced Raman Scattering", ACS Colloid and Surface Science Conference 2009, New York, NY. June 2009 \*supported by Agnes Hansen Travel Grant

Contributed lecture, "Development of a Surface-Enhanced Raman Sensor for the Detection of Environmental Pollutants", University of Minnesota Department of Chemistry 3<sup>rd</sup> Year Symposium, Minneapolis, MN. June 2009

Contributed poster, "Development of a Surface-Enhanced Raman Sensor for the Detection of Environmental Pollutants", Minnesota Society of Applied Spectroscopy Poster Session, St. Paul, MN. May 2009

Contributed lecture, "Effects of Crystallinity in Partition Layer Sensors", PittCon, Chicago, IL. March 2009

Contributed poster, "Evaluation of Novel Surface-Enhanced Raman Spectroscopy (SERS) Substrates and Partition Layers for Trace Polychlorinated Biphenyl (PCB) Detection", PittCon, New Orleans, LA. March 2008 \*supported by Pfizer Travel Award

---

## Co-Authored Grant Application

---

"Surface-Enhanced Raman Scattering Detection of Secreted Lipids", National Science Foundation, 2009

---

## Teaching Experience

---

University of Minnesota

Department of Chemistry

CHEM 8152: Analytical Spectroscopy

Fall 2010

*Guest Lecturer*

- Acted as substitute lecturer for Dr. Christy Haynes for two lectures and helped write exam questions.

CHEM 2121: Process Analytical Chemistry

Spring 2010 & Spring 2011

*Guest Lecturer*

- Acted as substitute lecturer for Dr. Christy Haynes for two lectures and helped write exams.

CHEM 1011: Introductory Chemistry

Fall 2006, Fall 2007, Spring 2008

*Teaching Assistant*

- Led lab sections for two sections of 20+ students; graded lab reports; held tutor and office hours.

CHEM 4121: Process Analytical Chemistry Lab

Spring 2007

*Teaching Assistant*

- Led lab section of 20+ students; responsible for setting up UV-vis lab; graded lab reports.

---

### **Professional Development**

---

COACH Workshop: Making the Most of the Moment

March 2011

- Developed more effective communication and leadership skills

Minnesota Analytical Professor Meeting

April 2010 & 2011

- Learned about new teaching techniques and tools (e.g. POGIL and an online chromatography tool)
- Engaged in discussions on teaching/research at small and large undergraduate institutions.

MACTLAC Meeting

October 2010

- Engaged in discussions about teaching/research at small liberal arts colleges

University of Minnesota

Mentoring Program for Aspiring Chemistry Teachers

Spring 2010

*Teaching Mentee*

- Observed class lectures, led two lectures and helped write exams for CHEM 2121.

Preparing Future Faculty

Spring 2009

GRAD 8101: Teaching in Higher Education

- Explored implementing active learning strategies other educational theory.
- Learned course and curriculum development.

---

### **Professional Memberships**

---

American Chemical Society

Coblentz Society

Society for Applied Spectroscopy

---

## Professional and Community Service

---

### University of Minnesota

Student Seminar Committee Member 2008-present

- Organized seminar speakers' visits to campus

West 7<sup>th</sup> Community Center Outreach 2007-present

- Annually prepared and ran chemistry demonstrations and activities for ~50 kids

Centennial Elementary Chemistry Day 2009

- Prepared and ran chemistry demonstrations, activities and educational worksheet for ~15 kids

Women in Science and Engineering Cool Chem Day 2008

- Organized a chemistry related activity for middle school aged girls

Student Mentoring 2007-present

- Directed rotation student Daniel Sadowsky's research on SERS detection of polychlorinated biphenyls
- Directed undergraduate Courtney Jones' research on polycyclic aromatic hydrocarbon detection via modified SERS substrate
- Directed undergraduate Chelsea DeRuyter's research on microcontact printing for the fabrication of novel SERS substrates
- Directed undergraduate Ivan Lenov's summer research on SERS of bisphenol-A and electrochemical analysis of self-assembled monolayers on SERS substrates
- Directed undergraduate Özge Kurtulus' summer research on creating novel nanorod SERS substrates for detection of PGD<sub>2</sub>.
- Directed undergraduate Heidi Nelson's research on utilizing localized surface plasmon resonance to determine the packing efficiency of alkanethiol monolayers on SERS substrates.